Numerical Methods for Fluid-Structure Interaction: Analysis and Simulations

by

Yue Yu

A dissertation submitted in partial fulfillment of the
requirements for the degree of Doctor of Philosophy
in the Division of Applied Mathematics at Brown University

PROVIDENCE, RHODE ISLAND

May 2014

Abstract of "Numerical Methods for Fluid-Structure Interaction: Analysis and Simulations" by Yue Yu, Ph.D., Brown University, May 2014

In recent years, there has been great interest in fluid-structure interaction (FSI) problems due to their relevance in structural engineering and biomedical applications. However, several difficulties have hindered the development of partitioned FSI algorithms in large-scale simulations: the relatively small values of the mass ratio between the arterial wall and the blood will cause instabilities in coupled solvers; the arterial wall responses are very complicated therefore difficult to be described by classical structural models; accurate simulations in patient-specific geometries require large CPU time; and so on. To resolve these difficulties, design and analysis of efficient and stable numerical schemes for structure solver, fluid solver, and fluid-structure interaction procedure are considered in this thesis, with contributions on:

- developing and accelerating the spectral/*hp* element method structure solvers for linear elastic, hyperelastic and viscoelastic models;
- validating the spectral/*hp* element method fluid solver in image-based computational biofluid mechanics;
- stabilizing the partitioned fluid-structure interaction procedure and resolving the added-mass effect;
- developing and employing fractional PDEs solvers to model the complex biomechanical viscoelastic properties of patient-specific arteries.

Specifically, on the structure side firstly a *mixed formulation* for nearly incompressible nonlinear elasticity is investigated, which has superior accuracy and efficiency compared with the displacement-only formulation. Moreover, a *semi-local* solver is developed for spectral/*hp* element discretization of the linear elasticity equations, from which we obtain good scalability in large scale parallel computing. To better capture the complex biomechanical viscoelastic properties of soft tissue in arteries, the governing equations for structure are extended to fractional viscoelasticity models, and their sensitivities to the patient-specific viscoelastic coefficients are numerically investigated. On the fluid side, the spectral element method solver is validated by comparing the simulation results with clinical angiographic images and with numerical solutions from other research groups. Lastly, two new schemes (*fictitious methods* and *stabilized explicit algorithm*) for fluid-structure interaction (FSI) are designed to stabilize and accelerate the communications between fluid and structure solvers, with analysis for choosing the optimal coefficients provided. To validate the optimal coefficient analysis, the FSI framework is applied to patient-specific aneurysms and also to deepwater offshore risers covered with fairings, hence demonstrating the general applicability of the developed methodology.

© Copyright 2014 by Yue Yu

This dissertation by Yue Yu is accepted in its present form
by the Division of Applied Mathematics as satisfying the
dissertation requirement for the degree of Doctor of Philosophy.

Date_____ _____

George Em Karniadakis, Advisor

Recommended to the Graduate Council

Date_____ _____

Marco Lucio Bittencourt, Reader

Date_____ _____

Johnny Guzman, Reader

Date_____ _____

Martin Maxey, Reader

Approved by the Graduate Council

Date_____ _____

Peter M. Weber, Dean of the Graduate School

Acknowledgments

This thesis would not have come to fruition without the help of many important individuals. In particular, I want express my gratitude to the following people:

I first would like to express my special and tremendous thanks to my advisor, Professor George Em Karniadakis, who has leaded me to grow as a scientist and also an individual. With his countless hours in advising and encouraging me in my research, he helped me to make this thesis possible. He is the one who has taught me what research is and how to do it. I could not thank him enough for his motivation, guidance, and correction which have supported me for years and will continue inspiring me in the future. With his curiosity, insight into problems, and methodology, he will always be my academic idol.

I also want to deeply thank Professor Marco Lucio Bittencourt, Professor Johnny Guzman and Professor Martin Maxey, for their great help and precious advice towards the thesis, and also for teaching me the courses and introducing me to the field of finite element method and fluid mechanics. I am very thankful to Professor Marco Lucio Bittencourt for his numerous of valuable advices and guidance over these five years. He is the one who has taught me hand by hand from the beginning of my research. I want to express my gratitude to Professor Johnny Guzman, for his comments, suggestions and ideas during our collaboration. His mentoring truly had a positive impact in my academic life. Professor Martin Maxey has been patient and available for every meeting I have with him. He is the one who has taught me biophysics and his insights in fluid mechanics have amazed me all the time.

I extend my thanks to Professor Peter Richardson and Professor Chiwang Shu, for their supports and encouragements. I owe many thanks to Professor Peter Richardson for his considerate mentoring and answers, and also for the warm family atmosphere. He has directed every of my steps in my years at Brown, and I will always respect him as a kind and amiable grandfather. Professor Chiwang Shu has guided and encouraged me whenever I felt lost or low. I was very lucky to meet such a nice teacher.

I would like to express my appreciation to all the faculties, staff and students in the Division of Applied Math for providing me such a nice academic environment and countless help as well. I want to thank my fellows and friends in the crunch group for their support and help in my graduate study, and for laugthers and meals that I have shared with them. I also acknowledge that this work was not possbile without codes and tools which have been developed by many previous crunch members. I want to especially thank Professor Steve Dong, Dr. Hyoungsu Baek, Dr. Leopold

Grinberg and Paris Perdikaris for their development and guidance into the details of the spectral element method and NEKTAR.

Special thanks go to my collaborators for sharing their results and thoughts. I am also deeply thankful to NSF, NIH, Brown graduate school and the Simon Ostrach fellowship for their funding and fellowship support.

Last, and most importantly, I wish to thank my parents for their love, understanding, encouragement, and support. It would have been impossible for me to finish this work without them.

Contents

List of Tables

List of Figures

Chapter 1

Introduction

Cerebral aneurysm is pathological dilatation of intracranial artery, and its rupture is the leading cause of subarachnoid hemorrage [2]. However, the current clinical technology could not provide a lot of detailed information *in vivo*. Computational simulations then appear as an effective alternative approach for understanding the mechanisms behind aneurysm growth and rupture, which rely heavily on the fluid-structure interaction (FSI) methods. Regarding the numerical approaches, the high-order spectral/*hp* element method has demonstrated particular advantages because of its high resolution in space which makes it possible to capture the complicated patient-specific aneurysm geometry, and to predict possible flow instabilities. Moreover, similar FSI coupling approaches are also required in offshore engineering, and in particular in vortex-induced vibrations of long rises. Therefore, this thesis will focus on developing and bringing to real-life applications high-fidelity and high-performance numerical tools for fluid-structure interaction, with spectral/*hp* element methods.

To accelerate the structure solver, we first present a mixed formulation for high-order spectral/*hp* element methods in chapter 2.1, and investigate its stability in large strain analysis of nearly incompressible solids. Specifically, we employ the displacement/pressure formulation and use a pressure projection method along with general Jacobi polynomial bases to derive the discrete equations. We first study the convergence of the method for smooth and singular solutions of elastic and hyperelastic problems for various combinations of mixed elements. Subsequently, we investigate numerically the validity of ellipticity and *inf-sup* conditions for various test problems including cases with large deformation. We find that the *inf-sup* condition is satisfied even when the pressure interpolation order O_p is equal to the displacement order O_u, but to resolve the locking-free behavior it is required that $O_p = O_u - 1$, and this choice also gives the best convergence rate. In large deformation analysis, surprisingly the results are more stable for $O_u \geq O_p \geq O_u - k$ because the ellipticity

in kernel is better satisfied, with higher k as O_u increases. Compared to the displacement-only formulation, the mixed formulation seems to have superior accuracy and it is overall more efficient, especially for problems with high bulk modulus.

Moreover, in the simulations we have realized that the conjugate gradient procedure in the structure solver is a bottle-neck for efficiency. In chapter 2.2 we therefore develop an efficient semi-local method for speeding up the solution of linear systems arising in spectral/hp element discretization of the linear elasticity equations. The main idea is to approximate the element-wise residual distribution with a new localization operator, and subsequently solve the local linear system. Additionally, we decouple the three directions of displacement in the localization operator, hence enabling the use of an efficient low energy preconditioner for the conjugate gradient solver. In numerical tests, we verify that there is no loss of accuracy in the semi-local method, and we obtain good parallel scalability and substantial speed-up compared to the original formulation. In particular, our tests of fluid-structure interaction problems modeling a 3D patient-specific brain aneurysm show that this semi-local method benefits the partitioned FSI procedure without increasing the required subiteration numbers in each time step.

Furthermore, we develop fundamental new numerical methods for fractional order PDEs, and investigate the fractional order models for arterial walls in chapter 2.3. Specifically, the arterial wall is a heterogeneous soft tissue with complex biomechanical properties, and its constitutive laws are typically derived using integer-order differential equations. However, recent simulations on 1D model [3] have indicated that fractional order models may offer a more powerful alternative for describing arterial wall mechanics, because they are less sensitive to the parameter estimation compared with the integer-calculus-based models. We study the specific fractional PDEs that better model the properties of the 3D arterial walls, and for the first time employ them into FSI simulations for patient-specific arterial flows in chapter 4.3.

We now turn to the fluid side in chapter 3.1, in which we investigate the predictive capacity of the image-based computational fluid dynamics model for the study of blood flow dynamics. Firstly, to see if the model indeed reproduces the *in vivo* hemodynamic environment, we develop a parallel advection-diffusion solver with high-order spectral/hp element method and mimic the dye injection procedure. For the purpose of validating patient-specific CFD models, a time-series of virtual angiographic images is constructed from the computed 3D contract agent flow dynamics, and is shown to be in excellent agreement with the corresponding clinical images. To further validate our solver directly, we participated in the CFD challenge workshop organized by Prof David Steinman [1]. The sensitivity of CFD predictions to different solvers is evaluated across many research groups, by comparing the blood flow simulation results on the same giant aneurysm geometry

but with different numerical solvers. Concordance of pressure drop predictions are obtained in the comparison across a wide range of solvers and solution strategies.

To stabilize the fluid-structure interaction solver, in chapter 4.1 we present a new fictitious pressure method for fluid-structure interaction (FSI) problems in incompressible flow, by generalizing the fictitious mass and damping methods published previously in [4]. The fictitious pressure method involves modification of the fluid solver whereas the fictitious mass and damping methods modify the structure solver. We analyze *all* fictitious methods for simplified problems and obtain explicit expressions for the optimal reduction factor (convergence rate index) at the FSI interface [5]. This analysis also demonstrates an apparent similarity of fictitious methods to the FSI approach based on Robin boundary conditions, which have been found to be very effective in FSI problems. We implement all methods, including the semi-implicit Robin based coupling method, in the context of spectral element discretization, which is more sensitive to temporal instabilities than low-order methods. In numerical tests, we verify the selection of optimal values for the fictitious parameters for simplified problems and for vortex-induced vibrations (VIV) even at zero mass ratio ("for-ever-resonance"). We also develop an empirical *a posteriori* analysis for complex geometries and apply it to 3D patient-specific flexible brain arteries with aneurysms for very large deformations. We demonstrate that the fictitious pressure method enhances stability and convergence, and is comparable or better in most cases to the Robin approach or the other fictitious methods.

Although the fictitious methods have successfully stabilized the FSI solver, it could only be applied on the implicit coupling procedure where subiterations are employed in each time step. In section 4.2 we further develop a new stabilized explicit coupling partitioned scheme for the fluid-structure interaction problem, to the case where the pressure and velocity are decoupled, i.e. the fluid part is solved with projection methods. Specifically, proper penalty terms are applied on the displacement, pressure and velocity solvers separately, to control the variations at the interface. Using energy stability analysis, it can be shown that the scheme is stable independent of the fluid-structure density ratio. Numerical examples are provided to show that although the penalty terms will degrade the time accuracy of the scheme to half order, optimal accuracy can be recovered by performing defect-correction subiterations. On vortex-induced vibration problems the performance of this stabilized explicit algorithm is investigated for low fluid-structure density ratios, and very stable results are achieved.

On the other hand, we extend the fictitious methods into an important application for offshore oil operations–fairings, and quantify numerically for the first time various salient features of free-to-rotate devices for VIV suppression and relate them to modified flow structures in the near wake. Specifically, fairings are nearly-neutrally buoyant devices, which are fitted along the axis of long

circular risers to suppress vortex-induced vibrations (VIV) and possibly reduce the drag force. In chapter 4.4 we study numerically how VIV can be practically eliminated by using free-to-rotate fairings. Since the rotational inertia is low for the fairings, direct numerical simulations based on standard fluid-structure interaction algorithms may fail because of the so-called added mass effect. With the fictitious inertia method we successfully stabilize the simulations. We then investigate the effect of rotational friction C_f on the stabilization effect of the fairings. In particular, we find that when the Reynolds number is low (Re=100), $C_f = 0$ is the most effective choice in suppressing VIV. Moreover, at this low Reynolds number there exists a critical value of C_f around which large oscillations and non-symmetric trajectories are observed. On the other hand, at higher Reynolds number (Re=500) a different behavior emerges, i.e. VIV are suppressed continuously as C_f increases.

Lastly, we summarize in chapter 5, and suggest several problems as a natural next step.

Chapter 2

Solid Mechanics: Models and Algorithms

2.1 Mixed formulation for nearly-incompressible nonlinear elasticity

2.1.1 Overview and difficulties

High-order finite elements, especially the $p-$ and $hp-$versions, lead to exponential convergence rate for smooth solutions and for singular solutions ($hp-$version) [6, 7, 8, 9]; they also enable flexibility in discretization as their accuracy does not depend strongly on the aspect ratio of the elements [6]. In the field of solid mechanics, $p-$FEM and $hp-$FEM have been studied theoretically [10, 11, 12, 13, 14, 15] for linear elasticity, and numerical results have been provided for hyperelastic [16, 17, 18] and plastic materials [19], exhibiting locking-free behavior for both nearly-incompressible [12, 17, 18] and plate/shell problems [13, 20, 21, 22, 23, 24, 25, 26].

From the numerical standpoint, the spectral/hp element version based on general Jacobi polynomials provides further flexibility in generating elements (e.g., hexahedral, tetrahedral, triangular prisms and even pyramids). Moreover, the polynomial basis is hierarchical and is well conditioned for enhanced computational efficiency and scalability. These aspects have led to the implementation of a displacement formulation of the method for linear elasticity and geometrically nonlinear problems in [27], where high accuracy and parallel scalability were demonstrated for several prototype problems as well as for arterial mechanics problems.

With regards to nearly incompressible problems, there are two main strategies for overcom-

ing volumetric locking: the displacement-only formulation with higher-order elements and the modified variational forms, including the mixed formulations and reduced integration methods. Both analytical and computational results were provided for the first strategy, e.g. [12, 17, 18], demonstrating that locking-free results can be obtained by using sufficiently high polynomial order O_u for displacement. However, when the Poisson ratio is close to 0.5 (or bulk modulus for hyperelastic materials satisfies $k \gg 1$), one has to increase O_u to resolve the volumetric locking problem, see, e.g. [12, 18]. On the other hand, the modified variational form does not have this problem, and hence it exhibits the correct approximability for both $h-$ and $p-$versions [10]. Among the methods of the second strategy there are several interesting modifications, e.g. enhanced strain formulations [28, 29, 30, 31, 32] and displacement/pressure formulations [10, 11, 15, 20, 33, 34, 35, 36, 37, 38, 39, 40, 41]. Here we will concentrate on the later. For the large deformation problems, these formulations were mainly applied to lower-order elements (usually $O_u \leq 3$), although combining the mixed formulations and high-order elements was proposed in the analysis of [10]. Also, the violation of ellipticity condition in large deformation problems was found for the displacement/pressure formulations but has not been investigated for different combinations of high-order elements, e.g. see [41, 42, 43]. Therefore, for large deformation problems, computational results of mixed formulation on high-order elements are needed to investigate both the locking phenomena and ellipticity condition. In addition, a reduced-integration method (noted also as reduced-constraint method in [15], or pressure projection method in [38, 39] and herein) for hyperelastic material was introduced by [38, 39], hence the displacement/pressure formulation can be reduced to displacement only without losing the similarity to mixed formulations [15].

We extend the method presented in [27] to fully nonlinear elastic problems with large deformations following a *mixed formulation* and using a pressure projection scheme [38, 39] unlike the displacement-only formulation employed in [27]. Unfortunately, the mixed formulation approach complicates both the numerical implementation as well as the theoretical framework of the method as compatibility of the spaces for the displacement and pressure fields should be established even for linear elasticity problems, e.g. see [33]. In addition, for large deformations the issue of ellipticity of the discrete formulation will be addressed following [41, 42], where the conditions for lower order elements were studied. To this end, upon formulating and implementing in 3D the mixed formulation, we set up several numerical tests that address these issues and highlight the fast convergence, the locking-free behavior, and the stability of the high-order mixed method in large deformation analysis of nearly incompressible solids. Compared to the displacement-only formulation of p-type finite elements presented in [17, 18], which also overcomes volume locking for sufficiently large interpolation order, our numerical results here demonstrate that the mixed formulation – despite

the aforementioned difficulties and the added computational efforts – seems to be more efficient, especially for problems with high values of the bulk modulus.

We consider the problem in Lagrangian coordinates $\mathbf{X}$, both for infinitesimal and finite deformations. Specifically, we aim to obtain the displacement field $\boldsymbol{\eta}(\mathbf{X})$ in a 3D solid domain $\Omega \subset \mathbf{R}^3$, with given traction and body forces, satisfying [44, 45]

$$\mathrm{div}(\mathbf{S}) + \mathbf{f} = 0 \tag{2.1.1}$$

in some weak sense, where $\mathbf{f}$ is the body force and $\mathbf{S}$ is the appropriate stress tensor. In our implementation, we employ the hierarchical shape functions based on Jacobi polynomials for spatial discretization (see Appendix A.1) to obtain high-order accuracy. In the mixed formulation, we introduce the hydrostatic pressure $p = \frac{tr\mathbf{S}}{3}$ into the equilibrium equation, and solve for $(\boldsymbol{\eta}, p)$ [41]. However, by introducing another variable p, the computational cost for inverting the linear system increases. To this end, we employ a pressure projection method [38, 39], by which we only need to compute (once or iteratively via Newton-Raphson in the nonlinear case) the linear system for the $\boldsymbol{\eta}$ part, while the pressure field is obtained from the displacement field [38].

The chapter is organized as follows: In section 2.1.2 we present briefly the linear and nonlinear material models we use, and in section 2.1.3 we present the weak formulation and the projection method. In section 2.1.4 we demonstrate the convergence rates of the method for linear and nonlinear elasticity problems. In sections 2.1.5-2.1.6 we present the main results, first focusing on the issue of stability in section 2.1.5, by investigating numerically the validity of the ellipticity and *inf-sup* conditions, then turning to the locking phenomena in section 2.1.6. We finish in section 2.1.7 with the main conclusions.

2.1.2 Material models

We mainly consider two models represented by the following strain energy density functions:

- Linear elastic model [44, 45]:

$$\Psi(\mathbf{E}) = \frac{\lambda}{2}(\mathrm{tr}\mathbf{E})^2 + \mu\mathbf{E} : \mathbf{E}, \tag{2.1.2}$$

where $\mathbf{E} = \frac{1}{2}\left(\left(\frac{\partial\boldsymbol{\eta}}{\partial\mathbf{X}}\right)^T + \left(\frac{\partial\boldsymbol{\eta}}{\partial\mathbf{X}}\right)\right)$ is the strain tensor, and μ, λ are the shear and Lame modulus, respectively.

- Mooney-Rivlin model [38, 39, 45]:

$$\Psi(\mathbf{E}) = A_{10}(I_1 J^{-2/3} - 3) + A_{01}(I_2 J^{-4/3} - 3) + \frac{k}{2}(J-1)^2, \tag{2.1.3}$$

where $\mathbf{E} = \frac{1}{2}\left(\left(\frac{\partial \boldsymbol{\eta}}{\partial \mathbf{X}}\right)^T + \left(\frac{\partial \boldsymbol{\eta}}{\partial \mathbf{X}}\right) + \left(\frac{\partial \boldsymbol{\eta}}{\partial \mathbf{X}}\right)^T \left(\frac{\partial \boldsymbol{\eta}}{\partial \mathbf{X}}\right)\right)$ is the Green Lagrange strain tensor, A_{10}, A_{01} are constants describing the behavior of the material, and k is the bulk modulus. Also I_1, I_2, J are related with the deformation gradient $\mathbf{F} = \mathbf{I} + \frac{\partial \boldsymbol{\eta}}{\partial \mathbf{X}}$ and the right Green deformation tensor $\mathbf{C} = \mathbf{F}^T\mathbf{F}$ as

$$I_1 = \mathrm{tr}(\mathbf{C}),\ I_2 = \frac{1}{2}((\mathrm{tr}\mathbf{C})^2 - \mathrm{tr}(\mathbf{C}^2)),\ J = \det(\mathbf{F}).$$

This model is a simple isotropic approximation for materials with rubber-like properties [46], in the region of large deformation and large strain. In this expression, we separate the distortional and dilatational deformation using Penn's approach [47] as this facilitates the use of the pressure projection technique we will use in the next section; see also [38].

By using the hyper-elasticity relations, the second Piola-Kirchhoff stress tensor $\mathbf{S} = \frac{\partial \Psi}{\partial \mathbf{E}}$ for these two cases can be expressed as

- Linear elastic model:

$$\mathbf{S} = \lambda(\mathrm{tr}\mathbf{E})\mathbf{I} + 2\mu\mathbf{E}. \tag{2.1.4}$$

- Mooney-Rivlin model:

$$\begin{aligned}\mathbf{S} =& 2A_{10}J^{-2/3}\mathbf{I} + 4A_{01}J^{-4/3}((\mathrm{tr}\mathbf{E}+1)\mathbf{I} - \mathbf{E}) \\ &+ (-\frac{2}{3}A_{10}I_1J^{-2/3} - \frac{4}{3}A_{01}I_2J^{-4/3} + kJ(J-1))\mathbf{C}^{-1}.\end{aligned} \tag{2.1.5}$$

After introducing the hydrostatic pressure p, the models can be re-written as

- Linear elastic model [33]:

$$\Psi(\mathbf{E}) = \frac{p}{2}\mathrm{tr}\mathbf{E} + \mu\mathbf{E} : \mathbf{E}, \tag{2.1.6}$$

where the hydrostatic pressure $p = \lambda \mathrm{tr}\mathbf{E}$.

- Mooney-Rivlin model [45]:

$$\Psi(\mathbf{E}) = A_{10}(I_1 J^{-2/3} - 3) + A_{01}(I_2 J^{-4/3} - 3) + \frac{p}{2}(J-1), \tag{2.1.7}$$

where the hydrostatic pressure $p = k(J-1)$, and the last term corresponds to the "material constraint" [48].

Correspondingly, the second Piola-Kirchhoff stress tensor $\mathbf{S} = \frac{\partial \Psi}{\partial \mathbf{E}}$ related with the hydrostatic pressure can be expressed as

- Linear elastic model:

$$\mathbf{S} = p\mathbf{I} + 2\mu\mathbf{E}. \tag{2.1.8}$$

- Mooney-Rivlin model:

$$\begin{aligned}\mathbf{S} =& 2A_{10}J^{-2/3}\mathbf{I} + 4A_{01}J^{-4/3}((\mathrm{tr}\mathbf{E}+1)\mathbf{I} - \mathbf{E}) \\ &+ (-\frac{2}{3}A_{10}I_1J^{-2/3} - \frac{4}{3}A_{01}I_2J^{-4/3} + Jp)\mathbf{C}^{-1}.\end{aligned} \tag{2.1.9}$$

2.1.3 Formulation

Next, we will derive the formulation for solving the displacement field $\boldsymbol{\eta}(\mathbf{X})$ in a three dimensional object occupying domain $\Omega \subset \mathbf{R}^3$ with boundary $\partial\Omega = \partial\Omega_D \cup \partial\Omega_N$. Here Dirichlet type boundary conditions are provided on $\partial\Omega_D$, Neumann type boundary conditions (traction) on $\partial\Omega_N$, Ω stands for the initial configuration of the object, and Ω_e stands for the initial configuration of each element.

Linear elastostatics

First, we consider infinitesimal deformations. The weak form of the equilibrium equation can be expressed as follows [44]:

$$\int_\Omega \mathbf{S} : \nabla\mathbf{v} d\Omega - \int_{\partial\Omega_N} \mathbf{T}\cdot\mathbf{v} d\Gamma - \int_\Omega \rho\mathbf{f}\cdot\mathbf{v} d\Omega = 0,\ \forall\mathbf{v}\in\mathbf{U}_0, \tag{2.1.10}$$

where the displacement field $\boldsymbol{\eta}(\mathbf{X}) \in \mathbf{U} = \{\mathbf{w}(\mathbf{X}) \in [H^1(\Omega)]^3 | \mathbf{w}(\mathbf{X}) = \boldsymbol{\eta}_D(\mathbf{X}) \text{ on } \partial\Omega_D\}$, and $\mathbf{U}_0 = \{\mathbf{w}(\mathbf{X}) \in [H^1(\Omega)]^3 | \mathbf{w}(\mathbf{X}) = \mathbf{0} \text{ on } \partial\Omega_D\}$. $\mathbf{S}$, $\mathbf{T}$, $\mathbf{f}$ and ρ are the stress tensor, external traction force (non-follower load) on $\partial\Omega_N$, external body force, and mass density, respectively.

For the linear elastic model (2.1.2), we can rewrite the problem as follows [33]: find the displacement field $\boldsymbol{\eta}(\mathbf{X}) \in \mathbf{U}$ such that

$$\mu\int_\Omega \epsilon(\boldsymbol{\eta}) : \epsilon(\mathbf{v}) d\Omega + \lambda\int_\Omega \mathrm{div}(\boldsymbol{\eta})\,\mathrm{div}(\mathbf{v}) d\Omega - \int_{\partial\Omega_N} \mathbf{T}\cdot\mathbf{v} d\Gamma - \int_\Omega \rho\mathbf{f}\cdot\mathbf{v} d\Omega = 0, \quad \forall\mathbf{v}\in\mathbf{U}_0, \tag{2.1.11}$$

where the operator ϵ is defined as $\epsilon(\cdot) = \frac{1}{2}\left(\left(\frac{\partial(\cdot)}{\partial\mathbf{X}}\right)^T + \left(\frac{\partial(\cdot)}{\partial\mathbf{X}}\right)\right)$. We will refer to the above form as

the *displacement formulation*. For the discretization of (2.1.11), one can see [27] for details.

For the *mixed formulation*, model (2.1.6) is considered. Problem (2.1.11) should be modified following [33]:

$$\mu \int_\Omega \epsilon(\boldsymbol{\eta}) : \epsilon(\mathbf{v}) d\Omega + \int_\Omega p \operatorname{div}(\mathbf{v}) d\Omega - \int_{\partial\Omega_N} \mathbf{T} \cdot \mathbf{v} d\Gamma - \int_\Omega \rho \mathbf{f} \cdot \mathbf{v} d\Omega = 0, \quad \forall \mathbf{v} \in \mathbf{U}_0, \tag{2.1.12}$$

along with the weak form of the definition for hydrostatic pressure p:

$$\int_\Omega \operatorname{div}(\boldsymbol{\eta}) q d\Omega = \frac{1}{\lambda} \int_\Omega p q d\Omega, \quad \forall q \in L^2(\Omega). \tag{2.1.13}$$

Next, we consider the discretization of (2.1.12). Based on the shape functions defined in Appendix A.1, on each element we expand the displacement $\boldsymbol{\eta}_e = ((\eta_e)_1, (\eta_e)_2, (\eta_e)_3)$ and the test function $\mathbf{v}_e = ((v_e)_1, (v_e)_2, (v_e)_3)$:

$$(\eta_e)_i(\mathbf{X}) = \sum_{k=1}^{(N_e)_u} (\hat{\eta}_e)_{ik} \phi_k(\mathbf{X}), \quad (v_i)_e(\mathbf{X}) = \sum_{k=1}^{(N_e)_u} (\hat{v}_e)_{ik} \phi_k(\mathbf{X}), \quad i = 1, 2, 3, \tag{2.1.14}$$

where $(N_e)_u$ is the total number of shape functions for displacement on this element, $\phi_k(\mathbf{X})$ are the shape functions, and $(\hat{\eta}_e)_{ik}$, $(\hat{v}_e)_{ik}$ are the expansion coefficients. For the local hydrostatic pressure p_e, with the set of shape functions for pressure $\{\phi_k(\mathbf{X}),\, k = 1, \cdots, (N_e)_p\} \subseteq \{\phi_k(\mathbf{X}),\, k = 1, \cdots, (N_e)_u\}$, we can expand the pressure p_e:

$$p_e(\mathbf{X}) = \sum_{k=1}^{(N_e)_p} (\hat{p}_e)_k \phi_k(\mathbf{X}), \tag{2.1.15}$$

where $(\hat{p}_e)_k$ are the corresponding expansion coefficients.

Following the steps in [38], we carry out the projection of the hydrostatic pressure p_e at the element level onto the selected pressure function space. For the linear case, this reduced constraint method is actually equivalent to the mixed formulation [15]. Here we consider the problem of approximating p_e at the element level in a least-squares sense, by a linear combination of a sequence of shape functions $\{\phi_k(\mathbf{X}),\, k = 1, \cdots, (N_e)_p\}$ in $L^2(\Omega_e)$ as in (2.1.15). That is, we choose

$$\mathbf{P}_e = [(\hat{p}_e)_1,\ \cdots,\ (\hat{p}_e)_k,\ (\hat{p}_e)_{k+1},\ \cdots,\ (\hat{p}_e)_{(N_e)_p}]^T. \tag{2.1.16}$$

to minimize

$$||p_e - \mathbf{Q}\mathbf{P}_e||^2_{L^2(\Omega_e)} \tag{2.1.17}$$

where $||\cdot||_{L^2(\Omega_e)}$ is the L^2 norm in the element domain Ω_e and

$$\mathbf{Q}(x) = [\phi_1(\mathbf{X}), \phi_2(\mathbf{X}), \cdots, \phi_{(N_e)_p}(\mathbf{X})]. \tag{2.1.18}$$

So the minimization leads to

$$(\mathbf{M}_e)_p \mathbf{P}_e = \mathbf{D}_e, \tag{2.1.19}$$

where the element mass matrix for the pressure is of size $(N_e)_p \times (N_e)_p$ as follows:

$$(\mathbf{M}_e)_p = \begin{bmatrix} m_{11} & \cdots & m_{1(N_e)_p} \\ \vdots & \ddots & \vdots \\ m_{(N_e)_p 1} & \cdots & m_{(N_e)_p (N_e)_p} \end{bmatrix}, \quad m_{ij} = \int_{\Omega_e} \phi_i \phi_j d\Omega_e, \tag{2.1.20}$$

and the right hand side of (2.1.19) is a vector of size $(N_e)_p$:

$$\begin{aligned} \mathbf{D}_e &= [\int_{\Omega_e} \phi_1 p_e d\Omega_e, \int_{\Omega_e} \phi_2 p_e d\Omega_e, \cdots, \int_{\Omega_e} \phi_{(N_e)_p} p_e d\Omega_e] \\ &= [\lambda \int_{\Omega_e} \phi_1 \mathrm{div} \boldsymbol{\eta}_e d\Omega_e, \lambda \int_{\Omega_e} \phi_2 \mathrm{div} \boldsymbol{\eta}_e d\Omega_e, \cdots, \lambda \int_{\Omega_e} \phi_{(N_e)_p} \mathrm{div} \boldsymbol{\eta}_e d\Omega_e] \\ &= \lambda ((\mathbf{K}_e)_p)^T \mathbf{U}_e, \end{aligned} \tag{2.1.21}$$

where the vector of unknown expansion coefficients for displacement $\mathbf{U}$ has length $3(N_e)_u$. In order to have smaller bandwidth for the coefficient matrix [27], it is organized in a way such that the three displacement components corresponding to a particular mode are adjacent, as follows:

$$\begin{aligned} &\mathbf{U}_e = [((\mathbf{U}_e)_1)^T \ \cdots, \ ((\mathbf{U}_e)_k)^T, \ ((\mathbf{U}_e)_{k+1})^T, \ \cdots, \ ((\mathbf{U}_e)_{(N_e)_u})^T]^T, \\ &(\mathbf{U}_e)_k = [(\hat{\eta}_e)_{1k}, \ (\hat{\eta}_e)_{2k}, \ (\hat{\eta}_e)_{3k}]. \end{aligned} \tag{2.1.22}$$

The pressure matrix $(\mathbf{K}_e)_p$ with size $3(N_e)_u \times (N_e)_p$ is composed of $(N_e)_u \times (N_e)_p$ numbers of 3×1 submatrices:

$$\begin{aligned} &(\mathbf{K}_e)_p = \begin{bmatrix} ((\mathbf{K}_e)_p)_{11} & \cdots & ((\mathbf{K}_e)_p)_{1(N_e)_p} \\ \vdots & \ddots & \vdots \\ ((\mathbf{K}_e)_p)_{(N_e)_u 1} & \cdots & ((\mathbf{K}_e)_p)_{(N_e)_u (N_e)_p} \end{bmatrix}, \\ &((\mathbf{K}_e)_p)_{ij} = [\int_{\Omega_e} \frac{\partial \phi_i}{\partial X} \phi_j d\Omega_e, \int_{\Omega_e} \frac{\partial \phi_i}{\partial Y} \phi_j d\Omega_e, \int_{\Omega_e} \frac{\partial \phi_i}{\partial Z} \phi_j d\Omega_e]^T, \\ &i = 1, \cdots, (N_e)_u, \quad j = 1, \cdots, (N_e)_p. \end{aligned} \tag{2.1.23}$$

Therefore, the element coefficients for the projected hydrostatic pressure should be

$$\mathbf{P}_e = \lambda((\mathbf{M}_e)_p)^{-1}((\mathbf{K}_e)_p)^T\mathbf{U}_e. \tag{2.1.24}$$

We assemble the local displacement expansion coefficients $\mathbf{U}_e$ of all elements into a global form $\mathbf{U}$ and upon substitution into (2.1.12), we obtain

$$-(\mathbf{K}_u + \mathbf{K}_u^*)\mathbf{U} + \mathbf{F} = 0, \tag{2.1.25}$$

where $\mathbf{K}_u$ is the stiffness matrix for $\mu\int_\Omega \epsilon(\boldsymbol{\eta}) : \epsilon(\mathbf{v})d\Omega$, and $\mathbf{K}_u^*$ corresponds to $\int_\Omega p\,\mathrm{div}(\mathbf{v})d\Omega$. Here, the $3(N_e)_u \times 3(N_e)_u$ matrix $(\mathbf{K}_e)_u$ for each element is organized into a matrix of $(N_e)_u \times (N_e)_u$ blocks, and the 3×3 submatrix $((\mathbf{K}_e)_u)_{ij}$ $(i,j = 1,\cdots,(N_e)_u)$ is given by $((\mathbf{K}_e)_u)_{ij} = \int_{\Omega_e}(\mathbf{D}\phi_i)^T\mathbf{B}(\mathbf{D}\phi_j)d\Omega_e$, where

$$\mathbf{D}\phi_i = \begin{bmatrix} \frac{\partial\phi_i}{\partial X} & 0 & 0 & \frac{\partial\phi_i}{\partial Y} & 0 & \frac{\partial\phi_i}{\partial Z} \\ 0 & \frac{\partial\phi_i}{\partial Y} & 0 & \frac{\partial\phi_i}{\partial X} & \frac{\partial\phi_i}{\partial Z} & 0 \\ 0 & 0 & \frac{\partial\phi_i}{\partial Z} & 0 & \frac{\partial\phi_i}{\partial Y} & \frac{\partial\phi_i}{\partial X} \end{bmatrix}^T, \quad \mathbf{B} = \mu\begin{bmatrix} 2\mathbf{I} & & \\ & \mathbf{I} & \\ & & \mathbf{I} \end{bmatrix}. \tag{2.1.26}$$

On the other hand, the matrix $\mathbf{K}_u^*$ is assembled based on local matrices from the element-wise pressure projections

$$(\mathbf{K}_e^*)_u = \lambda(\mathbf{K}_e)_p((\mathbf{M}_e)_p)^{-1}((\mathbf{K}_e)_p)^T. \tag{2.1.27}$$

On each element, the vector of the external forces $\mathbf{F}_e$ has the same length and ordering of indices as $\mathbf{U}_e$. That is, $\mathbf{F}_e = [((\mathbf{F}_e)_1)^T,\ \cdots,\ ((\mathbf{F}_e)_k)^T,\ ((\mathbf{F}_e)_{k+1})^T,\ \cdots,\ ((\mathbf{F}_e)_{(N_e)_u})^T]^T$, where $(\mathbf{F}_e)_k = [(F_e)_{1k},\ (F_e)_{2k},\ (F_e)_{3k}]$, $(F_e)_{ik} = \int_{\partial(\Omega_e)_N} T_i\phi_k d\Gamma_e + \int_{\Omega_e}\rho f_i\phi_k d\Omega_e$ and T_i, f_i $(i = 1,2,3)$ are the components of the external traction and body forces, respectively.

In the implementation, the contribution from known expansions (due to Dirichlet boundary conditions $\partial\Omega_D$) are moved to the right-hand-side before the equation is solved.

Although (2.1.25) is equivalent to solving the larger system $(\mathbf{U},\mathbf{P})$, the size of unknowns is by one-fourth smaller. For details on the iterative solution of the linear system, we refer the reader to [27].

Nonlinear elastostatics

Next we consider a solid object with finite deformation. Similar to the linear elastostatics, $\mathbf{X}$ stands for the position vector of a material point in the initial configuration Ω, and $\mathbf{x}(\mathbf{X})$ denotes the position vector in the deformed configuration. The weak form of displacement formulation for the

equilibrium is: find the displacement field $\boldsymbol{\eta}(\mathbf{X}) \in \mathbf{U} = \{\mathbf{w}(\mathbf{X}) \in [H^1(\Omega)]^3 | \mathbf{w}(\mathbf{X}) = \boldsymbol{\eta}_D(\mathbf{X}) \text{ on } \partial\Omega_D\}$ (where Ω_D denotes the Dirichlet boundary in the initial configuration), which satisfies

$$\begin{aligned}\mathcal{P}(\boldsymbol{\eta}) &= \int_\Omega \mathbf{S} : \frac{1}{2}\left(\left(\frac{\partial \mathbf{v}}{\partial \mathbf{X}}\right)^T \mathbf{F}(\boldsymbol{\eta}) + \mathbf{F}(\boldsymbol{\eta})^T \left(\frac{\partial \mathbf{v}}{\partial \mathbf{X}}\right)\right) d\Omega - \int_{\partial\Omega_N} \mathbf{T}\cdot\mathbf{v} d\Gamma - \int_\Omega \rho\mathbf{f}\cdot\mathbf{v} d\Omega \\ &= 0,\ \forall \mathbf{v} \in \mathbf{U}_0,\end{aligned} \tag{2.1.28}$$

where $\mathbf{U}_0$, $\mathbf{T}$, $\mathbf{f}$ and ρ have the same meaning as for linear elastostatics case, but with respect to the initial configuration. Note here that we assume the external $\mathbf{T}$ to be deformation-independent (i.e., non-follower load). Also, $\mathbf{F}(\boldsymbol{\eta})$ is the deformation gradient tensor defined as $\mathbf{F}(\boldsymbol{\eta}) = \frac{\partial \mathbf{x}}{\partial \mathbf{X}} = \mathbf{I} + \frac{\partial \boldsymbol{\eta}}{\partial \mathbf{X}}$.

To rewrite (2.1.28) into the mixed formulation framework, we consider $\mathbf{S}$ related with the hydrostatic pressure as in (2.1.9), and divide it into two parts: with and without the pressure term p. Although it can be generalized to other cases, here we take $\mathbf{S}$ as in (2.1.9), i.e., $\mathbf{S}$ can be divided as

$$\tilde{\mathbf{S}} = 2A_{10}J^{-2/3}\mathbf{I} + 4A_{01}J^{-4/3}((\text{tr}\mathbf{E}+1)\mathbf{I} - \mathbf{E}) + (-\frac{2}{3}A_{10}I_1J^{-2/3} - \frac{4}{3}A_{01}I_2J^{-4/3})\mathbf{C}^{-1}, \tag{2.1.29}$$

$$\overline{\mathbf{S}} = Jp\mathbf{C}^{-1}. \tag{2.1.30}$$

Correspondingly, the elasticity tensor $\mathcal{C} = \frac{\partial \mathbf{S}}{\partial \mathbf{E}}$ can also be divided into two parts (see [48, 40] for the explicit expressions for these two fourth-order tensor of Mooney-Rivlin model):

$$\tilde{\mathcal{C}} = \frac{\partial \tilde{\mathbf{S}}}{\partial \mathbf{E}}, \quad \overline{\mathcal{C}} = \frac{\partial \overline{\mathbf{S}}}{\partial \mathbf{E}}, \tag{2.1.31}$$

where $\mathbf{E}$ is the Green Lagrange strain tensor, with $\mathbf{E}(\boldsymbol{\eta}) = \frac{1}{2}(\mathbf{F}^T(\boldsymbol{\eta})\mathbf{F}(\boldsymbol{\eta}) - \mathbf{I})$. Also, $\overline{\mathcal{C}}$ can be further divided into two parts

$$\overline{\mathcal{C}} = \overline{\mathcal{C}}^1 + \overline{\mathcal{C}}^2, \quad \overline{\mathcal{C}}^1 = p\frac{\partial(J\mathbf{C}^{-1})}{\partial \mathbf{E}}, \quad \overline{\mathcal{C}}^2 = J\mathbf{C}^{-1}\frac{\partial p}{\partial \mathbf{E}}. \tag{2.1.32}$$

Following [27], we use $\mathcal{P}^{int}(\boldsymbol{\eta}, p)$ to denote the virtual work due to the internal stress, which is the first term in (2.1.28), and we use $\mathcal{P}^{ext}(\boldsymbol{\eta})$ to denote the last two terms, representing the virtual work due to the external forces. Separating the stress tensor and the elasticity tensor into

volumetric and distortional parts, we can rewrite (2.1.28) as

$$\begin{aligned}\mathcal{P}(\boldsymbol{\eta}, p) = &\int_\Omega (\tilde{\mathbf{S}}(\boldsymbol{\eta}) + \overline{\mathbf{S}}(\boldsymbol{\eta})) : \frac{1}{2}\left(\left(\frac{\partial \mathbf{v}}{\partial \mathbf{X}}\right)^T \mathbf{F}(\boldsymbol{\eta}) + \mathbf{F}(\boldsymbol{\eta})^T \left(\frac{\partial \mathbf{v}}{\partial \mathbf{X}}\right)\right) d\Omega \\ &- \int_{\partial\Omega_N} \mathbf{T}\cdot\mathbf{v} d\Gamma - \int_\Omega \rho\mathbf{f}\cdot\mathbf{v} d\Omega \\ =&0,\end{aligned} \tag{2.1.33}$$

which, along with the weak form of the definition for hydrostatic pressure p:

$$\int_\Omega (J(\boldsymbol{\eta}) - 1) q d\Omega = \frac{1}{k}\int_\Omega p q d\Omega, \quad \forall q \in L^2(\Omega), \tag{2.1.34}$$

forms a closed system for mixed formulation [45].

Assuming that p can be approximated by a function of $\boldsymbol{\eta}$ as in the linear case, in (2.1.33) $\mathcal{P}$ is nonlinear with respect to $\boldsymbol{\eta}$, so we need to solve for $\boldsymbol{\eta}$ iteratively. In our implementation we employed the Newton-Raphson iterative procedure. Let $\boldsymbol{\eta}^k$ denote the solution at the kth iteration, this procedure can be written as:

Loop over k until convergence is reached for a pre-specified tolerance:

1. Based on the known information $\boldsymbol{\eta}^k$, update the derivative of $\mathcal{P}$ with respect to $\boldsymbol{\eta}$, which is denoted as $\mathbb{D}\mathcal{P}[\boldsymbol{\eta}](\boldsymbol{\eta}^k)$.

2. Solve the following system of equations for the increment $\triangle\boldsymbol{\eta}$ with a linear solver:

$$\mathbb{D}\mathcal{P}[\boldsymbol{\eta}](\boldsymbol{\eta}^k)\triangle\boldsymbol{\eta} = -\mathcal{P}(\boldsymbol{\eta}^k), \quad \forall \mathbf{v} \in \mathbf{U}_0. \tag{2.1.35}$$

3. Update the solution

$$\boldsymbol{\eta}^{k+1} = \boldsymbol{\eta}^k + \triangle\boldsymbol{\eta}. \tag{2.1.36}$$

Before spatial discretization, we write out the explicit form for the derivative:

$$
\begin{aligned}
&\mathbb{D}\mathcal{P}[\boldsymbol{\eta}](\boldsymbol{\eta})(\triangle\boldsymbol{\eta}) \\
=&(\mathbb{D}\mathcal{P}^{int}[\boldsymbol{\eta}](\boldsymbol{\eta})+\mathbb{D}\mathcal{P}^{ext}[\boldsymbol{\eta}](\boldsymbol{\eta}))(\triangle\boldsymbol{\eta}) \\
=&\int_\Omega \frac{1}{2}\left(\left(\frac{\partial \mathbf{v}}{\partial \mathbf{X}}\right)^T \mathbf{F}(\boldsymbol{\eta})+\mathbf{F}(\boldsymbol{\eta})^T\left(\frac{\partial \mathbf{v}}{\partial \mathbf{X}}\right)\right):(\tilde{\mathcal{C}}(\boldsymbol{\eta})+\overline{\mathcal{C}}(\boldsymbol{\eta})):\frac{1}{2}\left(\left(\frac{\partial(\triangle\boldsymbol{\eta})}{\partial \mathbf{X}}\right)^T \mathbf{F}(\boldsymbol{\eta})\right. \\
&\left.+\mathbf{F}(\boldsymbol{\eta})^T\left(\frac{\partial(\triangle\boldsymbol{\eta})}{\partial \mathbf{X}}\right)\right)d\Omega+\int_\Omega(\tilde{\mathbf{S}}(\boldsymbol{\eta})+\overline{\mathbf{S}}(\boldsymbol{\eta})):\left(\left(\frac{\partial(\triangle\boldsymbol{\eta})}{\partial \mathbf{X}}\right)^T\left(\frac{\partial \mathbf{v}}{\partial \mathbf{X}}\right)\right)d\Omega \\
=&\int_\Omega \frac{1}{2}\left(\left(\frac{\partial \mathbf{v}}{\partial \mathbf{X}}\right)^T \mathbf{F}(\boldsymbol{\eta})+\mathbf{F}(\boldsymbol{\eta})^T\left(\frac{\partial \mathbf{v}}{\partial \mathbf{X}}\right)\right):(\tilde{\mathcal{C}}(\boldsymbol{\eta})+\overline{\mathcal{C}}^1(\boldsymbol{\eta})):\frac{1}{2}\left(\left(\frac{\partial(\triangle\boldsymbol{\eta})}{\partial \mathbf{X}}\right)^T \mathbf{F}(\boldsymbol{\eta})\right. \\
&\left.+\mathbf{F}(\boldsymbol{\eta})^T\left(\frac{\partial(\triangle\boldsymbol{\eta})}{\partial \mathbf{X}}\right)\right)d\Omega+\int_\Omega \frac{1}{2}\left(\left(\frac{\partial \mathbf{v}}{\partial \mathbf{X}}\right)^T \mathbf{F}(\boldsymbol{\eta})+\mathbf{F}(\boldsymbol{\eta})^T\left(\frac{\partial \mathbf{v}}{\partial \mathbf{X}}\right)\right):(J\mathbf{C}^{-1}\mathrm{d}p)d\Omega \\
&+\int_\Omega(\tilde{\mathbf{S}}(\boldsymbol{\eta})+\overline{\mathbf{S}}(\boldsymbol{\eta})):\left(\left(\frac{\partial(\triangle\boldsymbol{\eta})}{\partial \mathbf{X}}\right)^T\left(\frac{\partial \mathbf{v}}{\partial \mathbf{X}}\right)\right)d\Omega
\end{aligned}
\tag{2.1.37}
$$

where

$$
\mathrm{d}p=\frac{1}{2}kJ\mathbf{C}^{-1}:\left(\left(\frac{\partial(\triangle\boldsymbol{\eta})}{\partial \mathbf{X}}\right)^T \mathbf{F}(\boldsymbol{\eta})+\mathbf{F}(\boldsymbol{\eta})^T\left(\frac{\partial(\triangle\boldsymbol{\eta})}{\partial \mathbf{X}}\right)\right) \tag{2.1.38}
$$

with $\mathbf{C}^{-1}$ denoting the inverse of the right Green deformation tensor $\mathbf{C}$. Note that the external loads are deformation-independent under our assumption, thus $\mathbb{D}\mathcal{P}^{ext}[\boldsymbol{\eta}](\boldsymbol{\eta})=0$.

Similar to the linear elastostatics case, the discretization for the displacement formulation was detailed in [27]. For the mixed formulation, to discretize (2.1.35) in one element we expand $\triangle\boldsymbol{\eta}_e$ in terms of the shape functions as in (2.1.14):

$$
(\triangle\boldsymbol{\eta}_e)_i(\mathbf{X})=\sum_{k=1}^{(N_e)_u}(\triangle\hat{\eta}_e)_{ik}\phi_k(\mathbf{X}),\ i=1,2,3. \tag{2.1.39}
$$

Also, the local hydrostatic pressure p_e is expanded as in (2.1.15), while the increment of hydrostatic pressure $\mathrm{d}p_e$ is expanded as

$$
\mathrm{d}p_e(\mathbf{X})=\sum_{k=1}^{(N_e)_p}(\mathrm{d}\hat{p}_e)_k\phi_k(\mathbf{X}), \tag{2.1.40}
$$

where $(\triangle\hat{\eta}_e)_{ik}$ and $(\mathrm{d}\hat{p}_e)_k$ are the corresponding expansion coefficients.

Similarly as in the previous section, we carry out the projections on each element for both hydrostatic pressure p_e and its increment $\mathrm{d}p_e$. For the p_e part, we write the coefficients as in (2.1.16), and we minimize the function as in (2.1.17). So the minimization leads to (2.1.19) with

the element mass matrix for pressure the same as in (2.1.20) and the right hand side of size $(N_e)_p$:

$$\begin{aligned}\mathbf{D}_e &= \left[\int_{\Omega_e}\phi_1 p_e d\Omega_e, \int_{\Omega_e}\phi_2 p_e d\Omega_e, \cdots, \int_{\Omega_e}\phi_{(N_e)_p} p_e d\Omega_e\right] \\ &= \left[k\int_{\Omega_e}\phi_1(J(\boldsymbol{\eta}_e)-1)d\Omega_e, k\int_{\Omega_e}\phi_2(J(\boldsymbol{\eta}_e)-1)d\Omega_e, \cdots, k\int_{\Omega_e}\phi_{(N_e)_p}(J(\boldsymbol{\eta}_e)-1)d\Omega_e\right].\end{aligned} \tag{2.1.41}$$

Therefore, the projected hydrostatic pressure p_e^* can be approximated as

$$p_e^* = \mathbf{Q}((\mathbf{M}_e)_p)^{-1}\mathbf{D}_e. \tag{2.1.42}$$

For the increment of hydrostatic pressure, a similar procedure can be followed. We organize the coefficients $\mathbf{dP}_e$ for $\mathrm{d}p_e$ as in (2.1.16) and we minimize

$$||\mathrm{d}p_e - \mathbf{Q}\mathbf{dP}_e||^2_{L^2(\Omega_e)}, \tag{2.1.43}$$

to obtain

$$(\mathbf{M}_e)_p\mathbf{dP}_e = \mathbf{dD}_e, \tag{2.1.44}$$

with

$$\begin{aligned}\mathbf{dD}_e &= \left[\int_{\Omega_e}\phi_1 dp_e d\Omega_e, \int_{\Omega_e}\phi_2 dp_e d\Omega_e, \cdots, \int_{\Omega_e}\phi_{(N_e)_p} dp_e d\Omega_e\right]^T \\ &= \frac{k}{2}\left[\int_{\Omega_e}\phi_1 J\mathbf{C}^{-1} : \left(\left(\frac{\partial(\triangle\boldsymbol{\eta})_e}{\partial\mathbf{X}}\right)^T\mathbf{F}(\boldsymbol{\eta}) + \mathbf{F}(\boldsymbol{\eta})^T\left(\frac{\partial(\triangle\boldsymbol{\eta})_e}{\partial\mathbf{X}}\right)\right)d\Omega_e, \cdots,\right. \\ &\left.\int_{\Omega_e}\phi_{(N_e)_p} J\mathbf{C}^{-1} : \left(\left(\frac{\partial(\triangle\boldsymbol{\eta})_e}{\partial\mathbf{X}}\right)^T\mathbf{F}(\boldsymbol{\eta}) + \mathbf{F}(\boldsymbol{\eta})^T\left(\frac{\partial(\triangle\boldsymbol{\eta})_e}{\partial\mathbf{X}}\right)\right)d\Omega_e\right]^T \\ &= k((\mathbf{K}_e)_p)^T\triangle\mathbf{U}_e,\end{aligned} \tag{2.1.45}$$

where $\triangle\mathbf{U}_e$ are the coefficients for $\triangle\boldsymbol{\eta}_e$ organized in the same way as in (2.1.22), and the matrix $(\mathbf{K}_e)_p$ is a $3(N_e)_u \times (N_e)_p$ matrix organized into $(N_e)_u \times (N_e)_p$ matrix of blocks, with each block being a 3×1 submatrix $((\mathbf{K}_e)_p)_{ij}$ $(i = 1, \cdots, (N_e)_u,\ j = 1, \cdots, (N_e)_p)$:

$$((\mathbf{K}_e)_p)_{ij,m} = \sum_{k,l=1}^{3}\int_{\Omega_e} J\phi_j\mathbf{C}^{-1}_{kl}\frac{1}{2}\left(\frac{\partial\phi_i}{\partial X_k}\mathbf{F}_{ml} + \mathbf{F}_{mk}\frac{\partial\phi_i}{\partial X_l}\right)d\Omega_e, \qquad m = 1,2,3, \tag{2.1.46}$$

where $\mathbf{F}_{ij}$, $\mathbf{C}^{-1}_{ij}$ and X_i are the components for the deformation tensor $\mathbf{F}$, the inverse of the right Green deformation tensor $\mathbf{C}$ and the position vector in initial configuration $\mathbf{X}$, respectively.

Therefore, the projected increment for the hydrostatic pressure $\mathrm{d}p_e^*$ can be approximated as

$$\mathrm{d}p_e^* = k\mathbf{Q}((\mathbf{M}_e)_p)^{-1}((\mathbf{K}_e)_p)^T(\triangle\mathbf{U})_e. \tag{2.1.47}$$

Similarly as in (2.1.25), we assemble the local displacement expansion coefficients $(\triangle\mathbf{U})_e$ of all elements into the global form $\triangle\mathbf{U}$ and substitute it into (2.1.35), to obtain

$$(\mathbf{K}_u + \mathbf{K}_u^* + \mathbf{K}_u^{**})\triangle\mathbf{U} = \mathbf{R}_u, \tag{2.1.48}$$

where $\mathbf{K}_u$, $\mathbf{K}_u^*$ and $\mathbf{K}_u^{**}$ are the stiffness matrices for the discretization of

$$\begin{aligned}&\int_\Omega \frac{1}{2}\left(\left(\frac{\partial \mathbf{v}}{\partial \mathbf{X}}\right)^T \mathbf{F}(\boldsymbol{\eta}) + \mathbf{F}(\boldsymbol{\eta})^T\left(\frac{\partial \mathbf{v}}{\partial \mathbf{X}}\right)\right) : \tilde{\mathcal{C}}(\boldsymbol{\eta}) : \frac{1}{2}\left(\left(\frac{\partial(\triangle\boldsymbol{\eta})}{\partial \mathbf{X}}\right)^T \mathbf{F}(\boldsymbol{\eta}) + \mathbf{F}(\boldsymbol{\eta})^T\left(\frac{\partial(\triangle\boldsymbol{\eta})}{\partial \mathbf{X}}\right)\right) d\Omega \\ &+ \int_\Omega \tilde{\mathbf{S}}(\boldsymbol{\eta}) : \left(\left(\frac{\partial(\triangle\boldsymbol{\eta})}{\partial \mathbf{X}}\right)^T\left(\frac{\partial \mathbf{v}}{\partial \mathbf{X}}\right)\right) d\Omega,\end{aligned} \tag{2.1.49}$$

$$\begin{aligned}&\int_\Omega \frac{1}{2}\left(\left(\frac{\partial \mathbf{v}}{\partial \mathbf{X}}\right)^T \mathbf{F}(\boldsymbol{\eta}) + \mathbf{F}(\boldsymbol{\eta})^T\left(\frac{\partial \mathbf{v}}{\partial \mathbf{X}}\right)\right) : \overline{\mathcal{C}}^1(\boldsymbol{\eta}) : \frac{1}{2}\left(\left(\frac{\partial(\triangle\boldsymbol{\eta})}{\partial \mathbf{X}}\right)^T \mathbf{F}(\boldsymbol{\eta}) + \mathbf{F}(\boldsymbol{\eta})^T\left(\frac{\partial(\triangle\boldsymbol{\eta})}{\partial \mathbf{X}}\right)\right) d\Omega \\ &+ \int_\Omega \overline{\mathbf{S}}(\boldsymbol{\eta}) : \left(\left(\frac{\partial(\triangle\boldsymbol{\eta})}{\partial \mathbf{X}}\right)^T\left(\frac{\partial \mathbf{v}}{\partial \mathbf{X}}\right)\right) d\Omega,\end{aligned} \tag{2.1.50}$$

and

$$\int_\Omega \frac{1}{2}\left(\left(\frac{\partial \mathbf{v}}{\partial \mathbf{X}}\right)^T \mathbf{F}(\boldsymbol{\eta}) + \mathbf{F}(\boldsymbol{\eta})^T \cdot \left(\frac{\partial \mathbf{v}}{\partial \mathbf{X}}\right)\right) : (J\mathbf{C}^{-1}\mathrm{d}p) d\Omega \tag{2.1.51}$$

respectively.

Therefore, on each element the stiffness matrices $(\mathbf{K}_e)_u$ and $(\mathbf{K}_e^*)_u$ are $3(N_e)_u \times 3(N_e)_u$ matrix organized into $(N_e)_u \times (N_e)_u$ matrix blocks, with each block being a 3×3 submatrix $((\mathbf{K}_e)_u)_{ij}$ $(i, j = 1, \cdots, (N_e)_u)$ given by

$$\begin{aligned}((\mathbf{K}_e)_u)_{ij,ms} = &\sum_{p,q,k,l=1}^{3} \int_{\Omega_e} \frac{1}{2}\left(\frac{\partial \phi_i}{\partial X_p}\mathbf{F}_{mq} + \mathbf{F}_{mp}\frac{\partial \phi_i}{\partial X_q}\right)\tilde{\mathcal{C}}_{pqkl}\frac{1}{2}\left(\frac{\partial \phi_j}{\partial X_k}\mathbf{F}_{sl} + \mathbf{F}_{sk}\frac{\partial \phi_j}{\partial X_l}\right) d\Omega_e \\ &+ \delta_{ms}\sum_{p,q=1}^{3} \int_{\Omega_e} \tilde{\mathbf{S}}_{pq}\frac{\partial \phi_i}{\partial X_p}\frac{\partial \phi_j}{\partial X_q} d\Omega_e, \qquad m, s = 1, 2, 3,\end{aligned} \tag{2.1.52}$$

and

$$
\begin{aligned}
((\mathbf{K}_e^*)_u)_{ij,ms} = & \sum_{p,q,k,l=1}^{3} \int_{\Omega_e} \frac{1}{2}\left(\frac{\partial \phi_i}{\partial X_p}\mathbf{F}_{mq} + \mathbf{F}_{mp}\frac{\partial \phi_i}{\partial X_q}\right) \overline{\mathcal{C}}^{1*}_{pqkl} \frac{1}{2}\left(\frac{\partial \phi_j}{\partial X_k}\mathbf{F}_{sl} + \mathbf{F}_{sk}\frac{\partial \phi_j}{\partial X_l}\right) d\Omega_e \\
& + \delta_{ms} \sum_{p,q=1}^{3} \int_{\Omega_e} \overline{\mathbf{S}}^*_{pq} \frac{\partial \phi_i}{\partial X_p}\frac{\partial \phi_j}{\partial X_q} d\Omega_e, \qquad m,s = 1,2,3,
\end{aligned}
\tag{2.1.53}
$$

respectively. For the local matrix $(\mathbf{K}_e^{**})_u$ on each element, upon substitution of (2.1.47) into (2.1.51), we have

$$
\begin{aligned}
((\mathbf{K}_e^{**})_u)_{ij,ms} &= k \sum_{p,q=1}^{3} \sum_{a=1}^{(N_e)_p} \int_{\Omega_e} \frac{1}{2}\left(\frac{\partial \phi_i}{\partial X_p}\mathbf{F}_{mq} + \mathbf{F}_{mp}\frac{\partial \phi_i}{\partial X_q}\right) J(\mathbf{C}^{-1})_{pq}\phi_a (((\mathbf{M}_e)_p)^{-1}((\mathbf{K}_e)_p)^T)_{aj,s} d\Omega_e \\
&= k \sum_{p,q=1}^{3} \sum_{a=1}^{(N_e)_p} \int_{\Omega_e} \frac{1}{2}\left(\frac{\partial \phi_i}{\partial X_p}\mathbf{F}_{mq} + \mathbf{F}_{mp}\frac{\partial \phi_i}{\partial X_q}\right) J(\mathbf{C}^{-1})_{pq}\phi_a d\Omega_e (((\mathbf{M}_e)_p)^{-1}((\mathbf{K}_e)_p)^T)_{aj,s} \\
&= k \sum_{a=1}^{(N_e)_p} ((\mathbf{K}_e)_p)_{ia,m} (((\mathbf{M}_e)_p)^{-1}((\mathbf{K}_e)_p)^T)_{aj,s} \\
&= k((\mathbf{K}_e)_p((\mathbf{M}_e)_p)^{-1}((\mathbf{K}_e)_p)^T)_{ij,ms}.
\end{aligned}
\tag{2.1.54}
$$

In the above expressions, $\mathbf{F}_{ij}$, $\tilde{\mathbf{S}}_{ij}$, $\overline{\mathbf{S}}_{ij}$, $\tilde{\mathcal{C}}_{ijkl}$, $\overline{\mathcal{C}}_{ijkl}$, $(\mathbf{C}^{-1})_{ij}$ and X_i are the components for the deformation tensor $\mathbf{F}$, the distortional part of the second Piola-Kirchhoff tensor $\tilde{\mathbf{S}}$, the volumetric part $\overline{\mathbf{S}}$, the distortional part of elasticity tensor $\tilde{\mathcal{C}}$, the volumetric part $\overline{\mathcal{C}}$, the inverse of the right Green deformation tensor $\mathbf{C}$ and the position vector in initial configuration $\mathbf{X}$, respectively. Also, δ_{ms} stands for the Kronecker delta. The $*$ symbols for $\overline{\mathcal{C}}^{1*}_{pqkl}$ and $\overline{\mathbf{S}}^*_{pq}$ in (2.1.53) means they are dependent on the hydrostatic pressure p_e, while in these expressions the local hydrostatic pressure after projection p_e^* is substituted in.

Regarding the residual vectors on each element, in (2.1.48) the right-hand-side $(\mathbf{R}_e)_u$ has length $3(N_e)_u$, with the same ordering as $\triangle\mathbf{U}_e$. Similarly to what we did for $\mathcal{P}$, we can divide this vector into two contributions (here we denote its element as $((\mathbf{R}_e)_u)_{ij}$, $i = 1,2,3$ and $j = 1,\cdots,(N_e)_u$):

$$
(\mathbf{R}_e)_u = ((\mathbf{R}_e)_u)^{int} + ((\mathbf{R}_e)_u)^{ext}, \tag{2.1.55}
$$

where $((\mathbf{R}_e)_u)^{int}$ represents the contribution from the internal stress

$$
((\mathbf{R}_e)_u)^{int}_{ij} = -\sum_{k,l=1}^{3} \int_{\Omega_e} (\tilde{\mathbf{S}}_{kl} + \overline{\mathbf{S}}^*_{kl}) \frac{1}{2}\left(\frac{\partial \phi_j}{\partial X_k}\mathbf{F}_{il} + \mathbf{F}_{ik}\frac{\partial \phi_j}{\partial X_l}\right) d\Omega_e, \tag{2.1.56}
$$

and $((\mathbf{R}_e)_u)^{ext}$ represents the contribution from the external loads

$$((\mathbf{R}_e)_u)_{ij}^{ext} = \int_{\partial(\Omega_e)_N} T_i \phi_j d\Gamma_e + \int_{\Omega_e} \rho f_i \phi_j d\Omega_e. \tag{2.1.57}$$

Here $\overline{\mathbf{S}}$ is also marked with $*$ in (2.1.56) because the hydrostatic pressure after projection p_e^* is employed.

Correspondingly, the Newton-Raphson iterative procedure with pressure projection will be modified as follows:

Loop over k until the convergence tolerance is reached:

1. Based on the known information $\mathbf{U}^k$, update for the projected hydrostatic pressure p_e^*.
2. Update the volumetric stress tensor $\overline{\mathbf{S}}^*$ and volumetric elasticity tensor $\overline{\mathcal{C}}^{1*}$ based on (2.1.30) and (2.1.32).
3. Update the stiffness matrices (2.1.52), (2.1.53) and (2.1.54) if needed. Update the internal right hand side as in (2.1.56).
4. Solve (2.1.48) for the increment $\triangle\mathbf{U}$ with a linear solver.
5. Update for displacement
$$\mathbf{U}^{k+1} = \mathbf{U}^k + \triangle\mathbf{U}. \tag{2.1.58}$$

2.1.4 Convergence studies

Now we investigate the accuracy of the pressure projection method in nearly incompressible problems by comparing simulation results against analytical solutions.

Linear elastostatics

We first investigate the convergence of the scheme for linear elastostatic problems and solve the equilibrium equations for infinitesimal deformation (2.1.12) using the pressure projection method. Three kinds of convergence (p, h, hp) are studied for solutions with and without singularities. For the material properties, we will use Young's modulus E and the Poisson ratio ζ, which are related with the material properties λ and μ in (2.1.2) by

$$\mu = \frac{E}{2(1+\zeta)}, \quad \lambda = \frac{\zeta E}{(1+\zeta)(1-2\zeta)}. \tag{2.1.59}$$

Linear elastostatics with smooth solution: $p-$convergence

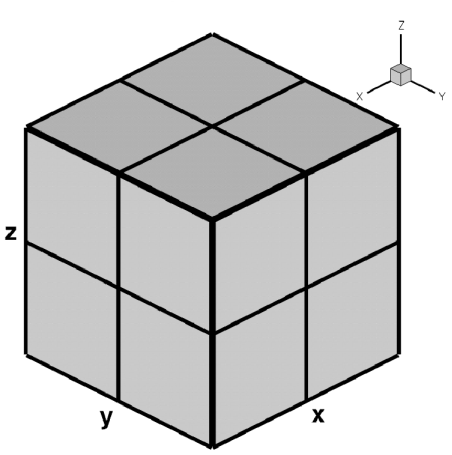

Figure 2.1: $p-$convergence test: cubic object discretized with 8 hexahedral elements.

To study the $p-$convergence, we consider the deformation of a cubic solid occupying the domain $0 \leq X \leq 1$, $0 \leq Y \leq 1$ and $0 \leq Z \leq 1$ discretized by 8 hexahedral elements as in Figure 2.1, where the thick solid lines mark the edges of the elements. For the test example, we use an analytic solution similar to [27], but with $\zeta = 0.49$, that is, which corresponds to nearly incompressible material. The displacements on the face $X = 0$ are

$$\eta_1 = 0.0, \quad \eta_2 = B \sin bY, \quad \eta_3 = 0, \tag{2.1.60}$$

where η_1, η_2 and η_3 are the displacements in X, Y and Z directions, respectively; also, B, b are prescribed constants. A traction force field, $\mathbf{T} = (T_1, T_2, T_3)$, is applied on the rest of the faces and is given by

$$\begin{aligned} &T_1 = n_x \lambda (aA(\frac{1}{\zeta} - 1) \cos aX + bB \cos bY), \; T_2 = n_y \lambda (bB(\frac{1}{\zeta} - 1) \cos bY + aA \cos aX), \\ &T_3 = n_z \lambda (aA \cos aX + bB \cos bY), \end{aligned} \tag{2.1.61}$$

where $\mathbf{n} = (n_x, n_y, n_z)$ is the outward-pointing unit vector normal to the surface, and A, a are also prescribed constants. A body force field, $\rho \mathbf{f} = (f_1, f_2, f_3)$ is applied on the solid with components:

$$f_1 = \frac{\lambda(1-\zeta)}{\zeta} a^2 A \sin aX, \quad f_2 = \frac{\lambda(1-\zeta)}{\zeta} b^2 B \sin bY, \quad f_3 = 0. \tag{2.1.62}$$

This problem has the following analytic solution for the displacement of the object:

$$\begin{cases} \eta_1 &= A \sin aX, \\ \eta_2 &= B \sin bY, \\ \eta_3 &= 0, \end{cases} \tag{2.1.63}$$

so we see that the object is not totally incompressible ($p = \lambda(aA \cos aX + bB \cos bY)$).

In our test, we use the following parameters:

$$A = B = 0.2,\ a = b = 5.0,\ E = 1000,\ \zeta = 0.49, \tag{2.1.64}$$

to study the convergence behavior. We first vary the element order O_u for displacement (i.e., highest polynomial degree in the expansions) from 1 to 10, for various pressure orders $O_p = 0$, 1, 3, 5, as in the upper plots of Figure 2.2. Then in the lower plots, for fixed displacement orders $O_u = 4$, 6, 8, 10 we show the results for different choices of pressure orders O_p. To compare the computational errors with respect to the exact solution, for each element order pair (O_u, O_p) we calculate the relative errors for pressure in the L^2 norm, and for displacement in the energy norm as follows

$$e_p = \frac{||p_a - p_c||_2}{||p_a||_2}, \quad e_u = \frac{||\boldsymbol{\eta}_a - \boldsymbol{\eta}_c||_E}{||\boldsymbol{\eta}_a||_E}, \tag{2.1.65}$$

where $p_a = \lambda \text{div}(\boldsymbol{\eta}_a)$ and $\boldsymbol{\eta}_a$ are the analytic solutions for pressure and displacement, respectively, while p_c and $\boldsymbol{\eta}_c$ are results from computation. We plot these errors in logarithmic scale, as a function of O_u (or O_p in the lower plots) which is in linear scale.

From the upper plots of Figure 2.2, we see that for every fixed interpolation order O_p of pressure, the computational results do not converge to the analytic solution when O_u increases. On the other hand, in the lower plots, for each fixed O_u considered approximately straight lines are obtained in the range of $O_p < O_u$, indicating that the numerical errors decrease exponentially fast as the element order O_p for pressure increases. So for slightly compressible problems, the element order O_p for pressure is more important for obtaining accurate results. Also, as shown in the upper right plot, for each fixed O_p, the two cases with $O_u = O_p$ and $O_u = O_p + 1$ give the best results for displacement. Combining these results with results of the the upper left plot, which shows that $O_u = O_p$ gives the largest pressure error, we can see that in this test $O_u = O_p + 1$ is the best choice for accuracy.

Linear elastostatics with smooth solution: $h-$convergence

Now we focus on the $h-$convergence on the problem described in equations (2.1.60)-(2.1.63)

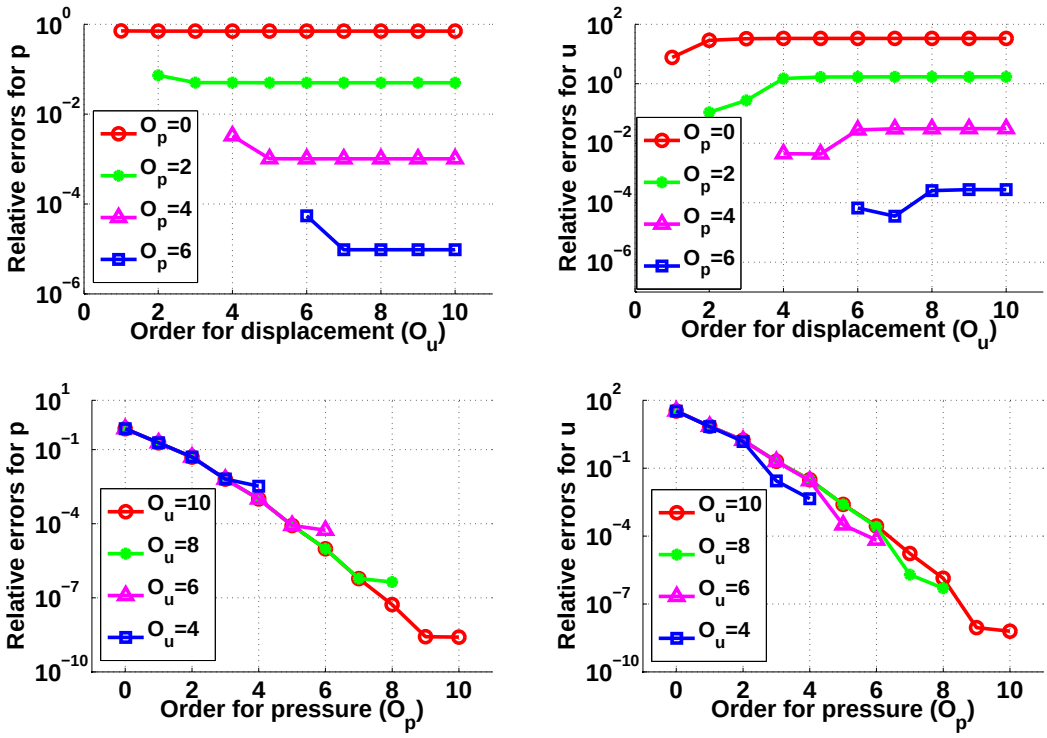

Figure 2.2: $p-$refinement test for the smooth problem in linear case: upper: relative errors as a function of the element order O_u for displacement; lower: relative errors as a function of the element order O_p for pressure; left column: relative errors for pressure; right column: relative errors for displacement.

using uniform tesselations with $i \times i \times i$ $(i = 1, 2, \cdots, 8)$ hexahedral elements, while $i = 2$ was used for all cases in the $p-$convergence tests (seeing Figure 2.1). The displacement order $O_u = 5$ is employed here while runs with four choices of pressure orders $O_p = 1, 3, 4, 5$ are tested. Similar to the $p-$convergence tests, in Figure 2.3 we calculate the relative errors of pressure and displacement in appropriate norms. We plot these errors in logarithmic scale as a function of element size $h = \frac{1}{i}$ which is in inverse logarithmic scale.

From Figure 2.3, we see that in most of cases, a fixed element order O_p for pressure gives a $O_p + 1$ order accuracy for $h-$convergence, except when $O_p = O_u$ which shows an O_p order. The results, especially those for the case of $O_p = O_u - 2$, are consistent with the analysis in [10, 15]. Also, the right plot shows a 5.5 order accuracy with the choice $O_p = O_u - 1 = 4$ (green curve), which is the best convergence rate we obtain from $h-$refinement in this test.

Linear elastostatics with singularities in its solution: $p-$convergence

Now we will investigate the $p-$convergence for problems with singularities. As in the previous two tests, we consider the deformation of a cubic solid occupying the domain $0 \leq X \leq 1, 0 \leq Y \leq 1$

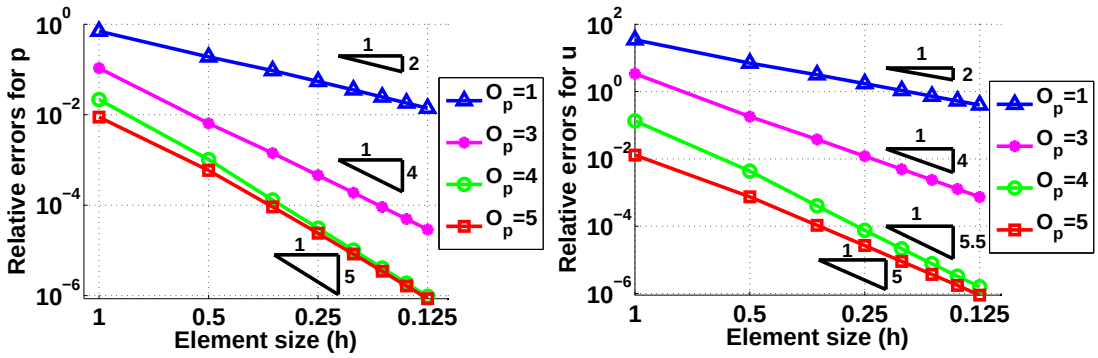

Figure 2.3: $h-$refinement test for the smooth problem in linear case: relative errors as a function of the element size. Left: relative errors for pressure. Right: relative errors for displacement.

and $0 \leq Z \leq 1$, but discretized by i $(i = 1, 2, \cdots, 7)$ layers of prismatic elements. In Figure 2.4 we show the $1-$ and $3-$ layer meshes, with the thick solid lines marking the edges of the elements.

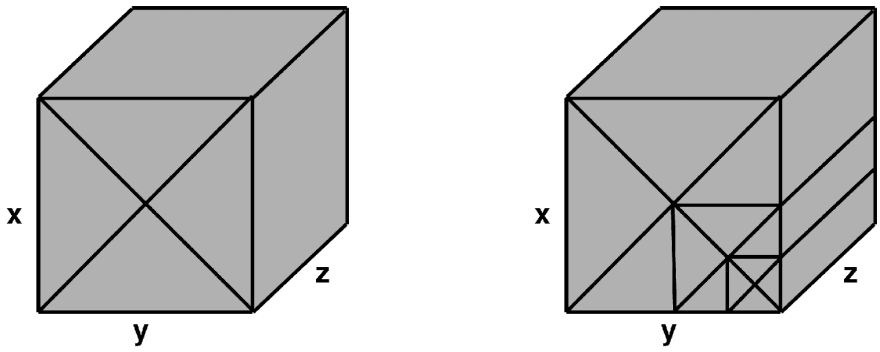

Figure 2.4: Multi-layer meshes refined near the singularities of the solution. Left: $1-$layer mesh. Right: $3-$layer mesh.

We use a similar analytic solution as in [7, 8], which is singular at the line $X = Y = 0$. The displacements on the faces $X = 0$, $Y = 0$ and $Z = 0, 1$ are known

$$\eta_1 = A\sqrt{X^2 + Y^2}, \quad \eta_2 = B\sqrt{X^2 + Y^2}, \quad \eta_3 = 0, \tag{2.1.66}$$

where A, B are prescribed constants. On face $X = 1$, a traction force field $\mathbf{T} = (T_1, T_2, T_3)$ is applied as

$$T_1 = -\frac{\lambda(AX - BY - \frac{AX}{\zeta})}{\sqrt{X^2 + Y^2}}, \; T_2 = \frac{\mu(BX + AY)}{\sqrt{X^2 + Y^2}}, \; T_3 = 0, \tag{2.1.67}$$

and on face $Y = 1$

$$T_1 = \frac{\mu(BX + AY)}{\sqrt{X^2 + Y^2}},\ T_2 = \frac{\lambda(AX - BY + \frac{BY}{\zeta})}{\sqrt{X^2 + Y^2}},\ T_3 = 0. \tag{2.1.68}$$

The body force field $\rho\mathbf{f} = (f_1, f_2, f_3)$ applied on the solid can be described as:

$$\begin{aligned} f_1 &= \frac{\lambda(AX^2(2\zeta - 1) + 2AY^2(\zeta - 1) + BXY)}{2\zeta(X^2 + Y^2)^{3/2}}, \\ f_2 &= \frac{\lambda(2BX^2(\zeta - 1) + BY^2(2\zeta - 1) + AXY)}{2\zeta(X^2 + Y^2)^{3/2}}, \\ f_3 &= 0. \end{aligned} \tag{2.1.69}$$

In this problem the displacement of the object has the following analytic solution:

$$\begin{cases} \eta_1 &= A\sqrt{X^2 + Y^2}, \\ \eta_2 &= B\sqrt{X^2 + Y^2}, \\ \eta_3 &= 0. \end{cases} \tag{2.1.70}$$

We test this problem on $1-$, $2-$ and $3-$ layer meshes, with the following parameters:

$$A = B = 1.0,\ E = 1000,\ \zeta = 0.49, \tag{2.1.71}$$

to study the convergence behavior. On each mesh, we systematically vary the element order O_u for displacement from 1 to 16. Based on our previous results of smooth solutions, all errors presented correspond to the (best) choice $O_p = O_u - 1$. In Figure 2.5, we give the relative errors for pressure and displacement in logarithmic scale as a function of O_u which is also in logarithmic scale. We see that all results from the $1-$layer mesh are approximately on a straight line with O_u increasing. Instead of the exponential convergence for smooth solutions as in the $p-$convergence tests, a second-order convergence rate is obtained. Although $2-$ and $3-$layer meshes are refined near the singularity leading to smaller errors compared with what from the $1-$layer mesh, when O_u becomes sufficiently large (say, larger than 3 in the right plot), they also show a second-order convergence. These results correspond to slightly higher convergence rates compared to the estimates in [10, 15], because the r^α type of singularity is at an endpoint of the element, and this type of mesh gives a $2 - \epsilon$ order accuracy for this case according to [8].

Linear elastostatics with singularities in its solution: $hp-$convergence

We now study the $hp-$convergence on the same problem introduced in equations (2.1.66)-

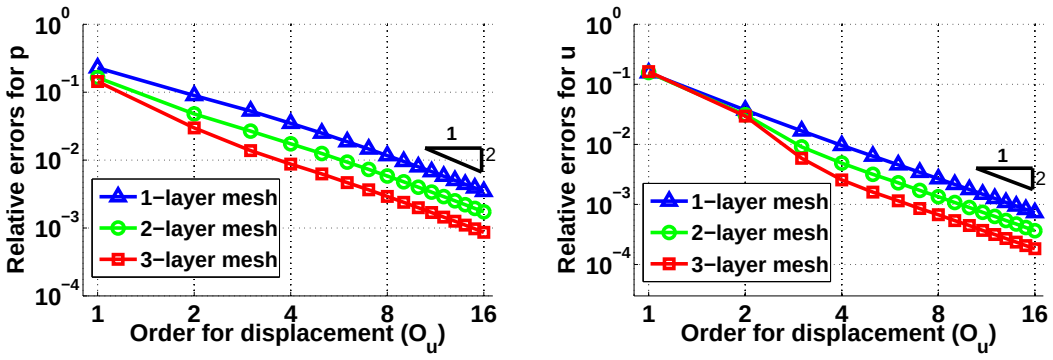

Figure 2.5: $p-$refinement test for the singular problem in linear case: elative errors as a function of the element order O_u for displacement. Left: relative errors for pressure. Right: relative errors for displacement.

(2.1.70). Similar as in [7, 8, 9], we refine the meshes graduately as the element order increases. Namely, for increasing displacement order O_u, we use $i = O_u$ layers mesh in the test. In Figure 2.6 we calculate the relative errors of pressure and displacement in appropriate norms, for $O_p = O_u - 2$, $O_p = O_u - 1$ and $O_p = O_u$. We plot these errors in logarithmic scale, as a function of element order O_u for displacement (also the number of layers) which is in linear scale. We see that approximately straight lines are obtained for all cases, which indicates the exponential convergence, as expected from the analysis in [7, 8]. Also, consistent with the previous tests, we obtain larger errors when $O_p = O_u - 2$, while the results from $O_p = O_u - 1$ and $O_p = O_u$ are similar with each other.

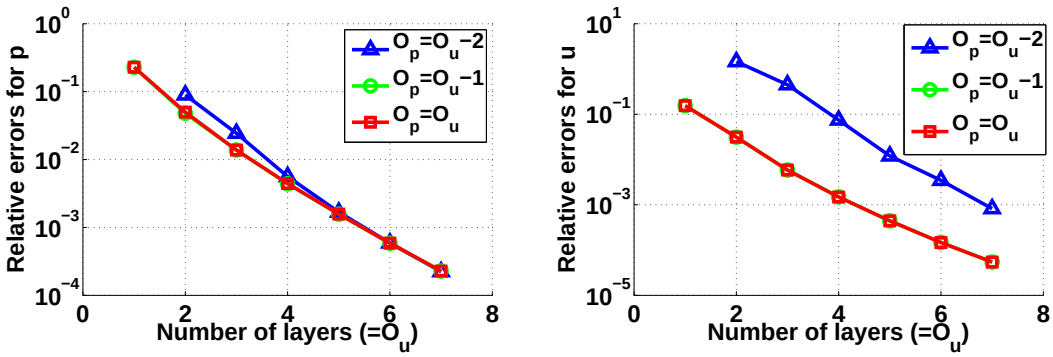

Figure 2.6: $hp-$refinement test for the singular problem in linear case: elative errors as a function of the element order O_u for displacement (which is equal to the number of mesh layers). Left: relative errors for pressure. Right: relative errors for displacement.

Nonlinear elastostatics

Next we investigate the convergence of the projection spectral/hp element method for nonlinear elastostatic problems. We employ the Mooney-Rivlin model (2.1.3), and solve the equilibrium equation (2.1.33). We consider the same domain as in the linear case shown in Figure 2.1, and both $h-$ and $p-$convergence tests are preformed for problems with smooth solutions.

Nonlinear elastostatics with smooth solution: $p-$convergence

In this test example, we choose the material property parameters as

$$A_{10} = A_{01} = 1, \quad k = 100. \tag{2.1.72}$$

The face $X = 0$ is clamped, and the displacements on the rest of the faces are given as follows:

$$\eta_1 = A \sin aX, \ \eta_2 = 0, \ \eta_3 = 0; \tag{2.1.73}$$

where A, a are prescribed constants. A body force field, $\rho\mathbf{f} = (f_1, f_2, f_3)$ is also applied on the object:

$$\begin{aligned} f_1 =& \frac{4Aa^2 \sin aX}{9(aA\cos aX + 1)^{10/3}}((225(aA\cos aX)^3 + 625(aA\cos aX)^2 + 675aA\cos aX + 225) \\ & (aA\cos aX + 1)^{1/3} + aA\cos aX((aA\cos aX + 1)^{2/3} - 1)(aA\cos aX + 2) \\ & + 6 + 6(aA\cos aX + 1)^{2/3}), \\ f_2 =& f_3 = 0. \end{aligned} \tag{2.1.74}$$

The displacements of the solid for this problem can be expressed by the following analytic functions :

$$\begin{cases} \eta_1 &= A\sin aX, \\ \eta_2 &= 0, \\ \eta_3 &= 0, \end{cases} \tag{2.1.75}$$

and pressure $p = k(aA\cos aX)$, with constants $A = 0.04$, $a = 2.0$. Similar as in the linear case, this problem is not totally incompressible.

Similar to the linear case, we study the $p-$convergence by two ways: first vary the element order O_u for displacement up to 7, with fixed orders of pressure $O_p = 0, 1, 2, 3$; then exchange the positions of O_u and O_p, i.e., compare the results from different O_u ($O_u = 7, 6, 5, 4$) for increasing O_p in the range of $0 \le O_p \le O_u$. We calculate the relative errors of the computed displacement

and pressure fields for each element order pair as in previous tests, see Figure 2.7, these errors are plotted in logarithmic scale as a function of element order (in linear scale).

Consistent with the results from $p-$convergence tests for the linear case, we see that for each fixed O_u, increasing O_p gives almost exponential convergence, while for each fixed O_p and sufficiently high O_u, increasing O_u further does not help to decrease the errors. Also, among the cases in the upper plots, the best results are obtained by the choice $O_u = O_p + 1$; this is also similar to Figure 2.2 for the linear case.

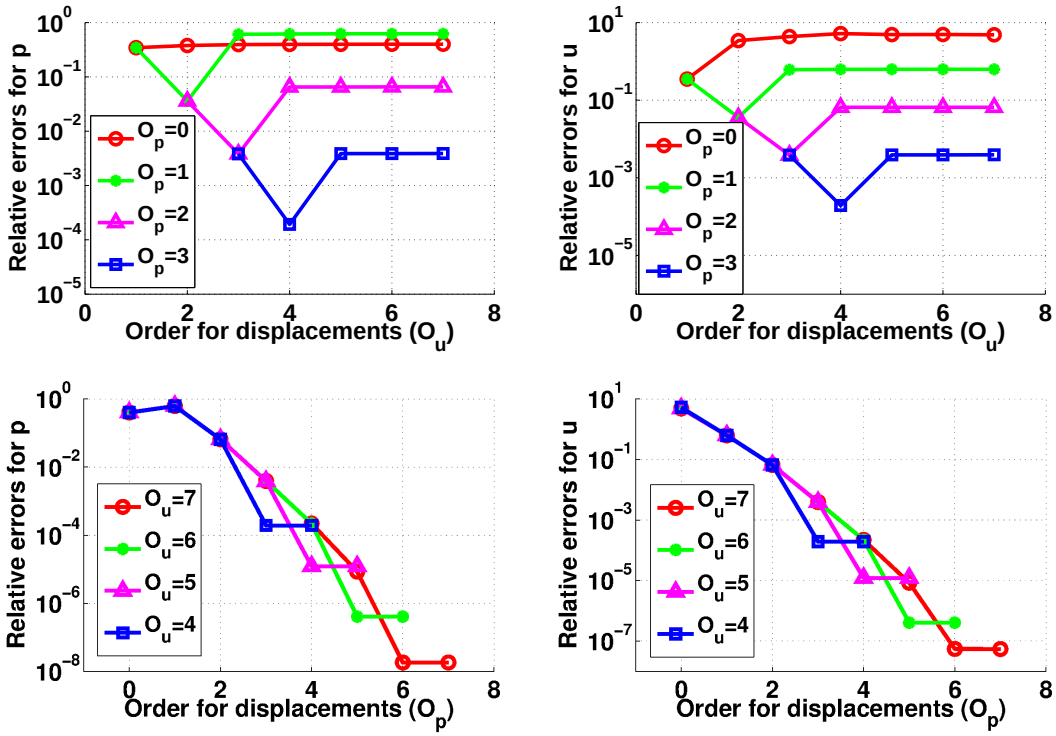

Figure 2.7: $p-$refinement test for the smooth problem in nonlinear case: upper: relative errors as a function of the element order O_u for displacement; lower: relative errors as a function of the element order O_p for pressure; left column: relative errors for pressure; right column: relative errors for displacement.

Nonlinear elastostatics with smooth solution: $h-$convergence

In this section, the same problem as in the $p-$convergence tests is used, but with coefficients $A = 0.01$, $a = 2.0$ for stability. To study the $h-$convergence, we perform the tests on evenly discretized meshes with $i \times i \times i$ $(i = 1, 2, \cdots, 8)$ hexahedral elements as previously for the linear case. With a fixed displacement order $O_u = 4$, results from different pressure orders $O_p = 0, 2, 3, 4$ are studied. In Figure 2.8 we show the relative errors of pressure and displacement, and plot these

errors in logarithmic scale, as a function of element size $h = \frac{1}{i}$ which is in inverse logarithmic scale. We see similar results as in Figure 2.3 for the linear case: when $O_p < O_u$, convergence rate of $O_p + 1$ order is obtained; when $O_p = O_u$, only O_p order is given. Here results from $O_p = O_u$ and $O_p = O_u - 1$ have similar convergence rates, while in the linear case the former gave a $1/2$ order higher.

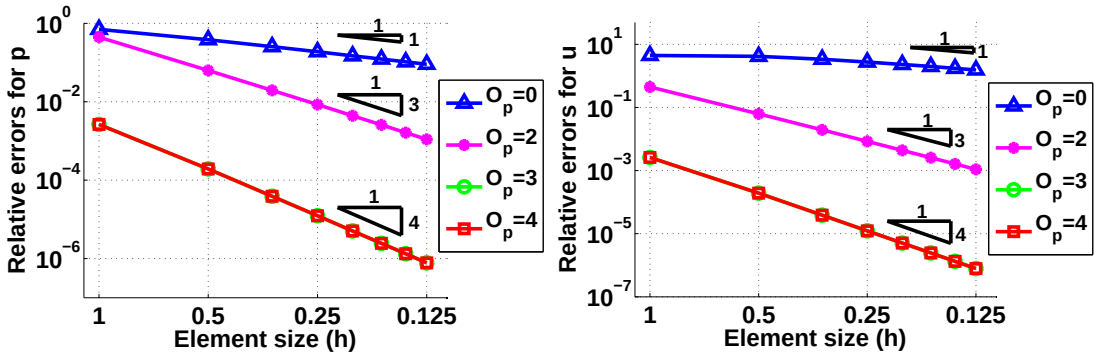

Figure 2.8: $h-$refinement test for the smooth problem in nonlinear case: relative errors as a function of the element size. Left: relative errors for pressure. Right: relative errors for displacement.

2.1.5 Stability: ellipticity condition and $inf - sup$ condition

In this section we perform several numerical tests in order to investigate the performance of the high-order projection method with respect to ellipticity condition and the *inf-sup* condition.

Ellipticity condition and large deformation

As mentioned in [41, 43], for the large deformation cases, sometimes the solver fails even when the element satisfies the $inf - sup$ condition because the ellipticity condition fails in the discrete problem (i.e., (2.1.48)). Here, we will test the ellipticity condition following proposition 6 of [42].

With $(\hat{\boldsymbol{\eta}}, \hat{p})$ denoting the initial conditions, and test function $q \in L^2(\Omega)$, considering static and nearly incompressible problems for which $k >> 1$, (2.1.34) can be approximated as

$$\int_\Omega (J-1) q d\Omega = 0 \tag{2.1.76}$$

and we linearize it, to obtain

$$b(\triangle\boldsymbol{\eta}, q) = \int_\Omega \frac{1}{2}\left(\left(\frac{\partial(\triangle\boldsymbol{\eta})}{\partial \mathbf{X}}\right)^T \mathbf{F}(\hat{\boldsymbol{\eta}}) + \mathbf{F}(\hat{\boldsymbol{\eta}})^T \left(\frac{\partial(\triangle\boldsymbol{\eta})}{\partial \mathbf{X}}\right)\right) : (J\mathbf{C}^{-1})(\hat{\boldsymbol{\eta}}) q d\Omega = 0, \tag{2.1.77}$$

where $\triangle\boldsymbol{\eta}$ denotes the increment of u for each step in the Newton-Raphson iteration. In the

continuous problem, by denoting $\hat{\mathbf{U}}$ and $\hat{P}$ the admissible displacement and pressure spaces, the ellipticity in kernel is

$$\inf_{\mathbf{v}\in\mathbb{K}} \frac{a(\mathbf{v},\mathbf{v})}{||\mathbf{v}||^2} > 0, \tag{2.1.78}$$

where

$$\mathbb{K} = \{\mathbf{v} \in \hat{\mathbf{U}} \,\text{and}\, b(\mathbf{v}, q) = 0,\, \forall\, q \in \hat{P}\} \tag{2.1.79}$$

$$\begin{aligned} a(\mathbf{v},\mathbf{v}) = &\int_\Omega \frac{1}{2}\left(\left(\frac{\partial \mathbf{v}}{\partial \mathbf{X}}\right)^T \mathbf{F}(\hat{\boldsymbol{\eta}}) + \mathbf{F}(\hat{\boldsymbol{\eta}})^T\left(\frac{\partial \mathbf{v}}{\partial \mathbf{X}}\right)\right) : (\tilde{\mathcal{C}}(\hat{\boldsymbol{\eta}}) + \overline{\mathcal{C}}^{1*}(\hat{\boldsymbol{\eta}}, \hat{p})) \\ &: \frac{1}{2}\left(\left(\frac{\partial \mathbf{v}}{\partial \mathbf{X}}\right)^T \mathbf{F}(\hat{\boldsymbol{\eta}}) + \mathbf{F}(\hat{\boldsymbol{\eta}})^T\left(\frac{\partial \mathbf{v}}{\partial \mathbf{X}}\right)\right) d\Omega \\ &+ \int_\Omega (\tilde{\mathbf{S}}(\hat{\boldsymbol{\eta}}) + \overline{\mathbf{S}}^*(\hat{\boldsymbol{\eta}}, \hat{p})) : \left(\left(\frac{\partial \mathbf{v}}{\partial \mathbf{X}}\right)^T \left(\frac{\partial \mathbf{v}}{\partial \mathbf{X}}\right)\right) d\Omega. \end{aligned} \tag{2.1.80}$$

On the other hand, after discretization, the ellipticity in kernel is:

$$\inf_{\mathbf{V}\in\mathbb{K}_h} \frac{\mathbf{V}^T(\mathbf{K}_u + \mathbf{K}_u^*)\mathbf{V}}{||\mathbf{V}||^2} > 0, \tag{2.1.81}$$

where

$$\mathbb{K}_h = \{\mathbf{V} | \mathbf{K}_p^T \mathbf{V} = 0\}. \tag{2.1.82}$$

We consider two test examples, and we investigate the influence of different element orders for pressure on the ellipticity condition. From intuition, we can see that for the same element order of displacement, the smaller element order we use for pressure, the larger $\mathbb{K}_h$ will be, and therefore the more likely is that the ellipticity condition will be violated. We will demonstrate the extent of this violation by obtaining the minimum eigenvalue of $\mathbf{K}_u(\eta_h, p_h)$ in $\mathbb{K}_h(\eta_h, p_h)$, where (η_h, p_h) is the projection of an analytic solution (see below) in the space formed by the shape functions. A similar strategy was employed in [41] for testing the ellipticity condition.

In our first example, the Mooney-Rivlin model is considered with the following material property coefficients:

$$A_{10} = 2.0,\ A_{01} = 0.2,\ k = 1000, \tag{2.1.83}$$

and the domain for initial configuration is as in Figure 2.9. In this test, a prescribed displacement L is applied on $X = 1$:

$$\eta_1 = -L,\ \eta_2 = 0,\ \eta_3 = 0 \tag{2.1.84}$$

to describe the extent of compression. For the faces $X = 0$, $Y = 0$, we clamp them in the normal direction. That is, on $X = 0$, we fix $\eta_1 = 0$, and on $Y = 0$, we fix $\eta_2 = 0$. To balance the system,

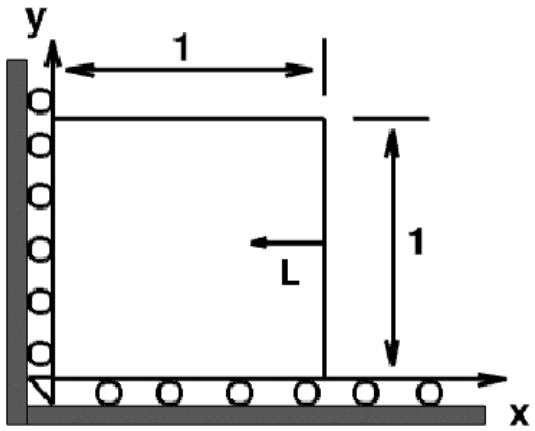

Figure 2.9: Domain for elllipticity and $inf - sup$ condition tests.

on $Y = 1$ a traction force field is applied as

$$T_1 = T_3 = 0,\ T_2 = 0.4L\frac{(4L^2 - 16L + 27)L - 22}{L - 1}. \tag{2.1.85}$$

Here we employ a 3D code to obtain a 2D solution and hence we impose on $Z = 0$ and $Z = 1$ periodic boundary conditions, i.e., $\boldsymbol{\eta}|_{Z=0} = \boldsymbol{\eta}|_{Z=1}$.

Using a single hexahedral element as the mesh for this domain, we obtain the minimum eigenvalues of the stiffness matrix as in (2.1.81) which is evaluated at the projected exact solution (η, p). Next we study the minimum eigenvalues of $\mathbf{K}_u(\eta_h, p_h)$ in $\mathbb{K}_h(\eta_h, p_h)$ by systematically changing the element orders of displacement and pressure. Similar to what we did for the convergence rate tests, fixing the element order O_u of displacement ($O_u = 2, 3, 4, 5$), the minimum eigenvalue versus L for different element orders O_p of pressure ($O_p = 0, \cdots, O_u$) are plotted in Figure 2.10: The horizontal axis denotes the displacement L on $X = 1$, which represents the extent the object is compressed. The different lines correspond to different constant k which represents the element order combinations ($O_u, O_p = O_u - k$).

In Figure 2.10, we see that for a fixed element order pair (O_u, O_p), as L increases, the minimum eigenvalues should decrease. That means, the larger the deformation is, the more severe the ellipticity is violated, which was also demonstrated in [42, 43] for low-order elements. We also notice that for a fixed element order O_p for pressure, when $O_u - O_p \leq 1$, the minimum eigenvalues are

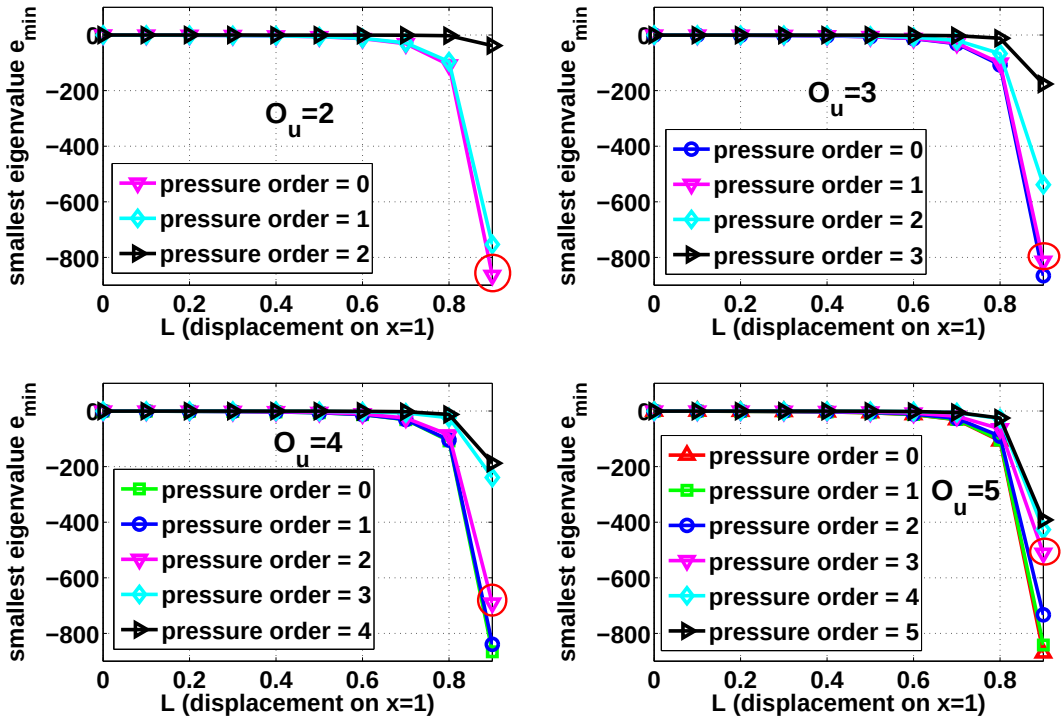

Figure 2.10: Ellipticity test: minimum eigenvalues for element order pairs (O_u, O_p). Upper left: $O_u = 2$. Upper right: $O_u = 3$. Lower left: $O_u = 4$. Lower right: $O_u = 5$.

much larger than for O_u satisfying $O_u - O_p \geq 2$. On the other hand, it is interesting that when $O_u - O_p \geq 2$, the minimum eigenvalues have about the same magnitude independent of an increase in O_u. For example, for $L = 0.9$, when $O_p = 1$ the minimum eigenvalue is -753.43 for $O_u = 2$, -814.11 for $O_u = 3$, -839.19 for $O_u = 4$ and -841.80 for $O_u = 5$. Similarly, when $O_p = 2$ the minimum eigenvalue is -379.38 for $O_u = 2$, -538.43 for $O_u = 3$, -691.14 for $O_u = 4$ and -733.14 for $O_u = 5$. These results suggest that for a fixed integer k, the pair $(O_u, O_u - k)$ should yield better performance as O_u increases. For example, for $k = 2$ at $L = 0.9$ as highlighted by the red circles, we obtain the minimum eigenvalue for $(O_u, O_p) = (3, 1)$, $(4, 2)$ and $(5, 3)$ as -814.11, -691.14 and -511.86, respectively. These results point to a particular trend, namely that for high-order O_u of displacement there are more values of the pressure order O_p that lead to simultaneous validity of the ellipticity condition and of the $inf - sup$ condition.

In this second example we will investigate the aforementioned finding by testing the stability of the numerical solver for different pairs of interpolation order. We consider the cubic object $(0 \leq X \leq 1, 0 \leq Y \leq 1, 0 \leq Z \leq 1)$, with the mesh composed by a single hexahedral element. The

Mooney-Rivlin model is specified by the following material property coefficients:

$$A_{10} = A_{01} = 1.0,\ k = 1000. \tag{2.1.86}$$

For this case, the face $X = 0$ is clamped, and a traction force field (T_1, T_2, T_3) is applied on the rest of the faces:

At $X = 1$:

$$T_1 = -\frac{2X^2}{25},\ T_2 = \frac{4X}{5},\ T_3 = 0; \tag{2.1.87}$$

at $Y = 0$ and $Y = 1$:

$$T_1 = n_y(\frac{4X}{5} + \frac{2X^3}{125}),\ T_2 = -n_y\frac{2X^2}{25},\ T_3 = 0; \tag{2.1.88}$$

at $Z = 0$ and $Z = 1$:

$$T_1 = T_2 = T_3 = 0, \tag{2.1.89}$$

where $\mathbf{n} = (n_x, n_y, n_z)$ is the outward-pointing unit vector normal to the surface. The following body force $\rho\mathbf{f} = (f_1, f_2, f_3)$, is also applied on the object:

$$f_1 = \frac{4X}{25},\ f_2 = -\frac{4}{5},\ f_3 = 0. \tag{2.1.90}$$

This problem has the following analytic solution for the displacements of the object:

$$\eta_1 = \eta_3 = 0,\ \eta_2 = 0.1X^2. \tag{2.1.91}$$

For this test, the increment method (see Appendix A.2) is applied by separating the external load into $N = 10$ parts. In Table 2.1, we list the results of the stability study for different pairs of element order (O_u, O_p) ($O_p \leq O_u$ and $O_u = 2, \cdots, 11$); we leave the pairs with $O_p > O_u$ as blank because they were not tested. Also, we mark with $*$ the point where the range of choices for O_p, which yield stable results, increases. We can see that for $O_u \leq 5$, we can only use $O_p \geq O_u - 1$ to maintain stability; when $6 \leq O_u \leq 10$, the range is broadened to $O_p \geq O_u - 2$; and for $O_u \geq 11$, all $O_p \geq O_u - 3$ are appropriate to obtain numerical stability for this test problem.

$Inf - sup$ condition

In all the examples we presented so far (convergence and ellipticity tests) we obtained stable numerical results even when $O_p = O_u$. To further investigate the $inf - sup$ condition, we revisit here the problems defined in equation (2.1.75) and in figure 2.9, and perform further numerical tests

$O_u \backslash O_p$	0	1	2	3	4	5	6	7	8	9	10	11
2	×	√	√									
3	×	×	√	√								
4	×	×	×	√	√							
5	×	×	×	×	√	√						
6	×	×	×	×	*√	√	√					
7	×	×	×	×	×	√	√	√				
8	×	×	×	×	×	×	√	√	√			
9	×	×	×	×	×	×	×	√	√	√		
10	×	×	×	×	×	×	×	×	√	√	√	
11	×	×	×	×	×	×	×	×	*√	√	√	√

Table 2.1: Ellipticity test: stability test for the second test problem. A checkmark denotes stability whereas an "x" instability. The star "*" indicates transition in the stability behavior from one regime to another.

with many non-hexahedral elements, including distorted 3D elements, and compare the accuracy of the results. In addition, we compute the $inf - sup$ constant explicitly for different interpolation orders (O_u, O_p).

For both test problems we use three types of meshes with different number of elements as in Figure 2.11. Among these meshes, the prismatic elements might be especially problematic according to [49, 50]. For the problem defined in equation (2.1.75) and for any pairs of (O_u, O_p) we tested in the range of $O_u \in \{1, 2, 3, 4, 5, 6, 7\}$ and $O_p \leq O_u$, we did not observe any instabilities. The relative errors for the choices of $O_p = O_u - 2$, $O_p = O_u - 1$ and $O_p = O_u$ are shown in Figure 2.12. Although the magnitudes of these errors are different, all the lines are parallel to each other, indicating that we obtained the same convergence rate with either the $(O_u, O_p = O_u - 2)$, $(O_u, O_p = O_u - 1)$ or the $(O_u, O_p = O_u)$ pairs. For the problem defined in figure 2.9 and imposing a load $L = 0.1$, we found similar results. Also, following [51, 52, 53], we obtained the $inf - sup$ constant

$$\beta = \inf_{q \in \hat{P}} \sup_{v \in \hat{U}} \frac{b(v, q)}{|v|_{H^1} ||q||_{L^2}} \tag{2.1.92}$$

for a mesh with one hexahedron, where $b(v, q)$ is defined as in (2.1.77). The results are shown in Figure 2.13; we see that for $(O_u, O_p = O_u)$ cases, the constant $\beta > 0$ and is decreasing as O_u increases. However, for $(O_u, O_p = O_u - 1)$ the constant is at least an order of magnitude larger. By decreasing further the pressure interpolation order, i.e., for the pair $(O_u, O_p = O_u - 2)$ the results remain essentially the same as in the case $(O_u, O_p = O_u - 1)$.

2.1.6 Accuracy: volumetric and shear locking phenomena

In this section we perform several numerical tests in order to investigate the performance of the high-order projection method with respect to volumetric locking, and shear locking.

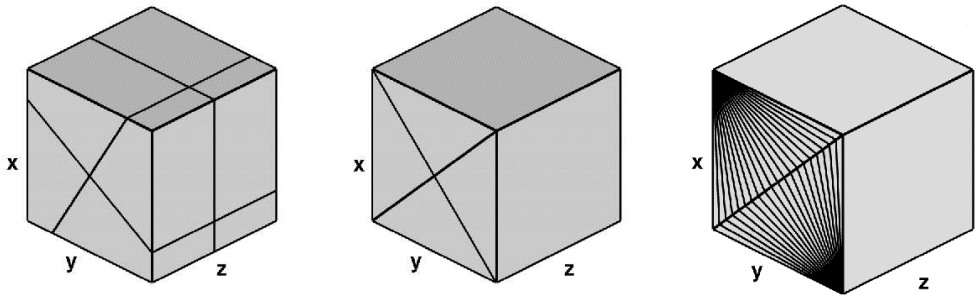

Figure 2.11: Meshes for $inf - sup$ condition test with example in 5.1.1: Left: skewed hexahedral elements (MESH1); Middle: prismatic elements (MESH2); Right: Many prismatic and distorted elements (MESH3).

Volumetric locking

For low-order elements the displacement-only formulation suffers from the volumetric locking behavior for problems with very high bulk modulus. This can be overcome by increasing the displacement order, i.e. typically for $O_u \geq 4$ [18]. Here, we compare the mixed formulation with the displacement formulation for a thick-walled tube benchmark problem, first proposed in [17], but here we are using a three-dimensional mesh. We use a neo-Hookean material model with $A_{01} = 0.0; A_{10} = 0.5$. Shown in Figure 2.14, the thick-walled tube is under pressure load $P_{inner} = 0.5$ MPa (applied along the radial direction); the tension on the outer surface is 0 MPa. The inner and outer radii are 10 mm and 30 mm, respectively. Along the $Y-$direction, the tube has length 30 mm. Therefore, on the inner and outer surfaces the boundary conditions are (here we use a follower load approach, see [45])

$$-\sigma_{rr}(10) = 0.5,\ \sigma_{rr}(30) = 0. \tag{2.1.93}$$

On surface $X = 0$ and $Z = 0$, the displacements vanish along the normal directions. In other words,

$$\eta_1 = 0 \,\text{on}\, X = 0; \quad \eta_3 = 0 \,\text{on}\, Z = 0. \tag{2.1.94}$$

In order to describe a tube with infinite length, on surfaces $Y = 0$ and $Y = 30$, the periodic boundary condition is applied: $\boldsymbol{\eta}|_{Y=0} = \boldsymbol{\eta}|_{Y=30}$. All the displacements are set to 0 as the initial configuration. As in Figure 2.14, the domain is decomposed into four hexahedral elements.

We test both mixed and displacement-only formulations for this problem, with displacement order $O_u = 2, 3, 4$ in the displacement formulation, and displacement/pressure order pairs $(O_u, O_p) = (2, 1), (3, 2), (4, 3)$ in the mixed formulation; in addition we perform a simulation with $O_u = 2, O_p =$

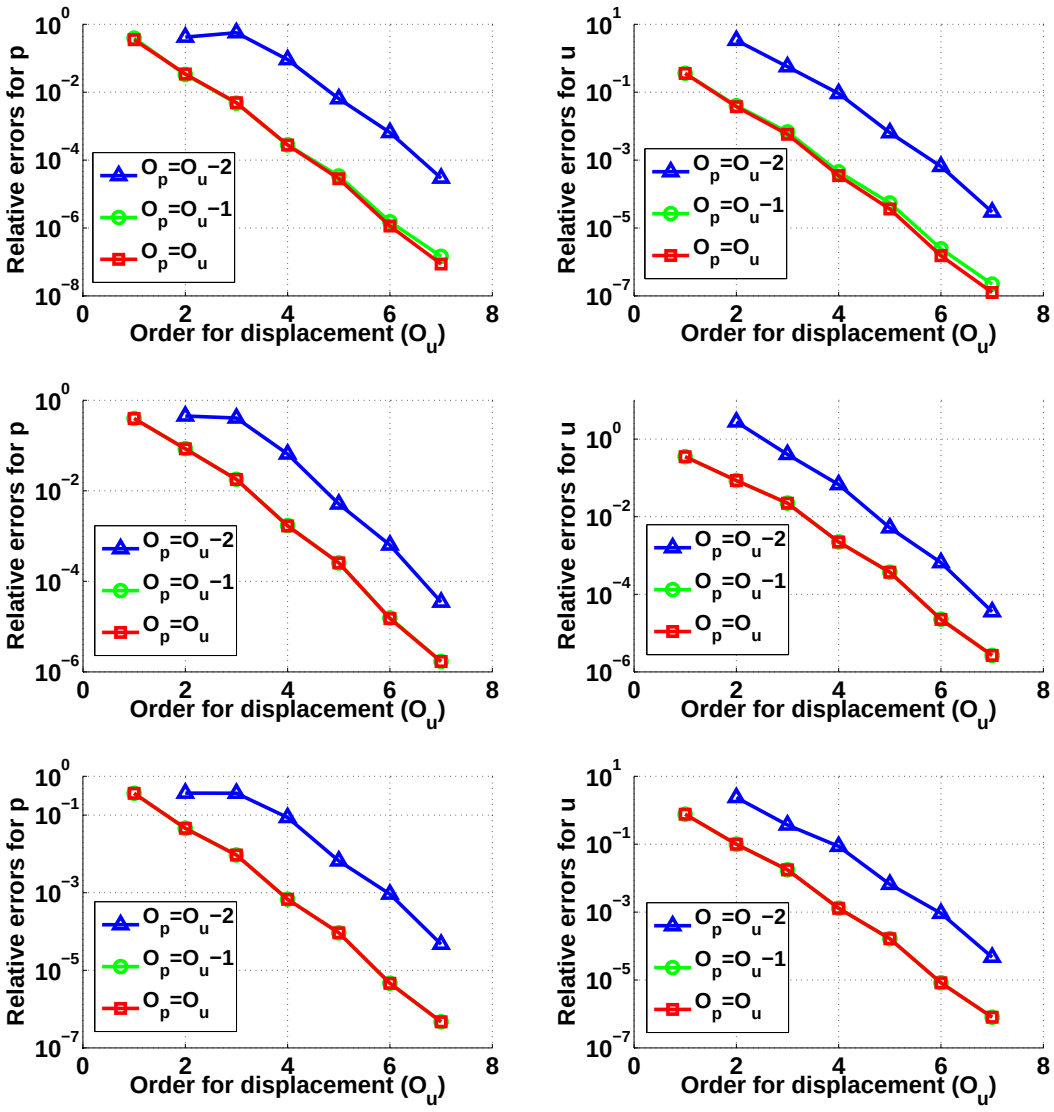

Figure 2.12: $Inf-sup$ condition test for the problem in 4.2.1., with relative errors as a function of the element order O_u for displacement: upper: results for MESH1; middle: results for MESH2; lower: results for MESH3; left column: relative errors for pressure; right column: relative errors for displacement.

2. The bulk modulus $k = 1, 10, 100, 1000, 10000, 100000$ are tested. The results for the maximum relative error of displacement along the radial r direction (marked as u_r) at the inner boundary $r = 10$ mm are showed in Figure 2.15. In this test, the increment method (see Appendix A.2) is applied by separating the external load into 10 parts.

From Figure 2.15 we can see that using low-order elements for displacement, the displacement-only formulation suffers from volumetric locking problem, while the mixed formulation does not.

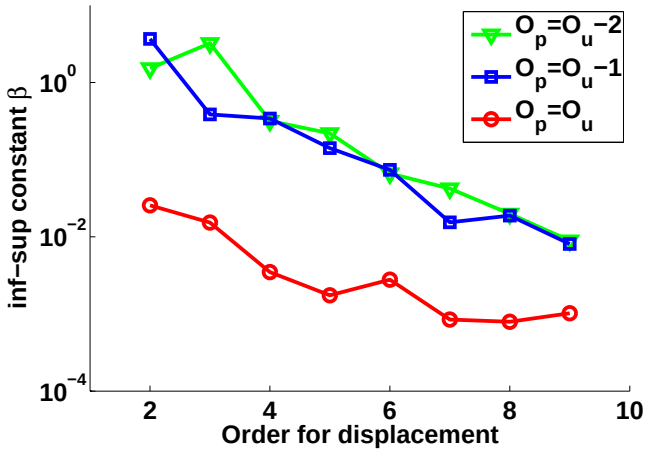

Figure 2.13: $Inf - sup$ test: $inf - sup$ constants for problem defined in figure 2.9 with one hexahedron element mesh.

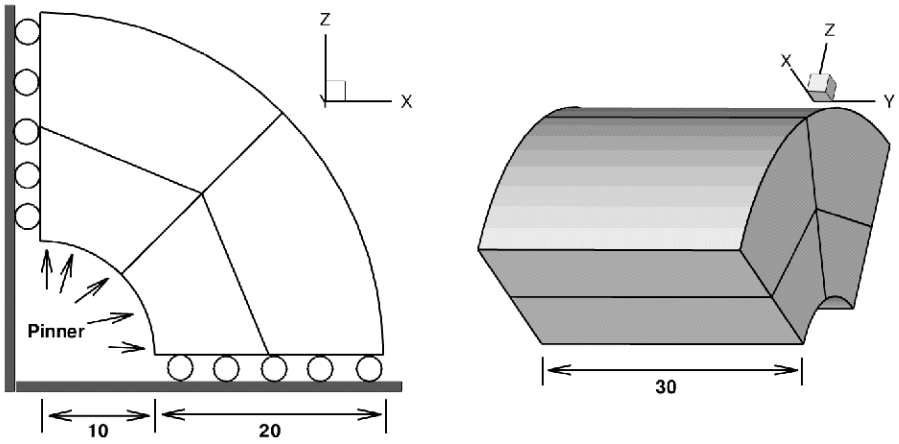

Figure 2.14: Volumetric locking test: mesh for thick-walled tube.

When the order O_u is increased to as high as 4, the displacement formulation overcomes the volumetric locking behavior. This result is in agreement with the findings of [18]. When the bulk modulus is larger than $10,000$ (MPa), the accuracy with mixed formulation is more than an order of magnitude higher than that of the displacement formulation, reaching almost two-orders of magnitude higher accuracy for $k = 100,000$. It is interesting to also note that the mixed formulation case of $O_p = O_u = 2$ leads to volumetric locking identical to the displacement-only formulation for $O_u = 2$.

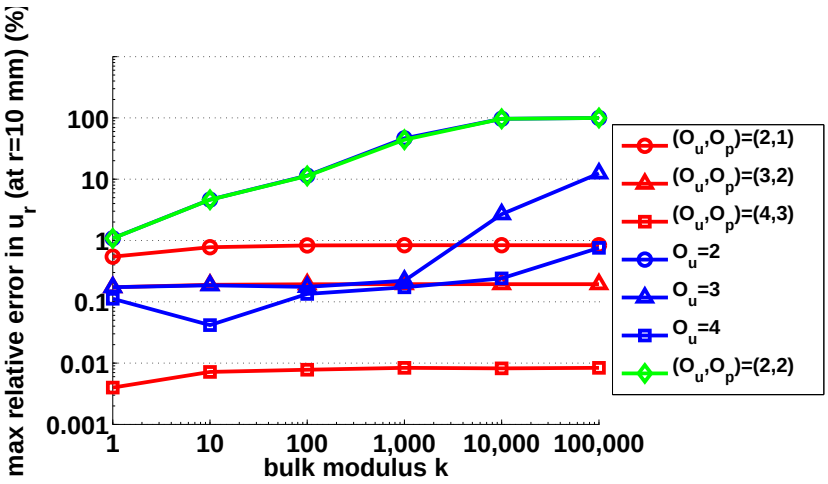

Figure 2.15: Volumetric locking test: maximum relative error for u_r at inner boundary $r = 10$ mm, with two formulations in thick-walled tube problem.

Shear locking

Next we investigate the performance of the high-order pressure projection method in shear locking with a numerical example very similar to [16]. It is known [16, 26, 54] that for thin plates, high-order elements can overcome the shear locking problem. Here we use a $5 \times 0.02 \times 5$ test mesh for the Mooney-Rivlin model. Based on our results for convergence rate tests, here we simply use $O_p = O_u - 1$ and consider polynomial orders O_u from 2 to 9.

In this example, we test the thin mesh by applying a traction $T_2 = 0.00001$ at the end $X = 5$. We choose the material coefficients for the Mooney-Rivlin material according to [54], as follows: $A_{01} = 0.045$, $A_{10} = 0.177$, and since incompressibility does not effect the shear locking phenomenon, we use a smaller bulk modulus $k = 0.66666$. The numerical results are summarized in Figure 2.16. We also compare the results for deformation length L between our formulation and the commercial code ABAQUS [55] in Tables 2.2-2.3. In ABAQUS, we used 2500 incompatible-mode elements to overcome the shear locking problem. We take the results with quadratic elements in ABAQUS as the reference solution L_s for the comparison of relative errors $e_R = \frac{|L - L_s|}{L_s}$.

	ABA Order 1	ABA Order 2	NEK Order 2	NEK Order 3	NEK Order 4
L	3.80724	3.78787	0.37777	2.34947	3.64134
	NEK Order 5	NEK Order 6	NEK Order 7	NEK Order 8	NEK Order 9
L	3.77218	3.77723	3.78631	3.79046	3.79920

Table 2.2: Shear locking test: comparison of length L (deformation on the end $X = 5$) between ABAQUS (ABA) with 2500 elements and our formulation (NEK) with one element.

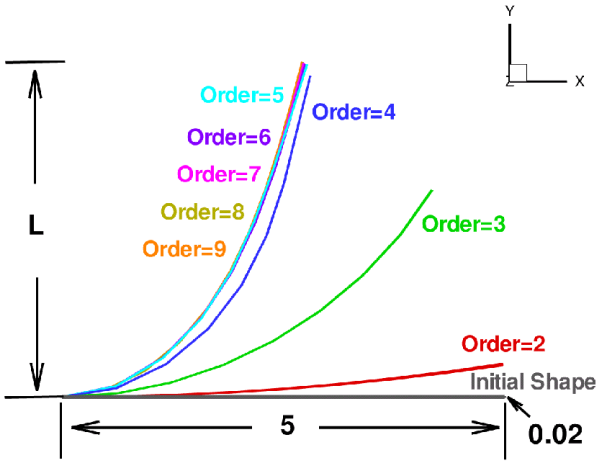

Figure 2.16: Shear locking test: Mooney-Rivlin model

	ABA Order 1	ABA Order 2	NEK Order 2	NEK Order 3	NEK Order 4
e_R	5.11369e-3	0	9.00268e-1	3.79738e-1	3.86840e-2
	NEK Order 5	NEK Order 6	NEK Order 7	NEK Order 8	NEK Order 9
e_R	4.14217e-3	2.80897e-3	4.11841e-4	6.83762e-4	2.99113e-3

Table 2.3: Shear locking test: comparison of relative errors for L between ABAQUS (ABA) with 2500 elements and our formulation (NEK) with one element.

From Figure 2.16 and Tables 2.2-2.3, we can see that using low-order polynomial interpolation the deformation is much smaller than the accurate solution, which indicates that the shear locking phenomenon appears. However, by using higher order elements, the deformation is larger and it finally converges to the accurate solution. Hence, we obtain converged solutions for this problem for $O_u \geq 4$, which is consistent with the observations in [26]. We note that for the shear locking test we obtained similar results with either the $(O_u, O_p = O_u - 1)$ or the $(O_u, O_p = O_u)$ pairs.

2.1.7 Summary

We have presented a pressure projection method for nearly incompressible materials in solid mechanics using a general Jacobi polynomial basis that can be used to generate 3D polymorphic high-order elements. We investigated the convergence rates of the method for both smooth and singular solutions of linear and nonlinear elasticity problems, and numerically in some depth the issue of stability of the method for large deformations. We found that for linear problems the mixed formulation is stable even for elements with pressure interpolation order O_p equal to the

displacement order O_u, while $O_p = O_u - 1$ gives the best solution accuracy. On the other hand, to resolve the volumetric locking problem for hyperelastic material, it is required that $O_p = O_u - 1$ and in that case we obtained accuracies superior to displacement-only formulation, especially at high values of the bulk modulus, e.g. by almost two orders of magnitude. For large deformations we examined the stability of the method by considering the discrete ellipticity in kernel as has been suggested previously for low-order elements [42]. In this case, stability is enhanced by *restricting the pressure space*, i.e. $O_u \geq O_p \geq O_u - k$, where k depends on the specific value of O_u. For example, our numerical tests suggest that for low values of $O_u \leq 5$ we require that $k = 1$; for intermediate values of $O_u \leq 10$ we require that $k = 2$, and for $O_u \geq 11$ we require that $k = 3$. These rather surprising results deserve further theoretical investigation, especially for understanding the interplay between the discrete ellipticity condition and the discrete *inf-sup* condition in large deformation analysis. From the practical standpoint, the present study suggests that the most robust choice of interpolation order in the mixed formulation is $O_p = O_u - 1$, leading to stable and accurate results for linear and nonlinear problems with large deformations, including resolution of the volumetric and shear locking phenomena.

2.2 Acceleration method for parallel linear solver

2.2.1 Overview and motivation

Because of its high convergence rate as well the flexibility in discretization, the spectral/hp element method has been applied on various applications during the past two decades [6, 56, 21, 15, 22, 18, 57, 58, 59, 60]. The bases of spectral/hp finite elements can be classified as two types: the modal bases which are constructed from hierarchical expansion basis, and the nodal bases which are associated with a set of nodal points. Regarding the choices of nodal points, the Gauss-Lobatto points are commonly used [56], which can be chosen by minimization of an electrostatic potential [61] or the Lebesgue constant (Fekete points) [62] for unstructured elements. For the modal bases, the mass matrix is generally not diagonal and therefore lumped or spectral diagonal mass matrix can not be easily applied without sacrificing the accuracy. However, one can choose the expansion bases to achieve better conditioning and sparsity [6, 63, 64]. Among all these choices, the Jacobi polynomials have been employed in the construction of several recent expansion bases [6, 65, 66, 67], and have been proved to be very successful in computational fluid dynamics. From the numerical standpoint, the spectral/hp element version based on general Jacobi polynomials gives a good sparsity and is well conditioned for enhanced computational efficiency and scalability as shown in [68, 69]. It also provides further flexibility in generating polymorphic elements, e.g., hexahedral,

tetrahedral, triangular prisms and even pyramids.

For problems of solid mechanics (especially elasticity), the high-order methods possess additional advantages, e.g., the accuracy does not depend strongly on the aspect ratio of the elements [6], and locking-free behavior with respect to the Poisson ratio for nearly incompressible materials [12, 17, 18]. The spectral/hp element methods are also extended in recent years to nonlinear problems [16, 17, 70, 19, 71] and plate/shell problems [25, 23]. However, in the computational tests we realized that the structure solver was a bottle neck in fluid-structure interaction (FSI) simulations, especially for large-scale cases such as the patient specific aneurysm problems. In general, the problem is more severe when higher-order polynomial order is employed, because the high-order mass and stiffness matrices are denser and require more operations for the solution of systems of equations by iterative methods.

The current work is motivated by two previous studies. The first one comes from [72] where an element-wise least square based algorithm was developed with high-order nodal expansion bases for the explicit time integration scheme. The solution was obtained based on an element-wise diagonal solver: the residual was first distributed on each element, then the element-wise mass matrix was inverted to achieve the element-wise results and finally the results on the element boundary were smoothed in the least square sense. All the operations are local, i.e., element-wise. However, this completely local method can only be applied to the nodal basis, and its stability is highly mesh-dependent while applying to problems subjected to distributed loads. To improve the method and apply it to the spectral/hp element discretization based on modal basis, a global inversion of the linear system is required to approximate the residual on each element, which calls for the second idea which comes from our three dimensional fluid solver. In the Navier-Stokes solver, we apply the rotational velocity-correction projection scheme in time [73, 74], and the three components of velocity and the pressure are all decoupled. A low energy preconditioner can be then applied in the conjugate gradient solver, to solve efficiently the Poisson problem for pressure and the three Helmholtz problems for the velocity components. This preconditioner is developed by a transformation from an analytic unstructured expansion, which ignores the Jacobian of the mapping to the physical elemental region, and the target matrix must be free of axis rotations. Numerical tests in [75, 76] showed great success of this preconditioner in improving the conditioning and therefore the computational cost compared to the diagonal preconditioner, especially for polynomial orders greater than 4.

In the current work, we perform all the operations in the solid solver locally, except when distributing the global residual. To approximate this element-wise distribution more efficiently, we decouple the three components of the solid solver, and extend the idea of low energy preconditioner

onto the linear solver for each component. The chapter is organized as follows: In section 2.2.2 we first present briefly the fully discretized formulation for the spectral/hp element method as a background. Then we introduce the main contribution of this chapter: a modified version of the original spectral/hp element formulation which we refer to as the semi-local method. In the last part of this section, the modified low energy preconditioner is illustrated for distributing the residual based on the localization operator of the semi-local method. To demonstrate convergence, in section 2.2.3 we test the $p-$, $t-$ and $h-$ convergences of the semi-local method. Finally, the main results for efficiency tests are presented in section 2.2.4, including an elastic tube case, which involves only the solid solver, and two fluid-structure interaction cases for a patient-specific aneurysm simulation. We finish in section 2.2.5 with a summary.

2.2.2 Formulation

In this section, we derive the formulation for the displacement field $\boldsymbol{\eta}(\mathbf{X}, t)$ in a three-dimensional object occupying the domain $\Omega \subset \mathbf{R}^3$ with boundary $\partial\Omega = \partial\Omega_D \cup \partial\Omega_N$. Here Dirichlet type boundary conditions are prescribed on $\partial\Omega_D$, Neumann type boundary conditions (traction) on $\partial\Omega_N$, and Ω stands for the initial configuration of the object. The linear elastic model with infinitesimal deformations is considered in this chapter. In the following, we will denote by A_e the element-wise expression for any given global quantity A.

Original spectral/hp element formulation

Before introducing the semi-local method, we first present the standard spectral/hp element method for linear elastic problems. The standard spectral/hp element formulation illustrated in the following will be referred as the *original spectral/hp element formulation*, to be contrasted with the modified version, i.e., the semi-local method.

For linear elasticity with infinitesimal deformations, we can write its strain energy density function as [44, 45]:

$$\Psi(\mathbf{E}) = \frac{\lambda}{2}(\mathrm{tr}\mathbf{E})^2 + \mu\mathbf{E} : \mathbf{E}, \tag{2.2.1}$$

where $\mathbf{E} = \frac{1}{2}\left(\left(\frac{\partial\boldsymbol{\eta}}{\partial\mathbf{X}}\right)^T + \left(\frac{\partial\boldsymbol{\eta}}{\partial\mathbf{X}}\right)\right)$ is the strain tensor, and μ, λ are the shear and Lame constants, respectively. The Cauchy stress tensor $\mathbf{S} = \frac{\partial\Psi}{\partial\mathbf{E}}$ can be expressed as in (2.1.4). Then the weak form of the equation describing the object deformation can be given as [44]:

$$\int_\Omega \rho\frac{\partial^2\boldsymbol{\eta}}{\partial t^2}\mathbf{v}d\Omega + \int_\Omega \mathbf{S} : \nabla\mathbf{v}d\Omega - \int_{\partial\Omega_N} \mathbf{T}\cdot\mathbf{v}d\Gamma - \int_\Omega \mathbf{f}\cdot\mathbf{v}d\Omega = 0,\ \forall\mathbf{v} \in \mathbf{U}_0, \tag{2.2.2}$$

where the displacement field $\boldsymbol{\eta}(\mathbf{X},t) \in \mathbf{U}(t) = \{\mathbf{w}(\mathbf{X},t) \in [H^1(\Omega)]^3 | \mathbf{w}(\mathbf{X},t) = \boldsymbol{\eta}_D(\mathbf{X},t) \text{ on } \partial\Omega_D\}$, and $\mathbf{U}_0 = \{\mathbf{w}(\mathbf{X}) \in [H^1(\Omega)]^3 | \mathbf{w}(\mathbf{X}) = \mathbf{0} \text{ on } \partial\Omega_D\}$; $\mathbf{T}$, $\mathbf{f}$ and ρ are the external traction force on $\partial\Omega_N$, external body force, and mass density, respectively.

Next, we consider the discretization of (2.2.2) similarly as in chapter 2.1. Based on the high-order hierarchical shape functions as defined in Appendix A.1, on each element we expand the displacement $\boldsymbol{\eta}_e = ((\eta_e)_1, (\eta_e)_2, (\eta_e)_3)$ and the test function $\mathbf{v}_e = ((v_e)_1, (v_e)_2, (v_e)_3)$:

$$(\eta_e)_i(\mathbf{X}) = \sum_{p=1}^{N_e} (\hat{\eta}_e)_{ip} \phi_p(\mathbf{X}), \quad (v_e)_i(\mathbf{X}) = \sum_{p=1}^{N_e} (\hat{v}_e)_{ip} \phi_p(\mathbf{X}), \quad i = 1,2,3, \tag{2.2.3}$$

where N_e is the total number of shape functions for displacement on this element, $\phi_k(\mathbf{X})$ are the shape functions, and $(\hat{\eta}_e)_{ip}$, $(\hat{v}_e)_{ip}$ are the expansion coefficients. Substituting expression (2.2.3) into the weak form (2.2.2) and assembling globally, we obtain

$$\mathbf{M}\frac{d^2\mathbf{U}}{dt^2} = -\mathbf{K}\mathbf{U} + \mathbf{F}. \tag{2.2.4}$$

Here $\mathbf{U}$ is the global vector of unknown expansion coefficients, which is assembled from the corresponding element expansion coefficient vectors $\mathbf{U}_e$. In order to have smaller bandwidth for the coefficient matrix, $\mathbf{U}_e$ is organized in a way such that the three displacement components corresponding to a particular mode are adjacent, as shown in (2.1.22). Since the interior modes are coupled with the boundary modes of the same element only, while assembling the local vector $\mathbf{U}_e$ into the global vector $\mathbf{U}$, we arrange the modes following the "vertex-edge-face-interior" sequence as in [6]. $\mathbf{F}$ is the global vector of the external forces organized in the same ordering of indices as $\mathbf{U}$. On each element, $\mathbf{F}_e$ is a vector of length $3N_e$, with components

$$(F_e)_{ip} = \int_{\partial(\Omega_e)_N} (T_e)_i \phi_p d\Gamma_e + \int_{\Omega_e} (f_e)_i \phi_p d\Omega_e, \; i = 1,2,3, \tag{2.2.5}$$

where $(T_e)_i$ and $(f_e)_i$ are the components of the external traction and body forces applied on this element, respectively. Correspondingly, on each element we have a $3N_e \times 3N_e$ local mass matrix $\mathbf{M}_e$, which is organized as a matrix of $N_e \times N_e$ blocks, with each block being a 3×3 submatrix:

$$\mathbf{M}_e = \begin{bmatrix} (\mathbf{M}_e)_{11} & \cdots & (\mathbf{M}_e)_{1N_e} \\ \vdots & \ddots & \vdots \\ (\mathbf{M}_e)_{N_e1} & \cdots & (\mathbf{M}_e)_{N_eN_e} \end{bmatrix}, \quad (\mathbf{M}_e)_{pq} = \left(\int_{\Omega_e} \rho \phi_p \phi_q d\Omega_e \right) \mathbf{I}. \tag{2.2.6}$$

Here $\mathbf{I}$ is the 3×3 identity matrix. Similarly, on each element we can organize the $3N_e \times 3N_e$

stiffness matrix $\mathbf{K}$ into $N_e \times N_e$ blocks, with each 3×3 submatrix $(\mathbf{K}_e)_{pq}$ being

$$(\mathbf{K}_e)_{pq} = \int_{\Omega_e} \begin{bmatrix} (\lambda+\mu)\frac{\partial\phi_p}{\partial X}\frac{\partial\phi_q}{\partial X} + \alpha & \lambda\frac{\partial\phi_p}{\partial X}\frac{\partial\phi_q}{\partial Y} + \mu\frac{\partial\phi_p}{\partial Y}\frac{\partial\phi_q}{\partial X} & \lambda\frac{\partial\phi_p}{\partial X}\frac{\partial\phi_q}{\partial Z} + \mu\frac{\partial\phi_p}{\partial Z}\frac{\partial\phi_q}{\partial X} \\ \lambda\frac{\partial\phi_p}{\partial Y}\frac{\partial\phi_q}{\partial X} + \mu\frac{\partial\phi_p}{\partial X}\frac{\partial\phi_q}{\partial Y} & (\lambda+\mu)\frac{\partial\phi_p}{\partial Y}\frac{\partial\phi_q}{\partial Y} + \alpha & \lambda\frac{\partial\phi_p}{\partial Y}\frac{\partial\phi_q}{\partial Z} + \mu\frac{\partial\phi_p}{\partial Z}\frac{\partial\phi_q}{\partial Y} \\ \lambda\frac{\partial\phi_p}{\partial Z}\frac{\partial\phi_q}{\partial X} + \mu\frac{\partial\phi_p}{\partial X}\frac{\partial\phi_q}{\partial Z} & \lambda\frac{\partial\phi_p}{\partial Z}\frac{\partial\phi_q}{\partial Y} + \mu\frac{\partial\phi_p}{\partial Y}\frac{\partial\phi_q}{\partial Z} & (\lambda+\mu)\frac{\partial\phi_p}{\partial Z}\frac{\partial\phi_q}{\partial Z} + \alpha \end{bmatrix} d\Omega_e, \tag{2.2.7}$$

where $\alpha = \mu\left(\frac{\partial\phi_p}{\partial X}\frac{\partial\phi_q}{\partial X} + \frac{\partial\phi_p}{\partial Y}\frac{\partial\phi_q}{\partial Y} + \frac{\partial\phi_p}{\partial Z}\frac{\partial\phi_q}{\partial Z}\right)$.

To discretize in time, two types of methods are employed: the Newmark scheme as a start up in the first two steps, and a three-step backward differentiation formula (BDF) [77] for the other steps. They can be defined by different expressions for the acceleration and velocity approximations. Let n denote the index of the time step, in the *Newmark scheme* based on the current displacement coefficients $\mathbf{U}^n$, previous time step displacement $\mathbf{U}^{n-1}$, velocity $\dot{\mathbf{U}}^{n-1}$ and acceleration $\ddot{\mathbf{U}}^{n-1}$, we can approximate the acceleration and velocity at the n-th step as:

$$\dot{\mathbf{U}}^n = \dot{\mathbf{U}}^{n-1} + \Delta t\left((1-\theta_1)\ddot{\mathbf{U}}^{n-1} + \theta_1\ddot{\mathbf{U}}^n\right), \tag{2.2.8a}$$

$$\ddot{\mathbf{U}}^n = \frac{1}{\Delta t^2\theta_2}\left(\mathbf{U}^n - \mathbf{U}^{n-1} - \Delta t\dot{\mathbf{U}}^{n-1} - \frac{\Delta t^2}{2}(1-2\theta_2)\ddot{\mathbf{U}}^{n-1}\right), \tag{2.2.8b}$$

where we have used " $\cdot$ " to denote the temporal derivatives. Substituting into (2.2.4), we obtain the fully discretized formulation for the Newmark scheme:

$$\left(\frac{\mathbf{M}}{\Delta t^2\theta_2} + \mathbf{K}\right)\mathbf{U}^n = \mathbf{F} + \frac{\mathbf{M}}{\Delta t^2\theta_2}\left(\mathbf{U}^{n-1} + \Delta t\dot{\mathbf{U}}^{n-1} + \frac{\Delta t^2}{2}(1-2\theta_2)\ddot{\mathbf{U}}^{n-1}\right). \tag{2.2.9}$$

Depending on the requirements of accuracy and stability, different values can be set for the parameters (θ_1, θ_2). In the following, we will use the parameters $(\theta_1, \theta_2) = (0.5, 0.25)$ which lead to a second-order scheme.

In the *three-step BDF scheme*, the acceleration and velocity approximations are also expressed based on the current information ($\mathbf{U}^n$, $\dot{\mathbf{U}}^n$) and previous time steps results ($\mathbf{U}^{n-i}$, $\dot{\mathbf{U}}^{n-i}$) as:

$$\dot{\mathbf{U}}^n = A_1\mathbf{U}^n + B_1\mathbf{U}^{n-1} + C_1\mathbf{U}^{n-2} + D_1\mathbf{U}^{n-3}, \tag{2.2.10a}$$

$$\ddot{\mathbf{U}}^n = A_2\dot{\mathbf{U}}^n + B_2\dot{\mathbf{U}}^{n-1} + C_2\dot{\mathbf{U}}^{n-2} + D_2\dot{\mathbf{U}}^{n-3}, \tag{2.2.10b}$$

and correspondingly the fully discretized formulation for the three-step BDF scheme is:

$$\begin{aligned}(A_1A_2\mathbf{M} + \mathbf{K})\,\mathbf{U}^n =& \mathbf{F} - \mathbf{M}(A_2(B_1\mathbf{U}^{n-1} + C_1\mathbf{U}^{n-2} + D_1\mathbf{U}^{n-3}) \\ &+ (B_2\dot{\mathbf{U}}^{n-1} + C_2\dot{\mathbf{U}}^{n-2} + D_2\dot{\mathbf{U}}^{n-3})).\end{aligned} \tag{2.2.11}$$

Here A_i, B_i, C_i and D_i $(i = 1, 2)$ are defined as follows

$$A_1 = \frac{\theta_1}{\Delta t},\ B_1 = \frac{2.5 - 3\theta_1}{\Delta t},\ C_1 = \frac{3\theta_1 - 4}{\Delta t},\ D_1 = \frac{1.5 - \theta_1}{\Delta t}, \tag{2.2.12a}$$

$$A_2 = \frac{\theta_2}{\Delta t},\ B_2 = \frac{2.5 - 3\theta_2}{\Delta t},\ C_2 = \frac{3\theta_2 - 4}{\Delta t},\ D_2 = \frac{1.5 - \theta_2}{\Delta t}, \tag{2.2.12b}$$

and (θ_1, θ_2) are also decided based on considerations of stability and dissipation. To be specific, we will use $(\theta_1, \theta_2) = (5/3, 5/3)$ in this chapter because of its enhanced stability [77]. This pair of parameters corresponds to a three-step second-order scheme.

While solving the linear system (2.2.9) or (2.2.11), a Schur complement reformulation is performed. Then all the interior modes are condensed out and the elemental boundary unknowns are solved with a direct solver on each element. Globally, only the boundary modes need to be solved with the preconditioned conjugate gradient solver, where the diagonal preconditioner is employed [27].

Semi-local method

In the semi-local method, we are solving for the displacement on each element. In the following, for any given global vector $\mathbf{V}$, we organize its components into three vectors as $\mathbf{Vi}$ $(i = 1, 2, 3)$. To be specific,

$$\mathbf{Vi} = [\cdots\ V_{i,p}\ V_{i,p+1}\ \cdots]^T. \tag{2.2.13}$$

is the collection of components in the corresponding direction. Here $a_{i,p}$ is defined following the same way as in (2.1.22).

To maintain the accuracy of the time integration schemes, on each step we perform subiterations until reaching the convergence tolerance ϵ

$$||\mathbf{U}^{n,k} - \mathbf{U}^{n,k-1}|| < \epsilon \tag{2.2.14}$$

at the n-th time step and k-th subiteration. In the semi-local method, the formulations (2.2.9) and (2.2.11) are modified as

$$\begin{aligned}
\text{Newmark: } \left(\frac{\mathbf{M}_e}{\Delta t^2 \theta_2} + \mathbf{K}_e\right) \mathbf{U}_e^{n,k} &= \mathcal{L}_e \left(\hat{\mathbf{F}}^{n,k-1} - \left(\frac{\mathbf{M}}{\Delta t^2 \theta_2} + \mathbf{K}\right) \mathbf{U}^{n,k-1}\right) \\
&\quad + \left(\frac{\mathbf{M}_e}{\Delta t^2 \theta_2} + \mathbf{K}_e\right) \mathbf{U}_e^{n,k-1}, \\
\text{BDF: } \left(A_1 A_2 \mathbf{M}_e + \mathbf{K}_e\right) \mathbf{U}_e^{n,k} &= \mathcal{L}_e \left(\hat{\mathbf{F}}^{n,k-1} - \left(A_1 A_2 \mathbf{M} + \mathbf{K}\right) \mathbf{U}^{n,k-1}\right) \\
&\quad + \left(A_1 A_2 \mathbf{M}_e + \mathbf{K}_e\right) \mathbf{U}_e^{n,k-1},
\end{aligned} \tag{2.2.15}$$

where $\hat{\mathbf{F}}$ is the right hand side of (2.2.9) and (2.2.11):

$$\begin{aligned}
\text{Newmark: } \hat{\mathbf{F}}^{n,k-1} &= \mathbf{F}^n + \frac{\mathbf{M}}{\Delta t^2 \theta_2}\left(\mathbf{U}^{n-1} + \Delta t \dot{\mathbf{U}}^{n-1} + \frac{\Delta t^2}{2}(1-2\theta_2)\ddot{\mathbf{U}}^{n-1}\right), \\
\text{BDF: } \hat{\mathbf{F}}^{n,k-1} &= \mathbf{F}^n - \mathbf{M}(A_2(B_1\mathbf{U}^{n-1} + C_1\mathbf{U}^{n-2} + D_1\mathbf{U}^{n-3}) \\
&\quad + (B_2\dot{\mathbf{U}}^{n-1} + C_2\dot{\mathbf{U}}^{n-2} + D_2\dot{\mathbf{U}}^{n-3})),
\end{aligned} \tag{2.2.16}$$

and $\mathcal{L}_e$ is a *localization operator* for each element e, which maps a global vector $\mathbf{a}$ onto a local vector $\mathbf{a}_e$. From expressions (2.2.15) , we can see that the function of localization operator $\mathcal{L}_e$ is to distribute the global residual from the last subiteration onto each element. By comparing with the original spectral/hp element method formulations (2.2.9) and (2.2.11), this operator should be taken as:

$$\begin{aligned}
\text{Newmark: } \mathcal{L}_e(\mathbf{a}) &= \left(\frac{\mathbf{M}_e}{\Delta t^2\theta_2} + \mathbf{K}_e\right)\left(\left(\frac{\mathbf{M}}{\Delta t^2\theta_2} + \mathbf{K}\right)^{-1}\mathbf{a}\right)_e, \\
\text{BDF: } \mathcal{L}_e(\mathbf{a}) &= (A_1A_2\mathbf{M}_e + \mathbf{K}_e)\left((A_1A_2\mathbf{M} + \mathbf{K})^{-1}\mathbf{a}\right)_e.
\end{aligned} \tag{2.2.17}$$

However, by doing so, we have to invert the original $3N \times 3N$ global linear system, and hence we gain no efficiency. We will therefore try to decompose the global linear system into three smaller $N \times N$ systems related with the three components of the displacement **U1**, **U2** and **U3**, which are the displacements in x, y and z directions, respectively. One possible way is to project the operator we proposed in (2.2.17) with respect to these components separately, which will be noted as $\mathcal{L}i_e$ $(i = 1, 2, 3)$. For the Newmark scheme, we have

$$\begin{aligned}
\mathcal{L}1_e(\mathbf{a1}) &= \left(\frac{\mathbf{M1}_e}{\Delta t^2\theta_2} + \mathbf{K1}_e\right)\left(\left(\frac{\mathbf{M1}}{\Delta t^2\theta_2} + \mathbf{K1}\right)^{-1}\mathbf{a1}\right)_e, \\
\mathcal{L}2_e(\mathbf{a2}) &= \left(\frac{\mathbf{M2}_e}{\Delta t^2\theta_2} + \mathbf{K2}_e\right)\left(\left(\frac{\mathbf{M2}}{\Delta t^2\theta_2} + \mathbf{K2}\right)^{-1}\mathbf{a2}\right)_e, \\
\mathcal{L}3_e(\mathbf{a3}) &= \left(\frac{\mathbf{M3}_e}{\Delta t^2\theta_2} + \mathbf{K3}_e\right)\left(\left(\frac{\mathbf{M3}}{\Delta t^2\theta_2} + \mathbf{K3}\right)^{-1}\mathbf{a3}\right)_e,
\end{aligned} \tag{2.2.18}$$

and for the BDF scheme, we have

$$\begin{aligned}
\mathcal{L}1_e(\mathbf{a1}) &= (A_1A_2\mathbf{M1}_e + \mathbf{K1}_e)\left((A_1A_2\mathbf{M1} + \mathbf{K1})^{-1}\mathbf{a1}\right)_e, \\
\mathcal{L}2_e(\mathbf{a2}) &= (A_1A_2\mathbf{M2}_e + \mathbf{K2}_e)\left((A_1A_2\mathbf{M2} + \mathbf{K2})^{-1}\mathbf{a2}\right)_e, \\
\mathcal{L}3_e(\mathbf{a3}) &= (A_1A_2\mathbf{M3}_e + \mathbf{K3}_e)\left((A_1A_2\mathbf{M3} + \mathbf{K3})^{-1}\mathbf{a3}\right)_e,
\end{aligned} \tag{2.2.19}$$

where **M1**, **M2**, **M3** are the projections of the mass matrix **M** related to **U1**, **U2** and **U3**,

respectively:

$$\mathbf{M1}_e = \mathbf{M2}_e = \mathbf{M3}_e = \begin{bmatrix} \int_{\Omega_e} \rho\phi_1\phi_1 d\Omega_e & \cdots & \int_{\Omega_e} \rho\phi_1\phi_{N_e} d\Omega_e \\ \vdots & \ddots & \vdots \\ \int_{\Omega_e} \rho\phi_{N_e}\phi_1 d\Omega_e & \cdots & \int_{\Omega_e} \rho\phi_{N_e}\phi_{N_e} d\Omega_e \end{bmatrix}, \tag{2.2.20}$$

and **K1**, **K2**, **K3** are the projections of the stiffness matrix **K**:

$$\mathbf{Ki}_e = \begin{bmatrix} (\mathbf{Ki}_e)_{11} & \cdots & (\mathbf{Ki}_e)_{1N_e} \\ \vdots & \ddots & \vdots \\ (\mathbf{Ki}_e)_{N_e1} & \cdots & (\mathbf{Ki}_e)_{N_eN_e} \end{bmatrix}, \quad i = 1, 2, 3, \tag{2.2.21}$$

$$\begin{aligned} (\mathbf{K1}_e)_{pq} &= \int_{\Omega_e} \left[(\lambda+\mu)\frac{\partial\phi_p}{\partial X}\frac{\partial\phi_q}{\partial X} + \alpha \right] d\Omega_e \\ (\mathbf{K2}_e)_{pq} &= \int_{\Omega_e} \left[(\lambda+\mu)\frac{\partial\phi_p}{\partial Y}\frac{\partial\phi_q}{\partial Y} + \alpha \right] d\Omega_e \\ (\mathbf{K3}_e)_{pq} &= \int_{\Omega_e} \left[(\lambda+\mu)\frac{\partial\phi_p}{\partial Z}\frac{\partial\phi_q}{\partial Z} + \alpha \right] d\Omega_e \end{aligned} \tag{2.2.22}$$

with $\alpha = \mu\left(\frac{\partial\phi_p}{\partial X}\frac{\partial\phi_q}{\partial X} + \frac{\partial\phi_p}{\partial Y}\frac{\partial\phi_q}{\partial Y} + \frac{\partial\phi_p}{\partial Z}\frac{\partial\phi_q}{\partial Z}\right)$. Since each 3×3 submatrix $(\mathbf{M}_e)_{pq}$ is proportional to the 3×3 identity matrix $\mathbf{I}$, all the information of the mass matrix $\mathbf{M}$ is kept while being projected into $\mathbf{Mi}$ $(i = 1, 2, 3)$. However, while projecting the stiffness matrix $\mathbf{K}$ into $\mathbf{Ki}$ $(i = 1, 2, 3)$, we abandon all the nondiagonal terms in (2.2.7). Therefore, the subiteration is required because of the loss of information in $\mathbf{K}$, i.e., the more $\mathbf{M}$ dominates the linear system, the less subiterations will be required to reach convergence.

In each subiteration, one has to generate a global expression for displacement $\mathbf{U}^{n,k}$ after the element-wise results $\mathbf{U}_e^{n,k}$ are obtained from (2.2.15). An *assembly globalization operator* $\mathcal{G}$ is therefore defined as the least square fit of the local solution. For the j-th global mode, which corresponds to the je-th mode on each related element Ω_e, we have

$$(\mathcal{G}(\mathbf{a}))_j = \frac{\sum_{e\in S_j}(measure(\Omega_e)(\mathbf{a}_e)_{je})}{\sum_{e\in S_j} measure(\Omega_e)}, \tag{2.2.23}$$

where $\mathbf{a}_e$ and $\mathcal{G}(\mathbf{a})$ are the local vector on element Ω_e and the global vector after assembling, respectively. Moreover, the $measure(\Omega_e)$ is the size of element Ω_e, and the set of elements S_j is the union of elements which contributes to the j-th global mode. To see this more clearly, the procedure for a case with two elements Ω_1 and Ω_2 is illustrated in Figure 2.17: the vertex $j1$-th mode of element Ω_1 and the vertex $j2$-th mode of element Ω_2 are related with the j-th mode of the

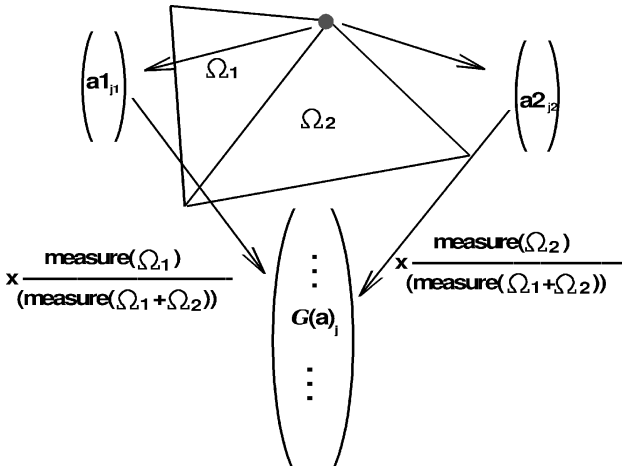

Figure 2.17: Sketch illustrating the construction of the assembly globalization operator $\mathcal{G}$, see text for details.

global vector, therefore the set of elements S_j in (2.2.23) is $\{\Omega_1, \Omega_2\}$. To generate the j-th number of the global vector $\mathcal{G}(\mathbf{a})$, two local vectors **a1** (from element Ω_1) and **a2** (from element Ω_2) are involved. More precisely, one should calculate the weighted average of the $j1$-th number in **a1** and the $j2$-th number of **a2**, where the weight is taken as the ratio of element size.

To summarize, at the n-th time step, we solve for the displacement coefficients $\mathbf{U}^n$ using the following algorithm:

1. Set
$$\boldsymbol{\eta}^{n,0} = \boldsymbol{\eta}^{n-1},\ \dot{\boldsymbol{\eta}}^{n,0} = \dot{\boldsymbol{\eta}}^{n-1},\ \ddot{\boldsymbol{\eta}}^{n,0} = \ddot{\boldsymbol{\eta}}^{n-1}, \tag{2.2.24}$$

2. **for** $k = 1 : k_{max}$, **do**

   (a) Update $\hat{\mathbf{F}}^{n,k-1}$ as in equation (2.2.16) and calculate the global residual:
$$\begin{aligned} &\text{Newmark: } \hat{\mathbf{F}}^{n,k-1} - \left(\frac{\mathbf{M}}{\Delta t^2 \theta_2} + \mathbf{K}\right) \mathbf{U}^{n,k-1}, \\ &\text{BDF: } \hat{\mathbf{F}}^{n,k-1} - (A_1 A_2 \mathbf{M} + \mathbf{K})\, \mathbf{U}^{n,k-1}. \end{aligned} \tag{2.2.25}$$

   (b) Distribute the global residual (2.2.25) onto each element with the localization operator $\mathcal{L}i_e$ $(i = 1, 2, 3)$ as defined in (2.2.18) and (2.2.19):
$$\begin{aligned} &\text{Newmark: } \mathcal{L}_e \left(\hat{\mathbf{F}}^{n,k-1} - \left(\frac{\mathbf{M}}{\Delta t^2 \theta_2} + \mathbf{K}\right) \mathbf{U}^{n,k-1}\right), \\ &\text{BDF: } \mathcal{L}_e \left(\hat{\mathbf{F}}^{n,k-1} - (A_1 A_2 \mathbf{M} + \mathbf{K})\, \mathbf{U}^{n,k-1}\right). \end{aligned} \tag{2.2.26}$$

(c) Obtain the element-wise approximation for displacement $\mathbf{U}_e^{n,k}$ following the formulation (2.2.15).

(d) Assemble the global expression for displacement coefficients with the assembly globalization operator $\mathcal{G}$ as defined in (2.2.23):

$$\mathbf{U}^{n,k} = \mathcal{G}(\mathbf{U}_e^{n,k}). \tag{2.2.27}$$

(e) Calculate the displacement approximation $\boldsymbol{\eta}^{n,k}$ and also the velocity and acceleration $\dot{\boldsymbol{\eta}}^{n,k}$ and $\ddot{\boldsymbol{\eta}}^{n,k}$ based on the Newmark scheme (2.2.8) or BDF scheme (2.2.10).

(f) Check convergence: if

$$||\boldsymbol{\eta}^{n,k} - \boldsymbol{\eta}^{n,k-1}|| < \epsilon, \tag{2.2.28}$$

set $k = k_{max}$ and update the results as

$$\boldsymbol{\eta}^{n} = \boldsymbol{\eta}^{n,k},\ \dot{\boldsymbol{\eta}}^{n} = \dot{\boldsymbol{\eta}}^{n,k},\ \ddot{\boldsymbol{\eta}}^{n} = \ddot{\boldsymbol{\eta}}^{n,k}. \tag{2.2.29}$$

Else, continue to the $(k+1)$-th subiteration.

3. Go to time step $n+1$.

Low energy preconditioner

While solving the three global $N \times N$ linear systems in (2.2.18) or (2.2.19), a parallel low energy preconditioner [75, 76] is used in the conjugate gradient solver, which greatly decreases the condition number and consequently increases the efficiency of the conjugate gradient solver, as shown in [75, 76]. For any given symmetric matrix $\mathbf{Si}$ which is arranged from the element-wise matrix $\mathbf{Si}_e$, on each element we apply the transformation matrix $\mathbf{R}_e$ such that $\mathbf{Ti}_e = \mathbf{R}_e\mathbf{Si}_e\mathbf{R}_e^T$ forms the low energy preconditioner. To decrease the condition number, $\mathbf{R}_e$ should be chosen to decouple the vertex, edge and face modes of the matrix $\mathbf{Si}_e$. Here we write the target elemental matrix $\mathbf{Si}_e$ into the form

$$\mathbf{Si}_e = \begin{bmatrix} (\mathbf{Si}_e)_{vv} & (\mathbf{Si}_e)_{v,ef} \\ (\mathbf{Si}_e)_{v,ef}^T & (\mathbf{Si}_e)_{ef,ef} \end{bmatrix} = \begin{bmatrix} (\mathbf{Si}_e)_{vv} & (\mathbf{Si}_e)_{ve} & (\mathbf{Si}_e)_{vf} \\ (\mathbf{Si}_e)_{ve}^T & (\mathbf{Si}_e)_{ee} & (\mathbf{Si}_e)_{ef} \\ (\mathbf{Si}_e)_{vf}^T & (\mathbf{Si}_e)_{ef}^T & (\mathbf{Si}_e)_{ff} \end{bmatrix}, \tag{2.2.30}$$

where $(\mathbf{Si}_e)_{vv}$ denotes all the couplings between the vertex modes, and $(\mathbf{Si}_e)_{v,ef}$ contains all the couplings between the vertex modes and edge/face modes. The other terms are defined similarly. The

transformation matrix $\mathbf{R}_e$ is arisen from a transformation of basis, which has an upper triangular form

$$\mathbf{R}_e = \begin{bmatrix} \mathbf{I} & (\mathbf{R}_e)_v \\ 0 & (\mathbf{R}_e)_{ef,ef} \end{bmatrix} = \begin{bmatrix} \mathbf{I} & (\mathbf{R}_e)_{ve} & (\mathbf{R}_e)_{vf} \\ 0 & \mathbf{I} & (\mathbf{R}_e)_{ef} \\ 0 & 0 & \mathbf{I} \end{bmatrix}, \tag{2.2.31}$$

where $(\mathbf{R}_e)_v = [(\mathbf{R}_e)_{ve}\ (\mathbf{R}_e)_{vf}]$. $(\mathbf{R}_e)_{ve}$, $(\mathbf{R}_e)_{vf}$ represent the modification of the vertex modes by the edges and faces modes respectively, and $(\mathbf{R}_e)_{ef}$ represents the modification of the edge modes by the face modes. Then, the transformed elemental matrix $\mathbf{Ti}_e$ can be expressed as

$$\mathbf{Ti} = \begin{bmatrix} \mathbf{Ti}_{vv} & ((\mathbf{Si}_e)_{v,ef} + (\mathbf{R}_e)_v(\mathbf{Si}_e)_{ef,ef})(\mathbf{R}_e)_{ef,ef}^T \\ (\mathbf{R}_e)_{ef,ef}((\mathbf{Si}_e)_{v,ef}^T + (\mathbf{Si}_e)_{ef,ef}(\mathbf{R}_e)_v^T) & \mathbf{Ti}_{ef,ef} \end{bmatrix} \tag{2.2.32}$$

where

$$\mathbf{Ti}_{ef,ef} = \begin{bmatrix} \mathbf{Ti}_{ee} & (\mathbf{Si}_e)_{ef} + (\mathbf{R}_e)_{vf}(\mathbf{Si}_e)_{ff} \\ (\mathbf{Si}_e)_{ef}^T + (\mathbf{Si}_e)_{ff}(\mathbf{R}_e)_{vf}^T & (\mathbf{Si}_e)_{ff} \end{bmatrix}. \tag{2.2.33}$$

$$\mathbf{Ti}_{vv} = (\mathbf{Si}_e)_{vv} + (\mathbf{R}_e)_v(\mathbf{Si}_e)_{v,ef}^T + (\mathbf{Si}_e)_{v,ef}(\mathbf{R}_e)_v^T + (\mathbf{R}_e)_v(\mathbf{Si}_e)_{ef,ef}(\mathbf{R}_e)_v^T,$$

$$\mathbf{Ti}_{ee} = (\mathbf{Si}_e)_{ee} + (\mathbf{R}_e)_{vf}(\mathbf{Si}_e)_{ef}^T + (\mathbf{Si}_e)_{ef}(\mathbf{R}_e)_{vf}^T + (\mathbf{R}_e)_{vf}(\mathbf{Si}_e)_{ff}(\mathbf{R}_e)_{vf}^T.$$

We first consider the case when **Si** is isotropic, and the problem is defined within a rotational symmetric standard element. To completely orthogonalize the vertex modes with the edge and face modes we require that

$$(\mathbf{R}_e)_v = -(\mathbf{Si}_e)_{ef,ef}^{-1}(\mathbf{Si}_e)_{v,ef}^T.$$

Similarly, to decouple the edge modes from the face modes, we should have

$$(\mathbf{R}_e)_{ef,ef} = -(\mathbf{Si}_e)_{ff}^{-1}(\mathbf{Si}_e)_{ef}^T.$$

However, in our localization procedure as in (2.2.18) and (2.2.19), we are considering $\mathbf{Si}_e = \dfrac{\mathbf{Mi}_e}{\Delta t^2\theta_2} + \mathbf{Ki}_e$ for the Newmark scheme and $\mathbf{Si}_e = A_1A_2\mathbf{Mi}_e + \mathbf{Ki}_e$ for the BDF scheme. It should be noted that: firstly, generally the elements are not rotationally symmetric; secondly, these matrices are not isotropic. From [75, 76] we can see that because of these two features, the transformation $\mathbf{R}_e$ generated from $\mathbf{Si}_e$ would destroy the boundary decomposition of the vertex and edges modes, which will cause difficulties in generating a global expansion from the elemental definitions. To resolve the first problem, in this section we will construct the transformation matrix $\mathbf{R}_e$ from the standard region, which means that we do not take account of the Jacobian of the mapping between

each element and the standard region. Accordingly, the edges in the global components will not be completely decoupled from the surrounding elements, but the low-energy basis will still provide a good preconditioner as demonstrated in [75, 76]. Regarding the second problem, to generate the transformation matrix $\mathbf{R}_e$ from an isotropic matrix we consider an approximation of $\mathbf{Si}_e$ as

$$\begin{aligned} \text{Newmark: } \hat{\mathbf{Si}}_e &= \frac{\mathbf{Mi}_e}{\Delta t^2 \theta_2} + \hat{\mathbf{K}}_e, \\ \text{BDF: } \hat{\mathbf{Si}}_e &= A_1 A_2 \mathbf{Mi}_e + \hat{\mathbf{K}}_e, \end{aligned} \tag{2.2.34}$$

where

$$(\hat{\mathbf{K}}_e)_{pq} = \alpha = \mu \left(\frac{\partial \phi_p}{\partial X} \frac{\partial \phi_q}{\partial X} + \frac{\partial \phi_p}{\partial Y} \frac{\partial \phi_q}{\partial Y} + \frac{\partial \phi_p}{\partial Z} \frac{\partial \phi_q}{\partial Z} \right).$$

In summary, before the simulation we can generate and save the transformation matrix $\mathbf{R}_e$ for the isotropic matrix $\hat{\mathbf{Si}}_e$ on the standard region for each element, then assemble the low energy preconditioner $\mathbf{Ti}$ from the element-wise matrix $\mathbf{Ti}_e = \mathbf{R}_e \mathbf{Si}_e \mathbf{R}_e^T$. This preconditioner $\mathbf{Ti}$ is applied in the conjugate gradient solver, while generating the localization operator as in equations (2.2.18) and (2.2.19).

2.2.3 Convergence studies

In this section, we investigate the accuracy of the semi-local method by comparing simulation results against analytical fabricated solutions. Three kinds of convergence (p, t, h) will be studied, and the errors will be compared with that from the original spectral/hp element formulation described in (2.2.4). For the material properties, we will use Young's modulus E and the Poisson ratio ζ, which are related to the material constants λ and μ in (2.2.1) by

$$\mu = \frac{E}{2(1+\zeta)}, \quad \lambda = \frac{\zeta E}{(1+\zeta)(1-2\zeta)}. \tag{2.2.35}$$

In this section, we take a tolerance as $\epsilon = 10^{-12}$ to check the subiteration convergence in each time step.

$p-$convergence

Now we will consider the deformation of a cubic solid occupying the domain $0 \leq X \leq 1$, $0 \leq Y \leq 1$ and $0 \leq Z \leq 1$ discretized by eight hexahedral elements as in the left plot of Figure 2.18, where the thick solid lines mark the edges of the spectral elements. For the test example, we use a fabricated problem as in [27]. The face $X = 0$ is clamped, and a traction force field $\mathbf{T} = (T_1, T_2, T_3)$

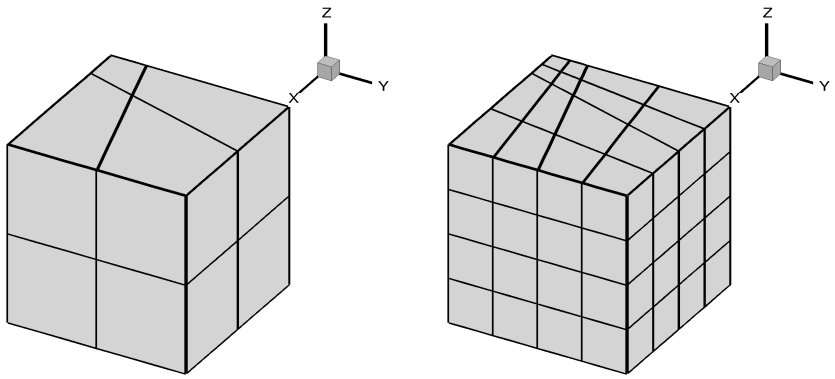

Figure 2.18: Meshes for convergence tests. Left: mesh for the p, t convergence tests and the $2\times2\times2$ mesh in the h convergence test. Right: the $4\times4\times4$ mesh in the h convergence test.

is applied on the rest of the faces, which is given by

$$\begin{aligned} T_1 &= n_x(\lambda+2\mu)(A+B\sin at+bC\cos bX),\\ T_2 &= n_y\lambda(A+B\sin at+bC\cos bX),\\ T_3 &= n_z\lambda(A+B\sin at+bC\cos bX), \end{aligned} \tag{2.2.36}$$

where $\mathbf{n}=(n_x,n_y,n_z)$ is the outward-pointing unit vector normal to the surface, and A, B, C, a, b are prescribed constants. A body force field $\mathbf{f}=(f_1,f_2,f_3)$ is applied on the solid with components:

$$f_1=(\lambda+2\mu)b^2C\sin bX/\rho-a^2BX\sin at,\quad f_2=f_3=0. \tag{2.2.37}$$

When $t=0$, the displacement and velocity fields are provided as the initial conditions:

$$\begin{aligned} \eta_1 &= AX+C\sin bX,\quad \eta_2=\eta_3=0,\\ \dot\eta_1 &= BaX,\quad \dot\eta_2=\dot\eta_3=0, \end{aligned} \tag{2.2.38}$$

where η_1, η_2 and η_3 are the displacements in X, Y and Z directions, respectively. This problem has the following analytic solution for the displacement of the object:

$$\eta_1=(A+B\sin at)X+C\sin bX,\ \eta_2=\eta_3=0. \tag{2.2.39}$$

In this test, we use the following parameters:

$$A=1.9,\ B=0.1,\ C=1.4,\ a=1.0,\ b=10.2,\ E=100,\ \rho=1000,\ \zeta=0.3,\ \Delta t=0.01, \tag{2.2.40}$$

to study the convergence behavior at time $T = 0.1$. We first vary the element order (i.e., highest polynomial degree in the expansions) from 1 to 13, as in the left plot of Figure 2.19. To compare the computational errors with respect to the exact solution, for each element order we calculate the errors in the relative energy norm. Here the relative energy norm is defined as in (2.3.21). We plot these errors in logarithmic scale, as a function of polynomial orders which is in linear scale. The red lines show the results from semi-local method, and the blue lines give the results from the original spectral/hp element formulation. From the left plot in Figure 2.19, we see that the numerical errors decrease exponentially fast as the element order increases, indicating an exponential convergence rate of the semi-local scheme spatially. On the other hand, the red and blue lines coincide, therefore the semi-local method achieves the same accuracy as the original spectral/hp element formulation.

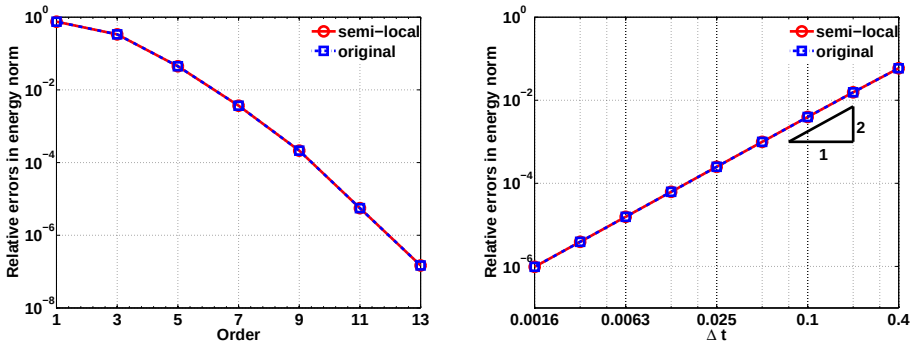

Figure 2.19: Left: errors as a function of the element order for displacement in $p-$refinement test. Right: errors as a function of the time step sizes in $t-$convergence test.

$t-$convergence

As in the $p-$convergence tests, we consider the deformation of the same cubic solid with the same mesh, but with parameter values

$$A = 1.2,\ B = 0.5,\ C = 0.01,\ a = 1.0,\ b = 0.02,\ E = 100,\ \rho = 1000,\ \zeta = 0.3. \tag{2.2.41}$$

to study the convergence behavior on time. Here we take a larger B and smaller C so that the errors from numerical integration in time dominate. All the tests are performed with polynomial order 6, and this structure problem is simulated from $t = 0$ to $t = 4$. In the right plot of Figure 2.19, we give the relative energy errors for displacement as a function of time step size Δt. Both the errors and the time step size are in the logarithmic scale. We see that the results from semi-local method are the same as that from the original spectral/hp element formulation, and all results are

approximately on a straight line with the polynomial order increasing. To be specific, a second-order convergence rate in time is obtained for the proposed semi-local method.

$h-$convergence

Now we focus on the $h-$convergence on the same problem employed by the $p-$*convergence* tests, and use 8 layers of meshes. These meshes are formed by $2i \times 2i \times 2i$ ($i = 1, 2, \cdots, 8$) hexahedral elements, while the first mesh ($i = 1$) was also employed for the cases in the previous two sections 2.2.1 and 2.2.1. The mesh for $i = 1$ is plotted in the left plot of Figure 2.18, and the mesh for $i = 2$ is given in the right plot. In this section, runs with three choices of polynomial orders 1, 2, 3 are tested. Similar to the previous tests, in Figure 2.20 we give the plot for the relative energy errors from the semi-local method and the original spectral/hp element formulation. All these errors are plotted in logarithmic scale as a function of the number of elements in each direction, which is also in logarithmic scale. From Figure 2.20, we see that the semi-local method has the same accuracy as the original formulation: a fixed element order P gives an P-th order in the relative energy norm. The results are consistent with the analysis of $h-$convergence for the original formulation for structure problems in [15].

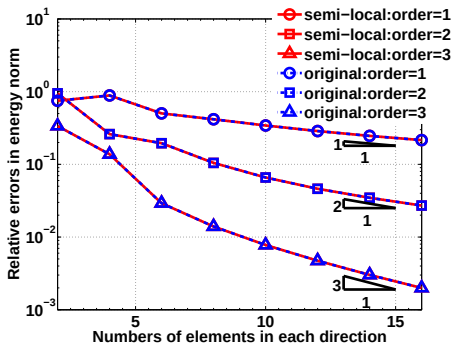

Figure 2.20: Errors as a function of element number in $h-$refinement test.

2.2.4 Efficiency tests: arterial walls and aneurysms

To test the efficiency of the method, we perform simulations for two cases: first, the structure-only simulations on a tube geometry, and then fluid-structure interaction (FSI) simulations on a patient-specific aneurysm model. In the following, the diagonal preconditioner is applied while solving the global $3N \times 3N$ linear system (2.2.9) or (2.2.11) in the original spectral/hp element formulation. For the semi-local method, while solving the three $N \times N$ systems in the localization

operator $\mathcal{L}i_e$ (2.2.18) or (2.2.19) we employ the low energy preconditioner in the conjugate gradient solver.

Structure only: tube case

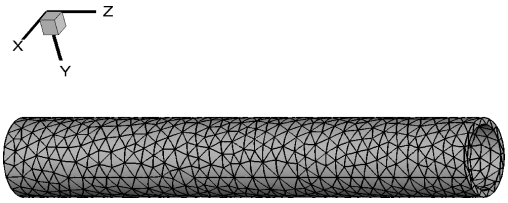

Figure 2.21: Mesh for arterial wall test.

In the following we investigate the performance of semi-local method with various polynomial orders, considering a straight tube as an idealization of the arterial wall. The geometry and mesh are as illustrated in Figure 2.21, with inner radius $2mm$, axial length $32mm$, and wall thickness $0.4mm$. The inlet is located at $Z = 0mm$, centered at the origin. The mesh is composed of 4383 tetrahedral elements, and modeled by linear elastic material with the structure density $1.27g/cm^3$ since the material density of the arterial wall is known to be close to that of the blood. The Poisson ratio is set to $\zeta = 0.3$, and the Young's modulus of the vessel walls is $E = 0.3MPa$, which is in the physiological range of intracranial vessels of size $2 - 4mm$ [78]. To simulate the pressure from the blood, a periodic traction load is applied on the interior surface of the arterial wall as

$$\begin{aligned} T_1 &= 1787 n_x \left(1 - \cos\left(\frac{2\pi t}{T}\right)\right) \ Pascal, \\ T_2 &= 1787 n_y \left(1 - \cos\left(\frac{2\pi t}{T}\right)\right) \ Pascal, \\ T_3 &= 1787 n_z \left(1 - \cos\left(\frac{2\pi t}{T}\right)\right) \ Pascal, \end{aligned} \tag{2.2.42}$$

where $\mathbf{n} = (n_x, n_y, n_z)$ is the outward-pointing unit vector normal to the surface. Here the length of one cardiac cycle is taken to be $T = 0.8sec$, with time step size $1.9 \times 10^{-6} sec$. On each time step, the subiteration convergence tolerance in (2.2.28) is taken as $\epsilon = 2 \times 10^{-11} mm$. With the inlet clamped, at $t = 1.5T$ we get the distribution of radial and axial displacements as shown in Figures 2.22. In Figure 2.23, the time traces for displacements at two sample points $(0, 2.4, 15.8)$ and $(-2.4, 0, 32)$ are displayed. From these figures we can see that the arterial wall deforms periodically, since the traction force is periodic and the problem is linear. The largest radial displacement reaches $0.14mm$, which is approximately 7% radial change. This is within the physiological radial change

as reported in [79, 80].

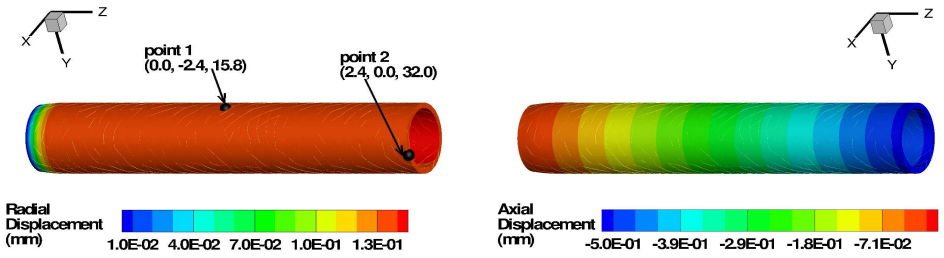

Figure 2.22: Displacements (in millimeters) for the arterial wall test at $t = 1.5T$. Left: radial displacement. Right: axial displacement.

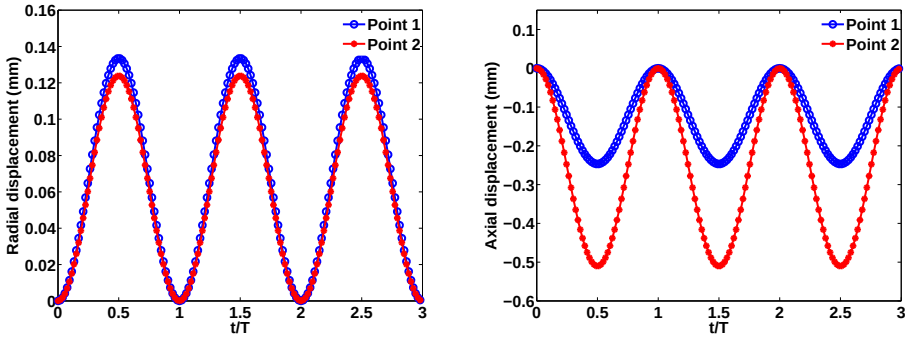

Figure 2.23: Time traces in the arterial wall test. Left: radial displacement at sample points. Right: radial velocity at sample points.

Next we compare the efficiencies of the original spectral/hp element formulation with that of the semi-local method, with the mesh shown in Figure 2.21 and polynomial orders from 2 to 7. The averaged subiteration numbers of a cardiac cycle required by the semi-local method are provided in Figure 2.24, as a function of the element orders. On the other hand, the averaged CPU time (sec) spent on each time step and each subiteration is shown in the left and right plots of Figure 2.25, respectively. Since there is no subiteration in the original spectral/hp element formulation, we consider the subiteration number as always 1 for each time step in its tests. We can observe that although the averaged subiteration number is increasing with the increase of polynomial orders, when the polynomial order is larger than 4, the semi-local method requires less time for each time step. To further compare these two formulations, in Figure 2.26 we plot the speed-up factor we can gain from replacing the original spectral/hp element formulation with the semi-local method. In this Figure, the left plot shows the speed-up factors per time step and the right plot gives the factors per subiteration. From the left plot, we can see that we generally get higher speed-up from

the semi-local method while using larger polynomial order elements. When using elements with polynomial order 7, the semi-local method accelerates the algorithm by almost 3 times for each time step. On the other hand, concerning the efficiency per subiteration, it is shown in the right plot of Figure 2.26 that we achieve as high as 25 times of speed-up from the semi-local method, when the element polynomial order reaches 7. Therefore, although for the semi-local method additional subiterations are required for each time step, and the averaged subiteration number is increasing with the polynomial order, it is still more efficient than the original formulation when using high order spectral/hp elements. Also, the larger the polynomial order is, the higher speed-up from this method should be expected.

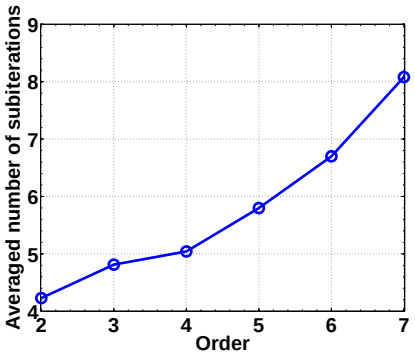

Figure 2.24: Averaged subiteration numbers of the semi-local method in the arterial wall test.

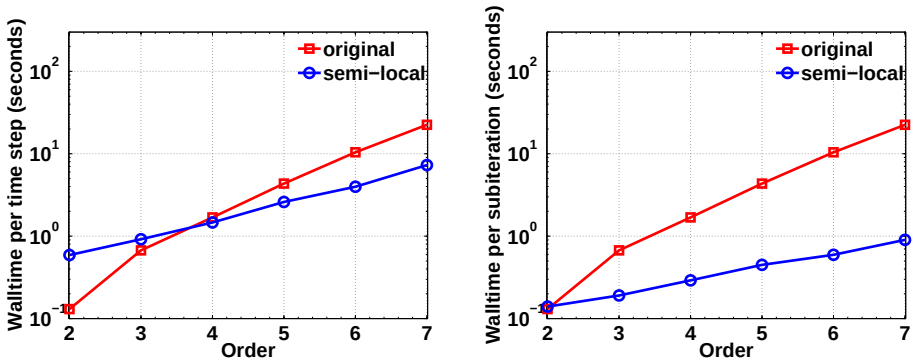

Figure 2.25: Averaged CPU time (Sec) in the arterial wall test. Left: each time step. Right: each subiteration.

Fluid-structure interaction: aneurysm case

In this part we consider patient-specific aneurysm models, with the arterial geometry extracted from Magnetic Resonance Imaging data [4]. This aneurysm is located in the cavernous segment

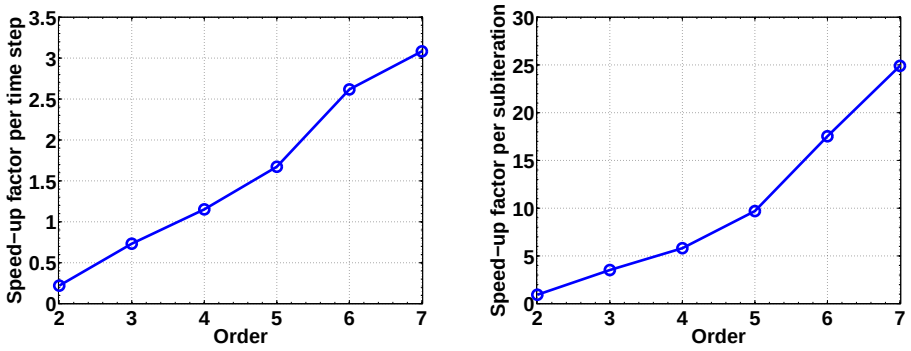

Figure 2.26: Speed-up factor from semi-local method in the arterial wall test. Left: each time step. Right: each subiteration.

of the right internal carotid artery at the eye level. We will perform our simulations with the partitioned fluid-structure interaction code documented in chapter 4.1. Here the structure solver employs our semi-local method. In these simulations, subiteration is needed on each time step to guarantee continuity at the interface, and it can be combined with the subiteration required by the semi-local method. Two sets of meshes will be tested: in Test I the structure subdomain covers the aneurysm sac only, as shown in Figure 2.27, while in Test II it covers the whole arterial wall as in Figure 2.28. In order to resolve the boundary layers, in both tests the fluid subdomain has finer elements near the vessel wall, while the solid subdomain is composed of two layers of triangular prismatic elements on the vessel wall. We imposed a Womersley velocity profile with eight harmonics at the inlet boundary of the fluid solver, and a zero Neumann boundary condition for velocity at the outlet. The outlet pressure $\bar{p}$ is flow-dependent and is determined from the flow rate $Q(t)$, the resistant R, and the capacitance C [4]

$$\bar{p}(t) + RC\frac{d\bar{p}(t)}{dt} = Q(t)R. \tag{2.2.43}$$

The arterial outlet is assumed to be undeformed when the outlet pressure $\bar{p}(t)$ reaches its lowest point at $t = 0.0571sec$. To generate the initial conditions, the fluid model is simulated separately for three cardiac cycles. We then start the FSI simulations from the resultant flow field (where we set $t = 0$ as the starting time of FSI). The structure is considered undeformed at $t = 0$. To integrate in time, we employ a second-order splitting scheme for the fluid solver [73, 74], and the BDF formula for the structure side. All the simulations are based on the physical and numerical parameters summarized in Table 2.4. Note that all the physical parameters are consistent with those in [81]. In the simulations, we take the subiteration tolerance on the structure side as $\epsilon = 10^{-7}mm$, and a relative tolerance as 10^{-5} on the fluid side.

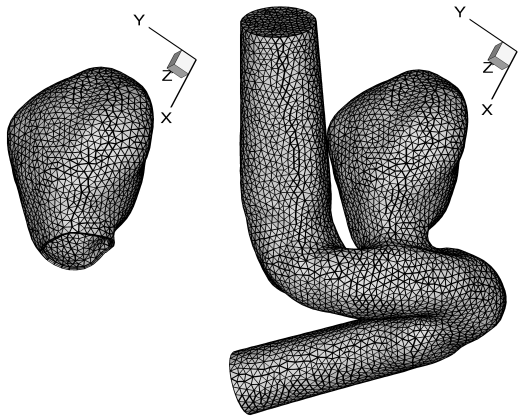

Figure 2.27: Meshes for patient-specific aneurysm model, test I. Left: structure mesh (with 5628 triangular prismatic elements); right: fluid mesh (with 58939 tetrahedral elements).

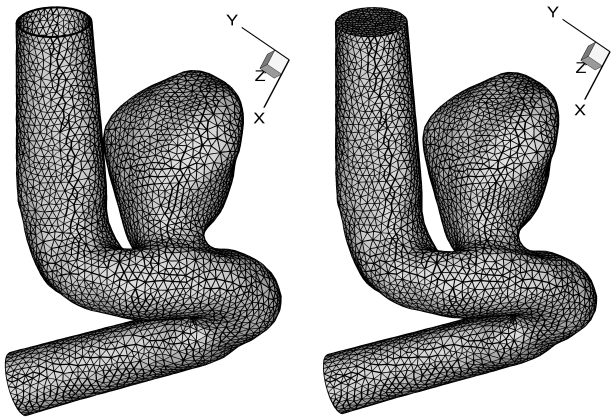

Figure 2.28: Meshes for patient-specific aneurysm model, test II. Left: structure mesh (with 16912 triangular prismatic elements); right: fluid mesh (with 42065 tetrahedral elements).

Fluid-structure interaction: blood flow in aneurysm test I

First we perform FSI simulations on the meshes as shown in Figure 2.27, with polynomial order three for each element for both the fluid and structure sides. To overcome the added-mass effect which causes the divergence of the subiterations [82, 83], a fictitious mass method [4, 81] is applied with an optimal coefficient 250, (this formulation is presented provided in Appendix A.3, and more details will be provided in chapter 4.1). Since the material density of the arterial wall is known to be close to that of the blood, we take the structure density ρ_s to be $1.06 g/cm^3$. In [84] the experimental results suggest a range for the moduli of arteries with cerebral aneurysms as

Poisson ratio	0.3
Blood density	$1.06 g/cm^3$
Wall thickness	$0.01 cm$
Inlet radius	$0.224 cm$
Kinematic viscosity	$3.8 \times 10^{-2} cm^2/s$
Womersley Number	4.2
Average flow rate	$70 ml/min$
Time step size	$4.29 \times 10^{-6} s$
Mass damping	$0.35 s^{-1}$
Stiffness damping	$2.9 \times 10^{-4} s$
Resistant	$7.844 \times 10^2 dyn \cdot s/cm^5$
Capacitance	$7.285 \times 10^{-5} cm^5/dyn$

Table 2.4: Parameters used in the patient-specific aneurysm simulations.

$0.9 - 4.0 MPa$, therefore the Young's modulus in this test is set to be $E = 3$MPa. To quantify the evolution of the aneurysm deformation we obtain displacement time traces for three points on the interface. The locations of these points are shown in Figure 2.29, when the wall deformation is near the maximum. The inlet flow profiles and the time traces for all three points are shown in Figure 2.30. To investigate the displacement distribution on the whole aneurysm, we take four time instants in a cardiac cycle: $2\frac{1}{7}T$, $2\frac{2}{7}T$, $2\frac{4}{7}T$, $2\frac{6}{7}T$ as marked by red lines in the bottom right plot of Figure 2.30, and show their corresponding displacement amplitudes in Figure 2.31. From the results we can see that the maximum deformation is achieved at $t = 2.3T$, which is right after the systolic peak. The maximum displacement amplitude is about $0.87 mm$ near the top of the aneurysm sac. This is consistent with the physiological range from the measurements as reported in [85].

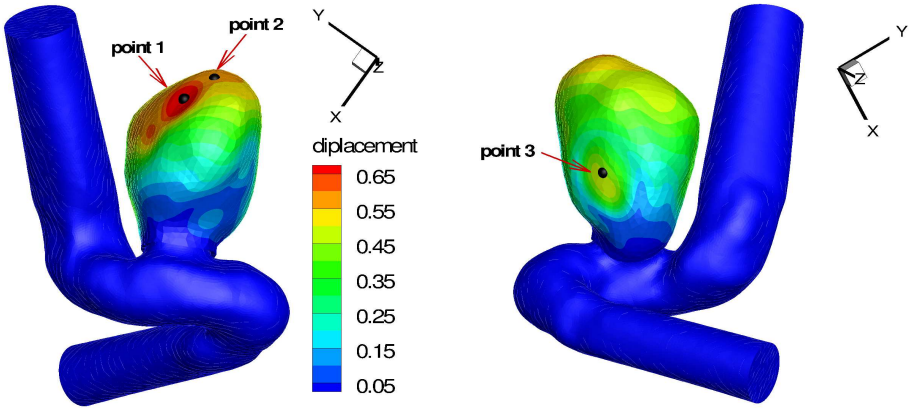

Figure 2.29: Positions of the history points in patient-specific aneurysm test I at $t = 2\frac{2}{7}T$.

To test the performance of the semi-local method, we employ polynomial orders $2 - 5$, with $16 - 128$ processors. In Table 2.5, we compare the averaged subiteration numbers required for the

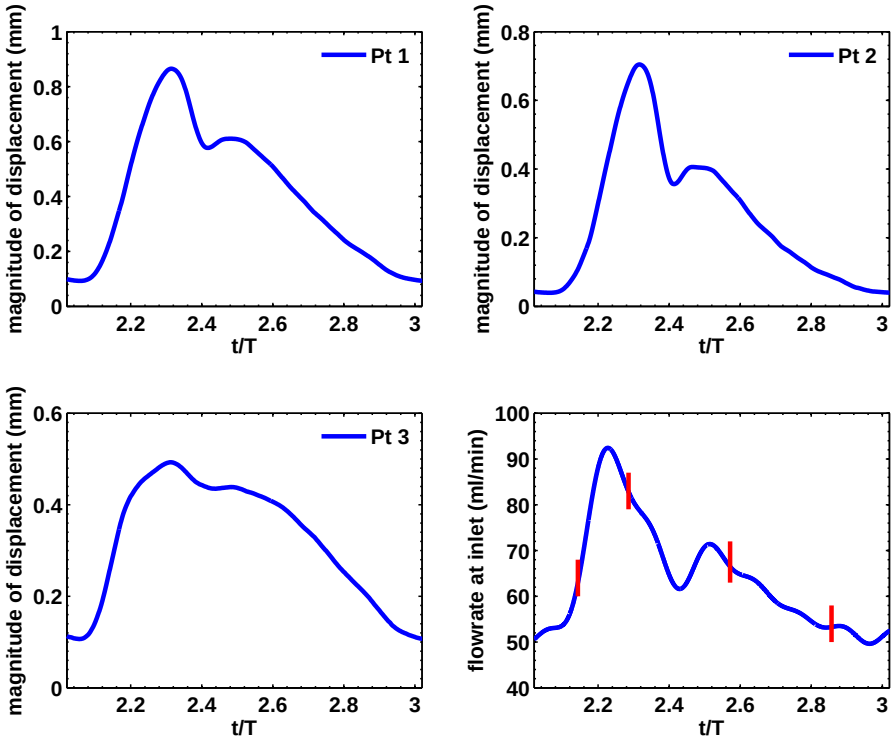

Figure 2.30: Time traces in patient-specific aneurysm test I. Upper left, upper right, bottom left: displacement profiles for corresponding points; bottom right: flow rate imposed at the inlet.

fluid-structure interaction simulation, while using the semi-local method or the original spectral/hp element formulation for the structure solver. From this table we can see that the semi-local method generally needs a comparable number of subiterations as that for the original spectral/hp element formulation. To further investigate the performance of the low energy preconditioner, the averaged iterations required by the conjugate gradient solver is compared in Table 2.6. We remind the reader that for the original spectral/hp element formulation a $3N \times 3N$ system is solved, while in the semi-local method we are solving three $N \times N$ systems. From this table we can see that when using the diagonal preconditioner, the semi-local method generally requires a smaller number of iterations in the conjugate gradient solver. While considering the comparison between preconditioners, in the semi-local method the conjugate gradient solver with the diagonal preconditioner needs more than 2 times of the iterations compared with the that with the low energy preconditioner, and this ratio increases with the polynomial order. On the other hand, the averaged CPU time is compared in Figure 2.32, where we also show the averaged speed-up factor we can gain from the semi-local method in each subiteration. It can be observed from the left plot that when using polynomial

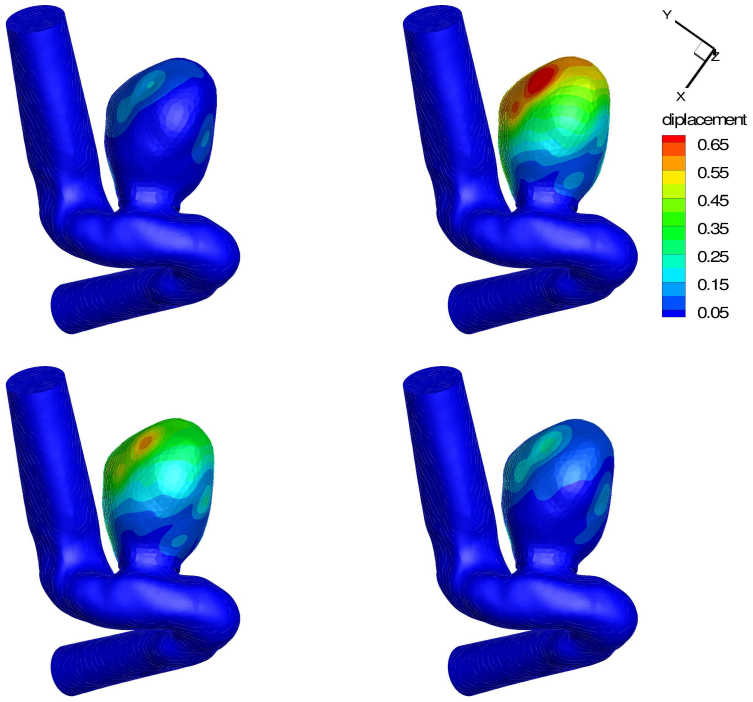

Figure 2.31: Displacements (in mm) for patient-specific aneurysm test I at $2\frac{1}{7}T$ (upper left), $2\frac{2}{7}T$ (upper right), $2\frac{4}{7}T$ (bottom left) and $2\frac{6}{7}T$ (bottom right).

Order	2	3	4	5
original formulation	23.6	25.5	25.3	23.1
semi-local method	26.3	23.2	24.2	26.4

Table 2.5: Blood flow in aneurysm test I: averaged subiteration number.

order larger than 2, the semi-local method is more efficient than the original spectral/hp element formulation. This can be seen more clearly from the right plot of Figure 2.32: the larger the polynomial order is, the more time we can save by using the semi-local method. While employing elements with polynomial order 5, the semi-local method accelerates the FSI solver nearly three times. Here we note that the speed-up factor for this case is smaller than that in the arterial wall test as shown in Figure 2.26, where polynomial order 5 elements accelerates the solver by about 10 times. That is because the CPU time counted here includes the time consumed by the fluid part, and the fluid mesh has a much larger number of elements than that in the structure part.

Order	2	3	4	5
original formulation	140.9	200.0	289.8	361.0
semi-local (low energy)	61.5	64.4	75.0	71.9
semi-local (diagonal)	130.0	161.3	236.9	295.4

Table 2.6: Blood flow in aneurysm test I: averaged number of conjugate gradient iterations.

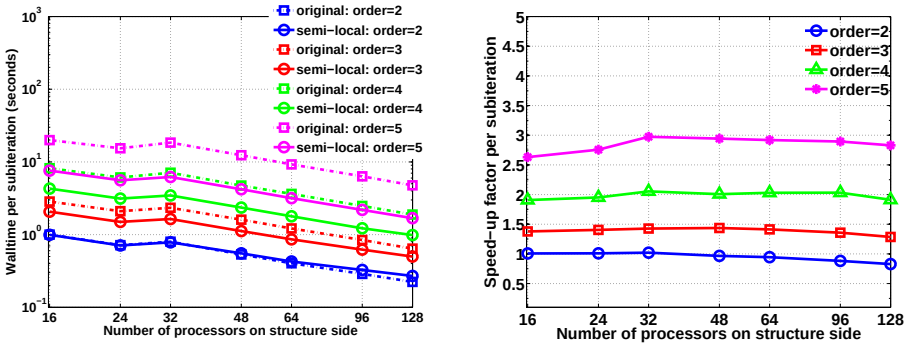

Figure 2.32: Blood flow in aneurysm test I. Left: averaged CPU time (Sec) in each subiteration. Right: speed-up factor in each subiteration.

Fluid-structure interaction: blood flow in aneurysm test II

Now we study a larger problem in which the structure mesh covers both the arteries and aneurysm, as shown in Figure 2.28. This test is performed with the same settings as in the patient-specific model test I, except with polynomial order two, the Young's modulus is $E = 3.6$MPa and structure density is $\rho_s = 2.12g/cm^3$. Since the arterial wall is also included in the structural subdomain, the added-mass operator becomes more complicated, resulting to slower subiteration convergence rates. To stabilize the fluid-structure interaction, the fictitious mass method with a larger optimal coefficient 425 is employed. To simulate the supports from the surrounding tissues, we put six support points on the arterial walls and at the neck of the aneurysm. At $t = 2\frac{4}{7}T$, the deformation reaches the maximum, and the displacement amplitudes are shown in Figure 2.33 where 4 sample points are marked out. Similarly as in the aneurysm test I, we provide the displacement time traces of these 4 points in Figure 2.34. The displacement distributions at four time instants $2\frac{1}{7}T$, $2\frac{2}{7}T$, $2\frac{4}{7}T$ and $2\frac{6}{7}T$ are shown in Figure 2.35, and these time instants are also as marked by red lines in the bottom right plot of Figure 2.30.

Similarly as in the aneurysm test I, in Table 2.7 we compare the averaged subiteration required by the semi-local method and the number required by the original spectral/hp element formulation. In these cases, the semi-local method also requires comparable numbers of subiterations compared with that for the original spectral/hp element formulation. In Table 2.6 we show the averaged

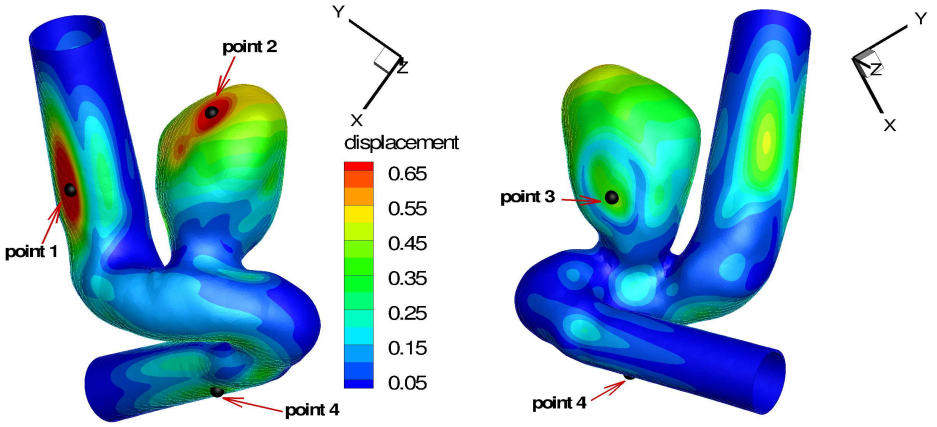

Figure 2.33: Positions of the history points in patient-specific aneurysm test II at $t = 2\frac{4}{7}T$.

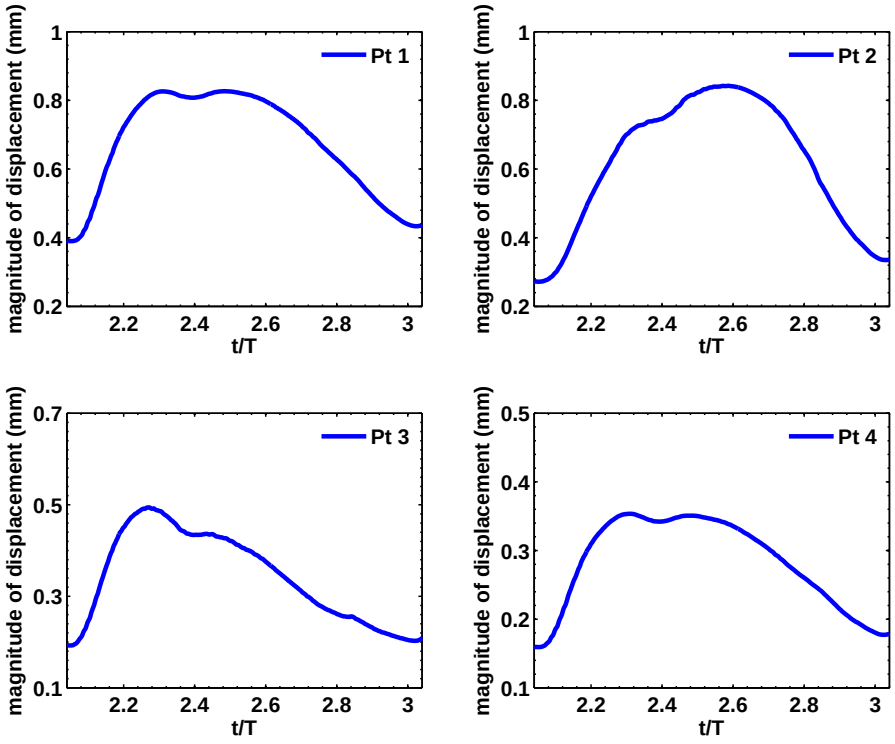

Figure 2.34: Time traces of displacement profiles for corresponding points in patient-specific aneurysm test II.

iterations required by the conjugate gradient solver. One can again observe that the semi-local method generally requires a smaller number of iterations than that for the original spectral/hp

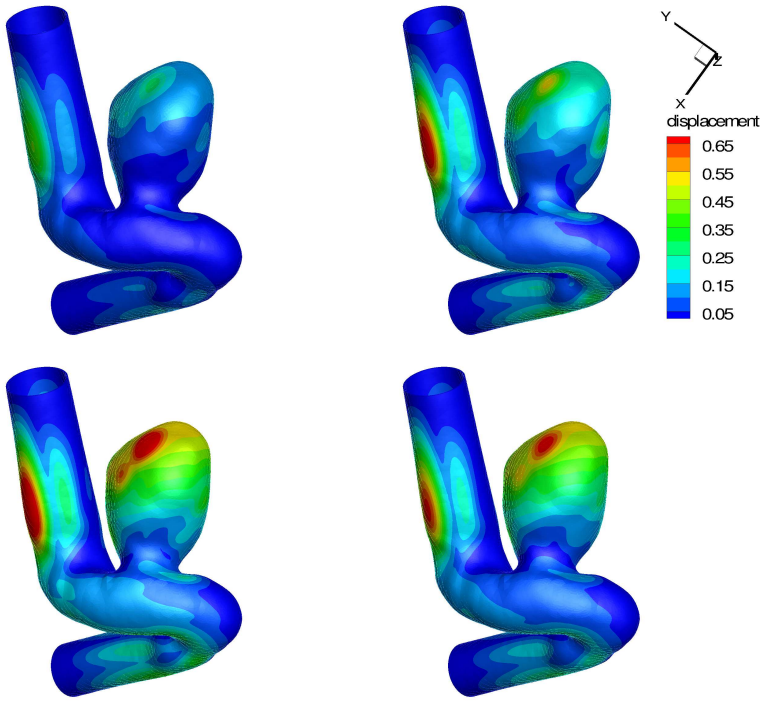

Figure 2.35: Displacements (in mm) for patient-specific aneurysm test II at $2\frac{1}{7}T$ (upper left), $2\frac{2}{7}T$ (upper right), $2\frac{4}{7}T$ (bottom left) and $2\frac{6}{7}T$ (bottom right).

Order	2	3	4	5
original formulation	81.3	81.8	99.8	84.9
semi-local method	88.4	87.6	81.6	76.2

Table 2.7: Blood flow in aneurysm test II: averaged subiteration number.

element formulation in the conjugate gradient solver, while using the diagonal preconditioner. On the other hand, the semi-local method with the low energy preconditioner is about three times faster than that with the diagonal preconditioner in the conjugate gradient solver. The averaged CPU time is compared in Figure 2.36, where we also show the speed-up factor from the semi-local method in each subiteration. When using polynomial order larger than 2, the semi-local method is more efficient than the original spectral/hp element formulation, and while employing elements with polynomial order 5, the speed-up factor can be as high as 4.5. This is larger than that in the test I, because the size of structure mesh in the case is larger, therefore more comparable with the size of the fluid mesh. In this case the slow original spectral/hp element formulation for the structure part consumes a larger percentage of the simulation time, therefore the faster semi-local method could help more in accelerating fluid-structure interaction simulations.

Order	2	3	4	5
original formulation	167.2	715.9	430.9	650.8
semi-local (low energy)	85.5	169.2	138.3	187.6
semi-local (diagonal)	165.0	452.0	330.0	475.0

Table 2.8: Blood flow in aneurysm test II: averaged number of conjugate gradient iterations.

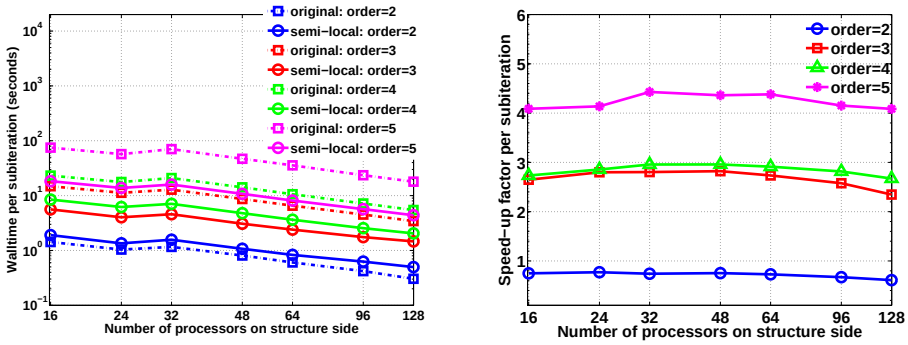

Figure 2.36: Blood flow in aneurysm test II. Left: averaged CPU time (Sec). Right: speed-up factor in each subiteration.

2.2.5 Summary

We have developed a fast solver for spectral/hp element discretization of the linear elasticity equations. A modal hierarchical trial basis is employed using Jacobi polynomials in polymorphic domains, including hexahedra, tetrahedra and triangular prisms. The solver is based on decoupling the three directions of displacement, hence enabling the use of an efficient low energy preconditioner for the conjugate gradient solver. The semi-local method could achieve the same order of accuracy with that of the original spectral/hp element formulation involving the coupled displacements.

We have performed several numerical tests to investigate the efficiency of the semi-local solver, considering both structure only as well as fluid-structure interaction problems. For the former, the semi-local method is more efficient than the original formulation when the polynomial order is high ($p \geq 4$), although subiterations are required by the semi-local method at each time step. For fluid-structure interaction tests, the subiteration in the semi-local method could be combined with the subiteration required by the partitioned algorithm for the coupled fluid-structure problem. In this case, using the semi-local method to replace the original formulation in the structure solver, the average subiteration number does not increase whereas the time spent on each subiteration decreases, especially for high polynomial orders.

With regards to nonlinear elasticity problems, the semi-local solver can also be used with the subiterations combined with the subiterations required by the Newton-Raphson procedure. However, the expected speed-up gains would not be as substantial as the linear elasticity case, because

the most time consuming part in the nonlinear elastic solver is in generating the stiffness matrix. On the other hand, additional savings can be realized if the global matrix in the residual distribution step involves only the vertex modes, instead of the currently employed full spectral modes. This would require further investigation on the effects of accuracy of the solution.

2.3 Fractional order models for viscoelastic materials

2.3.1 Overview and motivation

In this chapter, we are interested in developing fundamental numerical methods for nominally second-order fractional PDEs and performing complete numerical analysis for this new class of PDEs. Specifically, the arterial wall is a heterogeneous soft tissue with complex biomechanical properties, and these properties vary over locations and the temporal state of deformation. Because the arterial wall is composed by three different layers, to describe such a structure the model has to highlight two functions: the reversible energy storage (elasticity) and energy dissipation (viscosity).

Typically, constitutive laws for arterial walls are derived using integer-order differential equations that model stress-strain relations. Among those integer-order models, the Fung's quasilinear viscoelastic model [86] was widely employed, and one of its simplest example is the Kelvin-Zener (Standard Linear Solid or SLS) model. The SLS model accounts for creep, hysteresis and stress relaxation phenomena, and it can be described as a parallel combination of a spring with a spring and a dashpot in series. The second Piola-Kirchhoff stress tensor $\mathbf{S} = \frac{\partial \Psi}{\partial \mathbf{E}}$ for the 3D SLS model can be expressed as:

$$\mathbf{S} + \tau_S \frac{\partial \mathbf{S}}{\partial t} = \lambda(\mathrm{tr}(\mathbf{E} + \tau_E \frac{\partial \mathbf{E}}{\partial t}))\mathbf{I} + 2\mu(\mathbf{E} + \tau_E \frac{\partial \mathbf{E}}{\partial t}). \tag{2.3.1}$$

where $\mathbf{E} = \frac{1}{2}\left(\left(\frac{\partial \boldsymbol{\eta}}{\partial \mathbf{X}}\right)^T + \left(\frac{\partial \boldsymbol{\eta}}{\partial \mathbf{X}}\right)\right)$ is the strain tensor, and μ, λ are the shear and Lame modulus, respectively. τ_S, τ_E are the relaxation parameters which capture effects of creep and stress relaxation. Here we note that when $\tau_S = \tau_E$, the purely elastic model (2.1.2) is retrieved.

However, estimating the relaxation parameters remains a challenging task in clinic. On the other hand, it was reported in [87] that the Fung's quasilinear viscoelastic model is very sensitive to these parameters, which is a limiting factor for employing the interger-order models in fluid-structure interaction simulations for arterial flows. Therefore, the models based on fractional calculus have been introduced and studied, as an alternative approach to modeling the viscoelastic behavior of arteries[88, 87, 3]. Recent simulations on 1D model [3] have indicated that fractional order models are less sensitive to the parameter estimation compared with the integer-calculus-based models,

which motivates our current study on 3D simulations.

In the chapter, we will numerically investigate a 3D fractional-order SLS model [89, 90], by employing the Grüwald-Letnikov formula. We first briefly describe the model governing the arterial wall response as well as the numerical formulation in section 2.3.2. Then in section 2.3.3 we demonstrate the time convergence rates for the Grüwald-Letnikov formula on numerical examples with fabricated solutions, and conduct numerical simulations on a straight tube as an idealization of a section of arterial wall. Lastly, we finish in section 2.3.4 with the main conclusions.

2.3.2 Formulation

In the fractional-order SLS model, we generalize the SLS model described in (2.3.1) by employing the so-called spring-pot which interpolates between the purely viscous and elastic behaviors:

$$\mathbf{S} + \tau_S^\alpha \frac{\partial^\alpha \mathbf{S}}{\partial t^\alpha} = \lambda(\mathrm{tr}(\mathbf{E} + \tau_E^\alpha \frac{\partial^\alpha \mathbf{E}}{\partial t^\alpha}))\mathbf{I} + 2\mu(\mathbf{E} + \tau_E^\alpha \frac{\partial^\alpha \mathbf{E}}{\partial t^\alpha}), \tag{2.3.2}$$

where μ, λ are the shear and Lame modulus, and τ_S, τ_E are the relaxation parameters, respectively. Here we use the Riemann-Liouville definition for the fractional derivative of order α $(0 \leq \alpha < 1)$

$$ {}_a^{RL}\mathbf{D}_t^\alpha f(t) = \frac{1}{\Gamma(1-\alpha)} \frac{d}{dt} \int_a^t (t-\upsilon)^{-\alpha} f(\upsilon) d\upsilon \tag{2.3.3}$$

which is a non-local operator that depends on the history of function $f(t)$. The Γ function is defined as

$$\Gamma(r) = \int_0^\infty e^{-t} t^{r-1} dt.$$

From the physical point of view, the model in (2.3.2) is constructed as a parallel combination of a spring with a spring and a spring-pot in series. In this chapter, we study the infinitesimal deformations for simplicity, with the assumption that both the stress tensor $\mathbf{S}$ and the strain tensor $\mathbf{E}$ are continuously differentiable. One can observe that when $\tau_E = \tau_S$, (2.3.2) also reduces the purely elastic model (2.1.2). If further assume that the object is at a static status when $t \leq 0$, i.e., $\mathbf{S}$ and $\mathbf{E}$ vanish before $t = 0$, then we can set the lower limit of the fractional derivative (2.3.3) to be $a = 0$. Consequently, when $\alpha = 1$ the model (2.3.2) reduces to the integer-order SLS model as described in (2.3.1).

Next we will derive the formulation for solving the displacement field $\boldsymbol{\eta}(\mathbf{X})$, in a three dimensional object occupying domain $\Omega \subset \mathbf{R}^3$ with boundaries $\partial\Omega = \partial\Omega_D \cup \partial\Omega_N$. On $\partial\Omega_D$ and $\partial\Omega_N$ the Dirichlet type boundary condition and the Neumann type boundary conditions (traction) are provided, respectively. With test functions $\mathbf{v}$, the deformation of this object is governed by the

following weak formulation:

$$\int_\Omega \rho \frac{\partial^2 \boldsymbol{\eta}}{\partial t^2} \mathbf{v} d\Omega + \int_\Omega \mathbf{S} : \nabla \mathbf{v} d\Omega - \int_{\partial\Omega_N} \mathbf{T} \cdot \mathbf{v} d\Gamma - \int_\Omega \mathbf{f} \cdot \mathbf{v} d\Omega = 0, \ \forall \mathbf{v} \in \mathbf{U}_0, \tag{2.3.4}$$

where the displacement field $\boldsymbol{\eta}(\mathbf{X}, t) \in \mathbf{U}(t) = \{\mathbf{w}(\mathbf{X}, t) \in [H^1(\Omega)]^3 | \mathbf{w}(\mathbf{X}, t) = \boldsymbol{\eta}_D(\mathbf{X}, t) \text{ on } \partial\Omega_D\}$, and $\mathbf{U}_0 = \{\mathbf{w}(\mathbf{X}) \in [H^1(\Omega)]^3 | \mathbf{w}(\mathbf{X}) = \mathbf{0} \text{ on } \partial\Omega_D\}$; $\mathbf{T}$, $\mathbf{f}$ and ρ are the external traction force on $\partial\Omega_N$, external body force, and mass density, respectively.

While considering the temporal discretization for fractional derivative, based on the assumption that $\mathbf{S}$ and $\mathbf{E}$ are both continuously differentiable, the Riemann-Liouville fractional derivative (2.3.3) is equavalent to the Grüwald-Letnikov fractional derivative [91]

$${}_a^G\mathbf{D}_t^\alpha f(t) = \lim_{\Delta t \to 0^+} \frac{1}{\Delta t^\alpha} \sum_{r=0}^{(t-a)/\Delta t} (-1)^r \begin{pmatrix} \alpha \\ r \end{pmatrix} f(t - r\Delta t). \tag{2.3.5}$$

This fact enables a popular way of descritizing the fractional derivative, i.e., the Grüwald-Letnikov formula:

$${}_a^{RL}\mathbf{D}_t^\alpha f(t) = \lim_{\Delta t \to 0^+} \frac{1}{\Delta t^\alpha} \sum_{r=0}^{(t-a)/\Delta t} GL_r^\alpha f(t - r\Delta t) \tag{2.3.6}$$

with

$$GL_0^\alpha = 1, \quad GL_r^\alpha = \frac{r - \alpha - 1}{r} GL_{r-1}^\alpha. \tag{2.3.7}$$

Substituting (2.3.6) into (2.3.2), at the $n-$th time step we obtain that

$$\begin{aligned} &\mathbf{S}^n + \frac{\tau_S^\alpha}{\Delta t^\alpha} \left(\sum_{r=0}^{n} GL_r^\alpha \mathbf{S}^{n-r} \right) \\ =&\lambda \left(\mathrm{tr}(\mathbf{E}^n + \frac{\tau_E^\alpha}{\Delta t^\alpha} \left(\sum_{r=0}^{n} GL_r^\alpha \mathbf{E}^{n-r} \right) \right) \mathbf{I} + 2\mu \left(\mathbf{E}^n + \frac{\tau_E^\alpha}{\Delta t^\alpha} \left(\sum_{r=0}^{n} GL_r^\alpha \mathbf{E}^{n-r} \right) \right), \end{aligned} \tag{2.3.8}$$

which yields

$$\begin{aligned} \mathbf{S}^n =& \frac{\Delta t^{-\alpha}}{1 + \tau_S^\alpha \Delta t^{-\alpha}} \sum_{r=1}^{n} GL_r^\alpha (\tau_E^\alpha \left(\lambda \left(\mathrm{tr}\mathbf{E}^{n-r} \right) \mathbf{I} + 2\mu \mathbf{E}^{n-r} \right) \\ &- \tau_S^\alpha \mathbf{S}^{n-r}) + \frac{1 + \tau_E^\alpha \Delta t^{-\alpha}}{1 + \tau_S^\alpha \Delta t^{-\alpha}} \left(\lambda \left(\mathrm{tr}\mathbf{E}^n \right) \mathbf{I} + 2\mu \mathbf{E}^n \right). \end{aligned} \tag{2.3.9}$$

Therefore, the weak formulation (2.3.4) can be rewritten as

$$\begin{aligned}
&\int_\Omega \rho \frac{\partial^2 \boldsymbol{\eta}^n}{\partial t^2} \mathbf{v} d\Omega + \frac{\Delta t^{-\alpha}}{1+\tau_S^\alpha \Delta t^{-\alpha}} \sum_{r=1}^{n} GL_r^\alpha (\tau_E^\alpha \int_\Omega \mathbf{S}_0^{n-r} : \nabla \mathbf{v} d\Omega \\
&- \tau_S^\alpha \int_\Omega \mathbf{S}^{n-r} : \nabla \mathbf{v} d\Omega) + \frac{1+\tau_E^\alpha \Delta t^{-\alpha}}{1+\tau_S^\alpha \Delta t^{-\alpha}} \int_\Omega \mathbf{S}_0^n : \nabla \mathbf{v} d\Omega \\
=& \int_{\partial \Omega_N} \mathbf{T}^n \cdot \mathbf{v} d\Gamma + \int_\Omega \mathbf{f}^n \cdot \mathbf{v} d\Omega,
\end{aligned} \tag{2.3.10}$$

where

$$\mathbf{S}_0^n := \lambda \left(\mathrm{tr}\mathbf{E}^n\right) \mathbf{I} + 2\mu \mathbf{E}^n,$$

To approximate the acceleration $\dfrac{\partial^2 \boldsymbol{\eta}}{\partial t^2}$ at the $n-$th time step, we employed the Newmark scheme (2.2.8) as a start up in the first two steps, and a three-step backward differentiation formula (BDF) (2.2.10) for the other steps. Let n denote the index of the time step, in the *Newmark scheme* we obtain the temporal discretized formulation:

$$\begin{aligned}
&\int_\Omega \rho \frac{\boldsymbol{\eta}^n}{\Delta t^2 \theta_2} \mathbf{v} d\Omega + \frac{1+\tau_E^\alpha \Delta t^{-\alpha}}{1+\tau_S^\alpha \Delta t^{-\alpha}} \int_\Omega \mathbf{S}_0^n : \nabla \mathbf{v} d\Omega \\
=& \int_{\partial \Omega_N} \mathbf{T}^n \cdot \mathbf{v} d\Gamma + \int_\Omega \mathbf{f}^n \cdot \mathbf{v} d\Omega + \int_\Omega \rho \frac{1}{\Delta t^2 \theta_2} \left(\boldsymbol{\eta}^{n-1} + \Delta t \dot{\boldsymbol{\eta}}^{n-1} + \frac{\Delta t^2}{2} (1-2\theta_2) \ddot{\boldsymbol{\eta}}^{n-1} \right) \mathbf{v} d\Omega \\
&- \frac{\Delta t^{-\alpha}}{1+\tau_S^\alpha \Delta t^{-\alpha}} \sum_{r=1}^{n} GL_r^\alpha (\tau_E^\alpha \int_\Omega \mathbf{S}_0^{n-r} : \nabla \mathbf{v} d\Omega - \tau_S^\alpha \int_\Omega \mathbf{S}^{n-r} : \nabla \mathbf{v} d\Omega),
\end{aligned} \tag{2.3.11}$$

with the parameters $(\theta_1, \theta_2) = (0.5, 0.25)$ which lead to a second-order scheme. Similarly, in the *three-step BDF scheme* we obtain the temporal discretized formulation:

$$\begin{aligned}
&\int_\Omega \rho A_1 A_2 \boldsymbol{\eta}^n \mathbf{v} d\Omega + \frac{1+\tau_E^\alpha \Delta t^{-\alpha}}{1+\tau_S^\alpha \Delta t^{-\alpha}} \int_\Omega \mathbf{S}_0^n : \nabla \mathbf{v} d\Omega \\
=& \int_{\partial \Omega_N} \mathbf{T}^n \cdot \mathbf{v} d\Gamma + \int_\Omega \mathbf{f}^n \cdot \mathbf{v} d\Omega - \int_\Omega \rho (A_2 (B_1 \boldsymbol{\eta}^{n-1} + C_1 \boldsymbol{\eta}^{n-2} + D_1 \boldsymbol{\eta}^{n-3}) + \\
&(B_2 \dot{\boldsymbol{\eta}}^{n-1} + C_2 \dot{\boldsymbol{\eta}}^{n-2} + D_2 \dot{\boldsymbol{\eta}}^{n-3})) \mathbf{v} d\Omega \\
&- \frac{\Delta t^{-\alpha}}{1+\tau_S^\alpha \Delta t^{-\alpha}} \sum_{r=1}^{n} GL_r^\alpha (\tau_E^\alpha \int_\Omega \mathbf{S}_0^{n-r} : \nabla \mathbf{v} d\Omega - \tau_S^\alpha \int_\Omega \mathbf{S}^{n-r} : \nabla \mathbf{v} d\Omega),
\end{aligned} \tag{2.3.12}$$

where A_i, B_i, C_i and D_i $(i = 1, 2)$ are defined as

$$A_1 = \frac{\theta_1}{\Delta t},\ B_1 = \frac{2.5 - 3\theta_1}{\Delta t},\ C_1 = \frac{3\theta_1 - 4}{\Delta t},\ D_1 = \frac{1.5 - \theta_1}{\Delta t}, \tag{2.3.13a}$$

$$A_2 = \frac{\theta_2}{\Delta t},\ B_2 = \frac{2.5 - 3\theta_2}{\Delta t},\ C_2 = \frac{3\theta_2 - 4}{\Delta t},\ D_2 = \frac{1.5 - \theta_2}{\Delta t}, \tag{2.3.13b}$$

and we take $(\theta_1, \theta_2) = (5/3, 5/3)$ based on considerations of stability and dissipation.

To discretize in space, we employ the high-order hierarchical shape functions as defined in Appendix A.1. To avoid redundancy, we refer the interested readers to section 2.2.2 for further details. We mark $\mathbf{U}$ as the global vector of unknown expansion coefficients, which is assembled from the corresponding element expansion coefficient vectors $\mathbf{U}_e$ in (2.1.22). With the mass matrix $\mathbf{M}$ and stiffness matrix $\mathbf{K}$ as the global matrix assembled from the local mass matrix in (2.2.6) and the local stiffness matrix in (2.2.7), in each time step we calculate and store the memory load as

$$\begin{aligned}
HIS^n =& \frac{\Delta t^{-\alpha}}{1+\tau_S^\alpha \Delta t^{-\alpha}} (\tau_E^\alpha \int_\Omega \mathbf{S}_0^n : \nabla \mathbf{v} d\Omega - \tau_S^\alpha \int_\Omega \mathbf{S}^n : \nabla \mathbf{v} d\Omega) \\
=& \frac{\tau_E^\alpha \Delta t^{-\alpha}}{1+\tau_S^\alpha \Delta t^{-\alpha}} \mathbf{K}\mathbf{U}^n - \frac{\tau_S^\alpha \Delta t^{-\alpha}}{1+\tau_S^\alpha \Delta t^{-\alpha}} \int_\Omega \mathbf{S}^n : \nabla \mathbf{v} d\Omega \\
=& \frac{\tau_E^\alpha \Delta t^{-\alpha}}{1+\tau_S^\alpha \Delta t^{-\alpha}} \mathbf{K}\mathbf{U}^n - \frac{\tau_S^\alpha \Delta t^{-\alpha}}{1+\tau_S^\alpha \Delta t^{-\alpha}} \left(\frac{1+\tau_E^\alpha \Delta t^{-\alpha}}{1+\tau_S^\alpha \Delta t^{-\alpha}} \mathbf{K}\mathbf{U}^n \right. \\
& \left. + \frac{\Delta t^{-\alpha}}{1+\tau_S^\alpha \Delta t^{-\alpha}} \sum_{r=1}^{n} GL_r^\alpha \left(\tau_E^\alpha \int_\Omega \mathbf{S}_0^{n-r} : \nabla \mathbf{v} d\Omega - \tau_S^\alpha \int_\Omega \mathbf{S}^{n-r} : \nabla \mathbf{v} d\Omega \right) \right) \\
=& \left(\frac{\tau_E^\alpha \Delta t^{-\alpha}}{1+\tau_S^\alpha \Delta t^{-\alpha}} - \frac{\tau_S^\alpha \Delta t^{-\alpha}(1+\tau_E^\alpha \Delta t^{-\alpha})}{(1+\tau_S^\alpha \Delta t^{-\alpha})^2} \right) \mathbf{K}\mathbf{U}^n - \frac{\tau_S^\alpha \Delta t^{-\alpha}}{1+\tau_S^\alpha \Delta t^{-\alpha}} \sum_{r=1}^{n} GL_r^\alpha HIS^{n-r}.
\end{aligned} \tag{2.3.14}$$

Starting from the static status,

$$\mathbf{U}^0 = 0$$

we solve the system with Newmark scheme (2.3.11) or BDF scheme (2.3.12) following the algorithm:

- Set

$$\mathbf{U}^0 = 0,\ \dot{\mathbf{U}}^0 = 0,\ \ddot{\mathbf{U}}^0 = 0,\ HIS^0 = 0$$

- **for** the $n-$th time step, **do**

  1. When $n \leq 2$, solve for $\mathbf{U}^n$ with the Newmark scheme

$$\begin{aligned}
& \left(\frac{1}{\Delta t^2 \theta_2} \mathbf{M} + \frac{1+\tau_E^\alpha \Delta t^{-\alpha}}{1+\tau_S^\alpha \Delta t^{-\alpha}} \mathbf{K} \right) \mathbf{U}^n \\
=& \mathbf{F}^n - \sum_{r=1}^{n} GL_r^\alpha HIS^{n-r} + \frac{1}{\Delta t^2 \theta_2} \left(\mathbf{U}^{n-1} + \Delta t \dot{\mathbf{U}}^{n-1} + \frac{\Delta t^2}{2}(1-2\theta_2) \ddot{\mathbf{U}}^{n-1} \right) \mathbf{M};
\end{aligned} \tag{2.3.15}$$

else, solve with the three-step BDF scheme

$$\begin{aligned}&\left(A_1A_2\mathbf{M}+\frac{1+\tau_E^\alpha\Delta t^{-\alpha}}{1+\tau_S^\alpha\Delta t^{-\alpha}}\mathbf{K}\right)\mathbf{U}^n\\ =&\mathbf{F}^n-\sum_{r=1}^{n}GL_r^\alpha HIS^{n-r}-(A_2(B_1\mathbf{U}^{n-1}+C_1\mathbf{U}^{n-2}+D_1\mathbf{U}^{n-3})\\ &+(B_2\dot{\mathbf{U}}^{n-1}+C_2\dot{\mathbf{U}}^{n-2}+D_2\dot{\mathbf{U}}^{n-3}))\mathbf{M}.\end{aligned}\tag{2.3.16}$$

2. Calculate and store the memory load HIS^n following (2.3.14).
3. Approximate $\dot{\mathbf{U}}^n$ and $\ddot{\mathbf{U}}^n$ following (2.2.8) (Newmark scheme) or (2.2.10) (three-step BDF scheme).

- Go to time step $n+1$.

2.3.3 Numerical simulations

Convergence studies

Now we investigate the temporal accuracy of the forementioned formulation by comparing simulation results against analytical solutions. In this section, we will use Young's modulus E and the Poisson ratio ζ, for the material properties

$$\mu=\frac{E}{2(1+\zeta)},\quad \lambda=\frac{\zeta E}{(1+\zeta)(1-2\zeta)}.\tag{2.3.17}$$

We consider the deformation of a cubic solid occupying the domain $0\le X\le 1$, $0\le Y\le 1$ and $0\le Z\le 1$ discretized by eight hexahedral elements as in the left plot of Figure 2.18. For the test example, we use four fabricated problems with parameters as listed in Table 2.9

	α	τ_E	τ_S
FS1	0.25	0	10.5
FS2	0.75	0	10.5
FE1	0.25	10.5	0
FE2	0.75	10.5	0

Table 2.9: $t-$convergence tests for fractional-order SLS model: parameters for cases.

In cases FS1 and FS2, the face $X=0$ is clamped, and a traction force field $\mathbf{T}=(T_1,T_2,T_3)$ is

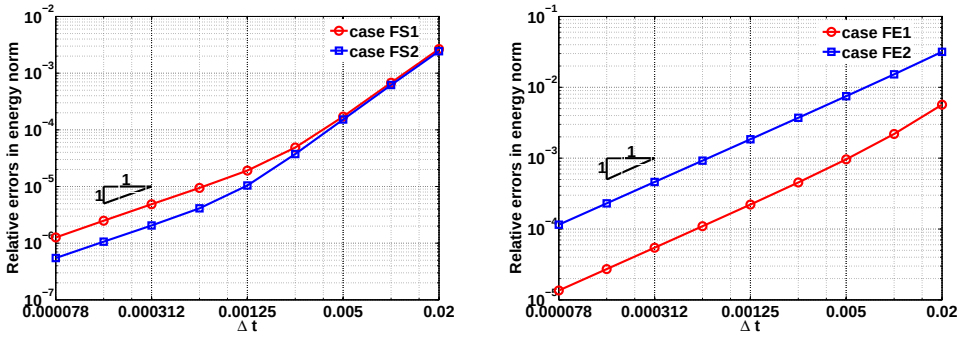

Figure 2.37: Errors as a function of the time step sizes in $t-$convergence test. Left: $\tau_E = 0$ cases. Right: $\tau_S = 0$ cases.

applied on the rest of the faces, which is given by

$$\begin{aligned} T_1 &= n_x(\lambda + 2\mu)t^{3+\alpha}, \\ T_2 &= n_y\lambda t^{3+\alpha}, \\ T_3 &= n_z\lambda t^{3+\alpha}, \end{aligned} \tag{2.3.18}$$

where $\mathbf{n} = (n_x, n_y, n_z)$ is the outward-pointing unit vector normal to the surface. A body force field $\mathbf{f} = (f_1, f_2, f_3)$ is applied on the subject with components:

$$f_1 = x((3+\alpha)(2+\alpha)t^{1+\alpha} + \tau_S^\alpha \Gamma(4+\alpha)t), \quad f_2 = f_3 = 0. \tag{2.3.19}$$

When $t = 0$, the displacement and velocity fields vanish. This problem has the following analytic solution for the displacement of the object:

$$\eta_1 = x\left(t^{3+\alpha} + \frac{\tau_S^\alpha \Gamma(4+\alpha)}{6}t^3\right), \ \eta_2 = \eta_3 = 0. \tag{2.3.20}$$

To study the convergence behavior at time $T = 0.4$, we vary the time step size Δt from 0.000078125 to 0.02, as in the left plot of Figure 2.37. To compare the computational errors with respect to the exact solution, for Δt we calculate the errors in the relative energy norm. Here the relative energy norm is defined as

$$||\boldsymbol{\eta}||_{RE} = \frac{||\boldsymbol{\eta}_a - \boldsymbol{\eta}_c||_E}{||\boldsymbol{\eta}_a||_E}, \tag{2.3.21}$$

where

$$||\mathbf{a}||_E = \mu \int_\Omega \epsilon(\mathbf{a}) : \epsilon(\mathbf{a}) d\Omega + \lambda \int_\Omega \mathrm{div}(\mathbf{a})\,\mathrm{div}(\mathbf{a}) d\Omega,$$

$\boldsymbol{\eta}_a$ are the analytic solutions for displacement, and $\boldsymbol{\eta}_c$ are results from computation. We plot

these errors in logarithmic scale, as a function of time step sizes which is also in logarithmic scale. Different colors of lines shows the results from different cases. From the left plot in Figure 2.37, we see that the numerical errors decrease almost in a straight line as the time step size decreases, indicating a first-order convergence rate in time.

In the FE1 and FE2 cases, the problem arises from the following fabricated solution for the displacement of the object:

$$\eta_1 = xt^{3+\alpha},\ \eta_2 = \eta_3 = 0. \tag{2.3.22}$$

The face $X = 0$ is also clamped, with a traction force field $\mathbf{T} = (T_1, T_2, T_3)$ applied on the rest of the faces as

$$\begin{aligned} T_1 &= n_x(\lambda + 2\mu)\left(t^{3+\alpha} + \frac{\tau_E^\alpha \Gamma(4+\alpha)}{6} t^3\right), \\ T_2 &= n_y \lambda \left(t^{3+\alpha} + \frac{\tau_E^\alpha \Gamma(4+\alpha)}{6} t^3\right), \\ T_3 &= n_z \lambda \left(t^{3+\alpha} + \frac{\tau_E^\alpha \Gamma(4+\alpha)}{6} t^3\right). \end{aligned} \tag{2.3.23}$$

Similar as in the FS cases, we apply a body force field $\mathbf{f} = (f_1, f_2, f_3)$ on the subject with components:

$$f_1 = x((3+\alpha)(2+\alpha)t^{1+\alpha}, \quad f_2 = f_3 = 0. \tag{2.3.24}$$

When $t = 0$, the displacement and velocity fields vanish. We numerically integrate this problem from $T = 0$ to $T = 0.4$, and compare the energy relative errors (2.3.21) for time step sizes from 0.000078125 to 0.02. We plot the relative energy errors as a function of time step sizes and both axis are in logarithmic scale, as shown in the right plot of Figure 2.37. Similar as in the FS cases, it can be observed that a first-order convergence rate in time is achieved.

Structure only: tube case

We now perform simulations on a slender tube geometry, which can be seen as an idealization of the arterial wall. Here we employ the same settings as that in the tube case of section 2.2.4, i.e., the tube is with inner radius $2mm$, axial length $32mm$, and wall thickness $0.4mm$. On the mesh as shown in Figure 2.21, the simulations are performed with spectral elements of polynomial order 4. The inlet is located at $Z = 0mm$, centered at the origin. We will investigate and compare the simulation results from a purely elastic wall model, interger order SLS models, and fractional order SLS models. All cases are with the structure density $1.27g/cm^3$ which is close to the density of the blood. The Poisson ratio is set to $\zeta = 0.3$, and the Young's modulus of the vessel walls is

$E = 0.3MPa$. To simulate the pressure from the blood, we apply a periodic traction load on the interior surface of the arterial wall as

$$\begin{aligned} T_1 &= 1787 n_x \left(1 - \cos\left(\frac{2\pi t}{T}\right)\right) \ Pascal, \\ T_2 &= 1787 n_y \left(1 - \cos\left(\frac{2\pi t}{T}\right)\right) \ Pascal, \\ T_3 &= 1787 n_z \left(1 - \cos\left(\frac{2\pi t}{T}\right)\right) \ Pascal. \end{aligned} \tag{2.3.25}$$

The length of one cardiac cycle is taken to be $T = 0.8sec$, with time step size $1.89 \times 10^{-3} sec$. Since our goal will be the comparison of different viscoelastic models, the elasticity parameters ζ and E will be kept the same for all cases. We will test different parameters (τ_S, τ_E) for the integer order SLS model (2.3.1), and various (α, τ_S, τ_E) for the fractional order SLS model (2.3.2). It should be noted that the nature of these paramters is patient- and location-specific, and we therefore focus on the paramter sets from the literatures [92, 93, 87, 94, 3]. Table 2.10 summarizes the viscoelastic models we are going to investigate, from which one can see that the parameters vary significantly between cases. With the inlet clamped, at $t = 9.5T$ we get the distribution of

	α	τ_E (sec)	τ_S (sec)
SLS1	N/A	0.05	0.025
SLS2	N/A	29.3	16.9
FOV-SLS1	0.29	1.84	0.076
FOV-SLS2	0.20	11.74	7.61

Table 2.10: Parameters employed in fractional-order SLS models: solid tube case.

radial and axial displacements as shown in Figures 2.39. Comparing with the results from purely elastic model as demonstrated in Figure 2.38, the viscoelastic models give smaller predictions to the wall deformations. In Figure 2.40, the time traces for radial displacements (left plot) and axial displacements (right plot) at point $(0, 2.4, 15.8)$ is displayed. From these figures we can see that although the largest radial displacement varies for different cases, it stays within the range of $0.08 - 0.13mm$ which is consistent with the physiological radial change as reported in [79, 80]. In figure 2.40 we observe that while the cases SLS1 and FOV-SLS2 lead to very similar deformation as that from the pure elastic model. In the other two cases (SLS2 and FOV-SLS1), the tube deformation is decreased by 38%, which also highlights the fact that the arterial wall response vary greatly among different patients and anatomic locations.

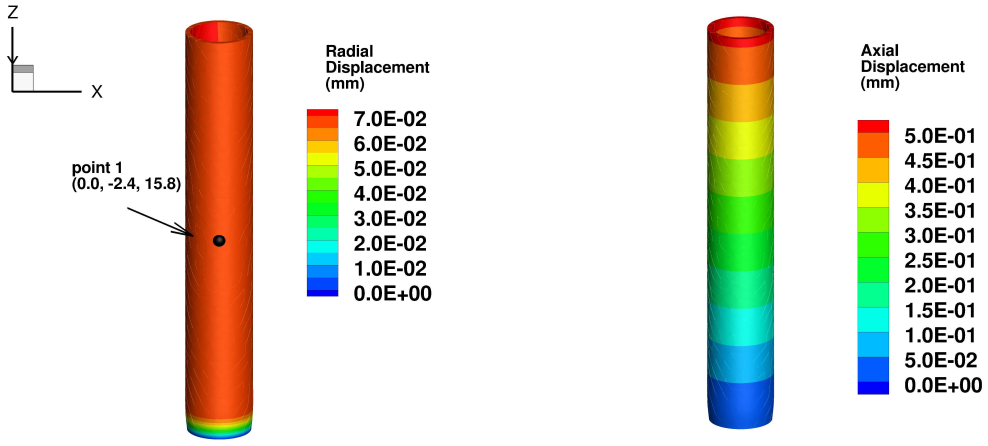

Figure 2.38: Displacements (in millimeters) for the arterial wall test at $t = 9.5T$, from elastic model. Left: radial displacement. Right: axial displacement.

To better understand the role of fractional order α and the relaxation parameters τ_E and τ_S, we vary the fractional order α between $0 \leq \alpha \leq 1$ while fixing the relaxation times as $\tau_E = 0.05$ (sec) and $\tau_S = 0.025$ (sec). The time traces for displacement at point $(0, 2.4, 15.8)$ are provided in Figure 2.41. On the other hand, in Figure 2.42 we illustrate the effects of varing τ_E and τ_S, with $\alpha = 0.2$ and $\alpha = 1$. Here we note that while $\alpha = 1$ the model returns the solution of the integer order SLS model. From Figure 2.41, it can be observed that while fixing the relaxation time parameters, varying α results to a relatively minor change in the structural displacement. When considering the model sensitivity to different relaxation parameters, in Figure 2.42 we can see that as the fractional order increases, the choice of relaxation times has a more significant impact on the computed solution, and this observation is consistent with [3].

2.3.4 Summary

We have developped a numerical method for the 3D fractional order standard linear solid (SLS) model (2.3.2) based on a general Jacobi polynomial basis that can be used to generate 3D polymorphic high-order elements. The convergence rates are investigated on a problem with fabricated solution, to show that this numerical scheme is of first-order accuracy. In numerical tests, we perform simulations on a straight tube subjected to periodic inner pressure, which can be seen as an idealization of a section of arterial wall. We have also observed that comparing to the interger-order SLS model, the fraction order SLS model is generally less sensitive to the selection of relaxation time parameters. Such observation verifies the findings in 1D simulations [3]. However, comparing with the 1D simulation results, the 3D fraction order SLS model is generally more affected by the

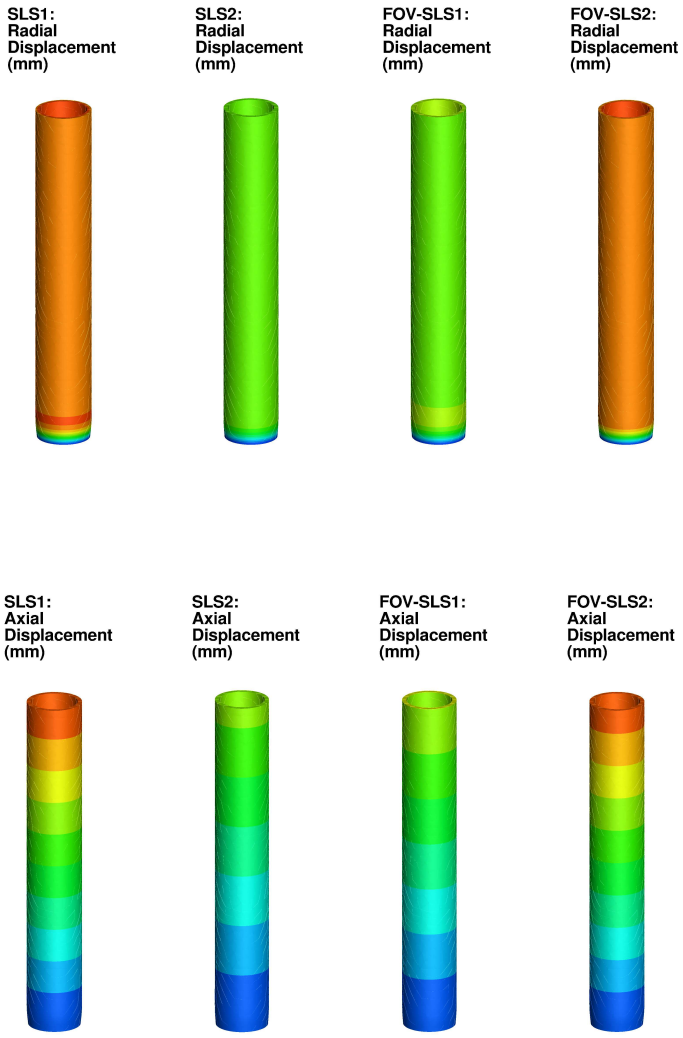

Figure 2.39: Displacements (in millimeters) for the arterial wall test at $t = 9.5T$, from different viscoelastic models. Upper row: radial displacement. Lower row: axial displacement.

variation of viscoelastic parameters (α, τ_E, τ_S).

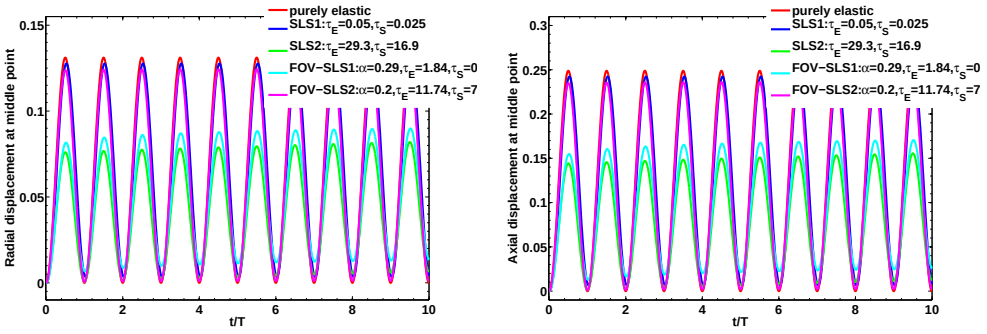

Figure 2.40: Time traces in the arterial wall test, from viscoelastic models listed in Table 2.10. Left: radial displacement at sample point. Right: radial velocity at sample point.

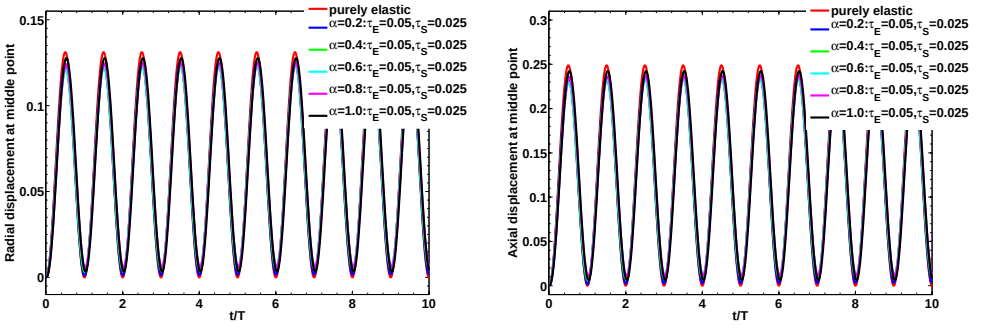

Figure 2.41: Time traces in the arterial wall test, from $\tau_E = 0.05$, $\tau_S = 0.025$ and $0 \leq \alpha \leq 1$. Left: radial displacement at sample point. Right: radial velocity at sample point.

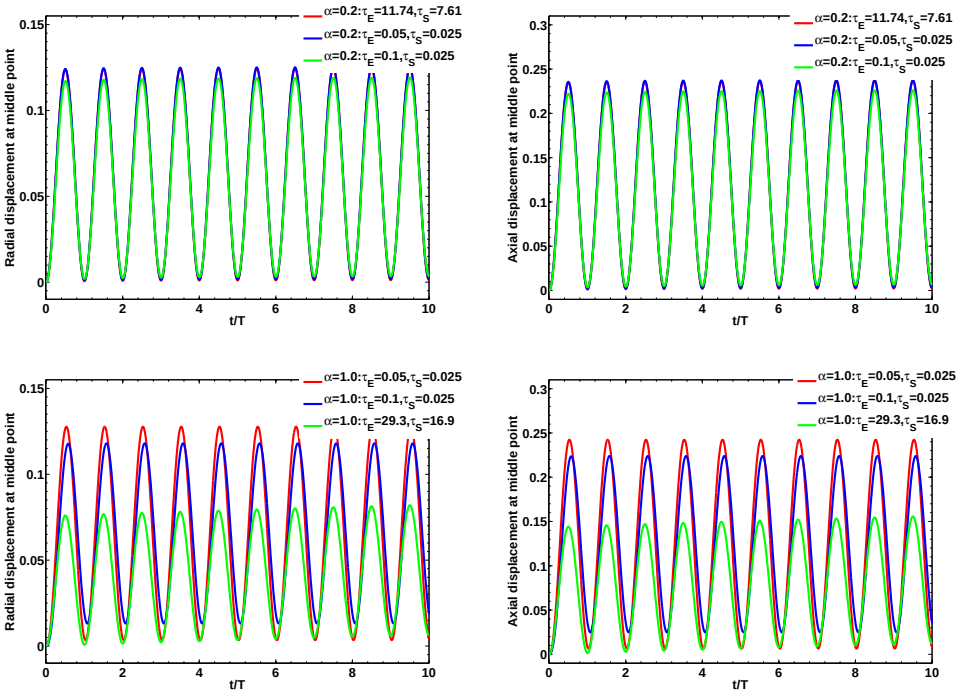

Figure 2.42: Time traces in the arterial wall test, from different τ_E and τ_S. Upper row: $alpha = 0.2$. Lower row: $\alpha = 1.0$. Left column: radial displacement at sample point. Right column: radial velocity at sample point.

Chapter 3

Bio-fluid Mechanics: Simulations

3.1 Blood flow simulation validation in patient-specific brain aneurysm geometries

3.1.1 Overview

Our spectral element based Navier-Stokes solver **NEKTAR** has been developped for more than 30 years, and has tackled problems in blood flow simulations [6]. Especially we have studied blood flow in the brain arterial network and aneurysms with emphasis on the computational scalability as well as flows from the clinical point of view [95]. To achieve the goal of helping the diagnosis and treatment of cardiovascular disease, we have employed the image-based computational fluid dynamics to develop patient-specific blood simulations. To be more specific, we derive the lumen geometry from 3D angiography, then conduct the numerical simulations for the blood flow on this patient-specific geometry. However, there is much uncertainty in the lumen geometry owing to the segmentation method and the imaging resolution, which might introduce variabilities into the CFD solutions. Moreover, in larger arteries the rigid wall and fully-developed inflow assumptions are thought to result a second order effect. Therefore, before the image-based computational fluid dynamics (CFD) models can be used in a predictive capacity, it must be shown that they indeed reproduce the *in vivo* hemodynamic enviroment.

In this chapter, we aim to validated the blood flow simulations in patient-specific brain aneurysm geometries, with two ways. Firstly, the governing equations of blood flow model and corresponding boundary conditions are briefly described in section 3.1.2. Then for the purpose of indirectly validating patient-specific CFD models, we implemented a parallel advection-diffusion solver with

high-order spectral/hp element method and simulated the the injection of contrast agent into a precomputed, patient-specific model. A time-series of virtual angiographic images were constructed from the computed 3D contract agent flow dynamics, and compared with corresponding clinical images in section 3.1.3. To further validate our solver directly, we participated in the CFD challenge workshop and evaluated the sensitivity of CFD predictions to different solvers, by simulating the blood flow in the same provided giant aneurysm geometry [1]. The variability in the prediction of pressures is then assessed cross research groups, as illustrated in section 3.1.4.

3.1.2 Navier-Stokes solver

With the assumption of rigid arterial walls, we model the blood flow as incompressible and Newtonian. Here we suppose that the blood occupies the volume Ω, and $\partial\Omega_i$, $\partial\Omega_o$ denote the inlet and outlet boundaries, respectively. A non-slip boundary condition is adopted at the arterial walls. The flow is then governed by the incompressible Navier-Stokes equations

$$\frac{\partial \mathbf{u}}{\partial t} + \mathbf{u}\cdot\nabla\mathbf{u} = -\frac{\nabla p}{\rho_f} + \nu\nabla^2\mathbf{u}, \quad \text{in } \Omega, \tag{3.1.1a}$$

$$\nabla\cdot\mathbf{u} = 0, \quad \text{in } \Omega. \tag{3.1.1b}$$

Here, $\mathbf{u}$, p, ρ_f, and ν stand for the blood velocity, pressure, density, and the kinematic viscosity, respectively. At the inlets $\partial\Omega_i$, the blood velocity is given as a problem-dependent pulsatile Womersley profile [96]. At the outlets, we assume that the velocity profile is fully developed, i.e., $\dfrac{\partial \mathbf{u}}{\partial \mathbf{n}} = 0$, and the pressure $\bar{p}$ is set to flow-rate dependent using RC-type boundary conditions [4]:

$$\bar{p}(t) + RC\frac{d\bar{p}(t)}{dt} = Q(t)R \tag{3.1.2}$$

determined by the flow rate $Q(t)$, the resistant R, and the capacitance C.

To solve numerical equations (3.1.1), we employ the parallel Navier-Stokes solver NEKTAR [73, 6]. The Navier-Stokes equations are discretized in time first using a high-order splitting scheme, and then one pressure Poisson equation and three Helmholtz equations for velocity components are discretized spatially via spectral elements. At each time step, the solver updates explicitly the previous time step solution with the nonlinear convection contribution. Then, the pressure is obtained by a Poisson equation using the updated intermediate velocity and Neumann pressure boundary conditions. At the third substep, the velocity is obtained by solving three inhomogeneous Helmholtz equations. To be more specific, at time step n we solve for $\mathbf{u}^n$ and p^n from previous

time step results $\mathbf{u}^{n-i}$ [97]:

$$\frac{\tilde{\mathbf{u}}^n - \sum_{i=1}^{J} \alpha_i \mathbf{u}^{n-i}}{\Delta t} = -\mathbf{N}^n, \tag{3.1.3a}$$

$$\frac{\tilde{\tilde{\mathbf{u}}}^n - \tilde{\mathbf{u}}^n}{\Delta t} = -\frac{\nabla p^n}{\rho_f}, \tag{3.1.3b}$$

$$\frac{\beta \mathbf{u}^n - \tilde{\tilde{\mathbf{u}}}^n}{\Delta t} = \nu \nabla^2 \mathbf{u}^n, \tag{3.1.3c}$$

where

$$\frac{\partial p^n}{\partial \mathbf{n}_f} = -\rho_f \left(\frac{\partial \mathbf{u}^n}{\partial t} + \nu \mathbf{R}^n + \mathbf{N}^n \right) \cdot \mathbf{n}_f, \quad \text{on } \partial\Omega_i. \tag{3.1.4}$$

and

$$\mathbf{N}^n = \sum_{i=1}^{J} \hat{\alpha}_i \mathbf{u}^{n-i} \cdot \nabla \mathbf{u}^{n-i}, \; \mathbf{R}^n = \sum_{i=1}^{J} \hat{\alpha}_i \nabla \times \nabla \times \mathbf{u}^{n-i}. \tag{3.1.5}$$

Here J denotes the time integration order, and α_i, β, $\hat{\alpha}_i$ are the corresponding coefficients of the $J-$th order backward differentiation formulas [6]. In this chapter, we take $J = 2$ for all numerical simulations of blood velocities and dye concentrations. In (3.1.4), $\mathbf{n}_f$ is the normal vector pointing outward on the boundaries. Hence, our parallel solver, NEKTAR, is categorized into velocity correction scheme and semi-implicit scheme treating the nonlinear term explicitly and the viscous term implicitly. The unknowns, i.e., velocity and pressure, are expressed as a linear combination of a Jacobi polynomial basis, and C_0 continuity is imposed at the boundary of the elements. Any type of elements and their hybridization can be used but tetrahedral elements with NEKTAR can deal with different types of 3D elements in space, including hexahedrons, prisms, tetrahedrons and pyramids, but in this chapter we employ the tetrahedral elements only.

3.1.3 Diffusion solver: comparison with tomography data

Contrast agents are typically used to improve the visibility of blood flow patterns in X-ray based imaging techniques. In computed tomography (CT), the contrast agent is usually iodine based and its concentration should be proportional to the change in signal intensity. Therefore, we could simulate the distribution of contrast agent concentration, and mimick the radiological procedure. A virtual angiogram can be constructed, by simulating the injection of constrast agent into a patient-specific aneurysm model. By simulating the attenuation of X-rays through the contrast agent flow dynamics, we can get a time-series of images, and compare the resulted virtual angiographic images with the corresponding clinical images.

In this section, we examine via visualization the structure of flow in internal carotid arteries laden with two different types of aneurysms:

- case1: a wide-necked saccular aneurysm,
- case2: two adjacent saccular aneurysms.

By comparing the concentration field calculated from simulated velocity field and the MRI images from dye injection, we aim to qualitatively validates our spectral element simulations for velocity field. On the other hand, since the complex geometry of aneurysms may cause instabilities in velocity field [98], we will investigate if the concentration field can also reveal this phenomenon.

Formulation

To generate a virtual angiogram, we first compute the blood velocity field by numerically solving the Navier-Stokes equation following (3.1.3), on the patient-specific geometries as shown in Figure 3.1. Then with the underlying velocity field $\mathbf{u}$, we can solve for the transport of the contrast agent.

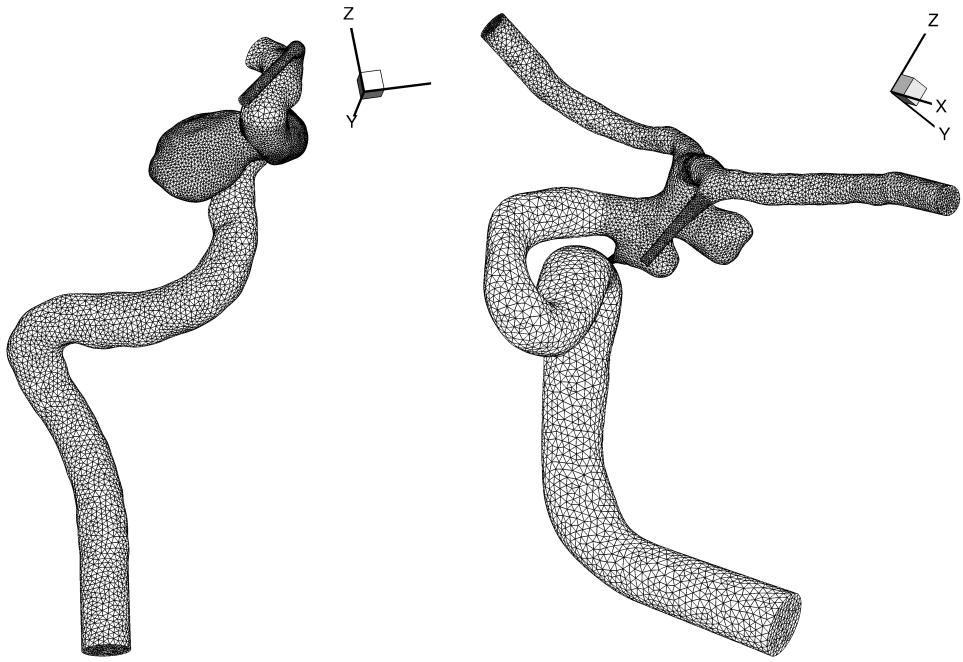

Figure 3.1: Meshes of patient-specific aneurysms for comparison with tomography. Left: case1; right: case2.

To avoid the heavy computational expense of coupling Navier-Stokes and transport equations, we assume that the solution of contrast agent transport and that of the blood flow may be decoupled. For this diffusing and passively advected dye, the relative concentration field c is governed by the

following equation

$$\frac{\partial c}{\partial t} + \mathbf{u} \cdot \nabla c = \kappa \nabla^2 c, \quad \text{in } \Omega. \tag{3.1.6a}$$

Here, κ stand for the dye diffusivity. The dye injection lasts for 1.5 secs, which is approximately two cardiac cycles. Since the injection takes place at relatively far upper stream and we do not have the detailed injection profile at the computational domain's inlet, we assume that the nondimensional concentration field c is evenly distributed at the inlet and during all time in this two cycles, i.e.,

$$c = 1, \quad \text{at } \partial\Omega_i, \quad \text{for } 0 \leq t \leq 1.5\text{secs}. \tag{3.1.7}$$

On the other hand, we assume that the injection starts ($t = 0$) when the inlet flow rate $Q(t)$ reaches its trough. At the arterial walls and the outlets, zero Neumann boundary conditions are applied, i.e., $\dfrac{\partial c}{\partial \mathbf{n}_f} = 0$. To solve (3.1.6) on the original tetrahedral element meshes, we employ the semi-implicit scheme similar to (3.1.3)

$$\frac{\tilde{c}^n - \sum_{i=1}^{J} \alpha_i c^{n-i}}{\Delta t} = -\sum_{i=1}^{J} \mathbf{u}^{n-i} \cdot \nabla c^{n-i}, \tag{3.1.8a}$$

$$\frac{\beta c^n - \tilde{c}^n}{\Delta t} = \nu \nabla^2 c^n, \tag{3.1.8b}$$

where

$$c = 0 \ \text{ on } \Omega \text{ when } t = 0. \tag{3.1.9}$$

Here $J = 2$ denotes the time integration order, and α_i, β are coefficients defined as that for the Navier-Stokes solver (3.1.3). Regarding the spatial discretization, the dye concentration field c is also expressed as a linear combination of a Jacobi polynomial basis as what described in section 2.1.3.

With characteristic velocity U and length D, we defined the Peclet number as

$$Pe = \frac{UD}{\kappa}$$

which can be seen a measure of the relative importance of advection to diffusion. If considering the molecular properties of blood and iodine-based contrast agent, the Peclet number tends to be as large as the order of $10^6 - 10^7$, i.e., $Pe \approx 10000Re$ where Re is the Reynolds number $Re = \frac{UD}{\nu}$. But with that we have to use very small time steps to keep the numerical stability. Fortunately, in virtual angiography such fine-scale gradients in the dye distribution can not be resolved using available

imaging modalities, and are therefore not particularly relevant. As reported in [99], as long as $Pe \gg 1$, the dynamics remains advection-dominated and increasing the effective diffusivity would still reasonably represent the coarse-grained concentration patterns. In Figure 3.2 we compare the virtual angiographic images from two increased Pe numbers: $Pe = Re$ and $Pe = Re/10$. It can be observed that the increasing Peclet number does not change the major pattern of the dye concentration. In the following contents we will fix $Pe = Re$ for all simulations.

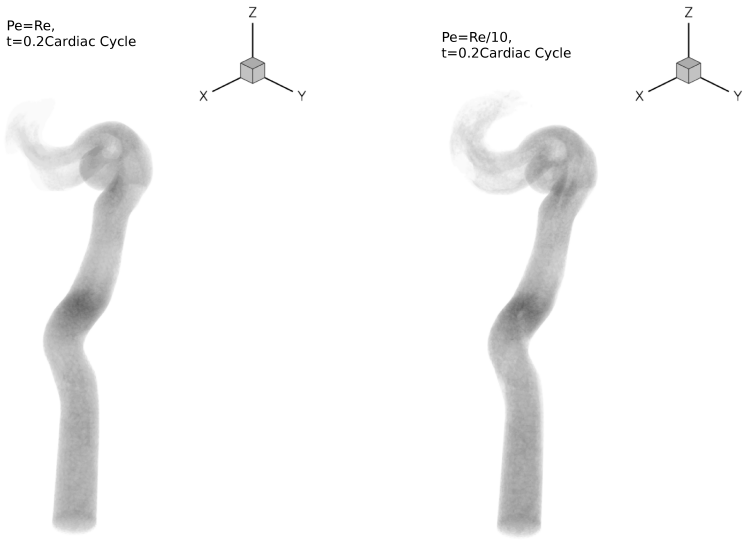

Figure 3.2: Virtual angiographic images from increased effective diffusivities. Left: $Pe = 77 = Re$; right: $Pe = 7.7 = Re/10$.

Results

For case1, figure 3.3 demonstrates the virtual cine X-ray angiograms from the computed CFD data, and compares with the real angiograms at corresponding time instants. It can be seen that generally the concentration field calculated from simulated velocity field looks similar with the real angiogram near the aneurysm region. However, at the region near the inlet, the idealized concentration profile (3.1.7) introduces errors. Unfortunately, in our case there is no available detailed information about the injection profile. In the future, we might consider the algorithm introduced in [99] to refine (3.1.7) and hopefully a more quantitative comparison can be achieved.

Moreover, it was reported in [98] that on case2, spatio-temporal changes of wall shear stress (WSS) vectors and velocity time traces revealed the speculated flow instability of about $20 - 50$Hz inside the aneurysm. Specificly, at the points marked in the left plot of figure 3.4, oscillations and directional changes of WSS and velocity vectors around impingement regions were quantified and

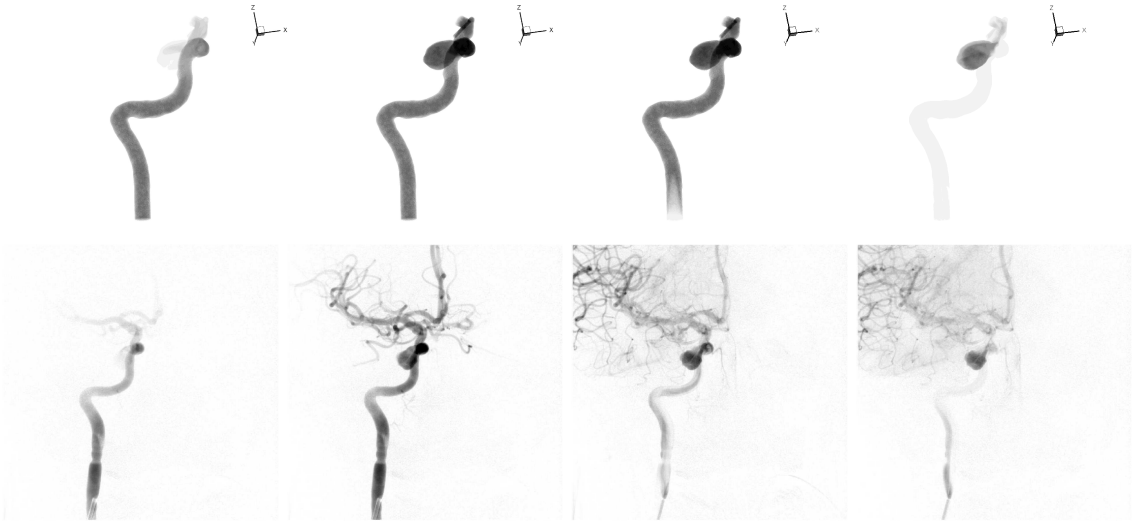

Figure 3.3: Comparison between virtual angiographic images and corresponding real angiograms. Upper row: virtual; lower row: real.

clarified. Now we will investigate if the dye injection process can reflect the instabilities of blood flow in complex blood vessel geometries. In the right plot of figure 3.4, we show the time traces of c at the sample points marked in the left plot. It can be observed that during the process of dye resolution filling aneurysm region, high frequency oscillations appear in these time traces near the systolic peak, which is also the period that WSS and velocity instabilities appear. Therefore, although the current technique could not provide enough temporal resolution (e.g., only 2 plots per second in case1), if with high enough time resolution the dye injection process has the potential to reveal the oscillated flow structures near aneurysms. Note that by using the real Peclet number of dye the smoothing out effect should be less, and therefore we can expect the real angiography to reveal these instabilities more obviously.

3.1.4 Navier-Stokes solver: cross-solver validation

In this section, we aim to determine the "real world" variability of CFD solutions. The same lumen geometry and flow rate boundary conditions are provided for 25 participated groups [1], then each group simulate the blood flow with various solution strategies and discretizations. On the other hand, we want to investigate how sensitive the results are to the non-patient-specific flow rates.

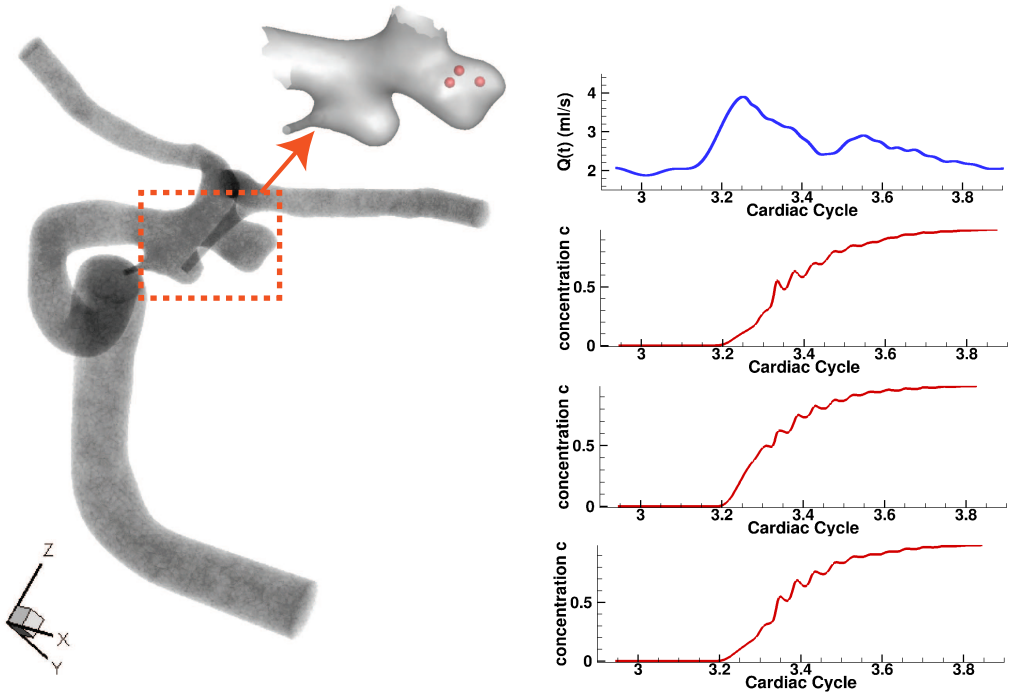

Figure 3.4: Time traces of dye concentration at sample points (case2). Left: position of sample points; right: flowrate and dye concentration time traces.

	Phase I	Phase II
Viscosity $(dyn - s/cm^2)$	0.0400	0.0401
Density (g/cm^3)	1.000	1.113
Period (sec)	0.990	1.164

Table 3.1: Prescribed fluid parameters in cross-solver Navier-Stokes solver validation.

Methods

Together with other 24 groups, we have participated in two phases of the CFD Challenge project: the phase I aims to compare the numerical solution in a cross-group way, to test the variability of the contributed solutions; the phase II aims to validate the computed pressure drops to those measured in physical model of the same geometry. Here we will focus more on the numerical simulation part, i.e., on phase I. The fluid and parameters for these two phases are summarized in Tables 3.1-3.2, and the computational domain includes a giant cerebral aneurysm with a constriction procimal to the aneurysm ostium, as shown in Figure 3.5. In each phase, two pulsatile inflow boundary conditions are provided based on the same Womersley profiles, but with different amplitudes. By doing so, we can investigate that how the choice of flow rate might affect the pressure drop. We also carry out four steady flow rate simulations in each phase, corresponding to the cycle-averaged

Phase I					
Steady1	Steady2	Steady3	Steady4	Pulsatile1	Pulsatile2
5.13	6.41	9.14	11.42	Peak=5.13, Mean=9.14	Peak=6.41, Mean=11.42
Phase II					
Steady1	Steady2	Steady3	Steady4	Pulsatile1	Pulsatile2
5.10	6.36	9.17	11.36	Peak=4.40, Mean=9.34	Peak=6.16, Mean=11.25

Table 3.2: Prescribed flow rates (mL/sec) in cross-solver Navier-Stokes solver validation.

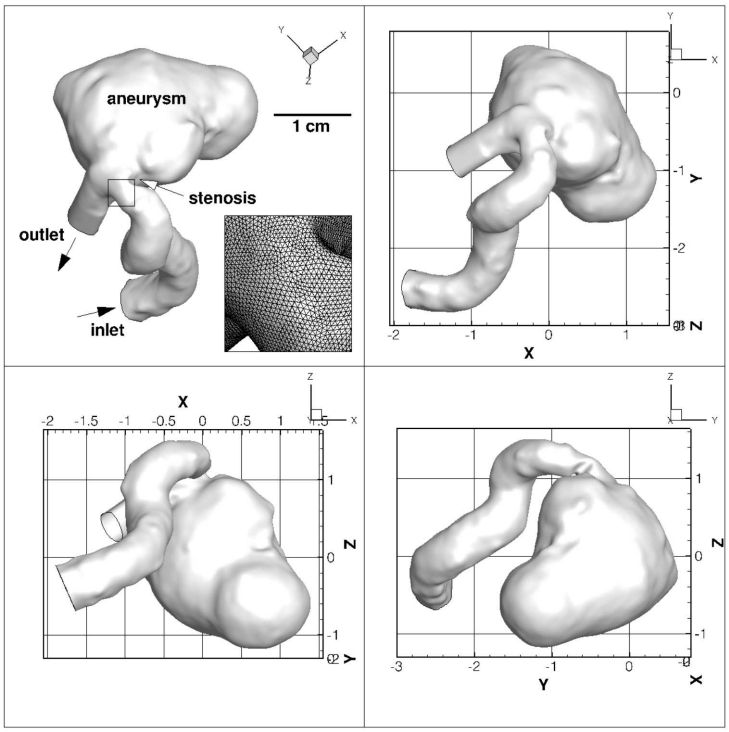

Figure 3.5: Geometry employed in cross-solver Navier-Stokes solver validation [1].

and peak-systolic inflow conditions for the two pulsatile cases.

Results

In our group, all simulations are performed on a parallel cluster at NICS, Kraken XT5 exploiting 42 nodes, i.e. 504 cpus. With polynomial order 6 basis, one cardiac cycle took 96 hours and steady cases took 200 hours in order to reach stationary state.

Convergence of solutions is confirmed in many different aspect; $h-$type refinement and $p-$type refinement tests are performed in steady and pulsatile cases. Three cardiac cycles are simulated to make sure that the third cycle reaches a solution. The time step size is 1.17×10^{-6}(sec) with number of steps 850000 in the pulsatile simulations for polynomial order 6; smaller time steps are used for higher polynomial order.

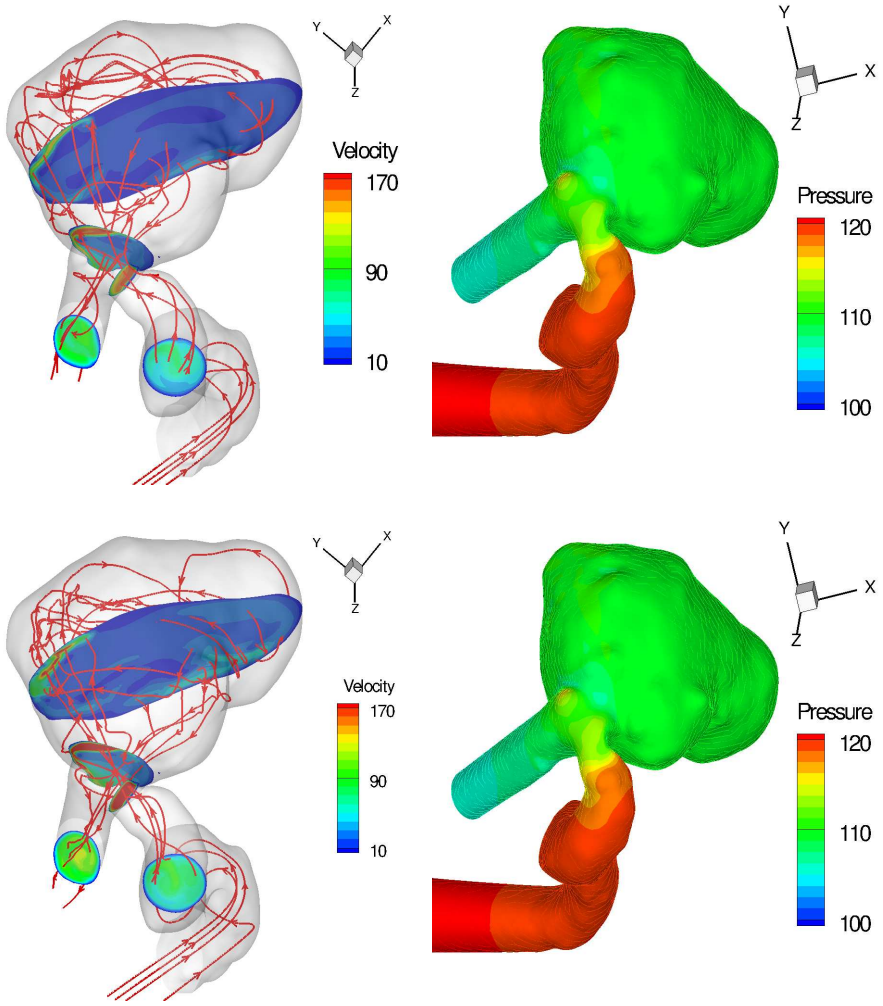

Figure 3.6: 3D flow patterns and surface pressures in CFD challenge phase I. Upper row: pulsatile case with average flow rate (VFR) $5.13ml/sec$; Bottom row: pulsatile case with VFR $6.41ml/sec$. Left column: velocity contours and streamlines; Right column: pressure contours.

To resolve the correct pressure patterns, we used polynomial order 6 and 8 elements for the pulsatile cases with average flow rate $5.13ml/sec$ and $6.41ml/sec$, respectively. For the steady cases, elements with polynomial order 6, 6, 10, 10 are employed for flow rate $5.13ml/sec$, $6.41ml/sec$, $9.14ml/sec$ and $11.42ml/sec$ cases, respectively.

For the pulsatile cases, the 3D flow patterns and surface pressures at the systolic peak are shown in Figure 3.6. The peak systolic and cycle-averaged pressures for the second pulsatile case is compared cross-groups in [1] with our results marked by letter "X", as shown in Figures 3.7-3.8. It can be seen that our solution agrees well with most solutions, approximating the pressure in aneurysm sac as around $105mmHg$ at the systolic peak (i.e., a pressure drop of $15mmHg$ from

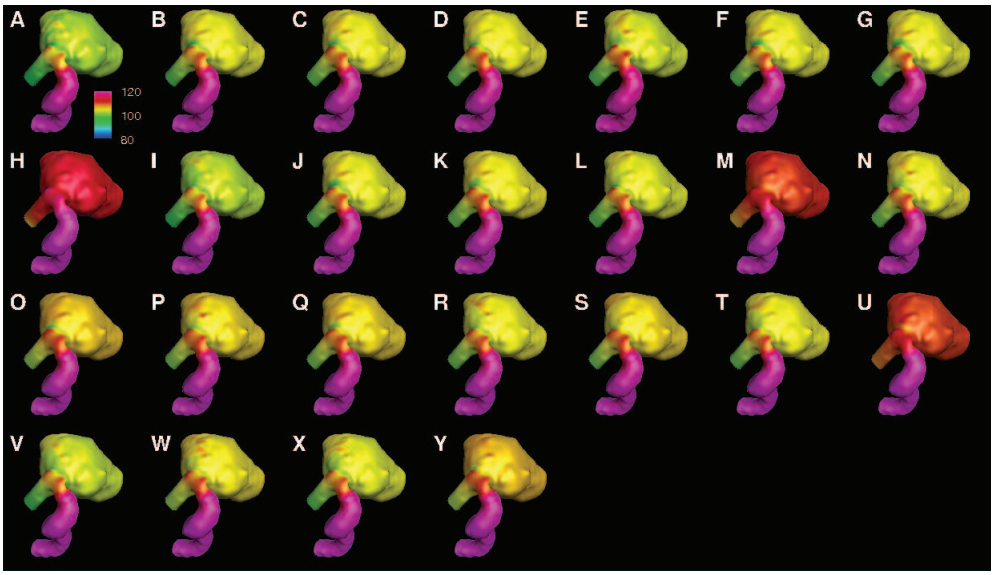

Figure 3.7: Surface maps of peak systolic pressures for pulsatile case 2 in phase I [1].

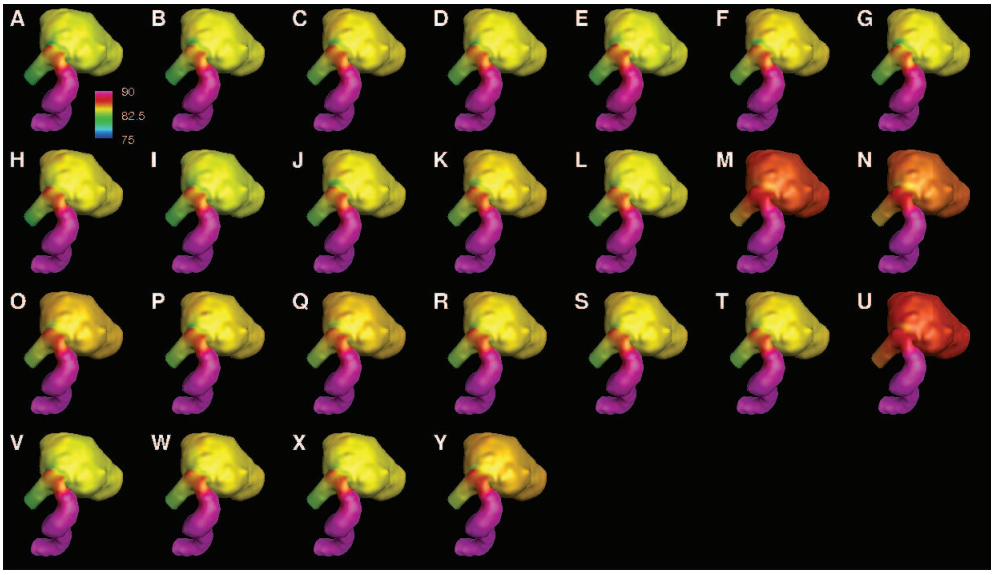

Figure 3.8: Surface maps of cycle-averaged pressures for pulsatile case 2 in phase I [1].

the inlet). Moreover, the velocity isosurfaces are also compared, as shown in Figures 3.7-3.8, which reveal a larger degree of variability among the solutions. Although the flow patterns from our solution look generally consistent with most of other solutions, at the systolic peak only several groups (including us) report evidence of flow instabilities in the velocity isosurfaces. This might due to the high temporal and spatial resolution we have employed. On the other hand, while considering the cycle-averaged flow patterns, the results are more similar across the solutions.

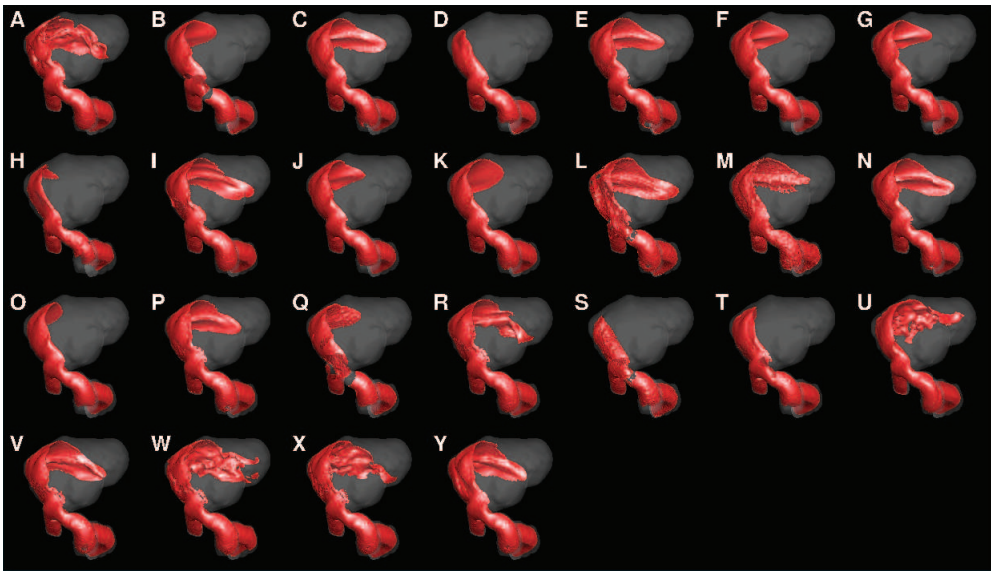

Figure 3.9: Systolic peak velocity isosurfaces of magnitude at $50cm/s$, for pulsatile case 2 in phase I [1].

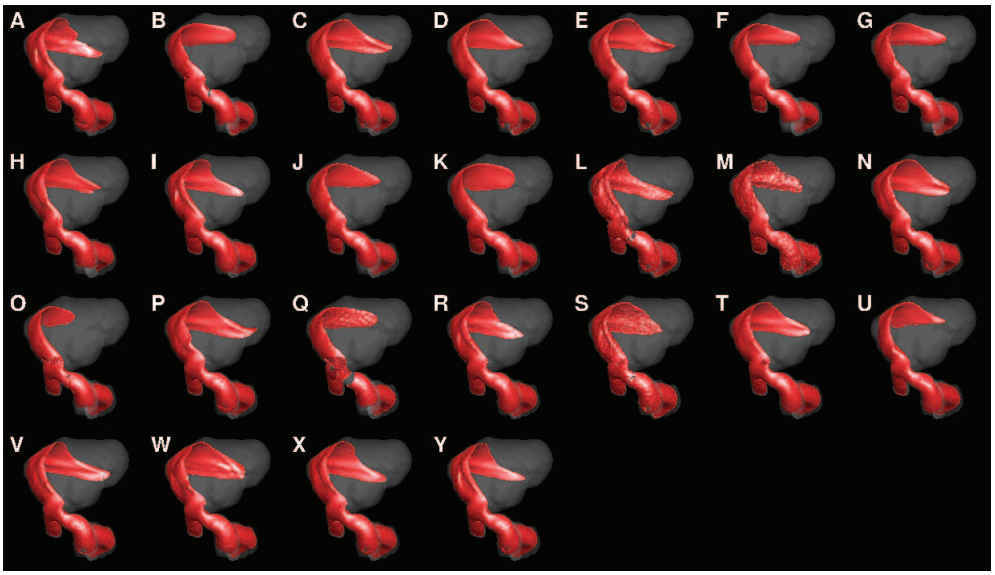

Figure 3.10: Cycle-average velocity isosurfaces of magnitude at $50cm/s$, for pulsatile case 2 in phase I [1].

To investigate the similarities between pulsatile solutions and steady solutions, we plot the pressure along the centerline in Figure 3.11. In the left plot the systolic peak pressures in pulsatile cases are compared with steady cases with corresponding inlet flow rates (case Steady 3 and Steady 4); while in the right plot the cycle-averaged pressures are compared with case Steady 1 and Steady

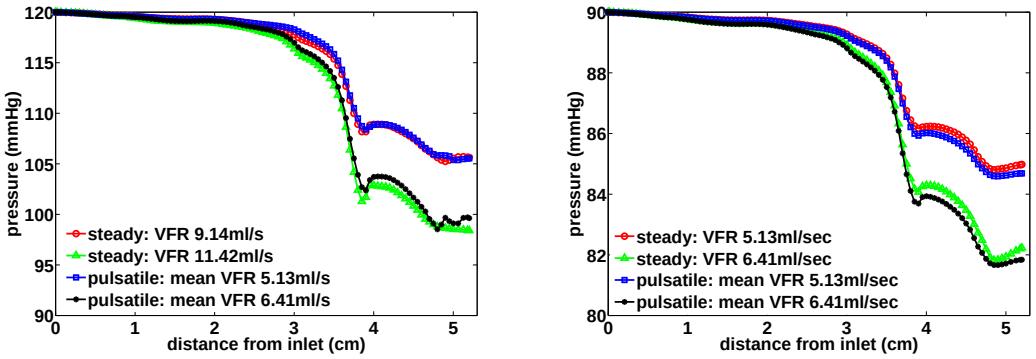

Figure 3.11: Pressure along the centerline. Left: comparison between systolic peak pressures and corresponding steady cases; Right: comparison between cycle-averaged pressures and corresponding steady cases.

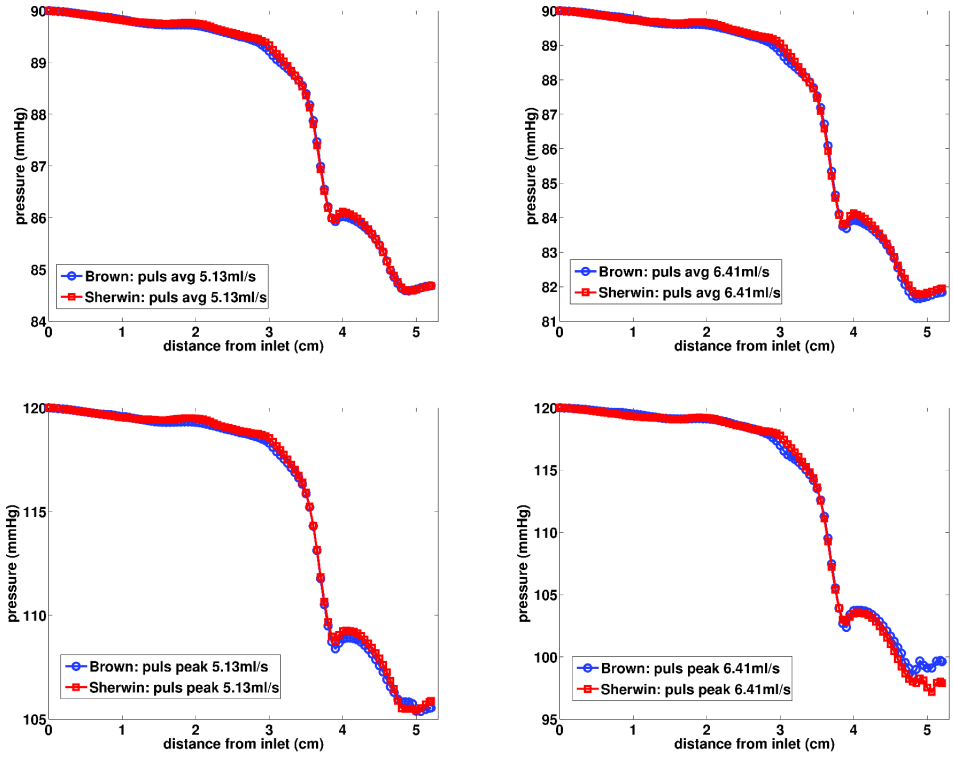

Figure 3.12: Pressure along the centerline comparison between our group and Prof Sherwin's group. Upper row: pusatile case 1; Lower row: pusatile case 2. Left column: cycle-averaged pressure; Right column: systolic peak pressure.

2. One can see that the differences for peak systolic and cycle-averaged pressure drops relative to their steady flow counterparts are almost negligible, which indicates the posibility of a quasi-steady approximation. Moreover, to compare across groups, we plot our centerline pressure results

against that from Veronique Peiffer, Yumnah Mohamied and Spencer Sherwin at Imperial College London, as shown in Figure 3.12. Except at the outlet region where outflow boundary conditions (RCR at Imperial college but RC at out group) introduce differences, remarkable consistency is demonstrated in Figure 3.12.

Regarding the instabilities, unstable and chaotic flows are generated even in the steady inflow, and the characteristic frequencies vary at different points of the artery. Generally, we observed higher frequencies after the stenosis and aneurysm, where the geometry complicates. At a given point in the artery, the characteristic frequencies increase if a larger inlet flow rate is imposed. Here we focus on the spectrum of 4 points: one at the stenosis, one at the center of aneurysm neck, one at the center of aneurysm, and the last at the outlet. In the steady case with flow rate $5.13ml/sec$, the velocities at these four points have characteristic frequencies from 4.70 to 4.88Hz. With flow rate $6.41ml/sec$, these frequencies increase to 5.33-8.1999Hz. When the flow rate is further increased to $9.14ml/sec$ and $11.42ml/sec$, the frequency spectrum is broadened to 22.30-39.11Hz and 34.66-97.05Hz, respectively. For the cases with pulsatile inflows, a significant unstable pattern starts at the systolic peak and becomes the strongest at the declining systole. When the average flow rate is $5.13ml/sec$, the velocities at those four points have frequencies from 13.96 to 24.52Hz. On the other hand, a higher flow rate ($6.41ml/sec$) gives frequencies 13.10-28.63Hz.

3.1.5 Summary

In this chapter, we have validated our Navier-Stokes solver in two ways: (1) by simulateing the distribution of contrast agent concentration and qualitatively comparing the virtual angiogram with the corresponding clinical X-ray images; (2) by comparing the velocity and pressure numerical solutions in a cross-group way. In both projects we have observed concordances in the comparisons, although the inflow and outflow boundary conditions may introduce errors. On the other hand, because of the unstable flows, instabilities appear in the time traces of concentration field inside/near aneurysm sac at the systolic peak. This suggests the possibility of observing flow instabilities in the dye injection process, if with high enough time resolution. Such instabilities are also observed in the second project especially in the pulsatile cases, which shows that although the steady flow cases provide a good approximation for the centerline pressure drops, they generally do not represent the unsteadiness of the pulsatile flow.

Chapter 4

Fluid-Structure Interaction: Algorithms and Simulations

4.1 Generalized fictitious methods

4.1.1 Overview

In recent years, there has been great interest in fluid-structure interaction (FSI) problems due to their relevance in structural engineering and biomedical applications. In particular, the hemodynamic problem has received more attention [100, 101, 102, 103, 104, 105, 106, 107, 108] not only because of its clinical importance but also due to the numerical challenges resulting from the relatively small values of the mass ratio between the structure and the fluid [83, 82, 109, 110]. Different numerical approaches have been proposed for FSI problems [111, 106, 112, 113, 114, 115, 116, 117, 118, 119, 120, 4], which can be broadly classified as either monolithic or partitioned. In the monolithic method, the fluid and structure equations are solved simultaneously as a large nonlinear system. This approach is advantageous from the stability standpoint because the energy balance between fluid and structure is automatically satisfied at each time step. On the other hand, in the partitioned method the FSI system is split into separate fluid and structure solvers so that software modularity is possible and hence different solvers can be re-used. Moreover, the partitioned method is scalable to large-scale parallel computing, and hence this is the approach we adopt in the current work with the aim of coupling our existed spectral element fluid solver NEKTAR [6] with the structure solver stressNektar [27, 121].

In the partitioned approach, a coupling algorithm is required with proper transmission condi-

tions to reinforce the energy balance. Specifically, in hemodynamic problems where the fluid and structure densities are close, convergence of the coupled solvers is especially problematic because of the so-called added-mass effect [83]. When the added-mass effect is strong, the weakly coupling schemes will be severely affected and may even become unstable, unless special treatments are introduced in the procedure [122, 123]. In these cases, a strong coupling is required to impose continuity at the interface through fixed-point iterations [113, 124, 125] or Newton-type iterations [109, 119, 114, 126, 127] at each time step. However, calculating the Jacobian in the Newton-type methods can be very expensive, and hence, several variants have be developed to reduce the computational cost [128, 109, 129, 116]. On the other hand, fixed-point iteration algorithms are relatively easier to implement but have slower convergence rate. To this end, additional acceleration schemes can be employed, e.g. the Aitken acceleration, to enhance the convergence rate [130, 124, 131].

A number of other approaches have been developed more recently to accelerate convergence of the partitioned algorithm, including the Robin-Robin scheme [112, 113, 114, 5, 120], the interface artificial compressibility [110, 132], the stabilized explicit method [133, 122], and our own fictitious mass and damping methods [4]. In the Robin-Robin method, velocity and stress continuity at the interface are treated with Robin type mixed transmission conditions. With optimized coefficients, this method achieves good convergence rates for strong added-mass effect problems. In the interface artificial compressibility method, a local and linearized version of the structural model is included in the flow equations in the form of pressure-dependent source terms. This method is able to enhance stability and has been shown to have some similarities with the Robin method [116]. The stabilized explicit method can be viewed as a numerical resolution of the monolithic formulation, where a time penalty term is added into the partitioned equations, which effectively controls the fluid pressure variations at the interface. The fictitious mass and damping methods aim to balance the added-mass effect by putting additional acceleration and damping terms in the structure solver. In this method, the mass matrix and stiffness matrix are kept unchanged, which greatly saves the effort of modifying any existing solvers. Moreover, the additional terms are applied to the entire structure domain, hence providing further stabilization for problems with large deformation rates.

In this chapter, we revisit and generalize the fictitious methods by developing a similar modified governing equation but for the flow solver. In addition, we demonstrate that the generalized fictitious methods can be interpreted analogously to recovering the exact coupled solution. We also develop a more rigorous analysis for predicting (a priori in simple geometries and a posteriori in more complex geometries) the values of the optimal coefficients for the fictitious methods, building upon some preliminary ideas first presented in [4]. We have implemented the generalized fictitious methods using the spectral/hp element method, which is in general more sensitive to temporal

instabilities. Therefore, we will also investigate the effect of polynomial order on the convergence rate in prototype FSI problems. In addition to convergence and accuracy verification tests, we also test the flexibility of the fictitious methods for different FSI problems, including vortex-induced vibrations (VIV) with mass ratio approaching zero [134, 135], and a large-scale hemodynamic problem with patient-specific arterial geometry [4]. Generalized fictitious methods can provide great flexibility for implementation; for example, one can combine a fluid open source code with a black box structure code by employing the fictitious pressure method or a fluid black box code with a structure open source code by employing the fictitious mass (or damping) method.

This chapter is organized as follows. In section 4.1.2 we describe the FSI governing equations and discretization methods and the interface transmission conditions. The FSI coupling procedure at each time step for the full partitioned algorithm is summarized. The fictitious pressure method is presented in section 4.1.3 including analysis of convergence rate for simplified problems. In section 4.1.4 we apply the fictitious methods on both $2D$ and $3D$ systems to confirm our aforementioned analysis and also to demonstrate the relative advantages of our solver by comparing with a Robin based semi-implicit coupling solver. We end in section 4.1.5 with a brief summary. The appendices A.4-A.8 include additional technical details on the analysis of the generalized fictitious methods and other formulations.

4.1.2 Settings and formulation

In FSI problems, the domain $\Omega \subset \mathbb{R}^3$ is composed of two parts: the fluid subdomain $\Omega_f(t)$ occupied by the fluid, and the structure subdomain Ω_s occupied by a compliant or deformable structure, as shown in Figure 4.1. There is a common boundary between the two subdomains, which is the fluid-structure interface $\Sigma(t) = \Omega_f(t) \cap \Omega_s$. The fluid problem will be stated in an arbitrary Lagrangian-Eulerian framework [136] since the fluid domain is changing with the movement of the interface, while for the structure kinematics a purely Lagrangian approach is adopted. Roughly speaking, we aim to solve for three sets of variables in this FSI system: the fluid velocity $\mathbf{u}(\mathbf{x}, t)$, the fluid mesh velocity $\mathbf{w}(\mathbf{x}, t)$, and the structure displacement $\boldsymbol{\eta}(\mathbf{X}, t)$. Here $\mathbf{x} = \mathbf{x}(t)$ and $\mathbf{X}$ are the position vectors in the deformed configuration and initial configuration, respectively.

In this section, we will present the models for fluid and structure subdomains, respectively, and describe a *strong* coupling partitioned method, which solves the FSI system with the standard Dirichlet-Neumann boundary condition at the interface. In the following, we assume that suitable Dirichlet or Neumann boundary conditions are imposed on the boundaries $\partial\Omega_f(t) \setminus \Sigma(t)$ and $\partial\Omega_s \setminus \Sigma(t)$, and will therefore omit them in our descriptions. To ensure the continuity on the interface, subiterations are employed on each time step. In the following sections, we will denote

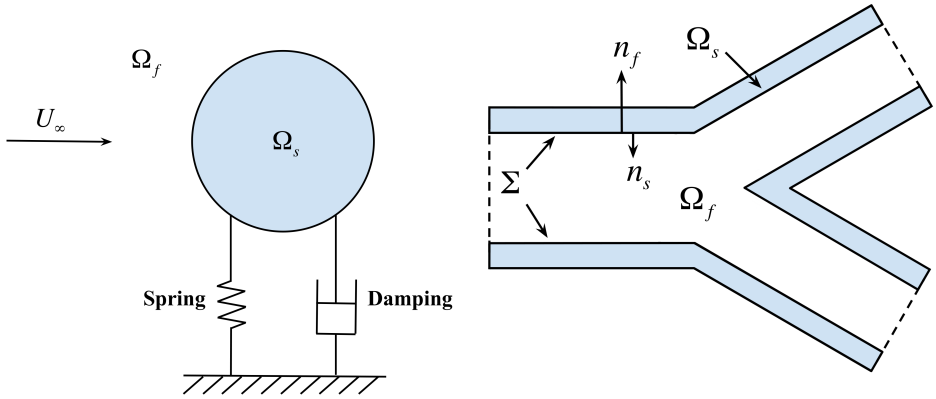

Figure 4.1: Sketches for problems of interest. Left: vortex induced vibration. Right: flow inside an arterial bifurcation.

the subiteration number by the subscript k, and the time step number by the superscript n.

Fluid model

The fluid is assumed to be incompressible and Newtonian, hence, it can be described by the incompressible Navier-Stokes equation in the arbitrary Lagrangian-Eulerian (ALE) framework,

$$\frac{\partial \mathbf{u}}{\partial t} + (\mathbf{u} - \mathbf{w}) \cdot \nabla \mathbf{u} = -\frac{\nabla p}{\rho_f} + \nu \nabla^2 \mathbf{u}, \quad \text{in } \Omega_f(t), \tag{4.1.1a}$$

$$\nabla \cdot \mathbf{u} = 0, \quad \text{in } \Omega_f(t), \tag{4.1.1b}$$

combined with the initial condition

$$\mathbf{u}(\mathbf{x}, t = 0) = \mathbf{u}_0(\mathbf{x}), \quad \text{in } \Omega_f(0), \tag{4.1.2}$$

and the Dirichlet boundary conditions on the interface, i.e.,

$$\mathbf{u} = \frac{\partial \boldsymbol{\eta}}{\partial t}, \quad \text{on } \Sigma(t), \tag{4.1.3}$$

which enforces the continuity of velocities. Here, $\mathbf{w}$, p, ρ_f, and ν stand for the mesh velocity, pressure, fluid density, and the kinematic viscosity, respectively.

The current configuration $\mathbf{x}$ of the fluid subdomain is defined as a lifting from the structure displacement on the interface: given the displacement on the interface $\boldsymbol{\eta}|_\Sigma$, we are looking for a mapping from the initial fluid configuration $\Omega_f(0)$ to the current configuration $\Omega_f(t)$. Here we

construct the mapping from a harmonic extension operator, i.e. the mesh velocity $\mathbf{w}$ satisfies

$$\nabla^2 \mathbf{w} = 0, \text{ in } \Omega_f(t), \tag{4.1.4a}$$

$$\mathbf{w} = \frac{\partial \boldsymbol{\eta}}{\partial t}, \text{ on } \Sigma(t), \tag{4.1.4b}$$

which is endowed with vanishing boundary conditions on the other boundaries:

$$\mathbf{w} = 0, \quad \text{in } \partial\Omega_f(t) \setminus \Sigma(t). \tag{4.1.5}$$

At each time step, the mesh position $\mathbf{x}$ will be obtained from the integration of the mesh velocity.

To solve numerical equations (4.1.1) and (4.1.4), we employ the parallel Navier-Stokes solver NEKTAR [6]. The spectral element method with Jacobi polynomial basis is used to represent the fluid velocity, fluid pressure and mesh velocity. It can deal with different types of 3D elements in space, including hexahedrons, prisms, tetrahedrons and pyramids. In NEKTAR, the Navier-Stokes equation is discretized in time using a high-order splitting scheme, with three parts: first the nonlinear terms are treated explicitly, then the pressure is obtained by a Poisson equation solver, and finally the viscous terms are treated implicitly [73]. In the strongly coupled FSI system, we employ subiterations to ensure continuity at the fluid-structure interface at each time step. Therefore, at time step n and subiteration step k, we solve for $\mathbf{u}_k^n$ and p_k^n from previous time step results $\mathbf{u}^{n-i}$ and previous subiteration solution $\mathbf{u}_{k-1}^n$ [97]:

$$\frac{\tilde{\mathbf{u}}^n - \sum_{i=1}^{J} \alpha_i \mathbf{u}^{n-i}}{\Delta t} = -\mathbf{N}_{k-1}^n, \tag{4.1.6a}$$

$$\frac{\tilde{\tilde{\mathbf{u}}}^n - \tilde{\mathbf{u}}^n}{\Delta t} = -\frac{\nabla p_k^n}{\rho_f}, \tag{4.1.6b}$$

$$\frac{\beta \mathbf{u}_k^n - \tilde{\tilde{\mathbf{u}}}^n}{\Delta t} = \nu \nabla^2 \mathbf{u}_k^n, \tag{4.1.6c}$$

where

$$\mathbf{N}_{k-1}^n = (\mathbf{u}_{k-1}^n - \mathbf{w}^{n-1}) \cdot \nabla \mathbf{u}_{k-1}^n, \tag{4.1.7}$$

and

$$\frac{\partial p_k^n}{\partial \mathbf{n}_f} = -\rho_f \left(\frac{\partial \mathbf{u}_k^n}{\partial t} + \nu \nabla \times \nabla \times \mathbf{u}_{k-1}^n + \mathbf{N}_{k-1}^n \right) \cdot \mathbf{n}_f, \quad \text{on } \Sigma(t). \tag{4.1.8}$$

Here J denotes the time integration order, and α_i, β are the corresponding coefficients of the $J-$th order backward differentiation formulas [6]. In (4.1.8), $\mathbf{n}_f$ is the normal vector of fluid subdomain pointing outward on the interface $\Sigma(t)$.

Similar to the Navier-Stokes equation, at each time step the mesh velocity is obtained by solving the Laplace equation (4.1.4) with the spectral element method. The current configuration $\mathbf{x}(t)$ is updated from:

$$\frac{\mathbf{x}^n - \sum_{i=1}^{J} \hat{\alpha}_i \mathbf{x}^{n-i}}{\Delta t} = \sum_{i=1}^{J} \hat{\hat{\alpha}}_i \mathbf{w}^{n-i}. \tag{4.1.9}$$

Here $\hat{\alpha}_i$ and $\hat{\hat{\alpha}}_i$ are the coefficients for the corresponding time integration schemes, as in [73]. For more details about the fluid solver, we refer the interested readers to [4].

Structure model

For the structure subdomain we follow the Lagrangian approach, so all physical variables are described in the initial configuration $\mathbf{X}$. A linear elastic model and infinitesimal deformations are mainly considered in this chapter, noting that a hyperelastic model with finite deformations [121] can readily be substituted in. The equation describing the deformation can be expressed as follows:

$$\rho_s \frac{\partial^2 \boldsymbol{\eta}}{\partial t^2} - \mathrm{div}(\mathbf{S}) = \rho_s \mathbf{f}, \quad \text{in } \Omega_s, \tag{4.1.10}$$

with the *Neumann* boundary condition at the interface

$$\mathbf{S}\mathbf{n}_s = -[-p\mathbf{I} + \rho_f \nu(\nabla \mathbf{u} + (\nabla \mathbf{u})^T)]\mathbf{n}_f, \quad \text{on } \Sigma(t), \tag{4.1.11}$$

and the proper initial deformation

$$\boldsymbol{\eta}(\mathbf{x}, t = 0) = \boldsymbol{\eta}_0(\mathbf{x}), \quad \text{in } \Omega_s. \tag{4.1.12}$$

In the above equations, $\mathbf{S}$, $\mathbf{f}$ and ρ_s are the second Piola-Kirchhoff stress tensor for the specific material, the body load on the structure, and the structure density, respectively. On the interface $\Sigma(t)$, $\mathbf{n}_s$ stands for the normal vector pointing outward from the structure subdomain. Considering the geometrically linear elastodynamics, the second Piola-Kirchhoff stress tensor is given by

$$\mathbf{S} = \frac{\zeta E}{2(1+\zeta)(1-2\zeta)} \left[\mathrm{tr} \left(\frac{\partial \boldsymbol{\eta}}{\partial \mathbf{x}} + \frac{\partial \boldsymbol{\eta}}{\partial \mathbf{x}}^T \right) \right] + \frac{E}{2(1+\zeta)} \left(\frac{\partial \boldsymbol{\eta}}{\partial \mathbf{x}} + \frac{\partial \boldsymbol{\eta}}{\partial \mathbf{x}}^T \right), \tag{4.1.13}$$

where E and ζ are the Young's modulus and the Poisson ratio of the material, respectively. On the right hand side of (4.1.11), we note that$-p\mathbf{I} + \rho_f \nu[\nabla \mathbf{u} + (\nabla \mathbf{u})^T]$ represents the hydrodynamic stresses at the interface from the flow. Therefore, while the transmission condition (4.1.3) enforces the continuity of velocities, the Neumann boundary condition in (4.1.11) enforces the continuity of

the normal stresses at the interface.

The structure problem is solved with a parallel spectral element method code, StressNEKTAR [27]. Spatially, the variables in StressNEKTAR are discretized in a similar way as in NEKTAR: a continuous Galerkin formulation is employed, with Jacobi polynomials as trial and test functions. To discretize in time, two types of methods are implemented in StressNEKTAR: the Newmark scheme and a three-step backward differentiation formula (BDF) [77]. They can be defined by different expressions for the displacement and velocity at the next time step. Let n denote the index of the time step, and k the index of subiteration step; from (4.1.10) and (4.1.11) we have

$$\rho_s \frac{\partial^2 \boldsymbol{\eta}_k^n}{\partial t^2} - \mathrm{div}(\mathbf{S}(\boldsymbol{\eta}_k^n)) = \rho_s \mathbf{f}_k^n, \tag{4.1.14}$$

and

$$\mathbf{S}(\boldsymbol{\eta}_k^n)\mathbf{n}_s = -[-p_{k-1}^n \mathbf{I} + \rho_f \nu(\nabla \mathbf{u}_{k-1}^n + (\nabla \mathbf{u}_{k-1}^n)^T)](\mathbf{n}_f)^n, \ \text{ on } \Sigma(t). \tag{4.1.15}$$

In the *Newmark scheme*, based on the current displacement $\boldsymbol{\eta}_k^n$, previous time step displacement $\boldsymbol{\eta}^{n-1}$, velocity $\dot{\boldsymbol{\eta}}^{n-1}$ and acceleration $\ddot{\boldsymbol{\eta}}^{n-1}$, we can approximate the acceleration and velocity at the n-th step as:

$$\dot{\boldsymbol{\eta}}_k^n = \dot{\boldsymbol{\eta}}^{n-1} + \Delta t[(1-\theta_1)\ddot{\boldsymbol{\eta}}^{n-1} + \theta_1 \ddot{\boldsymbol{\eta}}_k^n], \tag{4.1.16a}$$

$$\ddot{\boldsymbol{\eta}}_k^n = \frac{1}{\Delta t^2 \theta_2}\left(\boldsymbol{\eta}_k^n - \boldsymbol{\eta}^{n-1} - \Delta t \dot{\boldsymbol{\eta}}^{n-1} - \frac{\Delta t^2}{2}(1-2\theta_2)\ddot{\boldsymbol{\eta}}^{n-1}\right), \tag{4.1.16b}$$

where we have used " $\cdot$ " to denote the temporal derivatives. Depending on the requirements of accuracy and stability, different values can be set to the parameters (θ_1, θ_2). In the following, we will use the parameters $(\theta_1, \theta_2) = (0.5, 0.25)$.

In the *three-step BDF scheme*, the acceleration and velocity approximations are also expressed based on the current information $(\boldsymbol{\eta}_k^n, \dot{\boldsymbol{\eta}}_k^n)$ and previous time steps results $(\boldsymbol{\eta}^{n-i}, \dot{\boldsymbol{\eta}}^{n-i})$ as:

$$\dot{\boldsymbol{\eta}}_k^n = A_1 \boldsymbol{\eta}_k^n + B_1 \boldsymbol{\eta}^{n-1} + C_1 \boldsymbol{\eta}^{n-2} + D_1 \boldsymbol{\eta}^{n-3}, \tag{4.1.17a}$$

$$\ddot{\boldsymbol{\eta}}_k^n = A_2 \dot{\boldsymbol{\eta}}_k^n + B_2 \dot{\boldsymbol{\eta}}^{n-1} + C_2 \dot{\boldsymbol{\eta}}^{n-2} + D_2 \dot{\boldsymbol{\eta}}^{n-3}. \tag{4.1.17b}$$

Here A_i, B_i, C_i and D_i $(i = 1, 2)$ are related following the rule

$$A_1 = \frac{\theta_1}{\Delta t},\ B_1 = \frac{2.5 - 3\theta_1}{\Delta t},\ C_1 = \frac{3\theta_1 - 4}{\Delta t},\ D_1 = \frac{1.5 - \theta_1}{\Delta t}, \tag{4.1.18a}$$

$$A_2 = \frac{\theta_2}{\Delta t},\ B_2 = \frac{2.5 - 3\theta_2}{\Delta t},\ C_2 = \frac{3\theta_2 - 4}{\Delta t},\ D_2 = \frac{1.5 - \theta_2}{\Delta t}, \tag{4.1.18b}$$

and (θ_1, θ_2) are also decided based on considerations of stability and dissipation. To be specific, we will use $(\theta_1, \theta_2) = (5/3, 5/3)$ in this chapter because of its enhanced stability [77]. This pair of parameters corresponds to a three-step second-order scheme.

In some of our tests, we employ the Rayleigh damping to simulate the structural damping in the FSI problems. With damping parameters (ξ_1, ξ_2), our linear elastic model (4.1.10) is changed to

$$\rho_s \frac{\partial^2 \boldsymbol{\eta}}{\partial t^2} + \xi_1 \rho_s \frac{\partial \boldsymbol{\eta}}{\partial t} - \mathrm{div}(\mathbf{S}) - \xi_2 \mathrm{div}(\mathcal{S}(\frac{\partial \boldsymbol{\eta}}{\partial t})) = \rho_s \mathbf{f}, \quad \text{in } \Omega_s, \tag{4.1.19}$$

where the map $\mathcal{S} : \mathbb{R}^3 \mapsto \mathbb{R}^3$ is defined as

$$\mathcal{S}(\boldsymbol{c}) = \frac{\zeta E}{2(1+\zeta)(1-2\zeta)} \left(\mathrm{tr} \left(\frac{\partial \boldsymbol{c}}{\partial \mathbf{x}} + \frac{\partial \boldsymbol{c}}{\partial \mathbf{x}}^T \right) \right) + \frac{E}{2(1+\zeta)} \left(\frac{\partial \boldsymbol{c}}{\partial \mathbf{x}} + \frac{\partial \boldsymbol{c}}{\partial \mathbf{x}}^T \right). \tag{4.1.20}$$

Correspondingly, we can write the semi-discrete equation (4.1.14) with structure damping as

$$\rho_s \frac{\partial^2 \boldsymbol{\eta}_k^n}{\partial t^2} + \xi_1 \rho_s \frac{\partial \boldsymbol{\eta}_k^n}{\partial t} - \mathrm{div}(\mathbf{S}(\boldsymbol{\eta}_k^n)) - \xi_2 \mathrm{div}(\mathcal{S}(\frac{\partial \boldsymbol{\eta}_k^n}{\partial t})) = \rho_s \mathbf{f}_k^n, \tag{4.1.21}$$

where the acceleration and velocity can be approximated using either the Newmark (4.1.16) or the three-step BDF scheme (4.1.17), as presented before.

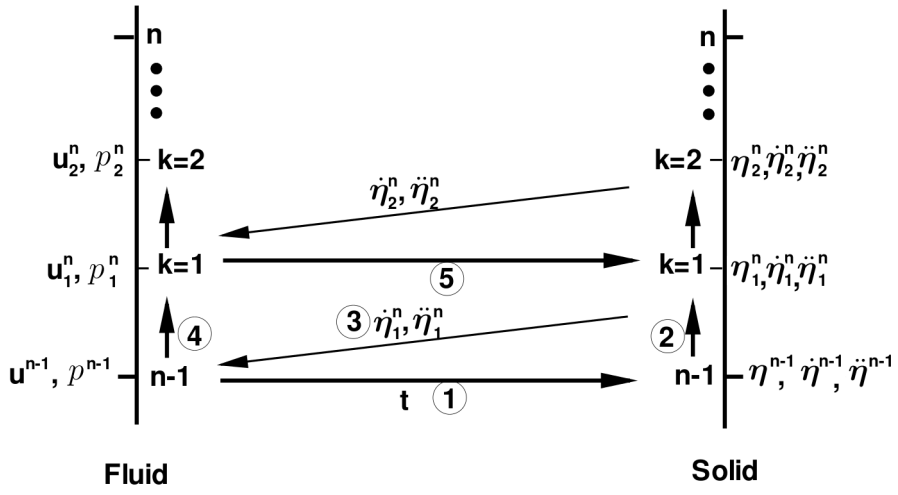

Figure 4.2: FSI coupling procedure at time step n and subiteration step k. Here $t = (-p\mathbf{I} + \rho_f \nu(\nabla \mathbf{u} + (\nabla \mathbf{u})^T))\mathbf{n}_f$ stands for the normal hydrodynamic stress at the interface, and circled numbers indicate the order of execution.

Partitioned algorithm

To strongly impose the continuity of the interface, at each time step we perform subiterations for the FSI system until a convergence is obtained. In each subiteration step, the fluid and structure solvers work separately, then interact by exchanging suitable transmission conditions at the interface $\Sigma(t)$, as sketched in Figure 4.2. Here the Aitken relaxation, see Appendix A.4, is employed in both the structure and fluid solvers, to accelerate the convergence. To be specific, at the n-th time step, we solve the FSI system following the fixed point algorithm:

1. Set

$$\text{(Solid) } \boldsymbol{\eta}_0^n = \boldsymbol{\eta}^{n-1},\ \dot{\boldsymbol{\eta}}_0^n = \dot{\boldsymbol{\eta}}^{n-1},\ \ddot{\boldsymbol{\eta}}_0^n = \ddot{\boldsymbol{\eta}}^{n-1}, \tag{4.1.22a}$$

$$\text{(Fluid) } \mathbf{u}_0^n = \mathbf{u}^{n-1},\ p_0^n = p^{n-1}. \tag{4.1.22b}$$

2. **for** $k = 1 : k_{max}$, **do**

   (a) (Solid) Solve the elastodynamics equation (4.1.14) with external traction force

   $$-[-p_{k-1}^n \mathbf{I} + \rho_f \nu(\nabla \tilde{\mathbf{u}}_{k-1}^n + (\nabla \tilde{\mathbf{u}}_{k-1}^n)^T)](\mathbf{n}_f)^n$$

   applied on the interface, and update the displacement results $\boldsymbol{\eta}_k^n$.

   (b) (Solid) Perform the Aitken relaxation on $\boldsymbol{\eta}_k^n$, and obtain the relaxed displacement $\tilde{\boldsymbol{\eta}}_k^n$.

   (c) (Solid) From $\tilde{\boldsymbol{\eta}}_k^n$, calculate the velocity and acceleration $\dot{\boldsymbol{\eta}}_k^n$ and $\ddot{\boldsymbol{\eta}}_k^n$ based on the Newmark scheme (4.1.16) or BDF scheme (4.1.17).

   (d) (Solid) Pass the velocity and acceleration at the interface to the fluid solver.

   (e) (Fluid) Update the velocity boundary condition $\mathbf{u}_k^n = \dot{\boldsymbol{\eta}}_k^n$ and the pressure boundary condition $\dfrac{\partial p_k^n}{\partial \mathbf{n}_f} = -\rho_f \left(\ddot{\boldsymbol{\eta}}_k^n + \nu \nabla \times \nabla \times \mathbf{u}_{k-1}^n + \mathbf{N}_{k-1}^n\right) \cdot (\mathbf{n}_f)^n$ at the interface.

   (f) (Fluid) Solve the Navier-Stokes equation (4.1.6), and obtain updated velocity and pressure $(\mathbf{u}_k^n, p_k^n)$.

   (g) (Fluid) Apply the Aitken relaxation on $\mathbf{u}_k^n$ to obtain the relaxed velocity $\tilde{\mathbf{u}}_k^n$.

   (h) (Fluid) Calculate the normal stress $-[-p_k^n \mathbf{I} + \rho_f \nu(\nabla \tilde{\mathbf{u}}_k^n + (\nabla \tilde{\mathbf{u}}_k^n)^T)](\mathbf{n}_f)^n$at the interface

   (i) (Fluid) Pass the normal stress at the interface to the structure solver.

   (j) (Solid and Fluid) Check convergence on both solvers. If

   $$||\tilde{\boldsymbol{\eta}}_k^n - \tilde{\boldsymbol{\eta}}_{k-1}^n||,\ ||\tilde{\mathbf{u}}_k^n - \tilde{\mathbf{u}}_{k-1}^n||,\ ||p_k^n - p_{k-1}^n|| < \epsilon, \tag{4.1.23}$$

set $k = k_{max}$ and update the results as

$$\text{(Solid) } \boldsymbol{\eta}^n = \tilde{\boldsymbol{\eta}}_k^n,\ \dot{\boldsymbol{\eta}}^n = \dot{\boldsymbol{\eta}}_k^n,\ \ddot{\boldsymbol{\eta}}^n = \ddot{\boldsymbol{\eta}}_k^n, \tag{4.1.24a}$$

$$\text{(Fluid) } \mathbf{u}^n = \tilde{\mathbf{u}}_k^n,\ p^n = p_k^n. \tag{4.1.24b}$$

Else, continue to the $(k+1)$-th subiteration.

3. (Mesh) Update the mesh velocity boundary condition at the interface with $\mathbf{w}^n = \dot{\boldsymbol{\eta}}^n$.
4. (Mesh) Get the mesh velocity $\mathbf{w}^n$ by solving (4.1.4).
5. (Mesh) Update the mesh positions for the fluid subdomain using the numerical integration as in (4.1.9).
6. Go to time step $n+1$.

4.1.3 Fictitious methods and analysis for optimal coefficients

It was shown in [83] that in the presence of large added-mass, the coupling procedure introduced in Figure 4.2 exhibits very slow convergence, or sometimes even no convergence at all. To overcome this problem, fictitious mass and damping methods were introduced in the structure solver [4], as an effective way of stabilization and convergence acceleration. A brief review of these methods will be given in this section, and the idea will be extended to the fluid solver, to develop *the fictitious pressure* method. Moreover, a convergence analysis will be provided for all cases for simplified problems, which will provide us with some guidance in choosing the optimal parameters in the applications.

Added mass effect

Before discussing the fictitious methods, we would like to simplify the FSI problem in order to motivate our approach. A half plane domain $\Omega = \{\mathbf{x} = (x, y) \in \mathbb{R}^2 : x \leq 0\}$ is considered, with the fluid subdomain Ω_f as

$$\Omega_f = \{\mathbf{x} = (x, y) \in \mathbb{R}^2 : x < 0\}, \tag{4.1.25}$$

and the FSI interface being the line

$$\Sigma = \{(x, y) \in \mathbb{R}^2 : x = 0\}. \tag{4.1.26}$$

In this simplified model, the structure subdomain Ω_s coincides with the interface Σ, and the deformation of the structure is assumed to be very small, therefore the fluid domain can be considered

fixed. Here we will use a linear incompressible inviscid model for the fluid, and a generalized string model as described in [137] for the structure:

$$\rho_f \frac{\partial \mathbf{u}}{\partial t} + \nabla p = 0, \text{ in } \Omega_f, \tag{4.1.27a}$$

$$\nabla \cdot \mathbf{u} = 0, \text{ in } \Omega_f, \tag{4.1.27b}$$

$$\mathbf{u} \cdot \mathbf{n} = \frac{\partial \eta}{\partial t}, \text{ on } \Sigma, \tag{4.1.27c}$$

$$p = \rho_s H_s \frac{\partial^2 \eta}{\partial t^2} + G_1 H_s \eta - G_2 H_s \frac{\partial^2 \eta}{\partial y^2}, \text{ on } \Sigma. \tag{4.1.27d}$$

Here H_s is the thickness of the structure, and $G_2 = \frac{KE}{1+\zeta}$ with K being the Timoshenko correction factor. The reaction term G_1 is introduced to take into account transverse membrane effects. For an arterial vessel with radius R_0, this term can be approximated as $G_1 \approx \frac{E}{(1-\zeta^2)R^2}$ under the assumption of linear elastic behavior, as illustrated in [137]. The displacement η in this problem lies in the x direction, which is also the direction normal to the interface. Moreover, from the left hand side of (4.1.27d) we can see that the continuity of normal stresses between the fluid and solid subdomains is naturally embedded in governing equation of the structure model.

Similarly as in [83], the fluid problem in system (4.1.27) could be reformulated as:

$$\begin{aligned} -\Delta p &= 0, \text{ in } \Omega_f, \\ \frac{\partial p}{\partial x} &= -\rho_f \frac{\partial^2 \eta}{\partial t^2}, \text{ on } \Sigma, \\ p = \overline{p}(t) \text{ or } \frac{\partial p}{\partial \mathbf{n}} &= 0, \text{ on } \partial\Omega_f \setminus \Sigma. \end{aligned} \tag{4.1.28}$$

and the value of the pressure at the interface can be decomposed into two parts:

$$p = -\rho_f \mathcal{M}(\frac{\partial^2 \eta}{\partial t^2}) + p_0, \tag{4.1.29}$$

where p_0 takes into account non-homogeneous boundary conditions on $\partial\Omega_f \setminus \Sigma$, and the map $\mathcal{M} : H^{-1/2}(\Sigma) \mapsto H^{1/2}(\Sigma)$ stands for the added-mass operator. This map is defined as: given $\omega \in H^{-1/2}(\Sigma)$, find $q(\omega) \in H^1(\Omega_f)$ such that

$$\begin{aligned} -\Delta q(\omega) &= 0, \text{ in } \Omega_f, \\ \frac{\partial q(\omega)}{\partial x} &= \omega, \text{ on } \Sigma, \\ q(\omega) = 0 \text{ or } \frac{\partial q(\omega)}{\partial \mathbf{n}} &= 0, \text{ on } \Omega_f \setminus \Sigma. \end{aligned} \tag{4.1.30}$$

and extract the values of the solution $q(\omega)$ on Σ; here, Δ is the Laplacian operator. From the above we see that the exact pressure condition on the interface involves a nonlocal operator. With the expression (4.1.29) for pressure, the continuity of stresses at the interface (4.1.27d) becomes

$$[\rho_s H_s + \rho_f \mathcal{M}]\frac{\partial^2 \eta}{\partial t^2} + G_1 H_s \eta - G_2 H_s \frac{\partial^2 \eta}{\partial y^2} = p_0. \tag{4.1.31}$$

From the above we can see that if we add a term in the structure momentum equation (4.1.19), which is of the same order as the added-mass operator, the FSI solver will perform more like an exact coupled solver, and hence a better convergence can be achieved. Similarly, by substituting the decomposed pressure into (4.1.27a), one could obtain that

$$\rho_f \frac{\partial \mathbf{u}}{\partial t} + \nabla \left[-\rho_f q \left(\frac{\partial^2 \eta}{\partial t^2} \right) + p_0 \right] = 0, \quad \text{in } \Omega_f. \tag{4.1.32}$$

Therefore, an additional term $f_p \nabla p$, which is of the same order as $\nabla \left(-\rho_f q \left(\frac{\partial^2 \eta}{\partial t^2} \right) \right)$, would also give a partitioned solution, which is closer to the exact coupled solution.

Fictitious mass and damping methods

In the fictitious mass and damping methods [4], the structure momentum equation (4.1.19) is solved with additional acceleration and damping terms. These terms aim to balance the added-mass operator as shown in (4.1.31). Considering the fictitious mass coefficient f_m and damping coefficient f_d, equation (4.1.21) is modified as

$$\begin{aligned} &\rho_s(1+f_m)\frac{\partial^2 \boldsymbol{\eta}_k^n}{\partial t^2} + \rho_s(\xi_1 + f_d)\frac{\partial \boldsymbol{\eta}_k^n}{\partial t} - \mathrm{div}(\mathbf{S}(\boldsymbol{\eta}_k^n)) - \xi_2 \mathrm{div}\left[\mathcal{S}(\frac{\partial \boldsymbol{\eta}_k^n}{\partial t}) \right] \\ &= \rho_s \mathbf{f}_k^n + \rho_s f_m \frac{\partial^2 \boldsymbol{\eta}_{k-1}^n}{\partial t^2} + \rho_s f_d \frac{\partial \boldsymbol{\eta}_{k-1}^n}{\partial t}. \end{aligned} \tag{4.1.33}$$

Here we note that when the subiteration is converged, we have $\boldsymbol{\eta}_k^n \approx \boldsymbol{\eta}_{k-1}^n$ and $\frac{\partial \boldsymbol{\eta}_k^n}{\partial t} \approx \frac{\partial \boldsymbol{\eta}_{k-1}^n}{\partial t}$. Therefore, the scheme with fictitious mass and damping of equation (4.1.33) should converge to the same results as the original scheme of equation (4.1.21) at the end of each time step. Moreover, if we substitute $\rho_s H_s f_m = \rho_f \mathcal{M}$ into (4.1.33), then we recover the right hand side of (4.1.31). So the fictitious mass method can be thought of as mimicking an exact coupled solver, with the optimal value of f_m being a good approximation to $\frac{\rho_f \mathcal{M}}{\rho_s H_s}$.

Fictitious pressure method

Now we will extend the idea of fictitious methods to the fluid solver, on the pressure term in (4.1.1a). By introducing the fictitious pressure coefficient f_p, the splitting scheme for the Navier-Stokes equation (4.1.6) can be written as

$$\frac{\beta \mathbf{u}_k^n - \sum_{i=1}^J \alpha_i \mathbf{u}^{n-i}}{\Delta t} + \mathbf{N}_{k-1}^n - f_p \frac{\nabla p_{k-1}^n}{\rho_f} = -(1+f_p)\frac{\nabla p_k^n}{\rho_f} + \nu \nabla^2 \mathbf{u}_k^n. \tag{4.1.34}$$

Similarly, a splitting scheme can be generated

$$\frac{\tilde{\mathbf{u}}^n - \sum_{i=1}^J \alpha_i \mathbf{u}^{n-i}}{\Delta t} = -\mathbf{N}_{k-1}^n, \tag{4.1.35a}$$

$$\frac{\tilde{\tilde{\mathbf{u}}}^n - \tilde{\mathbf{u}}^n}{\Delta t} - f_p \frac{\nabla p_{k-1}^n}{\rho_f} = -(1+f_p)\frac{\nabla p_k^n}{\rho_f}, \tag{4.1.35b}$$

$$\frac{\beta \mathbf{u}_k^n - \tilde{\tilde{\mathbf{u}}}^n}{\Delta t} = \nu \nabla^2 \mathbf{u}_k^n, \tag{4.1.35c}$$

with the definition of $\mathbf{N}_{k-1}^n$ the same as in (4.1.7). To be consistent with the new scheme, the pressure boundary condition on the interface should be modified as

$$(1+f_p)\frac{\partial p_k^n}{\partial \mathbf{n}_f} = f_p \frac{\partial p_{k-1}^n}{\partial \mathbf{n}_f} - \rho_f \left(\frac{\partial \mathbf{u}_k^n}{\partial t} + \nu \nabla \times \nabla \times \mathbf{u}_{k-1}^n + \mathbf{N}_{k-1}^n \right) \cdot \mathbf{n}_f. \tag{4.1.36}$$

As in the fictitious mass and damping methods, the new scheme (4.1.35) converges to the same values as the original one (4.1.6) at the end of each time step. Therefore, the fictitious pressure method will not change the physical solution of the FSI problem.

Analysis of a simplified problem

Now we will investigate the effects of fictitious methods on the simplified problem as described in (4.1.27). Let n be the time step index, and k the subiteration index, then the corresponding J-th order time splitting scheme for the simplified fluid model reads

$$\frac{\tilde{\mathbf{u}}^n - \sum_{i=1}^J \alpha_i \mathbf{u}^{n-i}}{\Delta t} = 0, \tag{4.1.37a}$$

$$\frac{\beta \mathbf{u}_k^n - \tilde{\mathbf{u}}^n}{\Delta t} = -\frac{\nabla p_k^n}{\rho_f}, \tag{4.1.37b}$$

combined with the Dirichlet velocity and Neumann pressure boundary conditions on the interface

$$u_k^n = \frac{\partial \eta_k^n}{\partial t}, \ \frac{\partial p_k^n}{\partial x} = -\frac{\partial u_k^n}{\partial t}. \tag{4.1.38}$$

Here we denote the velocity components in the x and y directions as u and v, respectively. On the other hand, the three-step BDF scheme is applied to the generalized string model:

$$\begin{aligned} &\rho_s H_s \ddot{\eta}_k^n + G_1 H_s \eta_k^n - G_2 H_s \frac{\partial^2 \eta_k^n}{\partial y^2} = p_{k-1}^n, \\ &\dot{\eta}_k^n = A_1 \eta_k^n + B_1 \eta^{n-1} + C_1 \eta^{n-2} + D_1 \eta^{n-3}, \\ &\ddot{\eta}_k^n = A_2 \dot{\eta}_k^n + B_2 \dot{\eta}^{n-1} + C_2 \dot{\eta}^{n-2} + D_2 \dot{\eta}^{n-3}. \end{aligned} \tag{4.1.39}$$

The entire partitioned algorithm can be rewritten as:

- Structure problem

$$A_1 A_2 \rho_s H_s \eta_k^n + G_1 H_s \eta_k^n - G_2 H_s \frac{\partial^2 \eta_k^n}{\partial y^2} = p_{k-1}^n + F_1, \text{ on } \Sigma, \tag{4.1.40}$$

- Fluid problem

$$\rho_f \frac{\beta \mathbf{u}_k^n}{\Delta t} + \nabla p_k^n + F_2 = 0, \text{ in } \Omega_f, \tag{4.1.41a}$$

$$\nabla \cdot \mathbf{u}_k^n = 0, \text{ in } \Omega_f, \tag{4.1.41b}$$

$$u_k^n = A_1 \eta_k^n + F_3, \text{ on } \Sigma, \tag{4.1.41c}$$

where F_1, F_2, F_3 account for terms at previous time steps. The following analysis will be performed on the n-th step, therefore we will omit the step numbers.

Similar to the analysis in [5], our convergence analysis will be based on the Fourier transform in the y direction, which is also the tangential direction to the fluid structure interface. For any function $c(x, y) \in L^2(\mathbb{R}^2)$, its Fourier coefficient $\hat{c}(x, \gamma)$ is defined as

$$\hat{c}(x, \gamma) = \int_{\mathbb{R}} e^{-i\gamma y} c(x, y) dy, \tag{4.1.42}$$

which corresponds to the frequency γ. To quantify the error for pressure at the k-th subiteration, on the interface we define a reduction factor in the frequency space

$$\rho_k(\gamma) := \frac{|\hat{p}_k(0, \gamma) - \hat{p}(0, \gamma)|}{|\hat{p}_{k-1}(0, \gamma) - \hat{p}(0, \gamma)|}, \tag{4.1.43}$$

where $\hat{p}(x, \gamma)$ is the Fourier coefficient of the exact pressure $p(x, y)$ at the current time, and $\hat{p}_k(x, \gamma)$ is the Fourier coefficient of the numerical approximation for pressure at the k-th subiteration, see equations (A.5.1)-(A.5.3) in Appendix A.5. If $\rho_k(\gamma)$ is less than 1 for all relevant frequencies at

every subiteration step, the algorithm converges. Moreover, the smaller this reduction factor is, the faster the rate of convergence will be.

Reduction factor of the fictitious mass and damping methods

In the fictitious mass and damping methods, the structure solver is modified, with the fluid solver unchanged. Denoting the fictitious mass and damping coefficients (f_m, f_d), the simplified structure model (4.1.40) becomes

$$\begin{aligned}&(1+f_m)A_1A_2\rho_sH_s\eta_k + f_dA_1\rho_sH_s\eta_k + G_1H_s\eta_k - G_2H_s\frac{\partial^2\eta_k}{\partial y^2}\\ &= p_{k-1} + f_mA_1A_2\rho_sH_s\eta_{k-1} + f_dA_1\rho_sH_s\eta_{k-1} + F_1.\end{aligned} \tag{4.1.44}$$

We have derived the following:

Property 4.1.1. With fictitious mass and damping coefficients f_m and f_d, respectively, the reduction factor of frequency γ is independent of the subiteration step and it is given by:

$$\rho^{FM}(\gamma) = \left|\frac{P_k(\gamma)-0}{P_{k-1}(\gamma)-0}\right| = \left|\frac{A_1[\beta\rho_f - \gamma(f_mA_2+f_d)\rho_sH_s\Delta t]}{\gamma\Delta t[(A_2+f_mA_2+f_d)A_1\rho_sH_s + G_1H_s + \gamma^2G_2H_s]}\right|, \tag{4.1.45}$$

where $P_k(\gamma)$ is defined in (A.5.3), β and A_i, $i = 1, 2$ are the coefficients of the J-th splitting scheme for the fluid solver and of the BDF scheme for the structure solver, respectively, and H_s, G_1, G_2 are the thickness and material coefficients of the structure model. The derivation details are provided in Appendix A.5.

To compare with the Dirichlet-Robin method in [5], we apply a first-order scheme for both the fluid and structure subdomains to obtain a reduction factor as

$$\bar{\rho}^{FM}(\gamma) = \left|\frac{\rho_f - \gamma(f_m + f_d\Delta t)\rho_sH_s}{\gamma\Delta t^2((1+f_m+f_d\Delta t)\frac{\rho_sH_s}{\Delta t^2} + G_1H_s + \gamma^2G_2H_s)}\right|. \tag{4.1.46}$$

Next we substitute $f_m + f_d\Delta t = \frac{\alpha_s\Delta t}{\rho_sH_s}$, where α_s is the coefficient for Robin boundary condition on the solid side as defined in [5]. The reduction factor for the fictitious mass and damping methods becomes

$$\bar{\rho}^{FM}(\gamma) = \left|\frac{\rho_f - \gamma\alpha_s\Delta t}{\gamma\Delta t^2(\frac{\rho_sH_s}{\Delta t^2} + \frac{\alpha_s}{\Delta t} + G_1H_s + \gamma^2G_2H_s)}\right|, \tag{4.1.47}$$

which has the same form as that for the Robin boundary condition on the solid side.

- • *Therefore, by tuning the coefficients properly, the fictitious mass and damping methods have*

the same effect on the reduction factor as the Dirichlet-Robin transmission conditions for this model problem.

Reduction factor of the fictitious pressure method

Now we will report the reduction factor from Fourier analysis for the coupling algorithm with the original structure solver (4.1.40) and the fictitious pressure fluid solver as defined in (4.1.35). Given a fictitious pressure coefficient f_p, the first equation of the fluid solver (4.1.41) can be rearranged as

$$\rho_f \frac{\beta \mathbf{u}_k}{\Delta t} + (1+f_p)\nabla p_k - f_p \nabla p_{k-1} + F_2 = 0, \quad \text{in } \Omega_f. \tag{4.1.48}$$

We have derived the following:

Property 4.1.2. The reduction factor for the fictitious pressure coefficient f_p of frequency γ can be written as

$$\rho^{FP}(\gamma) = \left| \frac{P_k(\gamma) - 0}{P_{k-1}(\gamma) - 0} \right| = \left| \frac{A_1\beta\rho_f - f_p \Delta t \gamma (A_1 A_2 \rho_s H_s + G_1 H_s + \gamma^2 G_2 H_s)}{(1+f_p)\Delta t \gamma (A_1 A_2 \rho_s H_s + G_1 H_s + \gamma^2 G_2 H_s)} \right|, \tag{4.1.49}$$

which is independent of the subiteration number k. Note that $P_k(\gamma)$ is defined similarly as in (A.5.3) in Appendix A.5, β is a parameter in the J-th splitting scheme for the fluid solver as defined in (4.1.6), A_1, A_2 are parameters in the BDF scheme for the structure solver as in (4.1.17), and H_s, G_1, G_2 are the thickness and material coefficients of the structure model. The derivation details are given in Appendix A.6.

For the cases with small Young's modulus E or small time step size, we have $G_1\Delta t \ll 1$ and $G_2\Delta t \ll 1$. It was reported in [83] that such cases suffer from severe added-mass effect, and therefore very slow convergence. For these cases, the reduction factor for the fictitious pressure method (4.1.49) can be approximated as

$$\rho^{FP}(\gamma) = \left| \frac{\beta\rho_f - f_p A_2 \Delta t \gamma \rho_s H_s}{(1+f_p) A_2 \Delta t \gamma \rho_s H_s} \right|, \tag{4.1.50}$$

which has the same expression as the reduction factor for the fictitious mass and damping methods (4.1.45)

$$\rho^{FM}(\gamma) = \left| \frac{\beta\rho_f - (f_m A_2 + f_d)\Delta t \gamma \rho_s H_s}{(A_2 + f_m A_2 + f_d)\Delta t \gamma \rho_s H_s} \right|, \tag{4.1.51}$$

by taking $f_p = f_m + f_d/A_2$. Therefore, when $G_1\Delta t \ll 1$ and $G_2\Delta t \ll 1$, the fictitious pressure method also has an equivalent reduction factor as the Dirichlet-Robin transmission condition given in [5], and its optimal coefficient should be comparable with that from the fictitious mass method.

On the other hand, when the material has a large modulus or we use a large time step size, i.e., $G_1\Delta t \gg 1$ and $G_2\Delta t \gg 1$, the reduction factor for the fictitious pressure method reads

$$\rho^{FP}(\gamma) = \left|\frac{f_p}{1+f_p}\right|. \tag{4.1.52}$$

Therefore a small f_p would be preferred for a faster convergence in these cases.

Remark: When the Young's modulus $E \to \infty$, we have $G_1, G_2 \to \infty$. The reduction factor (4.1.49) with $f_m = f_p = 0$ can be expressed as

$$\rho(\gamma) = \left|\frac{P_k(\gamma) - 0}{P_{k-1}(\gamma) - 0}\right| = \left|\frac{A_1\beta\rho_f}{\Delta t\gamma(A_1A_2\rho_s H_s + G_1H_s + \gamma^2 G_2 H_s)}\right| \to 0,$$

which indicates that the original partitioned procedure will be very stable and hence no fictitious method is needed.

Tube domain

Here we consider a simple model for an artery modeled as a straight tube. The problem is solved in a cylinder with radius R and length L, as shown in Figure 4.3, in which a Neumann boundary condition $\frac{\partial \mathbf{u}}{\partial \mathbf{n}} = 0$ is set on BC_1 and BC_2, and Dirichlet boundary condition $p = \bar{p}(t)$ for pressure. In the cylindrical coordinate system (r, θ, y), this problem is independent of the angle θ, therefore the fluid model degenerates into $\{(r, y) \in [0, R) \times [0, L]\} \subset \mathbb{R}^2$. Adopting the linear incompressible inviscid model for the fluid and the generalized string model for the structure, the structure subdomain coincides with the interface

$$\Sigma = \{(r, y) | r = R \text{ and } y \in [0, L]\}. \tag{4.1.53}$$

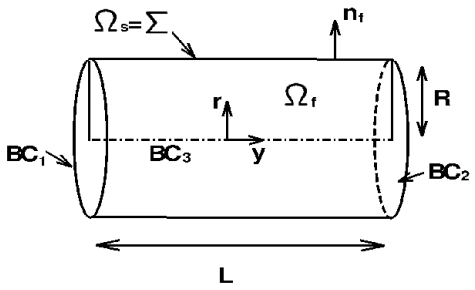

Figure 4.3: Domain for the flow in a tube model.

Similar to the assumptions for the simplified model in (4.1.27), the displacement $\eta \ll 1$, hence the fluid subdomain is considered fixed. The FSI system is governed by the following equations

$$\rho_f \frac{\partial \mathbf{u}}{\partial t} + \nabla p = 0, \text{ in } \Omega_f, \tag{4.1.54a}$$

$$\frac{1}{r}\frac{\partial (r u_r)}{\partial r} + \frac{\partial u_y}{\partial y} = 0, \text{ in } \Omega_f, \tag{4.1.54b}$$

$$\mathbf{u} \cdot \mathbf{n} = \frac{\partial \eta}{\partial t}, \text{ on } \Sigma, \tag{4.1.54c}$$

$$\frac{\partial \mathbf{u}}{\partial \mathbf{n}} = 0, \; p = \bar{p}(t) \text{ on } BC_1 \cup BC_2, \tag{4.1.54d}$$

$$p = \rho_s H_s \frac{\partial^2 \eta}{\partial t^2} + G_1 H_s \eta - G_2 H_s \frac{\partial^2 \eta}{\partial y^2}, \text{ on } \Sigma, \tag{4.1.54e}$$

where the components of $\mathbf{u}$ in r and y directions are denoted as u_r and u_y, respectively. In the structure model, the displacement η lies in the r direction, with H_s, G_1, G_2 as the thickness and the material coefficients. Here the pressure can be decomposed into two parts: one given by the interaction with the structure at the interface, and another one related to the other boundaries $\Omega_f \backslash \Sigma$ only, as in (4.1.29). Our main focus will be on the first part, which is influenced by the added-mass operator $\mathcal{M}$; the boundary conditions $p = \bar{p}(t)$ on $BC_1 \cup BC_2$ are assumed to be vanishing. We will therefore analyze the convergence of pressure to the zero solution. Since $p_k(r, y) = 0$ when $y = 0$ or $y = L$, for every fixed r, the Fourier sine series $\{\sin\left(\frac{\gamma \pi r}{L}\right)\}, \gamma = 1, 2, \cdots \infty$ forms a complete orthogonal basis for $p_k(r, y)$. In the following analysis, the reduction factor will be defined by the Fourier sine coefficients: given a function $c(x, y)$,

$$\hat{c}(x, \gamma) = \frac{2}{L} \int_0^L c(x, y) \sin\left(\frac{\gamma \pi y}{L}\right) dy. \tag{4.1.55}$$

Discretizing (4.1.54) in time with the J-th splitting scheme for fluid and three-step BDF scheme for the structure, similar as our derivations for the previous model as in Appendices A.5 and A.6, a general solution for the pressure can be obtained

$$\hat{p}_k(r, \gamma) = P_k(\gamma) I_0(\frac{\gamma \pi r}{L}) \tag{4.1.56}$$

for a suitable $P_k(\gamma)$. Here I_0 is the modified Bessel function

$$I_0(r) = \sum_{m=0}^{\infty} \frac{1}{m!} \left(\frac{r}{2}\right)^{2m}. \tag{4.1.57}$$

Therefore, the aforementioned reduction factors can be similarly derived for the fictitious mass and damping approach or the fictitious pressure, respectively:

$$\rho^{FM}(\gamma) = \left| \frac{A_1(\beta\rho_f - \mu(\gamma)(f_m A_2 + f_d)\rho_s H_s \Delta t)}{\mu(\gamma)\Delta t((A_2 + f_m A_2 + f_d)A_1\rho_s H_s + G_1 H_s + \gamma^2 G_2 H_s)} \right|, \tag{4.1.58}$$

$$\rho^{FP}(\gamma) = \left| \frac{A_1\beta\rho_f - f_p\Delta t\mu(\gamma)(A_1 A_2\rho_s H_s + G_1 H_s + \gamma^2 G_2 H_s)}{(1+f_p)\Delta t\mu(\gamma)(A_1 A_2\rho_s H_s + G_1 H_s + \gamma^2 G_2 H_s)} \right| \tag{4.1.59}$$

where

$$\mu(\gamma) := \frac{\gamma\pi I_0'(\frac{\gamma\pi R}{L})}{L I_0(\frac{\gamma\pi R}{L})}, \tag{4.1.60}$$

β is the coefficient of the J-th splitting scheme for the fluid solver as defined in (4.1.6), A_1, A_2 are the coefficients of the BDF scheme for the structure solver as in (4.1.17), and H_s, G_1, G_2 are the thickness and material coefficients of the structure model. Comparing with the added-mass operator given in [83], we can see that $1/\mu(\gamma)$ is actually the $\gamma-$th eigenvalue of the added-mass operator $\mathcal{M}$ in this case. We will check the validity of the formulas (4.1.58)-(4.1.59) with corresponding simulations in the next section.

4.1.4 Numerical simulations

In this section, we present a series of numerical tests using the fictitious methods. With these tests, we aim to provide a validation for our theoretical analysis, and to demonstrate the capability of our parallel code in solving realistic physiological problems in computational domains with a large number of elements. Since (4.1.45) suggests that the fictitious mass and fictitious damping methods will have the same effect by taking $f_m = f_d/A_2$, in the following tests we will only employ the fictitious mass method as a representative case. In particular, we consider two types of interesting FSI problems: the first one is related to vortex induced vibrations (VIV) in offshore structures while the second one models compliant brain arteries and blood flow. In both applications the mass ratio is relatively low, and in fact we consider even the case of zero mass in VIV simulations.

Vortex-induced vibrations (VIV)

In the following we consider a classical problem in vortex-induced vibration (VIV), namely the transverse free oscillation of a circular cylinder, as illustrated in the left plot of Figure 4.1. One of the open problems in numerical simulations of VIV is the case of structures with mass ratio approaching zero. This leads to the so-called "for-ever-resonance" effect, irrespective of the characteristic frequency. We will test our FSI code for a wide range of density ratios and with various fictitious methods and corresponding parameters. The simulations are performed in a 2D

domain $[-5, 20] \times [-5, 5]$, with a cylinder of radius 0.5 at the origin. At the inlet $x = -5$, a uniform steady flow with $U_\infty = 1$ is imposed, and at the outlet $x = 20$ a zero Neumann boundary condition is employed. Along the crossflow direction, a periodic boundary condition is applied. In this test, we assume the fluid density to be $\rho_f = 1$ and Reynolds number $Re = 100$ based on the cylinder radius. In these units, the added-mass coefficient is reported to be about 1.5 [138]. In the following simulations, a second-order splitting scheme is applied on the fluid, and Newmark scheme on the structure. To obtain a fair comparison between our cases, we take a uniform time step size $\Delta t = 0.01$. In the following tests, all the simulations are done using spectral elements with polynomial order 4.

Optimal coefficients

As discussed before, the fictitious mass method works the best if it approximates an exact coupled algorithm, which happens when $f_m \rho_s$ is close to the actual added-mass $\rho_a = 1.5$. Therefore, the optimal choice for f_m in our VIV tests should be $f_m = \frac{\rho_a}{\rho_s}$. In order to estimate the optimal value of the fictitious pressure coefficient, we will determine an equivalent f_p for any given f_m. Based on the standard VIV model as shown in [139], we have the modified structure solver with added-mass ρ_a as:

$$(\rho_s + \rho_a)\frac{\partial^2 \boldsymbol{\eta}_k^n}{\partial t^2} + \xi \frac{\partial \boldsymbol{\eta}_k^n}{\partial t} + \omega_n^2 \boldsymbol{\eta}_k^n = \oint (\mathbf{n}_f)^n \cdot [-p_{k-1}^n \mathbf{I} + 2\rho_f \nu (\nabla \mathbf{u}_{k-1}^n + (\nabla \mathbf{u}_{k-1}^n)^T)] ds + \rho_a \frac{\partial^2 \boldsymbol{\eta}_{k-1}^n}{\partial t^2}, \tag{4.1.61}$$

where ξ and ω_n are the structural damping coefficient and the natural frequency of the cylinder, respectively, and the integration is performed around the circumference of the cable. With the assumptions of small damping, small time step and small viscosity, the fictitious mass structure solver (4.1.61) and the standard fluid solver (4.1.1a) can be approximated as

$$(\rho_s + \rho_a)\frac{\partial^2 \boldsymbol{\eta}_k^n}{\partial t^2} = -\oint p_{k-1}^n (\mathbf{n}_f)^n ds + \rho_a \frac{\partial^2 \boldsymbol{\eta}_{k-1}^n}{\partial t^2}, \tag{4.1.62}$$

$$\frac{\partial \mathbf{u}_{k-1}^n}{\partial t} + (\mathbf{u}_{k-1}^n - \mathbf{w}^{n-1}) \cdot \nabla \mathbf{u}_{k-1}^n = -\frac{\nabla p_{k-1}^n}{\rho_f}, \tag{4.1.63}$$

which is equivalent to solving with the fictitious pressure method

$$\frac{\partial \mathbf{u}_{k-1}^n}{\partial t} + (\mathbf{u}_{k-1}^n - \mathbf{w}^{n-1}) \cdot \nabla \mathbf{u}_{k-1}^n = -(\rho_s + \rho_a)\frac{\nabla p_{k-1}^n}{\rho_s \rho_f} + \rho_a \frac{\nabla p_{k-2}^n}{\rho_s \rho_f}, \tag{4.1.64a}$$

$$\rho_s \frac{\partial^2 \eta_k^n}{\partial t^2} = -\oint p_{k-1}^n (\mathbf{n}_f)^n ds, \tag{4.1.64b}$$

which means the optimal value of fictitious pressure in this case is indeed $f_p = \frac{\rho_a}{\rho_s}$.

Effect of fictitious methods on number of subiterations

Next we investigate the numerical performance of our fictitious methods on a canonical VIV case with the mesh as shown in Figure 4.4, and verify our optimal coefficient estimations in the previous section. In the following we first set the density ratio between structure and fluid as $\frac{\rho_s}{\rho_f} = 1$ and the structural damping coefficient $\xi = 0.01$. The natural frequency of cylinder is set to be $\omega_n = 2\pi \times 0.215$, which is close to the vortex shedding frequency of the stationary cylinder, and therefore in the lock-in range. The time trace of the structural displacement is illustrated in Figure 4.5, starting from the convergent flow field generated by a fixed cylinder at $t = 0$. It can be observed that the cylinder is quickly excited by the resonance, then vibrates periodically with a response amplitude as large as 0.52.

For this case, we have studied systematically various coefficients for both fictitious mass and fictitious pressure methods. In the right plot of Figure 4.5 we show a zoom-in of displacement results from various test cases, from which one could see that the amplitude change between different cases is negligible. To demonstrate the effects of fictitious methods on accelerating the convergence, we take the average of subiteration numbers over one vortex shedding cycle (Strouhal period) as a comparison index. In table 4.1 we list these averaged subiteration numbers with different fictitious mass and fictitious pressure coefficients, where the values nearest to the optimal given above are marked by "(opt)". Comparing with the case "F1" where no fictitious method is applied, we can see that both the fictitious mass and fictitious pressure methods help decreasing the subiteration number, and therefore accelerating the convergence. Moreover, the smallest subiteration numbers are obtained when $\rho_s f_m$ or $\rho_s f_p$ is at 1.5, which is the approximate value for added-mass in this case. This observation validates our previous analysis. On the other hand, in the "FA" cases we tested the methods without the Aitken relaxation, from which we could see that the fictitious

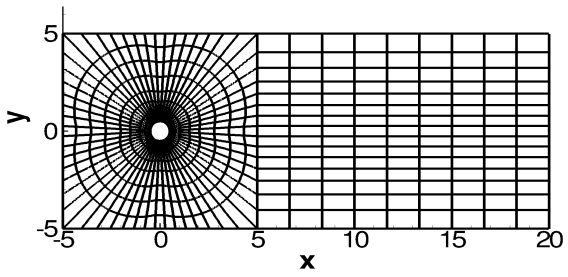

Figure 4.4: Mesh employed in the VIV test; only the spectral elements are shown.

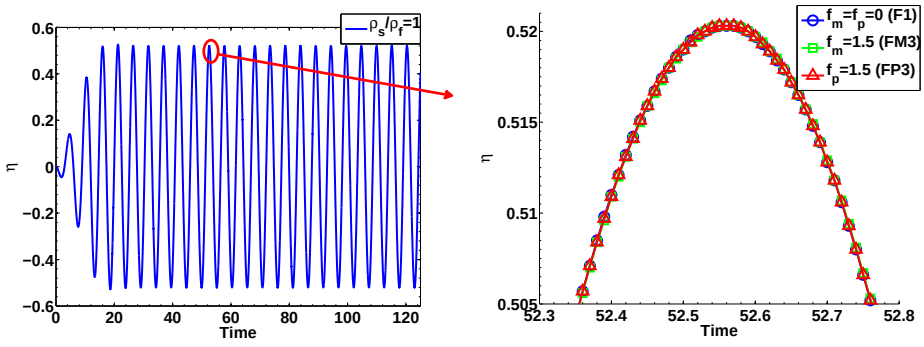

Figure 4.5: Time trace of displacement of the cylinder in the VIV test, when $\frac{\rho_s}{\rho_f} = 1$, $\xi = 0.01$ and $\omega_n = 2\pi \times 0.215$. The right plot is a zoom-in of the left plot, showing results from various fictitious parameters.

	f_m	f_p	Aitken	Avg subiteration
F1	0.0	0.0	Y	35.4
FM1	0.5	0.0	Y	14.1
FM2	1.0	0.0	Y	13.6
FM3	1.5(opt)	0.0	Y	13.1
FM4	2.0	0.0	Y	13.4
FP1	0.0	0.5	Y	15.4
FP2	0.0	1.0	Y	13.4
FP3	0.0	1.5(opt)	Y	13.0
FP4	0.0	2.0	Y	13.1
FA1	0.0	0.0	N	97.2
FA2	1.5	0.0	N	53.5
FA3	0.0	1.5	N	17.8

Table 4.1: Averaged subiteration number for VIV test, when $\frac{\rho_s}{\rho_f} = 1$, $\xi = 0.01$ and $\omega_n = 2\pi \times 0.215$.

methods still help stabilizing the solver in these cases, while the fictitious pressure method performs much better.

Approaching zero mass ratio

Here we present direct numerical simulations of VIV at zero mass ratio for the so-called "for-ever-resonance" case. In particular, it was demonstrated in [134, 140] that large amplitude vibrations appear for structure density less than a critical mass ratio, even when the vortex shedding frequency is much larger than the natural frequency of the cylinder. In this section, we will confirm this phenomenon in our numerical experiments, on a cylinder with vanished natural frequency $\omega_n = 0$ and zero structural damping $\xi = 0$. In order to appreciate the transition of response as the mass ratio changes, we vary the cylinder mass ratio from 0 to 0.75. As $\rho_s \to 0$, the optimal fictitious mass coefficient $f_m \to \infty$, and here we take $f_m \rho_s = 1.5$, which is the value suggested in our analysis. We also performed other simulations for the zero mass ratio case with different values of $f_m \rho_s$ in the

range of $1 - 2.5$ and similar convergence was obtained.

Starting from a fully converged flow field but for a fixed cylinder, the time traces of structural displacements for mass ratio 0, 0.05, 0.1 and 0.15 are plotted in Figure 4.6. Here we mark the starting time as 0, and all the simulations are performed until converged flow fields are reached. It can be seen in Figure 4.6 that from $\rho_s/\rho_f = 0.1$ to $\rho_s/\rho_f = 0.05$, the maximum displacement η_{max} in the converged flow field increases dramatically. When the density ratio is further decreased to 0, η_{max} is as large as 0.42, which is quite close to the maximum displacement of the resonant oscillation shwon in Figure 4.5. To further investigate these changes, we vary the density ratio from 0 to 0.75, and plot the corresponding response amplitudes and frequencies versus ρ_s/ρ_f in Figure 4.7. We can see that when the density ratio ρ_s/ρ_f is larger than 0.1, the response amplitudes are about the same, and all smaller than 0.1, showing the absence of any significant oscillations as can be expected from the classical assumptions [141]. However, if one further decreases this density ratio, the response amplitude curve exhibits a sudden jump between $\rho_s/\rho_f = 0.1$ and $\rho_s/\rho_f = 0.05$. On the other hand, the response frequency curve also has a turning point in that regime, as shown in the left plot of Figure 4.7. Noticing that the natural frequency is 0 in this test, this behavior actually illustrates that 'resonant' large-amplitude oscillations can be observed even when the oscillation frequencies are much larger compared to the natural frequency. Taken together, our findings suggest that for this low Reynolds number there exists a critical mass ratio, which lies between 0.05 and 0.1. This is lower than the experimental value of about 0.5 but for $Re = 4,000 - 22,000$, see [134].

Blood flow in an artery

In this section we investigate the performance of fictitious methods with optimized parameters, considering a straight tube with pulsatile inflow as an idealization of an arterial flow. The fluid domain is as illustrated in Figure 4.3, with $R = 1mm$ and $L = 4mm$. The arterial wall is modeled by a layer of linear elastic material on the tube wall, with thickness $H_s = 0.105mm$. In all tests we take the fluid density as $\rho_f = 1060kg/m^3$, and the structure density $\rho_s = 1.2\rho_f$ since the material density of the arterial wall is known to be close to that of the blood. On the fluid solver, a Womersley velocity profile with 8 Fourier coefficients is imposed at the inlet boundary, with a mean velocity $0.106m/sec$. On the outlet, a constant pressure boundary condition $p = 0MPa$ and a zero Neumann boundary condition for velocity are imposed. For the fluid model, the kinematic viscosity for the fluid is set to $3.8 \times 10^{-6}m^2/s$. In the structural model, the Poisson ratio is set to $\zeta = 0.3$, and the Young's modulus of the vessel walls $E = 0.6MPa$, which is in the physiological range of intracranial vessels of size $2 - 4mm$ [78]. In the following simulations, the first-order splitting

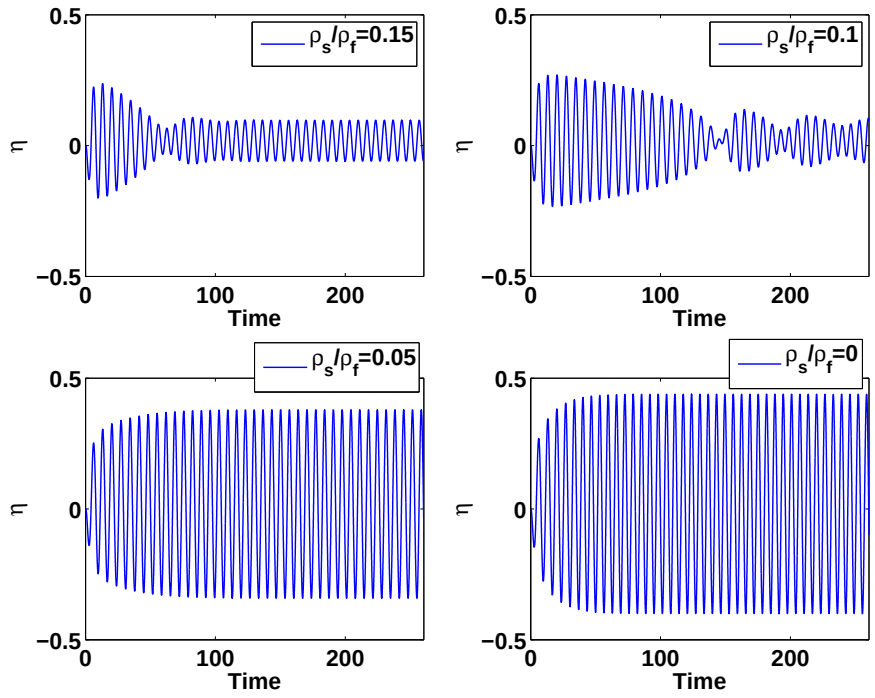

Figure 4.6: Cylinder displacement η for various density ratios. Upper left: $\rho_s/\rho_f = 0.15$; upper right: $\rho_s/\rho_f = 0.1$; lower left: $\rho_s/\rho_f = 0.05$; lower right: $\rho_s/\rho_f = 0$.

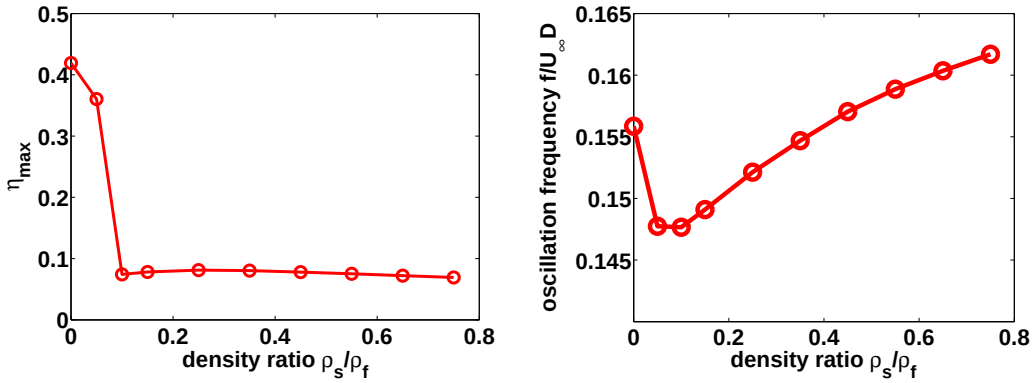

Figure 4.7: Response amplitude and frequency versus density ratio under the non-locking condition. Left: maximum displacements η_{max}; Right: oscillation frequency.

scheme ($\beta = 1.0$) is applied on the fluid, and the BDF scheme on the structure, with time step size $1.9 \times 10^{-5}(sec)$; we chose the first-order scheme and very small time step as this is one of the most difficult cases. The meshes for both subdomains are as shown in Figure 4.8; the inlet is located at

$z = 0mm$, with its center at the origin. To eliminate the influence of transients during start up, all the tests shown here are restarted from the end of the first cardiac cycle.

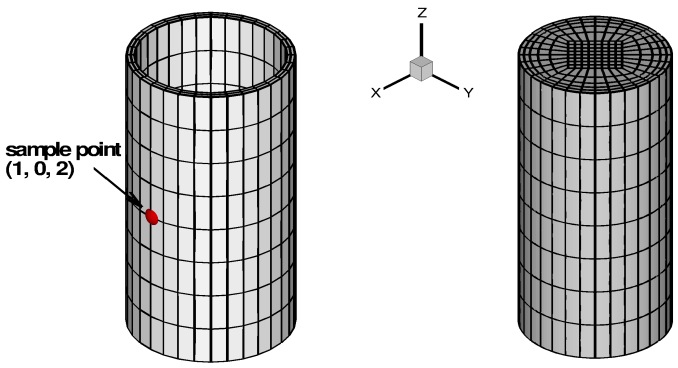

Figure 4.8: Meshes for blood flow in an artery. Left: structure mesh; right: fluid mesh.

With polynomial order 3 for the velocity, pressure and displacement elements, the results for fluid velocity and structural displacement are shown in Figures 4.9 and 4.10. In Figure 4.9, the time traces for inlet flow and the velocity/displacement at a sample point $(1, 0, 2)$ are displayed. In the bottom right plot of Figure 4.9, the red lines mark four time instants in the cardiac cycle, which correspond to $\frac{T}{11}$, $\frac{3T}{11}$, $\frac{6T}{11}$, $\frac{9T}{11}$. In Figure 4.10, we show the distribution of structural displacements at these time instants.

Effect of fictitious methods on number of subiterations

Next we investigate the optimal values of the fictitious coefficients for the cylindrical artery, and test the effect of these coefficients for both fictitious mass and fictitious pressure methods. In the following, all the simulations are performed with spectral elements of polynomial order 3, on the meshes shown in Figure 4.8.

The similarity between the fictitious methods and Dirichlet-Robin transmission conditions suggests that their optimized coefficients should be close, if the same time integration schemes are applied for the fluid and structure solvers. For the simplified model described in (4.1.27), when discretized the fluid and structure solvers in time with first-order accuracy an optimized coefficient $\alpha_s = \frac{2\rho_f}{\Delta t \gamma_{max}}$ was provided in [5] for the Dirichlet-Robin conditions, where γ_{max} is the maximum frequency supported by the numerical grid (which is 8 in our simulations). Therefore, for the cylindrical case with first-order splitting scheme (which gives $\beta = 1$) for the fluid and a three-step BDF formula (which gives $A_1 = A_2 = \frac{5}{3\Delta t}$) for structure, we can derive the optimal fictitious mass

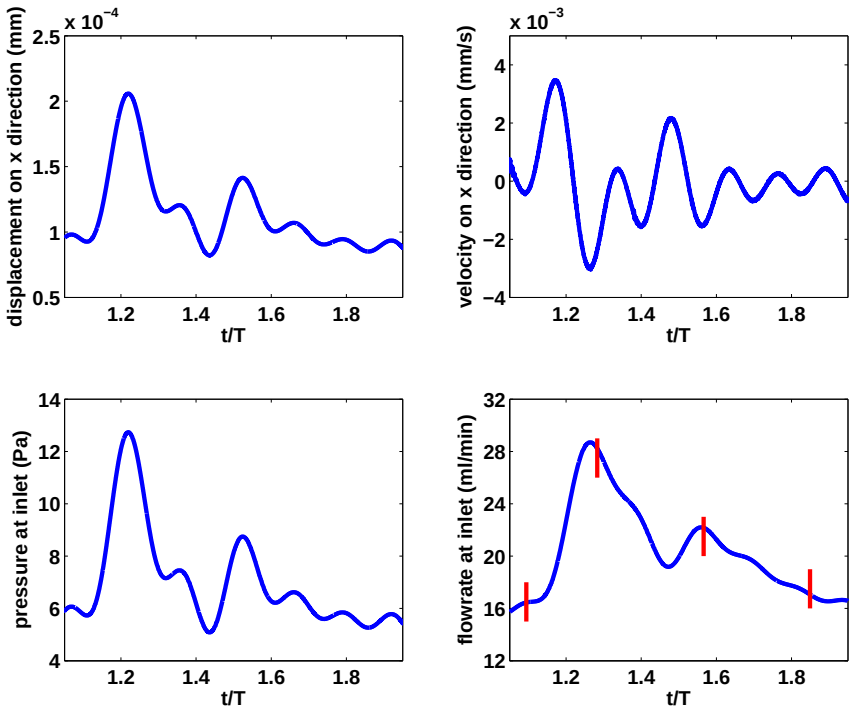

Figure 4.9: Time traces in the tube test. Upper left: radial displacement at point $(1, 0, 2)$; upper right: radial velocity at point $(1, 0, 2)$; bottom left: inlet pressure; bottom right: inlet flow rate.

coefficient for (4.1.58):

$$f_m = \frac{2\beta\rho_f}{\mu(\gamma_{max})A_2\rho_s H_s \Delta t} \approx 1.7 \tag{4.1.65}$$

and the optimal fictitious pressure coefficient for (4.1.59):

$$f_p = \frac{2\beta\rho_f A_1}{\mu(\gamma_{max})\Delta t(A_1A_2\rho_s H_s + G_1 H_s + \gamma_{max}^2 G_2 H_s)} \approx 1.3, \tag{4.1.66}$$

where $\Delta t = 1.89 \times 10^{-5} sec.$ The estimate in (4.1.66) is given based on the approximations that $G_1 \approx \frac{E}{(1-\zeta^2)R^2}$ and $G_2 \approx \frac{KE}{1+\zeta}$, with $K \approx \frac{(1+\zeta)}{2+\zeta}$ for the thin-walled cylinder [142].

To investigate the effect of different coefficients, we test the two fictitious methods with coefficients $f_p, f_m = \{0.44, 0.87, 1.3, 1.7, 2.16, 2.61\}$. The averaged subiteration numbers are listed in Table 4.2. To diminish the influence of transient starting phase, all the subiteration numbers are averaged after 2500 time steps. At the same time, in Figure 4.11, the subiteration numbers are plotted for the choices of $f_p = \{0.87, 1.3, 1.7\}$ and $f_m = \{1.3, 1.7, 2.16\}$. To get a better estimate of the trend, we smooth the curve over 100 steps, i.e., the subiteration number shown for step i is actually

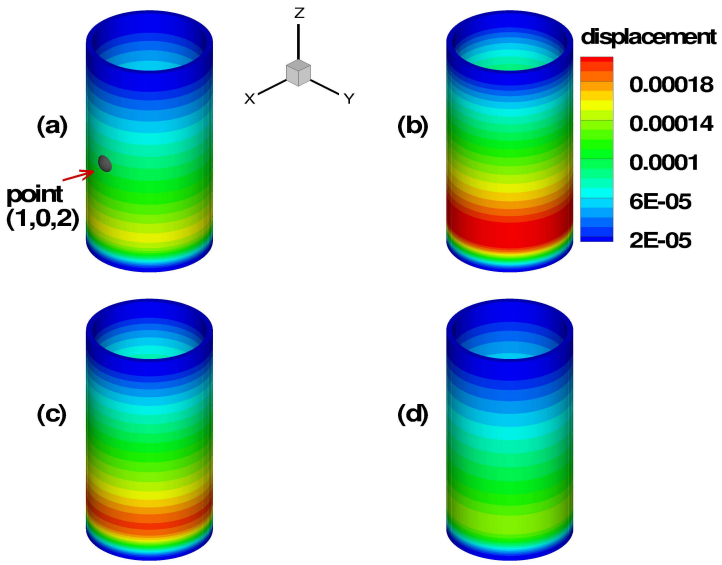

Figure 4.10: Displacements (in millimeters) for the tube test at $t = \frac{T}{11}$ (upper left), $t = \frac{3T}{11}$ (upper right), $t = \frac{6T}{11}$ (lower left), $t = \frac{9T}{11}$ (lower right).

the average for i to the $i + 99$ time steps. We can see that after the starting phase, the fictitious pressure methods generally require less subiteration steps compared to the fictitious mass. From Table 4.2 we can see that among all fictitious mass coefficients, the smallest subiteration number is obtained by $f_m = 2.16$, while the theoretically optimal choice $f_m = 1.7$ gives a subiteration number slightly larger than this. On the other hand, for the fictitious pressure method, $f_p = 0.87$, $f_p = 1.3$ and $f_p = 1.7$ obtained similar subiteration numbers, while $f_p = 1.3$ is the best case over all. This finding is consistent with our estimation in (4.1.66). In summary, in this case the fictitious pressure method gives a smaller subiteration number than the fictitious mass method.

Now we will investigate the effects of different fictitious methods with various Young's modulus and time step sizes. In all cases, the averaged subiteration numbers are obtained with the theoretical optimal coefficients

$$f_m = \frac{2\beta\rho_f}{\mu(\gamma_{max})A_2\rho_s H_s \Delta t}, \text{ or } f_p = \frac{2\beta\rho_f A_1}{\mu(\gamma_{max})\Delta t(A_1A_2\rho_s H_s + G_1 H_s + \gamma_{max}^2 G_2 H_s)}, \tag{4.1.67}$$

with all these approximated coefficients listed in Table 4.3. From this table we can observe that in the cases with large E and/or large Δt, the theoretical optimal values of f_p and f_m are close. On the other hand, when the Young's modulus E and/or Δt are small, the optimal f_p will be much smaller than f_m. This also validates our previous discussion motivated by the equations (4.1.50) and (4.1.52).

	Fic mass	Fic pressure	Avg subiteration
T1	0.0	0.0	no convergence
TM1	0.44	0.0	80.6
TM2	0.87	0.0	76.0
TM3	1.3	0.0	45.4
TM4	1.7(opt)	0.0	28.7
TM5	2.16	0.0	27.6
TM6	2.61	0.0	29.8
TP1	0.0	0.44	22.7
TP2	0.0	0.87	18.7
TP3	0.0	1.3(opt)	17.7
TP4	0.0	1.7	19.8
TP5	0.0	2.16	21.3
TP6	0.0	2.61	60.1

Table 4.2: Averaged subiteration number for the cylindrical artery test: effect of different methods. $E = 0.6$MPa, $\Delta t = 1.89 \times 10^{-5} sec$.

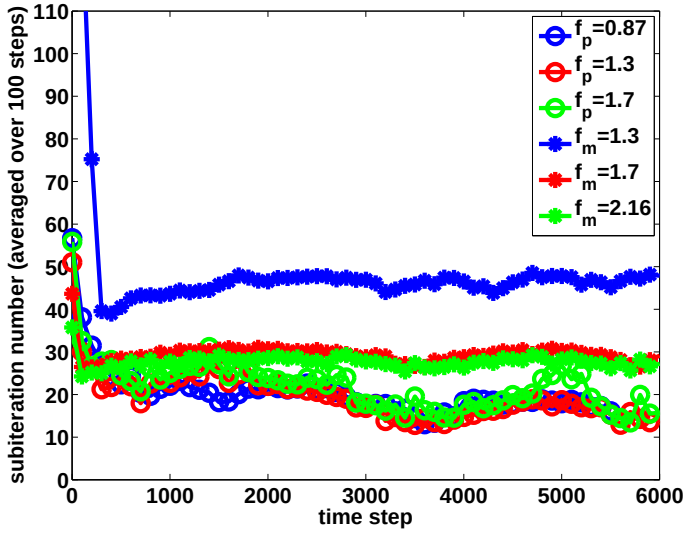

Figure 4.11: Subiteration number (averaged over 100 time steps) for the cylindrical arterial test. $E = 0.6$MPa, $\Delta t = 1.89 \times 10^{-5} sec$.

We first vary the Young's modulus from 0.15MPa to 19.2MPa with fixed time step size $\Delta t = 1.89 \times 10^{-5} sec$, and obtain the averaged subiteration numbers as shown in the left plot of Figure 4.12. It can be observed that when the Young's modulus is as small as 0.15MPa, the fictitious mass method requires 251.2 averaged subiterations while the fictitious pressure method only requires 29.5. When the Young's modulus increases, both methods converge faster and the averaged subiteration number from the fictitious mass method is closer to that from the fictitious pressure method, but the latter still performs better. On the other hand, we fix the Young's modulus as $E = 0.6$MPa and increase the time step sizes from $9.43 \times 10^{-6} sec$ to $1.51 \times 10^{-4} sec$. The averaged subiteration

E (MPa)	Δt (sec)	f_m	f_p
0.15	1.89×10^{-5}	1.7	1.57
0.3	1.89×10^{-5}	1.7	1.49
0.6	1.89×10^{-5}	1.7	1.34
1.2	1.89×10^{-5}	1.7	1.14
2.4	1.89×10^{-5}	1.7	0.87
4.8	1.89×10^{-5}	1.7	0.59
9.6	1.89×10^{-5}	1.7	0.36
19.2	1.89×10^{-5}	1.7	0.2
0.6	9.43×10^{-6}	1.7	1.57
0.6	1.89×10^{-5}	1.7	1.34
0.6	3.77×10^{-5}	1.7	0.87
0.6	7.55×10^{-5}	1.7	0.36
0.6	1.51×10^{-4}	1.7	0.11

Table 4.3: Optimal fictitious coefficients for the cylindrical artery test: various E and Δt.

numbers from the fictitious methods are plotted in the right plot of Figure 4.12, from which we can see that when $\Delta t = 9.43 \times 10^{-6} sec$, the fictitious pressure method performs better: the fictitious mass method takes 270.1 averaged subiterations while the fictitious pressure method only 34.7. However, this difference gets smaller when the time step size increases to $7.55 \times 10^{-5} sec$, where the fictitious mass method requires 20.3 subiterations while the fictitious pressure requires 19.2. If we further increase the time step size to $1.51 \times 10^{-4} sec$, the fictitious mass method preforms better (with 16.0 averaged subiteration number) than the fictitious pressure method (with 18.0 averaged subiteration number). Overall, from these results we can see that the fictitious pressure method is much more efficient when the Young's modulus and/or the time step size are small. When the Young's modulus and/or the time step size get increased, the performance from the fictitious mass method will become comparable with that from the fictitious pressure method, and might be even slightly better.

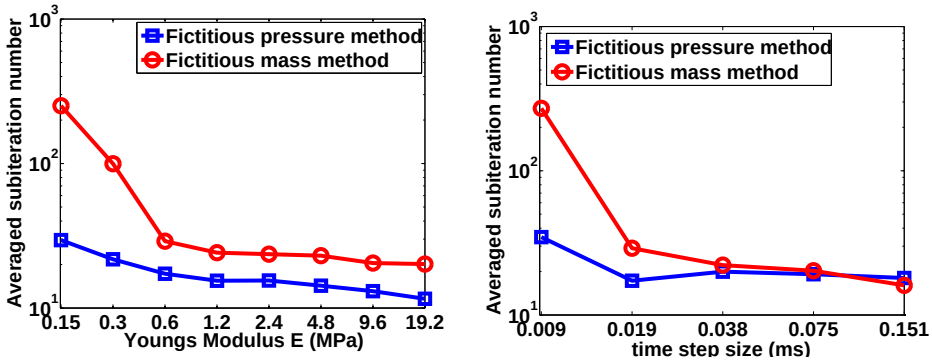

Figure 4.12: Averaged subiteration number for the cylindrical artery test. Left: varying Young's modulus; right: varying time step sizes.

Effect of different polynomial orders

It is known that the high order spectral element method may be more sensitive to time step restrictions and also to temporal instabilities. Here we test the effect of increasing element polynomial orders on fictitious methods. With the same settings as in the previous section Case TP3, polynomial orders 2, 3, 4 and 5 are tested, with the averaged subiteration number listed in Table 4.4, from which we can see that the averaged subiteration number is not changing much with the increase of element polynomial order. Therefore, with the optimal coefficient in the fictitious methods, p refinement will not degrade seriously the subiteration convergence in this case.

	Fic mass	Fic pressure	order	Avg subiteration
TP3	0.0	1.3	2	18.3
TP3	0.0	1.3	3	17.7
TP3	0.0	1.3	4	16.6
TP3	0.0	1.3	5	19.4

Table 4.4: Averaged subiteration number for the cylindrical artery test: effect of increasing polynomial orders.

Blood flow in a patient-specific aneurysm

In this section patient-specific aneurysm models will be tested, with the arterial geometry extracted from Magnetic Resonance Imaging data [4]. This aneurysm is located in the cavernous segment of the right internal carotid artery at the eye level. We will perform our simulations on the two sets of meshes as shown in Figures 2.27-2.28 of section 2.2.4. In order to resolve the boundary layers, in both tests the fluid subdomain has finer elements near the vessel wall, while the solid subdomain is composed of two layers of prismatic elements on the vessel wall. Similar to the cylindrical artery model in the previous section, we imposed a Womersley velocity profile with 8 harmonics at the inlet boundary of the fluid solver, and a zero Neumann boundary condition for velocity at the outlet. The outlet pressure $\bar{p}$ is flow-dependent and is determined from the flow rate $Q(t)$, the resistant R, and the capacitance C [4]

$$\bar{p}(t) + RC\frac{d\bar{p}(t)}{dt} = Q(t)R. \tag{4.1.68}$$

The arterial outlet is assumed to be undeformed when the outlet pressure $\bar{p}(t)$ reaches its lowest point at $t = 0.0571sec$. To generate the initial conditions, the fluid model is simulated separately for three cardiac cycles. We then start the FSI simulations from the resultant flow field (where we set $t = 0$ as the starting time of FSI). The structure is considered undeformed at $t = 0$. To integrate in time, we employed the second-order splitting scheme for the fluid solver, and the BDF formula

Parameter	value
Young's Modulus	$3Mpa$
Poisson ratio	0.45
Blood density	$1.06g/cm^3$
Wall thickness	$0.01cm$
Inlet radius	$0.224cm$
Kinematic viscosity	$3.8 \times 10^{-2} cm^2/s$
Womersley Number	4.2
Average flow rate	$70ml/min$
Time step size	$1.43 \times 10^{-3} s$
Mass damping parameter	$0.35s^{-1}$
Stiffness damping parameter	$2.9 \times 10^{-4} s$
Resistant parameter	$7.844 \times 10^2 dyn \cdot s/cm^5$
Capacitance parameter	$7.285 \times 10^{-5} cm^5/dyn$
Polynomial order	3

Table 4.5: Parameters used in the patient-specific aneurysm simulations.

for the structure side. All the simulations are done with the physical and numerical parameters summarized in Table 4.5. Note that all the physical parameters are consistent with those in [4], except the Young's modulus which we adjusted to be 3MPa according to [84], since the experimental results suggest a range for the moduli of arteries with cerebral aneurysms as $0.9 - 4.0MPa$.

Patient-specific model: test I

To quantify the evolution of the aneurysm deformation, we obtain velocity and displacement time traces for three points on the interface. The locations of these points are shown in Figure 4.13, at a specific time instant on the descending systole peak. In [4], it was reported that different density ratios have small impact on the results, while using a large Young's modulus $E = 33$MPa. To further investigate this with smaller modulus, we performed simulations for both $\rho_s/\rho_f = 1$ and $\rho_s/\rho_f = 2$. The inlet flow profiles and the time traces for all three points are shown in Figure 4.14-4.15, from which we can see that doubling the density ratio does not change the displacement and velocity results appreciably. To investigate the displacement distribution on the whole aneurysm, we take four time instants in a cardiac cycle: $\frac{T}{7}$, $\frac{2T}{7}$, $\frac{3T}{7}$, $\frac{5T}{7}$ as marked by red lines in the bottom right plot of Figure 4.15, and show their corresponding displacement amplitudes in Figure 4.16. We observe that the pressure drop is around $33mmHg$ between the diastole and systolic peak, which is within the range of physiological pressure variation in a healthy subject [143, 100]. The maximum displacement amplitude is about $0.8mm$, which is obtained near point 1. This is also consistent with the physiological range obtained from the measurements, as reported in [85].

Next, we will investigate the effect of various fictitious methods, by comparing the subiteration numbers. Before demonstrating any results, an estimation of the optimal coefficients is needed. Since the artery with aneurysm is a complicated geometry, we cannot obtain any reasonable ana-

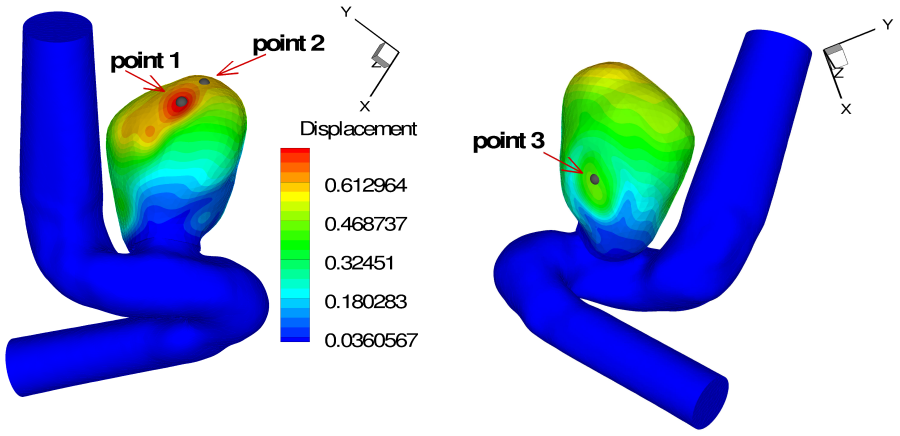

Figure 4.13: Positions of the history points in patient-specific aneurysm test I at $t = 3T/7$.

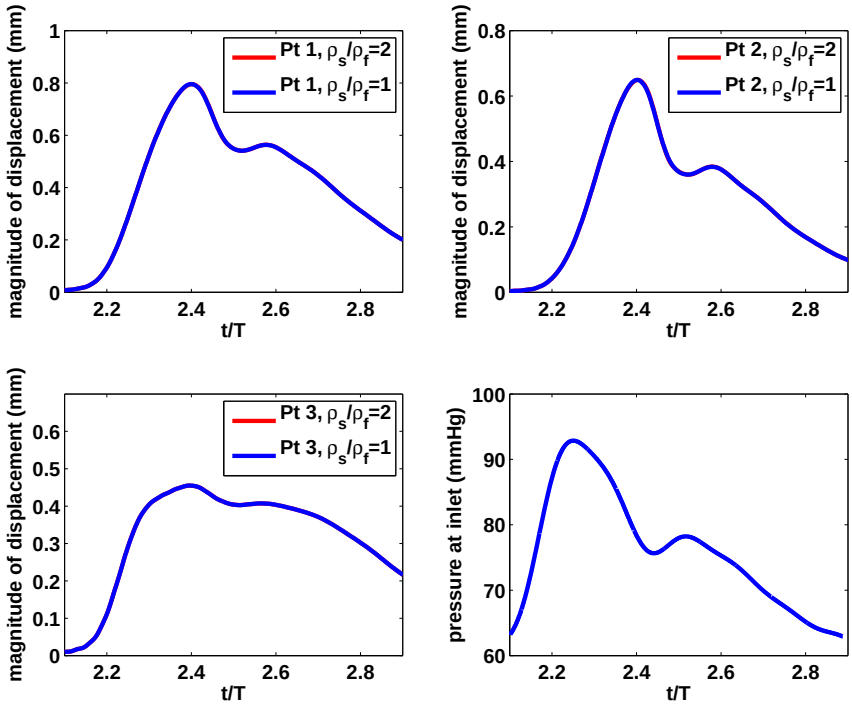

Figure 4.14: Time traces in patient-specific aneurysm test I. Upper left, upper right, bottom left: displacement profiles for corresponding points; bottom right: pressure imposed at the inlet.

lytical value from Fourier analysis. Instead, this value will be obtained from the post-processing of several sample tests. We assume that the added-mass operator for the arterial geometry can also be decomposed to a set of orthogonal basis, and therefore the reduction factors can be expressed

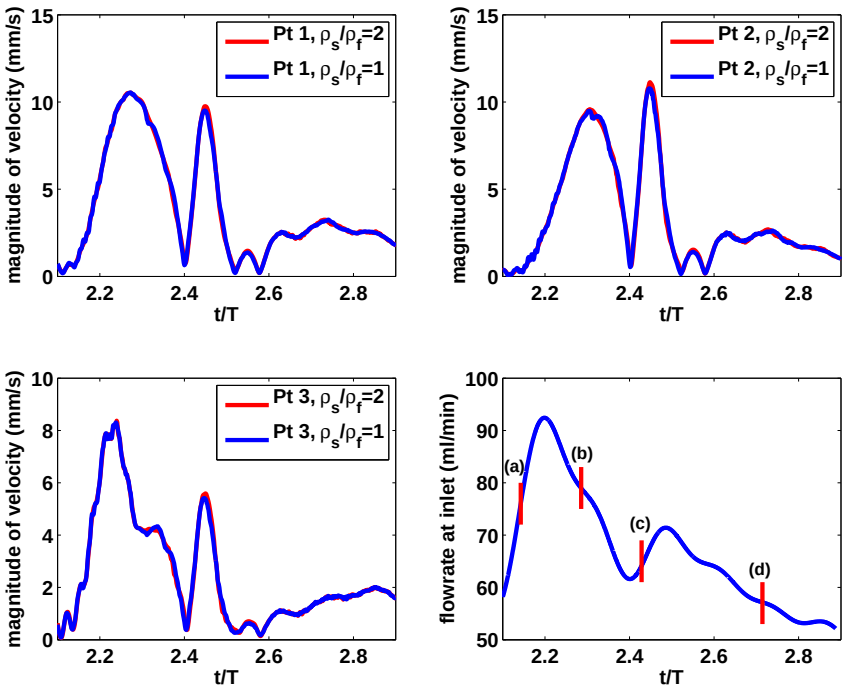

Figure 4.15: Time traces in patient-specific aneurysm test I. Upper left, upper right, bottom left: velocity profiles for corresponding points; bottom right: flow rate imposed at the inlet.

as in (4.1.58) and (4.1.59):

$$\rho^{FM}(\gamma_{cri}) = \left| \frac{A_1(\beta\rho_f - \mu(\gamma_{cri}) f_m A_2 \rho_s H_s \Delta t)}{\mu(\gamma_{cri})\Delta t((1+f_m)A_1 A_2 \rho_s H_s + G_1 H_s + \gamma_{cri}^2 G_2 H_s)} \right|, \tag{4.1.69}$$

$$\rho^{FP}(\gamma_{cri}) = \left| \frac{A_1\beta\rho_f - f_p \Delta t \mu(\gamma_{cri})(A_1 A_2 \rho_s H_s + G_1 H_s + \gamma_{cri}^2 G_2 H_s)}{(1+f_p)\Delta t \mu(\gamma_{cri})(A_1 A_2 \rho_s H_s + G_1 H_s + \gamma_{cri}^2 G_2 H_s)} \right| \tag{4.1.70}$$

with $\mu(\gamma_{cri})$ being the critical eigenvalue of the added-mass operator in this case, β the coefficient of the J-th splitting scheme for the fluid solver, A_1, A_2 the coefficients of the BDF scheme for the structure solver, and H_s, G_1, G_2 the thickness and material coefficients of the structure model. To diminish the effect of added-mass corresponding to the critical eigenvalue, we should have the fictitious mass coefficient $f_m(opt)$ and fictitious pressure coefficient $f_p(opt)$ satisfying

$$\rho^{FM}(\gamma_{cri}) = 0 \text{ and } \rho^{FP}(\gamma_{cri}) = 0.$$

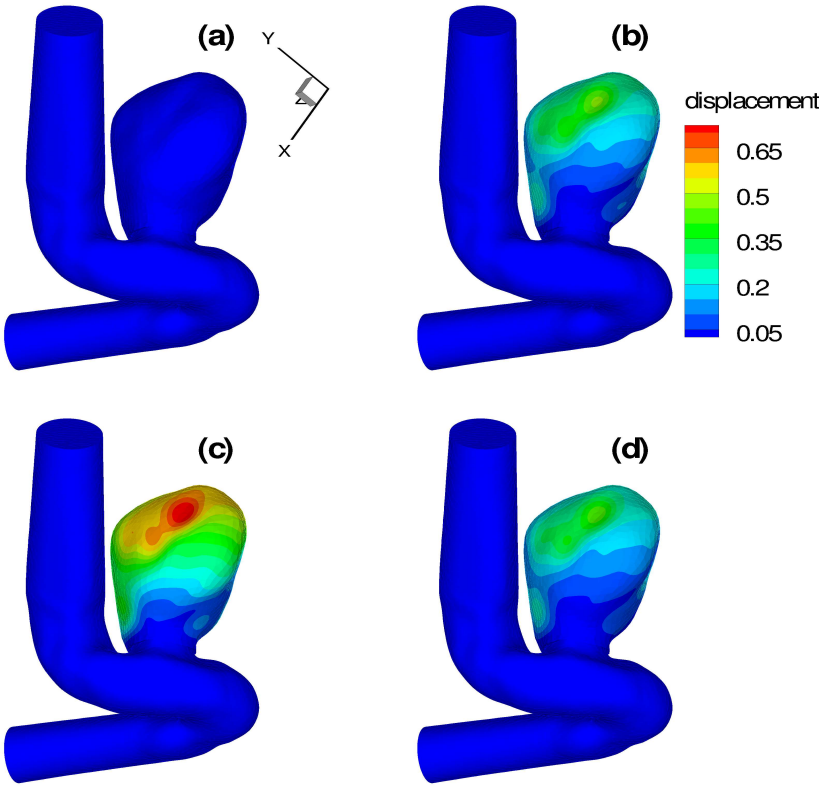

Figure 4.16: Displacements (in mm) for patient-specific aneurysm test I at $\frac{T}{7}$ (upper left), $\frac{2T}{7}$ (upper right), $\frac{3T}{7}$ (bottom left) and $\frac{5T}{7}$ (bottom right).

Therefore, the fictitious coefficients can be optimized as

$$f_m(opt) = \frac{\beta\rho_f}{\mu(\gamma_{cri})\Delta t A_2 \rho_s H_s}, \quad f_p(opt) = \frac{A_1\beta\rho_f}{\Delta t H_s \mu(\gamma_{cri})(A_1A_2\rho_s + G_1 + \gamma_{cri}^2 G_2)}. \tag{4.1.71}$$

Inserting (4.1.71) into the relation between $P_k(\gamma_{cri})$ and $P_{k-1}(\gamma_{cri})$ for the fictitious mass method as expressed in (A.5.11), we have the following:

$$\frac{P_k(\gamma_{cri}) - \hat{P}(\gamma_{cri})}{P_{k-1}(\gamma_{cri}) - \hat{P}(\gamma_{cri})} = \frac{f_m(test) - f_m(opt)}{f_m(test) + f_m(opt)/f_p(opt)}, \tag{4.1.72}$$

where P_k is the coefficient from the k-th subiteration pressure results p_k, as defined in (4.1.56), and $\hat{P}$ is the coefficient from the accurate solution. Similarly, for the fictitious pressure method, we can

derive the relation from (A.6.6):

$$\frac{P_k(\gamma_{cri}) - \hat{P}(\gamma_{cri})}{P_{k-1}(\gamma_{cri}) - \hat{P}(\gamma_{cri})} = \frac{f_p(test) - f_p(opt)}{1 + f_p(test)}. \tag{4.1.73}$$

For any given tolerance ϵ at a fixed time step, the subiteration stops when $||p_k - p_{k-1}||_2 < \epsilon$. Therefore, in the last subiteration step we should have $||p_k - p_{k-1}||_2 = C\epsilon$ where the constant C satisfies $C = O(1)$. We will estimate the subiteration number N from

$$||p_N - p_{N-1}||_2 \approx \epsilon. \tag{4.1.74}$$

With γ_{cri} being the critical eigenvalue, its effect dominates p_k when $k \gg 1$, and hence we can further approximate (4.1.74) as

$$|P_N(\gamma_{cri}) - P_{N-1}(\gamma_{cri})| \approx ||p_N - p_{N-1}||_2 \approx \epsilon.$$

Dividing it by $|P_0(\gamma_{cri}) - \hat{P}(\gamma_{cri})|$ and combining with (4.1.72) and (4.1.73), this yields

$$\begin{aligned}
&\frac{\epsilon}{|P_0(\gamma_{cri}) - \hat{P}(\gamma_{cri})|} \\
\approx &\left| \frac{P_N(\gamma_{cri}) - P_{N-1}(\gamma_{cri})}{P_0(\gamma_{cri}) - \hat{P}(\gamma_{cri})} \right| \\
= &\left| \frac{(P_N(\gamma_{cri}) - \hat{P}(\gamma_{cri})) - (P_{N-1}(\gamma_{cri}) - \hat{P}(\gamma_{cri}))}{P_0(\gamma_{cri}) - \hat{P}(\gamma_{cri})} \right| \\
= &\begin{cases} \left| \left(\dfrac{f_m(test) - f_m(opt)}{f_m(test) + f_m(opt)/f_p(opt)} \right)^N - \left(\dfrac{f_m(test) - f_m(opt)}{f_m(test) + f_m(opt)/f_p(opt)} \right)^{N-1} \right|, & \text{for fic mass;} \\ \left| \left(\dfrac{f_p(test) - f_p(opt)}{1 + f_p(test)} \right)^N - \left(\dfrac{f_p(test) - f_p(opt)}{1 + f_p(test)} \right)^{N-1} \right|, & \text{for fic pressure;} \end{cases} \\
:= &\hat{\rho}(test).
\end{aligned} \tag{4.1.75}$$

Based on these formulas, we can estimate $f_m(opt)$ and $f_p(opt)$ from simulation of any three runs: given the averaged subiteration numbers N_i, $(i = 1, 2, 3)$, we can write the corresponding expression of $\hat{\rho}(test)$ for each case, and estimate the optimal coefficients $f_m(opt)$ and $f_p(opt)$ from

$$|\hat{\rho}(test1)| \approx \frac{\epsilon}{|P_0(\gamma_{cri}) - \hat{P}(\gamma_{cri})|} \approx |\hat{\rho}(test2)| \approx |\hat{\rho}(test3)|\,. \tag{4.1.76}$$

In the following we will confirm the previous estimate. The results will also be compared with

	Fic mass	Fic pressure	Robin coef	Avg subiteration
B1	0.0	0.0	0.0	18.4
BR1	0.0	0.0	350	12.4
BM1	0.5	0.0	0.0	16.2
BM2	2.08	0.0	0.0	12.4
BP1	0.0	0.2	0.0	14.7
BP2	0.0	0.119	0.0	12.3

Table 4.6: Averaged subiteration number in patient-specific aneurysm test I.

those from a Robin based semi-implicit coupling method proposed in [112] (see Appendix E for details of our implementation). Here all the simulations are performed with density ratio 1. Since the Young's modulus E is large here, based on our results in Table 4.3, here we take a smaller value for f_p as the initial guess. Firstly, the averaged subiteration numbers for three sample cases $B1 : f_m = f_p = 0$, $BM1 : f_m = 0.5, f_p = 0$ and $BP1 : f_m = 0, f_p = 0.2$ are computed, as shown in Table 4.6. Substituting these results into equation (4.1.75):

$$\begin{aligned} & \left|(-f_p(opt))^{18.4} - (-f_p(opt))^{17.4}\right| \\ \approx & \left| \left(\frac{0.5 - f_m(opt)}{0.5 + f_m(opt)/f_p(opt)}\right)^{16.2} - \left(\frac{0.5 - f_m(opt)}{0.5 + f_m(opt)/f_p(opt)}\right)^{15.2} \right| \\ \approx & \left| \left(\frac{0.2 - f_p(opt)}{1.2}\right)^{14.7} - \left(\frac{0.2 - f_p(opt)}{1.2}\right)^{13.7} \right| \end{aligned} \tag{4.1.77}$$

the estimates for $f_p(opt)$ and $f_m(opt)$ can be obtained: $f_p(opt) \approx 0.119$, $f_m(opt) \approx 2.08$. Note that the optimal coefficient for the fictitious pressure method is smaller than that for the fictitious mass method, and this is consistent with our previous discussion in the ananlysis for fictitious pressure method. The averaged subiteration numbers obtained from $f_p(opt) = 0.119$ and $f_m(opt) = 2.08$ are also listed in Table 4.6, while the smoothed (averaged over 20 neighboring steps) subiteration numbers are plotted in Figure 4.17. To demonstrate the effects of these coefficients, the subiteration numbers obtained from the Robin-based coupling method with its optimal coefficient 350 is also provided. It can be seen that the fictitious methods with estimated optimal coefficients require smaller subiteration numbers compared to the original sample simulations. Among all, the test with $f_p = 0.119$ has the best performance, which is slightly better than that from $f_m = 2.08$ and the Robin based coupling method. Comparing with the fictitious pressure method with its optimal coefficient, the optimized fictitious mass method has a similar efficiency here. Since the Young's modulus $E = 3MPa$ in these simulations is large, this finding actually confirms our previous discussion.

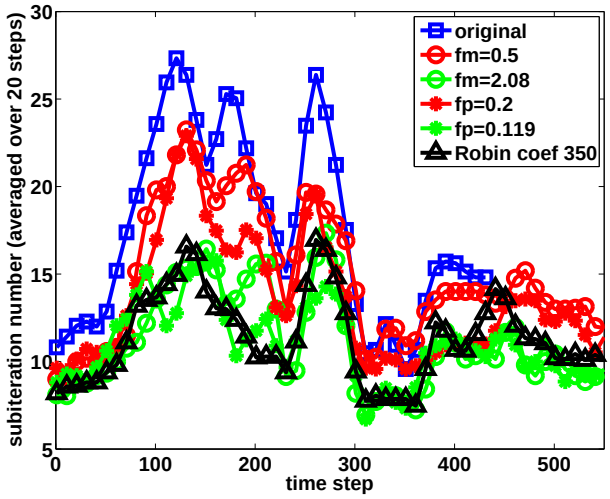

Figure 4.17: Subiteration numbers in patient-specific aneurysm test I.

Patient-specific model: test II

This test is performed with the same settings as in the patient-specific model test I, except with polynomial order 2 elements and on different meshes, as shown in Figure 2.28. Since the arterial wall is also included in the structural subdomain, the added-mass operator becomes more complicated, resulting to slower subiteration convergence rates. To simulate the supports from the surrounding tissues, we put 6 support points on the arterial walls and at the neck of the aneurysm. At $t = 3T/7$ when the deformation reaches the maximum, the displacement amplitudes are shown in the left plot of Figure 4.18. Comparing with the displacement distribution from patient-specific aneurysm test I at the same time instant, we can see that the model including arterial walls generates much larger deformations. All the simulations are done with the density ratio $\rho_s/\rho_f = 2.0$.

The optimal coefficients are approximated from formula (4.1.75). In this case we cannot get convergence from the original solver. Therefore we test with one fictitious pressure coefficient $FP1 : f_p = 1$ and two mass coefficients $FM1 : f_m = 25$, $FM2 : f_m = 50$. The averaged subiteration numbers are as listed in Table 4.7. Based on these results, the procedure in (4.1.77)

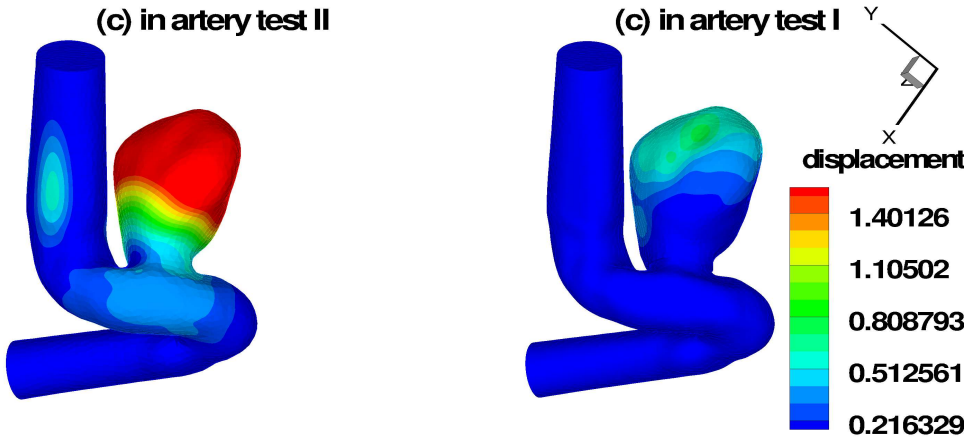

Figure 4.18: Displacements (in mm) for Patient-specific aneurysm tests, at $\frac{3T}{7}$. Left: test II (structure domain covering both arterial walls and the aneurysm); right: test I (structure domain covering the aneurysm sac only).

can be repeated

$$\begin{aligned} & \left| \left(\frac{1 - f_p(opt)}{2} \right)^{85.2} - \left(\frac{1 - f_p(opt)}{2} \right)^{84.2} \right| \\ \approx & \left| \left(\frac{25 - f_m(opt)}{25 + f_m(opt)/f_p(opt)} \right)^{88.0} - \left(\frac{25 - f_m(opt)}{25 + f_m(opt)/f_p(opt)} \right)^{87.0} \right| \\ \approx & \left| \left(\frac{50 - f_m(opt)}{50 + f_m(opt)/f_p(opt)} \right)^{89.6} - \left(\frac{50 - f_m(opt)}{50 + f_m(opt)/f_p(opt)} \right)^{88.6} \right| \end{aligned} \tag{4.1.78}$$

and we obtain the following estimates

$$f_p(opt) \approx 1.365, \quad f_m(opt) \approx 34.93.$$

The results from these two coefficients and from the optimized Robin-based coupling method are also listed in Table 4.7, demonstrating that indeed the optimal fictitious mass coefficient requires the least subiteration numbers among all the simulations. This also validates our findings in Figure 4.12: when the Young's modulus and time step size are large, the efficiencies from the two fictitious methods tend to be similar, and the fictitious mass method may perform slightly better.

	Fic mass	Fic pressure	Robin coef	Avg subiteration
F1	0.0	0.0	0.0	no convergence
FR1	0.0	0.0	2500	128.3
FP1	0.0	1.0	0.0	85.2
FP2	0.0	1.365	0.0	77.2
FM1	25	0.0	0.0	89.0
FM2	50	0.0	0.0	89.6
FM3	34.93	0.0	0.0	75.2

Table 4.7: Averaged subiteration numbers in Patient-specific aneurysm test II.

4.1.5 Summary

In this chapter we generalized the idea of fictitious mass method first presented in [4], by introducing the fictitious pressure method. Both fictitious methods are obtained by changing the coefficients of the pressure or acceleration terms in the fluid or structure equations, respectively, which can be easily extended and implemented in any existing FSI solver. We also presented new theoretical analysis for simple geometries that provided optimal values for the fictitious parameters but also revealed a similarity with the Robin-based approach. We verified this a priori analysis with corresponding numerical tests. Taken together, the analysis and simulations suggest that for small Young's modulus and/or small time step size, the fictitious pressure method is a better choice for a faster convergence. However, when the Young's modulus or time step size increases, the performance of the fictitious pressure and fictitious mass methods is comparable, and the fictitious mass method might be slightly better in cases with large time step. In the analysis of section 4.1.3, the fictitious methods are shown to be equivalent to the Robin boundary condition on the structure side at least for the prototype problem. However, published results [5, 113], suggest that the Robin condition on the fluid side may be even more effective than other interface conditions. In principle, it may be possible to extend the generalized fictitious methods to mimic the Robin-Neumann or Robin-Robin conditions.

4.2 Explicit coupling method

4.2.1 Overview and motivation

As mentioned in chapter 4.1, in hemodynamic problems the fluid and solid densities are close, which causes instability because of the severe added-mass effect. In such situations explicit coupling (where the fluid and structure are only solved once per time step) is known to be insufficient, unless special treatments are introduced in the procedure [122, 123]. An implicit coupling is oftenly required to impose continuity at the interface through additional subiterations between fluid and solid solvers at each time step. Although many recent approaches, including our fictitious method

[81], have been introduced to stabilize and accelerate the convergence of these subiterations, they still consume a huge computational effort. Therefore, many efforts have been put on developping a stable explicit coupling method for fluid-structure interaction (FSI) [122, 144]. In [122], Burman and Fernandez have proposed a stabilized explicit coupling scheme based on the Nitsche's method, by introducing a time penalty term at the fluid-structure interface to control the fluid pressure variations. They have proved that thie new scheme is stable irrespectively of the added-mass effect in the energy norm. However, the penalty term introduces additional errors, and therefore in [144] the authors proposed a penalty-free non-symmetric Nitshe method, where the main source of consistency error was eliminated but a non-symmetric stiffness matrix is evolved in the fluid solver. In both papers the fluid velocity and pressure are solved together, which increases the computational cost of the fluid solver.

In this chapter, we develop a new stabilized explicit coupling partitioned scheme or the fluid-structure interaction problem, to the case where the pressure and velocity are decoupled, i.e. the fluid part is solved with projection methods. Specifically, proper penalty terms are applied on the displacement, pressure and velocity solvers separately, to control the variations at the interface. Using energy stability analysis, it can be shown that the scheme is stable independent of the fluid-structure density ratio. All the implementations are done with the spectral element method as explained in chapter 4.1. Numerical examples are provided on problems with fabricated solutions, to show that although the penalty terms degrade the time accuracy of the scheme to half order, optimal accuracy can be recovered by performing defect-correction subiterations. Moreover, we verified this scheme on vortex-induced vibration problems, and numerically validated that with sufficiently large penalty coefficients, stability is achieved irrespective of the fluid-solid density ratio.

An outline of this chapter is as follows. First we introduce the numerical scheme in section 4.2.2, with energy based stability analysis provided. Then in section 4.2.3 we discuss the effect of the penalty terms might have on the numerical accuracy, and proposed the defect-correction version of the algorithm as a possible compensation. The performances of stabilized explicit algorithm are investigated on the vortex-induced vibration problem in section 4.2.4, to demonstrate that very low density ratio cases can be numerically simulated without suffering from the added-mass effect. We finish in section 4.2.5 with a brief summary.

4.2.2 Formulation and analysis

Similar as the model in chapter 4.1, we consider the domain Ω which is composed of the fluid subdomain $\Omega_f(t)$ and the structure subdomain Ω_s, with a common boundary $\Sigma(t)$. The partitioned

algorithm is adopted, where the FSI system is split into separate fluid and structure solvers. The fluid problem is described in an arbitrary Lagrangian-Eulerian framework, and the structure kinematics is in a purely Lagrangian approach. Three sets of variables in this FSI system are solved: the fluid velocity $\mathbf{u}(\mathbf{x}, t)$, the fluid mesh velocity $\mathbf{w}(\mathbf{x}, t)$, and the structure displacement $\boldsymbol{\eta}(\mathbf{X}, t)$.

Fluid/structure models and numerical solvers

The incompressible Navier-Stokes equation in the ALE framework can be written as:

$$\frac{\partial \mathbf{u}}{\partial t} + (\mathbf{u} - \mathbf{w}) \cdot \nabla \mathbf{u} = -\frac{\nabla p}{\rho_f} + \nu \nabla^2 \mathbf{u}, \quad \text{in } \Omega_f(t), \tag{4.2.1a}$$

$$\nabla \cdot \mathbf{u} = 0, \quad \text{in } \Omega_f(t), \tag{4.2.1b}$$

combined with the *Dirichlet* boundary conditions on the interface, i.e.,

$$\mathbf{u} = \frac{\partial \eta}{\partial t}, \quad \text{on } \Sigma(t), \tag{4.2.2}$$

which enforces the continuity of velocities. Here, $\mathbf{w}$, p, ρ_f, and ν are the mesh velocity, pressure, fluid density, and the kinematic viscosity, respectively. To get the current configuration $\mathbf{x}$, we construct a mapping from a harmonic extension operator, i.e., the mesh velocity $\mathbf{w}$ satisfies

$$\nabla^2 \mathbf{w} = 0, \text{ in } \Omega_f(t), \tag{4.2.3a}$$

$$\mathbf{w} = \frac{\partial \eta}{\partial t}, \text{ on } \Sigma(t), \tag{4.2.3b}$$

which is endowed with $\mathbf{w} = 0$ on the other boundaries. The mesh position $\mathbf{x}$ can then be obtained from the integration of $\mathbf{w}$. To solve for $\mathbf{u}$ we employ the velocity-correction method as described in chapter 4.1, but without subiterations. Moreover, in analysis we take first order non-incrememtal velocity correction scheme for simplicity:

$$\frac{\tilde{\mathbf{u}}^n - \mathbf{u}^{n-1}}{\Delta t} = -\mathbf{N}^n, \tag{4.2.4a}$$

$$\frac{\tilde{\tilde{\mathbf{u}}}^n - \tilde{\mathbf{u}}^n}{\Delta t} = -\frac{\nabla p^n}{\rho_f}, \tag{4.2.4b}$$

$$\frac{\mathbf{u}^n - \tilde{\tilde{\mathbf{u}}}^n}{\Delta t} = \nu \nabla^2 \mathbf{u}^n, \tag{4.2.4c}$$

where

$$\frac{\partial p^n}{\partial \mathbf{n}_f} = -\rho_f \left(\frac{\partial \mathbf{u}^n}{\partial t} + \mathbf{N}^n \right) \cdot \mathbf{n}_f, \quad \text{on } \partial\Omega_i. \tag{4.2.5}$$

and

$$\mathbf{N}^n = \mathbf{u}^{n-i} \cdot \nabla \mathbf{u}^{n-1}. \tag{4.2.6}$$

In (4.1.8), $\mathbf{n}_f$ is the normal vector of fluid subdomain pointing outward on the interface $\Sigma(t)$. This scheme is reported to be with 1st order accuracy for velocity and half order accuracy for pressure as the optimal convergence rate in the L^2 sense.

On the structure side, the equation describing the structure deformation can be expressed as:

$$\rho_s \frac{\partial^2 \eta}{\partial t^2} - \text{div}(\mathbf{S}) = \rho_s \mathbf{f}, \quad \text{in } \Omega_s, \tag{4.2.7}$$

with the *Neumann* boundary condition at the interface

$$\mathbf{S}\mathbf{n}_s = -[-p\mathbf{I} + \rho_f \nu(\nabla \mathbf{u} + (\nabla \mathbf{u})^T)]\mathbf{n}_f, \quad \text{on } \Sigma(t) \tag{4.2.8}$$

which enforces the continuity of the normal stresses at the interface. Here $\mathbf{f}$ and ρ_s are the body load and the structure density, respectively. On the interface $\Sigma(t)$, $\mathbf{n}_s$ stands for the normal vector pointing outward from the structure subdomain. Considering the geometrically linear elastodynamics for simplicity, the second Piola-Kirchhoff stress tensor is given by

$$\mathbf{S} = \frac{\zeta E}{2(1+\zeta)(1-2\zeta)} \left[\text{tr} \left(\frac{\partial \eta}{\partial \mathbf{x}} + \frac{\partial \eta}{\partial \mathbf{x}}^T \right) \right] + \frac{E}{2(1+\zeta)} \left(\frac{\partial \eta}{\partial \mathbf{x}} + \frac{\partial \eta}{\partial \mathbf{x}}^T \right), \tag{4.2.9}$$

where E and ζ are the Young's modulus and the Poisson ratio of the material, respectively. Note that a hyperelastic model with finite deformations [121] can also be substituted in. To integrate in time, in the analysis we consider a first order BDF scheme

$$\rho_s \frac{\delta \eta^n - \delta \eta^{n-1}}{\Delta t} - \text{div}(\mathcal{S}(\eta^{n-1/2})) = \rho_s \mathbf{f}^n, \tag{4.2.10}$$

here $\delta \eta^n := \frac{\eta^n - \eta^{n-1}}{\Delta t}$ and $\eta^{n-1/2} := \frac{\eta^n + \eta^{n-1}}{2}$. To enforces the continuity of the normal stresses at the interface, we set

$$\mathbf{S}(\boldsymbol{\eta}^{n-1/2})\mathbf{n}_s = -[-p^{n-1}\mathbf{I} + \rho_f \nu(\nabla \mathbf{u}^{n-1} + (\nabla \mathbf{u}^{n-1})^T)]\mathbf{n}_f, \quad \text{on } \Sigma(t). \tag{4.2.11}$$

A traditional explicit algorithm in weak form

From the fluid and structure models described above, on the $n-$th time step we can naturally have a explicit algorithm in the finite element method framework:

Structure side: Solve for η^n in the weak form with test function ψ:

$$\begin{aligned}&\int_{\Omega_s} \rho_s \frac{\delta\eta^n - \delta\eta^{n-1}}{\Delta t} \cdot \psi d\mathbf{x} = -\mathcal{S}(\eta^{n-1/2}, \psi) + \int_{\Omega_s} \rho_s \mathbf{f}^n \cdot \psi d\mathbf{x} \\ &- \int_\Sigma \left(\left(-p^{n-1} I + \nu(\nabla u^{n-1} + (\nabla u^{n-1})^T) \right) \cdot \mathbf{n}_f \right) \cdot \psi ds,\end{aligned} \tag{4.2.12}$$

here $\delta\eta^n = \frac{\eta^n - \eta^{n-1}}{\Delta t}$, $\eta^{n-1/2} = \frac{\eta^n + \eta^{n-1}}{2}$ and $\mathcal{S}(\eta^{n-1/2}, \psi) = \int_{\Omega_s} \mathbf{S}^{n-1/2} : \nabla\psi d\mathbf{x}$.

Fluid side: Neglecting the nonlinear advection term, we solve for $(\mathbf{u}^n, p^n)$ in the weak form with test functions (ϕ, ξ, q):

$$\begin{aligned}&\int_{\Omega_f} \nabla p^n \cdot \nabla q d\mathbf{x} = \int_\Sigma \left(-\frac{\delta\eta^n - \mathbf{u}^{n-1}}{\Delta t} \cdot \mathbf{n}_f \right) q ds - \int_{\Omega_f} \frac{1}{\Delta t} \nabla \cdot \mathbf{u}^{n-1} q d\mathbf{x}, \\ &\int_{\Omega_f} \frac{1}{\Delta t} (\tilde{\mathbf{u}} - \mathbf{u}^{n-1}) \cdot \xi d\mathbf{x} + \int_{\Omega_f} \nabla p^n \cdot \xi d\mathbf{x} = 0 \\ &\int_{\Omega_f} \frac{1}{\nu\Delta t} \mathbf{u}^n \cdot \phi d\mathbf{x} + \int_{\Omega_f} \nabla^2 \mathbf{u}^n \cdot \phi d\mathbf{x} = \int_{\Omega_f} \frac{1}{\nu\Delta t} \tilde{\mathbf{u}} \cdot \phi d\mathbf{x},\end{aligned} \tag{4.2.13}$$

with $\delta\eta^n = \mathbf{u}^n$ imposed on Σ at the last step. Here we take the fluid density ρ_f to be of one unit, and the fluid-structure density ratio therefore be ρ_s. Although this explicit algorithm looks very natural, when density ratio is small it suffers from added-mass effect and the simulation may blow up. In the following contents, we refer this natural explicit algorithm as the *standard explicit algorithm*, and our stabilized algorithm which is introduced in the next section as the *stabilized explicit algorithm*.

Stabilized explicit algorithm

In the standard explicit algorithm, the small disturbance in the structure solver

$$\int_\Sigma \left(\left(-(p^n - p^{n-1}) I + \nu(\nabla(u^n - u^{n-1}) + (\nabla(u^n - u^{n-1}))^T) \right) \cdot \mathbf{n}_f \right) \cdot \psi ds$$

breaks the normal stresses continuity and therefore also the energy balance. Then in the fluid solver the strong Dirichlet boundary condition $\delta\eta^n = \mathbf{u}^n$ at interface further reinforce the error and causes instability. Therefore, we consider two strategies to stabilize this system:

- treating the velocity continuity condition $\delta\eta^n = \mathbf{u}^n$ in a weak way;

- applying additional penalty terms to control the pressure variations at the interface [122],

and propose a stabilized explicit algorithm:

Structure side: Solve for η^n with the test functions ψ

$$\begin{aligned}&\int_{\Omega_s}\rho_s\frac{\delta\eta^n-\delta\eta^{n-1}}{\Delta t}\cdot\psi d\mathbf{x}+\mathcal{S}(\eta^{n-1/2},\psi)+\int_\Sigma\frac{b}{\Delta x}(\delta\eta^n-\mathbf{u}^{n-1})\cdot\psi ds-\int_{\Omega_s}\rho_s\mathbf{f}^n\cdot\psi d\mathbf{x}\\=&-\int_\Sigma\left(\left(-p^{n-1}I+\nu(\nabla u^{n-1}+(\nabla u^{n-1})^T)\right)\cdot\mathbf{n}_f\right)\cdot\psi ds\end{aligned}\tag{4.2.14}$$

Fluid side: Mark $\epsilon(\mathbf{u})=(\nabla\mathbf{u}+\nabla\mathbf{u}^T)/2$, we solve for $(\mathbf{u}^n,p^n)$ with the test functions (ϕ,ξ,q):

$$\int_{\Omega_f}\nabla p^n\cdot\nabla q d\mathbf{x}+\int_\Sigma\frac{a\Delta x}{\Delta t}(p^n-p^{n-1})qds \tag{4.2.15a}$$

$$=-\int_{\Omega_f}\frac{1}{\Delta t}\nabla\cdot\mathbf{u}^{n-1}qd\mathbf{x}+\int_\Sigma\left(-\left(\frac{\delta\eta^n-\mathbf{u}^{n-1}}{\Delta t}\right)\cdot\mathbf{n}_f\right)qds, \tag{4.2.15b}$$

$$\int_{\Omega_f}\frac{1}{\Delta t}(\tilde{\mathbf{u}}-\mathbf{u}^{n-1})\cdot\xi d\mathbf{x}+\int_{\Omega_f}\nabla p^n\cdot\xi d\mathbf{x}=0 \tag{4.2.15c}$$

$$\int_{\Omega_f}\frac{1}{\Delta t}(\mathbf{u}^n-\tilde{\mathbf{u}})\cdot\phi d\mathbf{x}++2\nu\int_{\Omega_f}\epsilon(\mathbf{u}^n):\epsilon(\phi)d\mathbf{x}+\int_\Sigma\frac{b}{\Delta x}(\mathbf{u}^n-\delta\eta^n)\cdot\phi ds \tag{4.2.15d}$$

$$=2\nu\int_\Sigma\epsilon(\mathbf{u}^{n-1})\cdot\mathbf{n}_f\phi ds+\int_\Sigma(p^n-p^{n-1})\mathbf{n}_f\cdot\phi ds. \tag{4.2.15e}$$

Here a and b are the penalty constants which can be adjusted to achieve the optimal balance of stability and accuracy. Note that in the implementation the step (4.2.15c) is actually in the strong form

$$\frac{1}{\Delta t}(\tilde{\mathbf{u}}-\mathbf{u}^{n-1})+\nabla p^n=0. \tag{4.2.16}$$

Energy based stability analysis

Assume that the external body load $\mathbf{f}=0$, next we prove that the stabilized explicit algorithm proposed above is stable when the constants a and b are large enough. From (4.2.15a) we have

$$\int_\Sigma\frac{\partial p^n}{\partial\mathbf{n}_f}qds=-\int_\Sigma\left(\left(\frac{\delta\eta^n-\mathbf{u}^{n-1}}{\Delta t}\right)\cdot\mathbf{n}_f\right)qds-\frac{a\Delta x}{\Delta t}\int_\Sigma(p^n-p^{n-1})qds, \tag{4.2.17}$$

which could be combined with (4.2.16) and yields

$$\begin{aligned}\int_\Sigma\tilde{\mathbf{u}}\cdot\mathbf{n}_f qds&=\int_\Sigma\mathbf{u}^{n-1}\cdot\mathbf{n}_f qds-\Delta t\int_\Sigma\frac{\partial p^n}{\partial\mathbf{n}_f}qds\\&=\int_\Sigma(\delta\eta^n\cdot\mathbf{n}_f)\,qds+a\Delta x\int_\Sigma(p^n-p^{n-1})qds.\end{aligned}\tag{4.2.18}$$

Taking proper test functions $q = (\Delta t)^2 p^n$, $\xi = \Delta t \tilde{\mathbf{u}}$, $\psi = \eta^n - \eta^{n-1} = \Delta t \delta\eta^n$, $\phi = \Delta t \mathbf{u}^n$ in equations (4.2.14) and (4.2.15) yields:

$$\begin{aligned}
&\frac{\rho_s}{2}\left(||\delta\eta^n||^2_{\Omega_s} + ||\delta\eta^n - \delta\eta^{n-1}||^2_{\Omega_s} - ||\delta\eta^{n-1}||^2_{\Omega_s}\right) + \frac{1}{2}\left(\mathcal{S}(\eta^n,\eta^n) - \mathcal{S}(\eta^{n-1},\eta^{n-1})\right) \\
&+ \frac{b\Delta t}{\Delta x}\int_\Sigma \left(\delta\eta^n - \mathbf{u}^{n-1}\right)\cdot\delta\eta^n ds - \Delta t\int_\Sigma p^{n-1}\mathbf{n}_f\cdot\delta\eta^n ds + 2\nu\Delta t\int_\Sigma \left(\epsilon(\mathbf{u}^{n-1})\cdot\mathbf{n}_f\right)\cdot\delta\eta^n ds = 0,
\end{aligned} \tag{4.2.19a}$$

$$\begin{aligned}
&(\Delta t)^2||\nabla p^n||^2_{\Omega_f} + a\Delta t\Delta x\int_\Sigma (p^n - p^{n-1})p^n ds + \Delta t\int_{\Omega_f}\nabla\cdot\mathbf{u}^{n-1}p^n d\mathbf{x} \\
&+ \Delta t\int_\Sigma \left(\delta\eta^n - \mathbf{u}^{n-1}\right)\cdot\mathbf{n}_f p^n ds = 0,
\end{aligned} \tag{4.2.19b}$$

$$\frac{1}{2}\left(||\tilde{\mathbf{u}}||^2_{\Omega_f} + ||\tilde{\mathbf{u}} - \mathbf{u}^{n-1}||^2_{\Omega_f} - ||\mathbf{u}^{n-1}||^2_{\Omega_f}\right) + \Delta t\int_{\Omega_f}\nabla p^n\cdot\tilde{\mathbf{u}} d\mathbf{x} = 0 \tag{4.2.19c}$$

$$\begin{aligned}
&\frac{1}{2}\left(||\mathbf{u}^n||^2_{\Omega_f} + ||\mathbf{u}^n - \tilde{\mathbf{u}}||^2_{\Omega_f} - ||\tilde{\mathbf{u}}||^2_{\Omega_f}\right) + 2\nu\Delta t||\epsilon(\mathbf{u}^n)||^2_{\Omega_f} - 2\nu\Delta t\int_\Sigma \left(\epsilon(\mathbf{u}^{n-1})\cdot\mathbf{n}_f\right)\cdot\mathbf{u}^n ds \\
&+ \frac{b\Delta t}{\Delta x}\int_\Sigma (\mathbf{u}^n - \delta\eta^n)\cdot\mathbf{u}^n ds = 0
\end{aligned} \tag{4.2.19d}$$

where the equality

$$a(a-b) = \frac{1}{2}(a^2 - b^2 + (a-b)^2)$$

is employed. Substituting (4.2.18) with $q = p^n$ into (4.2.19c), we could obtain

$$\begin{aligned}
0 =& \frac{1}{2}\left(||\tilde{\mathbf{u}}||^2_{\Omega_f} + ||\tilde{\mathbf{u}} - \mathbf{u}^{n-1}||^2_{\Omega_f} - ||\mathbf{u}^{n-1}||^2_{\Omega_f}\right) + \Delta t\int_{\Omega_f}\nabla p^n\cdot\tilde{\mathbf{u}} d\mathbf{x} \\
=& \frac{1}{2}\left(||\tilde{\mathbf{u}}||^2_{\Omega_f} + ||\tilde{\mathbf{u}} - \mathbf{u}^{n-1}||^2_{\Omega_f} - ||\mathbf{u}^{n-1}||^2_{\Omega_f}\right) + \Delta t\int_\Sigma p^n\mathbf{n}_f\cdot\tilde{\mathbf{u}} ds - \Delta t\int_{\Omega_f} p^n\nabla\cdot\tilde{\mathbf{u}} d\mathbf{x} \\
=& \frac{1}{2}\left(||\tilde{\mathbf{u}}||^2_{\Omega_f} + ||\tilde{\mathbf{u}} - \mathbf{u}^{n-1}||^2_{\Omega_f} - ||\mathbf{u}^{n-1}||^2_{\Omega_f}\right) + \Delta t\int_\Sigma \delta\eta^n\cdot\mathbf{n}_f p^n ds \\
&+ a\Delta t\Delta x\int_\Sigma (p^n - p^{n-1})p^n ds - \Delta t\int_{\Omega_f} p^n\nabla\cdot\tilde{\mathbf{u}} d\mathbf{x}.
\end{aligned} \tag{4.2.20}$$

Furthermore, with the fact from (4.2.18)

$$\Delta t\int_\Sigma (\delta\eta^n - \tilde{\mathbf{u}})\cdot\mathbf{n}_f q ds = -a\Delta t\Delta x\int_\Sigma (p^n - p^{n-1})q ds,$$

summing up (4.2.19b) and (4.2.20) yields

$$
\begin{aligned}
0 =& \frac{1}{2}\left(||\tilde{\mathbf{u}}||^2_{\Omega_f} + ||\tilde{\mathbf{u}} - \mathbf{u}^{n-1}||^2_{\Omega_f} - ||\mathbf{u}^{n-1}||^2_{\Omega_f}\right) + (\Delta t)^2||\nabla p^n||^2_{\Omega_f} + \Delta t\int_\Sigma \delta\eta^n \cdot \mathbf{n}_f p^n ds \\
&+ 2a\Delta t\Delta x\int_\Sigma (p^n - p^{n-1})p^n ds + \Delta t\int_{\Omega_f} p^n \nabla\cdot\left(\mathbf{u}^{n-1} - \tilde{\mathbf{u}}\right)d\mathbf{x} + \Delta t\int_\Sigma \left(\delta\eta^n - \mathbf{u}^{n-1}\right)\cdot\mathbf{n}_f p^n ds \\
=& \frac{1}{2}\left(||\tilde{\mathbf{u}}||^2_{\Omega_f} + ||\tilde{\mathbf{u}} - \mathbf{u}^{n-1}||^2_{\Omega_f} - ||\mathbf{u}^{n-1}||^2_{\Omega_f}\right) + (\Delta t)^2||\nabla p^n||^2_{\Omega_f} + \Delta t\int_\Sigma \delta\eta^n \cdot \mathbf{n}_f p^n ds \\
&+ 2a\Delta t\Delta x\int_\Sigma (p^n - p^{n-1})p^n ds + \Delta t\int_\Sigma p^n \mathbf{n}_f\cdot\left(\mathbf{u}^{n-1} - \tilde{\mathbf{u}}\right)ds \\
&- \Delta t\int_{\Omega_f} \nabla p^n \cdot\left(\mathbf{u}^{n-1} - \tilde{\mathbf{u}}\right)d\mathbf{x} + \Delta t\int_\Sigma \left(\delta\eta^n - \mathbf{u}^{n-1}\right)\cdot\mathbf{n}_f p^n ds \\
=& \frac{1}{2}\left(||\tilde{\mathbf{u}}||^2_{\Omega_f} + ||\tilde{\mathbf{u}} - \mathbf{u}^{n-1}||^2_{\Omega_f} - ||\mathbf{u}^{n-1}||^2_{\Omega_f}\right) + (\Delta t)^2||\nabla p^n||^2_{\Omega_f} + \Delta t\int_\Sigma \delta\eta^n \cdot \mathbf{n}_f p^n ds \\
&+ 2a\Delta t\Delta x\int_\Sigma (p^n - p^{n-1})p^n ds - (\Delta t)^2\int_{\Omega_f}\nabla p^n\cdot\nabla p^n d\mathbf{x} + \Delta t\int_\Sigma (\delta\eta^n - \tilde{\mathbf{u}})\cdot\mathbf{n}_f p^n ds \\
=& \frac{1}{2}\left(||\tilde{\mathbf{u}}||^2_{\Omega_f} + ||\tilde{\mathbf{u}} - \mathbf{u}^{n-1}||^2_{\Omega_f} - ||\mathbf{u}^{n-1}||^2_{\Omega_f}\right) + \Delta t\int_\Sigma \delta\eta^n \cdot \mathbf{n}_f p^n ds \\
&+ a\Delta t\Delta x\int_\Sigma (p^n - p^{n-1})p^n ds.
\end{aligned}
\tag{4.2.21}
$$

Combining (4.2.19a), (4.2.19d) and (4.2.21), we get

$$
\begin{aligned}
&\frac{\rho_s}{2}\left(||\delta\eta^n||^2_{\Omega_s} - ||\delta\eta^{n-1}||^2_{\Omega_s} + ||\delta\eta^n - \delta\eta^{n-1}||^2_{\Omega_s}\right) + \frac{1}{2}\left(\mathcal{S}(\eta^n,\eta^n) - \mathcal{S}(\eta^{n-1},\eta^{n-1})\right) \\
&+ \frac{1}{2}\left(||\mathbf{u}^n||^2_{\Omega_f} - ||\mathbf{u}^{n-1}||^2_{\Omega_f} + ||\tilde{\mathbf{u}} - \mathbf{u}^{n-1}||^2_{\Omega_f} + ||\mathbf{u}^n - \tilde{\mathbf{u}}||^2_{\Omega_f}\right) + 2\nu\Delta t||\epsilon(\mathbf{u}^n)||^2_{\Omega_f} \\
&+ 2\nu\Delta t\int_\Sigma \left(\epsilon(\mathbf{u}^{n-1})\cdot\mathbf{n}_f\right)\cdot(\delta\eta^n - \mathbf{u}^n)\,ds \qquad \leftarrow \mathbf{T_1} \\
&+ \frac{b\Delta t}{\Delta x}\int_\Sigma \left(\delta\eta^n - \mathbf{u}^{n-1}\right)\cdot\delta\eta^n + (\mathbf{u}^n - \delta\eta^n)\cdot\mathbf{u}^n ds \qquad \leftarrow \mathbf{T_2} \\
&+ a\Delta t\Delta x\int_\Sigma \left(p^n - p^{n-1}\right)p^n ds \qquad \leftarrow \mathbf{T_3} \\
&+ \Delta t\int_\Sigma \left(p^n - p^{n-1}\right)\mathbf{n}_f\cdot(\delta\eta^n - \mathbf{u}^n)ds \qquad \leftarrow \mathbf{T_4} \\
=&0
\end{aligned}
\tag{4.2.22}
$$

where

$$
\begin{aligned}
T_1 &= 2\nu\Delta t\int_\Sigma \epsilon(\mathbf{u}^{n-1})\cdot\mathbf{n}_f\cdot(\delta\eta^n - \mathbf{u}^n)ds \\
&\geq -\frac{\nu\Delta t\Delta x}{C_{ti}}||\epsilon(\mathbf{u}^{n-1}||^2_\Sigma - \frac{\nu\Delta t C_{ti}}{\Delta x}||\delta\eta^n - \mathbf{u}^n)||^2_\Sigma \\
&\geq -\nu\Delta t||\epsilon(\mathbf{u}^{n-1})||^2_{\Omega_f} - \frac{\nu\Delta t C_{ti}}{\Delta x}||\delta\eta^n - \mathbf{u}^n||^2_\Sigma
\end{aligned}
\tag{4.2.23}
$$

$$
\begin{aligned}
T_2 =& \frac{b\Delta t}{\Delta x}\Big(\int_\Sigma (\mathbf{u}^n - \delta\eta^n)\cdot\mathbf{u}^n ds + \int_\Sigma (\delta\eta^n - \mathbf{u}^{n-1})\cdot\delta\eta^n ds\Big)\\
=& \frac{b\Delta t}{\Delta x}\Big(||\mathbf{u}^n - \delta\eta^n||_\Sigma^2 + \int_\Sigma (\mathbf{u}^n - \mathbf{u}^{n-1})\cdot\delta\eta^n ds\Big)\\
=& \frac{b\Delta t}{\Delta x}\Big(||\mathbf{u}^n - \delta\eta^n||_\Sigma^2 + \int_\Sigma (\mathbf{u}^n - \mathbf{u}^{n-1})\cdot(\delta\eta^n - \mathbf{u}^n) ds\\
&+ \int_\Sigma (\mathbf{u}^n - \mathbf{u}^{n-1})\cdot\mathbf{u}^n ds\Big)\\
\geq& \frac{b\Delta t}{\Delta x}\Big(||\mathbf{u}^n - \delta\eta^n||_\Sigma^2 - \frac{1}{2}||\mathbf{u}^n - \mathbf{u}^{n-1}||_\Sigma^2 - \frac{1}{2}||\delta\eta^n - \mathbf{u}^n||_\Sigma^2\\
&+ \frac{1}{2}||\mathbf{u}^n||_\Sigma^2 - \frac{1}{2}||\mathbf{u}^{n-1}||_\Sigma^2 + \frac{1}{2}||\mathbf{u}^n - \mathbf{u}^{n-1}||_\Sigma^2\Big)\\
=& \frac{b\Delta t}{2\Delta x}\Big(||\mathbf{u}^n - \delta\eta^n||_\Sigma^2 + ||\mathbf{u}^n||_\Sigma^2 - ||\mathbf{u}^{n-1}||_\Sigma^2\Big)
\end{aligned}
\tag{4.2.24}
$$

$$
\begin{aligned}
T_3 &= a\Delta t\Delta x\int_\Sigma (p^n - p^{n-1})p^n ds\\
&= \frac{a\Delta t\Delta x}{2}\Big(||p^n||_\Sigma^2 - ||p^{n-1}||_\Sigma^2 + ||p^n - p^{n-1}||_\Sigma^2\Big)
\end{aligned}
\tag{4.2.25}
$$

$$
\begin{aligned}
T_4 &= \Delta t\int_\Sigma (p^n - p^{n-1})\mathbf{n}_f\cdot(\delta\eta^n - \mathbf{u}^n) ds\\
&\geq -\frac{\Delta t\Delta x}{b}||p^n - p^{n-1}||_\Sigma^2 - \frac{b\Delta t}{4\Delta x}||\delta\eta^n - \mathbf{u}^n||_\Sigma^2.
\end{aligned}
\tag{4.2.26}
$$

Here C_{ti} stands for the constant in the trace-inverse inequality satisfying

$$
||\mathbf{v}||_\Sigma^2 \leq \frac{C_{ti}}{\Delta x}||\mathbf{v}||_{\Omega_f}^2,
$$

which is determined by the shape and size of the fluid subdomain. Substituting equations (4.2.23)-(4.2.26) into (4.2.22), one could obtain the following

$$
\begin{aligned}
&\frac{1}{2}\Big(||\mathbf{u}^n||^2 - ||\mathbf{u}^{n-1}||^2 + \rho_s||\delta\eta^n||^2 - \rho_s||\delta\eta^{n-1}||^2 + \mathcal{S}(\eta^n,\eta^n) - \mathcal{S}(\eta^{n-1},\eta^{n-1})\Big)\\
&+ 2\nu\Delta t||\epsilon(\mathbf{u}^n)||_{\Omega_f}^2 - \nu\Delta t||\epsilon(\mathbf{u}^{n-1})||_{\Omega_f}^2 + \left(\frac{b\Delta t}{4\Delta x} - \frac{\nu\Delta t C_{ti}}{\Delta x}\right)||\dot{\eta}^n - \mathbf{u}^n||_\Sigma^2\\
&+ \frac{b\Delta t}{2\Delta x}\Big(||\mathbf{u}^n||_\Sigma^2 - ||\mathbf{u}^{n-1}||_\Sigma^2\Big) + \frac{a\Delta t\Delta x}{2}\Big(||p^n||_\Sigma^2 - ||p^{n-1}||_\Sigma^2\Big)\\
&+ \left(\frac{a\Delta t\Delta x}{2} - \frac{\Delta t\Delta x}{b}\right)||p^n - p^{n-1}||_\Sigma^2\\
&\leq 0.
\end{aligned}
\tag{4.2.27}
$$

Therefore, when

$$
b \geq 4\nu C_{ti}, \quad a \geq \frac{2}{b}
\tag{4.2.28}
$$

and mark the energy norm as

$$E^n = ||\mathbf{u}^n||^2 + \rho_s||\delta\eta^n||^2 + \mathcal{S}(\eta^n, \eta^n) + 4\nu\Delta t||\epsilon(\mathbf{u}^n)||, \tag{4.2.29}$$

we have

$$E^n + \frac{b\Delta t}{\Delta x}||\mathbf{u}^n||_\Sigma^2 + a\Delta t\Delta x||p^n||_\Sigma^2 \leq E^0 + \frac{b\Delta t}{\Delta x}||\mathbf{u}^0||_\Sigma^2 + a\Delta t\Delta x||p^0||_\Sigma^2.$$

Since a and b depends on the domain only, this stabilized explicit algorithm is stable irrespective of the fluid-structure density ratio, i.e., it resolves the added-mass effect.

4.2.3 Convergence studies

However, such superior stability is in the price of sacrifying accuracy. In (4.2.14) and (4.2.15) we introduced three penalty terms to stabilize the FSI procedure:

$$\int_\Sigma \frac{b}{\Delta x}(\delta\eta^n - \mathbf{u}^{n-1}) \cdot \psi ds$$

in the structure solver,

$$\int_\Sigma \frac{a\Delta x}{\Delta t}(p^n - p^{n-1}) q ds$$

in the pressure solver and

$$2\nu \int_\Sigma \epsilon(\mathbf{u}^n - \mathbf{u}^{n-1}) \cdot \mathbf{n}_f \phi ds + \int_\Sigma (p^n - p^{n-1})\mathbf{n}_f \cdot \phi ds$$

in the velocity solver.

While taking the time step size satisfying the CFL condition $\Delta t = O(\Delta x^2)$, these terms introduce errors of order $O(\Delta t^{\frac{1}{2}})$. Therefore, although the optimal convergence rates for velocity and displacement should be first order from the numerical schemes (4.2.4) and (4.2.10) we have adopted, we can only expect half order convergence in time for all variables $(\eta, \mathbf{u}, p)$ from the stabilized explicit algorithm. Fortunately, the optimal accuracy can be recovered by performing defect-correction subiterations in each time step:

$$\int_{\Omega_s} \rho_s \frac{\delta\eta_k^n - \delta\eta^{n-1}}{\Delta t} \cdot \psi d\mathbf{x} + \mathcal{S}(\eta_k^{n-1/2}, \psi) + \int_\Sigma \frac{b}{\Delta x}(\delta\eta_k^n - \mathbf{u}_{k-1}^n) \cdot \psi ds \tag{4.2.30a}$$

$$= -\int_\Sigma \left(\left(-p_{k-1}^n I + \nu(\nabla u_{k-1}^n + (\nabla u_{k-1}^n)^T) \right) \cdot \mathbf{n}_f \right) \cdot \psi ds. \tag{4.2.30b}$$

$$\int_{\Omega_f} \nabla p_k^n \cdot \nabla q d\mathbf{x} + \int_\Sigma \frac{a\Delta x}{\Delta t}(p_k^n - p_{k-1}^n) q ds \tag{4.2.30c}$$

$$= -\int_{\Omega_f} \frac{1}{\Delta t} \nabla \cdot \mathbf{u}^{n-1} q d\mathbf{x} + \int_\Sigma \left(-\left(\frac{\delta\eta_k^n - \mathbf{u}^{n-1}}{\Delta t} \right) \cdot \mathbf{n}_f \right) q ds, \tag{4.2.30d}$$

$$\int_{\Omega_f} \frac{1}{\Delta t}(\tilde{\mathbf{u}} - \mathbf{u}^{n-1}) \cdot \xi d\mathbf{x} + \int_{\Omega_f} \nabla p_k^n \cdot \xi d\mathbf{x} = 0 \tag{4.2.30e}$$

$$\int_{\Omega_f} \frac{1}{\Delta t}(\mathbf{u}_k^n - \tilde{\mathbf{u}}) \cdot \phi d\mathbf{x} + +2\nu \int_{\Omega_f} \epsilon(\mathbf{u}_k^n) : \epsilon(\phi) d\mathbf{x} + \int_\Sigma \frac{b}{\Delta x}(\mathbf{u}_k^n - \delta\eta_k^n) \cdot \phi ds \tag{4.2.30f}$$

$$= 2\nu \int_\Sigma \epsilon(\mathbf{u}_{k-1}^n) \cdot \mathbf{n}_f \phi ds + \int_\Sigma (p_k^n - p_{k-1}^n)\mathbf{n}_f \cdot \phi ds. \tag{4.2.30g}$$

After K corrections, the solution is expected to be of order $O(\Delta t + \Delta t^{K/2})$ for velocity and displacement and $O(\Delta t^{1/2})$ for pressure. That is, with 1 additional subiteration in each time step, we could recover the optimal convergence rates for the first order non-incremental velocity correction scheme and the first order BDF scheme.

Now we consider a simplified numerical experiment shown in Figure 4.19 by coupling the 2D Stokes equations with linear elasticity equations. All boundaries of either the fluid and solid subdomain are discretized into N_x even parts. The FSI system is numerically integrated till $T = 0.5$, with $\Delta t = \frac{25}{2N_x^2}$. Moreover, as inspired by (4.2.28) we take the penalty parameter $b = 10\nu$ which is proportional to the viscosity coefficient ν, and $a = 2/b$. This test is done with the opensource software *Freefem* [145]. P2 elements are employed for discretizing velocity and displacemenet in space, and P1 elements are used for the pressure. With prescribed constants A and B, on the fluid side the Dirichelet type boundary conditions are applied on all except the interface $\Sigma(t)$ as

$$\begin{aligned} u_1 &= -\sin(A\pi t)\cos(Bx)\sin(By); \\ u_2 &= \sin(A\pi t)\sin(Bx)\cos(By); \\ p &= -B\sin(Bx)\sin(By)\left(E\cos(A\pi t)/((1+\zeta)\pi A) + 2\nu\sin(A\pi t)\right). \end{aligned} \tag{4.2.31}$$

The whole fluid subdomain is subjected to a body force field $\rho\mathbf{f} = (f_1, f_2)$

$$\begin{aligned} f_1 &= -\frac{\cos(Bx)\sin(By)((2B^2\mu + A^2\pi^2)\cos(A\pi t) + 4AB^2\pi\nu\sin(A\pi t))}{A\pi}; \\ f_2 &= -\frac{\sin(Bx)\cos(By)\cos(A\pi t)(2B^2\mu - A^2\pi^2)}{A\pi}. \end{aligned} \tag{4.2.32}$$

On the structure side, the displacement field $\boldsymbol{\eta} = (\eta_1, \eta_2)$ is known on $\partial\Omega_s \setminus \Sigma(t)$

$$\begin{aligned} \eta_1 &= \cos(A\pi t)\cos(Bx)\sin(By)/\pi/A; \\ \eta_2 &= -\cos(A\pi t)\sin(Bx)\cos(By)/\pi/A. \end{aligned} \tag{4.2.33}$$

	E	ζ	ν	A	B	ρ_s
eg1	1	0.3	0.04	2	1	0.215
eg2	1	0.3	40	1	0.25	2.15

Table 4.8: Parameters employed in the convergence tests for stabilized explicit algorithm.

A body force field, $\rho\mathbf{f} = (f_1, f_2)$ is applied on the solid with components:

$$\begin{aligned} f_1 &= \frac{\cos(Bx)\sin(By)\cos(A\pi t)(2B^2\mu - A^2\pi^2\rho_s)}{A\pi}; \\ f_2 &= -\frac{\cos(A\pi t)\sin(Bx)\cos(By)(2B^2\mu - A^2\pi^2\rho_s)}{A\pi}. \end{aligned} \tag{4.2.34}$$

This problem has the following analytic solution for the displacement of the object:

$$\begin{aligned} \mathbf{u} &= \begin{cases} -\sin(A\pi t)\cos(Bx)\sin(By); \\ \sin(A\pi t)\sin(Bx)\cos(By); \end{cases} \\ p &= -B\sin(Bx)\sin(By)\left(E\cos(A\pi t)/((1+\zeta)\pi A) + 2\nu\sin(A\pi t)\right) \\ \eta &= \begin{cases} \cos(A\pi t)\cos(Bx)\sin(By)/\pi/A; \\ -\cos(A\pi t)\sin(Bx)\cos(By)/\pi/A; \end{cases} \end{aligned}$$

Two cases with different choices of ν and ρ_s are investigated, with parameters summarized in Table 4.8. We note that in case "eg1" the kinetic viscosity ν and ρ_s are closer to real values in arterial flows, and therefore we concentrate more on this case.

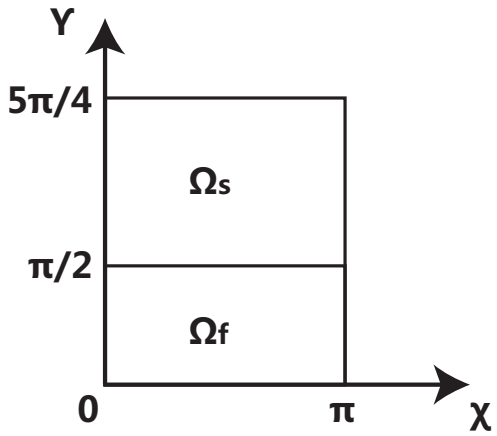

Figure 4.19: Geometry employed in the convergence tests for stabilized explicit algorithm.

First we investigate the impact of the added-mass effect on the stability by showing the time trace for pressure at the middle point of fluid-structure interface in Figure 4.20, with coefficients of case "eq1". Here different density ratios ρ_s are employed: in the left plot we take $\rho_s = 0.215$, and

in the right plot the density ratio is increased by 1000 times. The red line shows the results from the standard explicit algorithm, which blows up when $\rho_s = 0.215$ but works fine for larger ρ_s. This fact indicates that the standard explicit algorithm suffers from added-mass effect and lose stability when the density ratio is small. However, the results from stabilized explicit algorithm are stable in both plots. Therefore the stabilized algorithm successfully resolves the added-mass effect in this case.

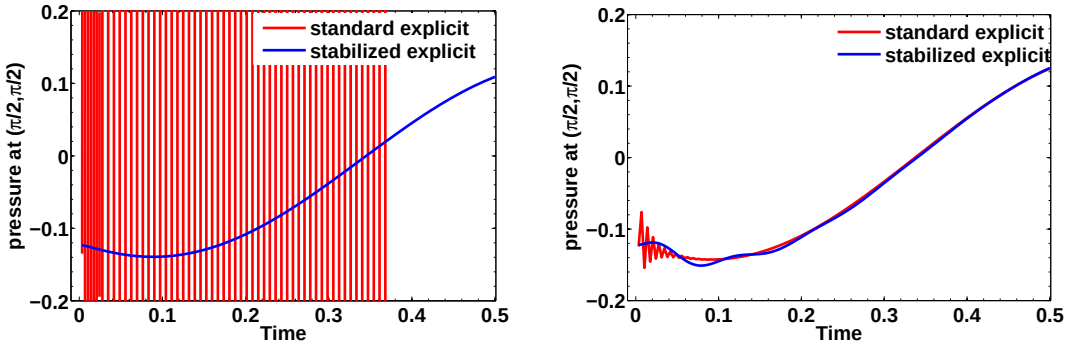

Figure 4.20: Time trace of pressure at $(\pi/2, \pi/2)$ for various density ratios in eg1. Left: $\rho_s = 0.215$. Right: $\rho_s = 215$.

To investigate the convergence rates for the two cases listed in Table 4.8, we vary the Δx and correspondingly Δt with $N_x = 10 - 60$ and study the L^2 errors of all variables. In all tests we employ the first order standard incremental velocity correction scheme for the fluid solver, and the first order BDF scheme for the structure solver, i.e., the optimal convergence rates for $(\eta, \mathbf{u}, p)$ are all first order. In Table 4.9 we list the convergence rates with respect to Δt, and in Figure 4.21 we plot the L^2 errors in logarithmic scale as a function of Δt which is also in logarithmic scale. It can be observed that half order accuracy in time is achieved for all variables, as we have predicted before. Secondly we focus on case "eg1" and investigate the effect of defect-correction subiterations, by varying the subiteration numbers K from 1 to 2 and 4. Note that when $K = 1$, the stabilized explicit algorithm with defect-correction subiterations (4.2.30) be equavalent to the one without subiterations (4.2.14)-(4.2.15). We list the convergence rates of time in Table 4.10, and plot the L^2 errors in logarithmic scale as a function of Δt in Figure 4.22. With one additional subiteration, i.e., $K = 2$, we have recovered the optimal convergence rates for all variables. Lastly, we investigate the performances of our stabilized explicit algorithm with different penalty parameters b, with the relation $a = 2/b$ fixed and no defect-correction subiteration applied. The results are provided in Table 4.11 and Figure 4.23. It could be observed that when we decrease b from 10ν to ν, the errors got decreased, and the optimal convergence rates are recovered for all variables although

	$\mathbf{u}$	p	η
eg1	0.4389	0.6562	0.7110
eg2	0.6545	0.4506	0.4481

Table 4.9: Convergence rate with respect to Δt, for different ν and ρ_s.

	$\mathbf{u}$	p	η
subiter 1	0.4389	0.6562	0.7110
subiter 2	0.8182	0.9179	0.8885
subiter 4	1.1355	0.9588	0.9704

Table 4.10: Convergence rate with respect to Δt, with defect-correction subiterations.

no subiteration is applied. However, if a smaller b is applied as 0.1ν, the algorithm becomes less accurate for this case. We are still working on the rigorous error analysis to explain this phenomena.

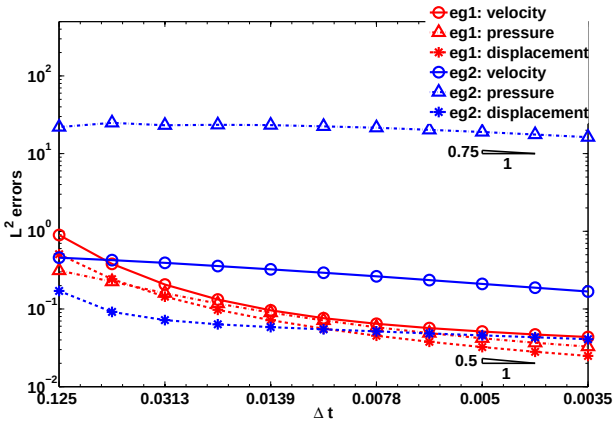

Figure 4.21: Errors tests in the linear case for cases "eg1" and "eg2", with standard incremental method and no defect-correction subiterations.

4.2.4 Numerical simulations

In the following we consider a vortex-induced vibration (VIV) problem of a circular cylinder, as illustrated in the left plot of Figure 4.1. To investigate the performances of the stabilized explicit algorithm on eliminating added-mass effect, we conduct tests for a wide range of density ratios. The simulations are performed in a 2D domain $[-5, 20] \times [-5, 5]$, with a cylinder of radius 0.5 at the origin. A uniform steady flow with $U_\infty = 1$ is imposed at the inlet $x = -5$, and a zero Neumann boundary condition is employed at the outlet $x = 20$. Along the crossflow direction, we take a periodic boundary condition, i.e., we are actually simulating a serie of cylinders. The fluid density is assumed to be $\rho_f = 1$ and Reynolds number $Re = 100$ based on the cylinder radius. All the

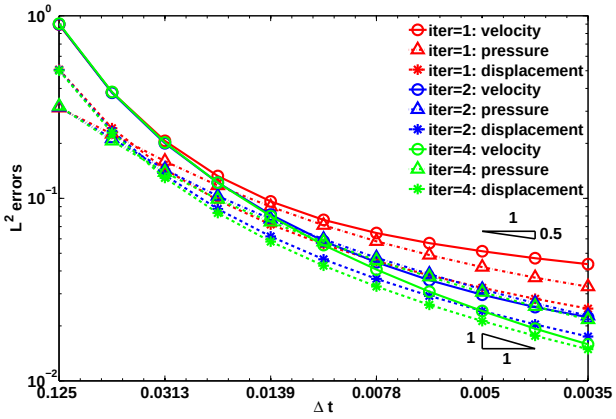

Figure 4.22: Errors tests in the linear "eg1" case, with standard incremental method and varying subiteration numbers.

	$\mathbf{u}$	p	η
$b = 10\nu$	0.4389	0.6562	0.7110
$b = \nu$	1.1617	0.9819	0.9746
$b = 0.1\nu$	1.1710	0.8884	1.0404

Table 4.11: Convergence rate with respect to Δt, with no defect-correction subiterations.

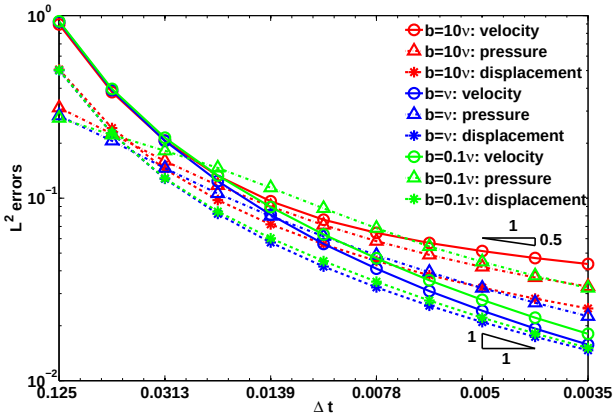

Figure 4.23: Errors tests in the linear "eg1" case, with no defect-correction subiteration and from different penalty parameter b.

results are obtained with polynomial order 3 elements, in our spectral element solver NEKTAR. A second order rotational increment velocity correction scheme is employed for the fluid solver, and the Newmark scheme is applied in the structure solver. Therefore, the optimal convergence rates for $(\eta, \mathbf{u}, p)$ are $(2, 2, 1.5)$, respectively. To obtain a fair comparison between our cases, we take a

uniform time step size $\Delta t = 0.005$ except in the time convergence studies. Note that in this section the cylinder can move in both transverse (y) and streamwise (y) directions. when $\rho_s/\rho_f = 4$, the time trace of displacements in x and y direction are plotted in Figure 4.24. We can see that the cylinder is quickly excited, then vibrates periodicly in both directions. In Figure we show the pressure coefficient contours and velocity vectors when the cylinder is crossing the line $y = 0$ from the bottom side, as marked by the red circle in Figure 4.25. Low pressure region is attached on the top side of the cylinder, which yields a total force to push up the cylinder.

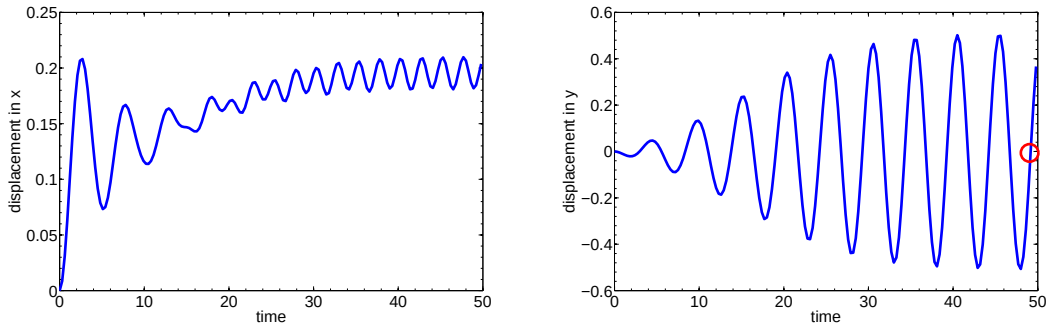

Figure 4.24: Time trace of displacement of the cylinder when $\rho_s = 4$.

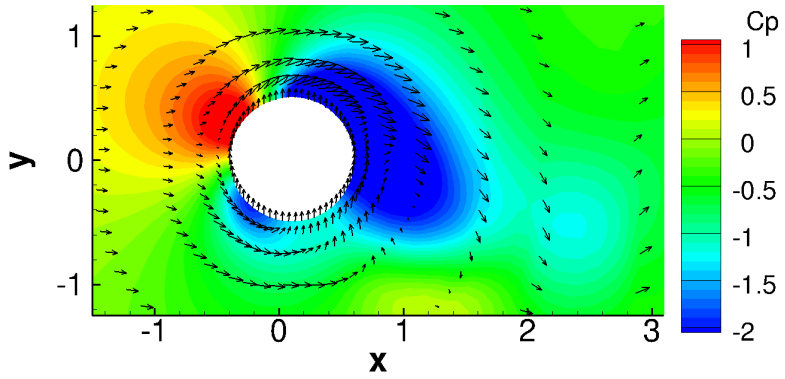

Figure 4.25: Pressure coefficient contours and velocity vectors when the velocity in y reaches maximum.

Now we investigate the convergence rates on this VIV case, by studying the errors of cylinder displacement in y direction at $T = 1$. The mesh is fixed, and the penalty parameters are taken as $\frac{b}{\Delta x} = 100$, $a\Delta x = \frac{2\Delta x}{b} = 0.02$. A reference solution is achieved from the implicit algorithm with $\Delta t = 0.0001$ and polynomial order 5 elements. Here implicit algorithm means that subiterations are employed in each time step as illustrated in Figure 4.2, while the fictitious mass method is

adopted with the fictitious coefficient $f_m = 1$ and the subiteration convergence tolerance is set as 10^{-9}. In the left plot of Figure 4.26, the convergence rates in time are studied for the stabilized explicit algorithm, with varying time step sizes from 0.0125 to 0.0625. We plot the errors of cylinder transverse displacement in logarithmic scale, as a function of time step size which is also in logarithmic scale. We see that a first order accuracy is obtained from the stabilized explicit algorithm, which is better than the half order accuracy we have expected from the previous analysis in section 4.2.3. On the other hand, from the implicit algorithm the optimal convergence rate (second order) is achieved. To demonstrate the effect of defect-correction subiterations, we fix $\Delta t = 0.005$ and vary the subiteration number K from 1 to 11. In the right plot of Figure 4.26, the transverse displacement errors are shown as a function of K. It can be observed that a much smaller error is achieved, by increasing K from 1 to 2. Moreover, if we further increase the subiteration number K to 11, the error get decreased by 1000 times. The finding is also validated in Figure 4.27, where we compare the time traces from various defect-correction subiteration numbers versus the reference solution. We can observe that when $K \geq 2$, the results are visually consistent with the reference solution. Therefore, we now take $K = 2$ defect-correction subiterations per time step, and investigate the impact of the added-mass effect by decreasing the density ratio ρ_s, as shown in Figure 4.28. Very stable results are obtained even when the density ratio is as low as $\rho_s = 0.5$, which could not be done with the standard explicit algorithm.

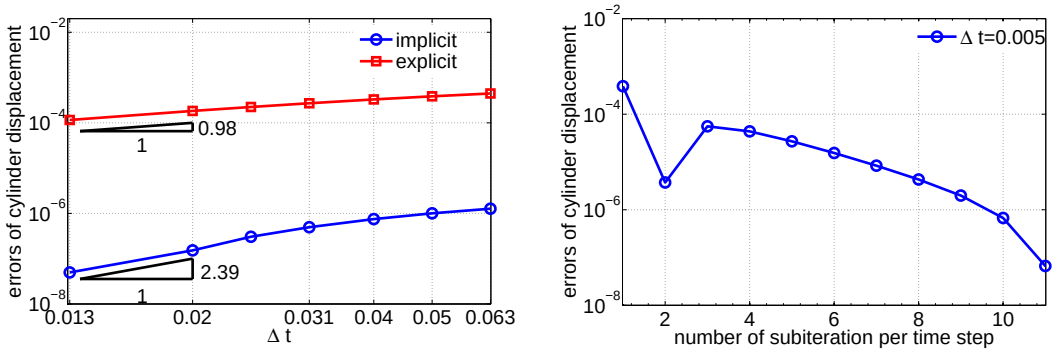

Figure 4.26: Convergence study for $\rho_s/\rho_f = 4$. Left: the convergence rate of stabilized explicit and and implicit algorithms. Right: the errors from increasing defect-correction subiteration number K when $\Delta t = 0.005$.

4.2.5 Summary

In this chapter, we proposed a new stabilized explicit coupling partitioned scheme for the fluid-structure interaction problem, where the pressure and velocity are decoupled. Using energy stability

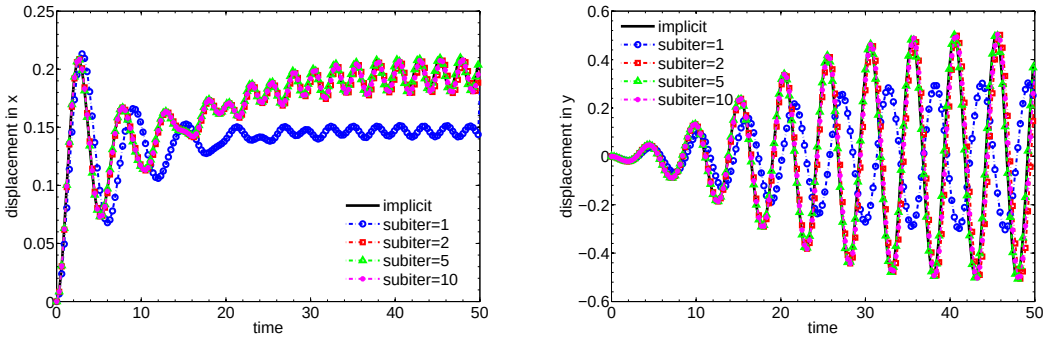

Figure 4.27: Time trace of displacement of the cylinder for various defect-correction subiteration number K, when $\Delta t = 0.005$ and $\rho_s/\rho_f = 4$.

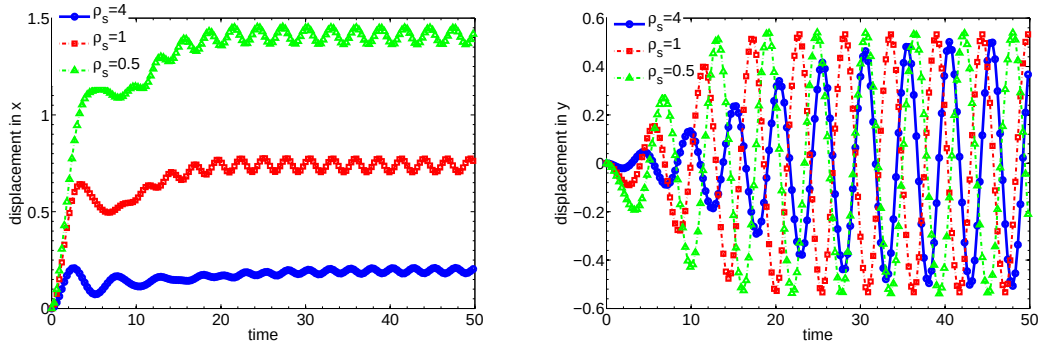

Figure 4.28: Time trace of displacement of the cylinder for various density ratios, with $\Delta t = 0.005$ and $K = 2$ defect-correction subiterations per time step.

analysis, it can be shown that the scheme is stable independent of the fluid-structure density ratio. However, the penalty terms degrade the time accuracy of the scheme, only half order accuracy in time can be expected for the structure displacement, fluid velocity and fluid pressure. Fortunately, the optimal accuracy can be recovered by performing several defect-correction subiterations in each time step. In the future, performances on higher order elements with more complicated geometries (eg. patient-specific aneurysm) should be investigated.

4.3 Fractional order structure model

As investigated in chapter 2.3, the fractional order models

$$\mathbf{S} + \tau_S^\alpha \frac{\partial^\alpha \mathbf{S}}{\partial t^\alpha} = \lambda(\mathrm{tr}(\mathbf{E} + \tau_E^\alpha \frac{\partial^\alpha \mathbf{E}}{\partial t^\alpha}))\mathbf{I} + 2\mu(\mathbf{E} + \tau_E^\alpha \frac{\partial^\alpha \mathbf{E}}{\partial t^\alpha}) \tag{4.3.1}$$

provide a more powerful alternative for describing arterial wall mechanics, because they are less sensitive to the parameter estimation compared with the integer-calculus-based models

$$\mathbf{S} + \tau_S \frac{\partial \mathbf{S}}{\partial t} = \lambda(\mathrm{tr}(\mathbf{E} + \tau_E \frac{\partial \mathbf{E}}{\partial t}))\mathbf{I} + 2\mu(\mathbf{E} + \tau_E \frac{\partial \mathbf{E}}{\partial t}). \tag{4.3.2}$$

Here $\mathbf{S}$, $\mathbf{E}$ are the second Piola-Kirchhoff stress tensor and the strain tensor, and μ, λ are the shear and Lame modulus, respectively. In this chapter, we employ the fractional order model for the structure part, and investigate the performances of viscoelastic models in simulating the coupled blood flow and arterial wall. This fluid-structure interaction (FSI) problem is numerically solved with the partitioned fluid-structure interaction procedure described in chapter 4.1, based on spectral element method. On the fluid side the parallel Navier-Stokes solver NEKTAR [6] is employed, and on the structure side we use the Grüwald-Letnikov formula as developed in section 2.3. To resolve the added-mass effect which appears in the hemodynamic FSI simulations, we adopt the fictitious mass method with optimal coefficients suggested by the analysis in chapter 4.1.

In this chapter, the contents are organized as follows. We first investigate the interaction of a rigid circular cylinder with surrounding flows in section 4.3.1, where the damping term is modeled by fractional derivatives. In section 4.3.2 we consider a straight tube with pulsatile inflow as an idealization of an arterial flow, and investigate the performance of fractional order arterial wall models with various viscoelastic parameters. To further assess the need for 3D simulations, the simulation results are compared with those obtained from 1D models in [3]. In section 4.3.3 a patient-specific aneurysm model is tested, whose arterial geometry is extracted from Magnetic Resonance Imaging data. We end in section 4.3.4 with a brief summary.

4.3.1 Vortex-induced vibrations

In the following we consider the transverse free oscillation of a circular cylinder excited by the vortex shedding of the surrounding fluids, as a classical problem in vortex-induced vibration (VIV). The cylinder movement in y direction is described by the fractional order model

$$\rho_s \frac{d^2\eta}{dt^2} + 2\rho_s \xi \omega_n \frac{d^\alpha \eta}{dt^\alpha} + \rho_s \omega_n^2 \eta = \oint \mathbf{n}_f \cdot [-p\mathbf{I} + 2\rho_f \nu(\nabla \mathbf{u} + \nabla \mathbf{u}^T)] ds, \tag{4.3.3}$$

where ξ and $f_n = \omega_n/(2\pi)$ are the structural damping factor and the natural frequency of the cylinder, respectively. α stands for the fractional order, with the fractional order derivative defined in the Riemann-Liouville sense as in (2.3.3). Here the spring-pot element $2\xi\omega_s \frac{\partial^\alpha \boldsymbol{\eta}}{\partial t^\alpha}$ [3] governs the damping behavior which interpolates between the purely elastic and viscous behaviors. To investigate the numerical performance of the fractional order model, we employ the mesh as shown

in Figure 4.4. To discretize in time, the second order derivative is approximated with the Newmark scheme (4.1.16), and for the fractional order derivative we employ the Grüwald-Letnikov formula (2.3.6). In the following, we take $\rho_s = 1$ for all tests and analysis, and assume that

$$\eta(t) = 0, \ \frac{d\eta(t)}{dt} = 0 \tag{4.3.4}$$

for $t \leq 0$. Under these assumptions, we have

$$\lim_{\alpha \to 0} \frac{d^\alpha \eta}{dt^\alpha} = \eta(t),$$

$$\lim_{\alpha \to 1} \frac{d^\alpha \eta}{dt^\alpha} = \frac{d\eta(t)}{dt}.$$

Therefore, $2\xi\omega_n$ can be viewed as a stiffness coefficient when $\alpha \to 0$, and it plays as a damping coefficient when $\alpha \to 1$.

Before the fluid-structure iteraction simulations, we first analyze the resonance frequency via Fourier expansion and validate the estimates in forced vibration cases. Taking a sinusoidal forcing term $F_0 \sin(\omega t)$, we could obtain the solution for

$$\frac{d^2\eta}{dt^2} + 2\xi\omega_n \frac{d^\alpha \eta}{dt^\alpha} + \omega_n^2 \eta = F_0 \sin(\omega t) \tag{4.3.5}$$

as

$$\eta(t) = \eta_0 \sin(\omega t - \phi) \tag{4.3.6}$$

where the ampitude η_0 is

$$\frac{F_0/m}{\sqrt{(\omega_n^2 - \omega^2 + 2\cos(\alpha\pi/2)\omega^\alpha \omega_n \xi)^2 + (2\sin(\alpha\pi/2)\omega^\alpha \omega_n \xi)^2}} \tag{4.3.7}$$

and the phase angle ϕ satisfies

$$\tan\phi = \left(\frac{2\sin(\alpha\pi/2)\omega^\alpha \omega_n \xi}{\omega_n^2 - \omega^2 + 2\cos(\alpha\pi/2)\omega^\alpha \omega_n \xi} \right). \tag{4.3.8}$$

Based on equation (4.3.7) we can estimate the resonant structural ω_n and the corresponding amplitude for any fixed forcing frequency ω. Taking $\omega = 1$, we can validate the above estimates in Table 4.12 for three α values 0.25, 0.75, 1.0 and different pairs of $(\omega_n, c = 2\xi\omega_n)$. One can see the

$\alpha = 0.25$						
(ω_n, c)	(0,1.0)	(0.283,1,0)	(0.4,1.0)	(0.707,1.0)	(1.0,1.0)	(0.283,0.5)
est η_0	2.56	2.61	2.55	1.75	1.0	2.0
comp η_0	2.57	2.62	2.56	1.75	1.0	2.0
$\alpha = 0.75$						
(ω_n, c)	(0,0.5)	(0.707,0.5)	(0.894,0.5)	(1.0,0.5)	(1.225,0.5)	(1.225,2.0)
est η_0	1.07	1.80	2.16	2.00	1.20	0.45
comp η_0	1.10	1.81	2.17	2.00	1.20	0.45
$\alpha = 1.0$						
(ω_n, c)	(0.935,0.468)	(0.987,0.494)	(0.88,0.44)	(0.82,0.41)	(1.04,0.52)	(2.0,1.0)
est η_0	2.07	2.02	2.02	1.91	1.91	0.32
comp η_0	2.07	2.02	2.02	1.91	1.91	0.32

Table 4.12: Estimated and computational oscillation ampitudes for fractional order cylinder body oscillator.

theoretical oscillation amplitude matches well with the computational results.

Now we will turn to the vortex-induced vibration cases. Similar as in section 4.1.4, the simulations are performed in a 2D domain $[-5, 20] \times [-5, 5]$, and the cylinder is of radius 0.5 with its center at the origin. A uniform steady flow with $U_\infty = 1$ is imposed at the inlet $x = -5$, and at the outlet $x = 20$ a zero Neumann boundary condition is applied. Along the crossflow direction, we set a periodic boundary condition. In this test, we assume both the fluid density and the cylinder mass to be of one unit: $\rho_f = \rho_s = 1$, and fix the damping factor as $\xi = 0.25$. The Reynolds number is set to be $Re = 100$ based on the cylinder radius. To obtain a fair comparison between our cases, we take a uniform time step size $\Delta t = 0.01$, and all the simulations are done using spectral elements with polynomial order 2. To investigate the lock-in region for different fractional order α, we vary the natural frequency f_n for each fixed fractional order $\alpha = 0.25$, 0.5, 0.75 and 1. With a static cylinder, this problem has corresponding fluid vortex shedding frequency as $f = \omega/(2\pi) = 0.1783$. In the left plot of Figure 4.29, we show the maximum cylinder displacement as a function of the fluid/cylinder natural frequency ratio $f/f_n = \omega/\omega_n$, and in the right plot the resultant VIV frequency f_o is displayed as a function of the structural natural frequency f_n. From the results we can see that when α increases, stronger damping can be observed. Concerning the effect of varying cylinder natual frequency f_n on vortex-induced vibration frequency f_o, the response from fractional order damping are still quite consistent with what for the classical VIV: when f_n is around $0.7f$ to $1.2f$ we have the lock-in region for VIV.

4.3.2 Blood flow in an artery

In this section, we consider a idealized model for an artery modeled as a straight tube. The fluid subdomain is taken as a cylinder with radius $1mm$ and length $4mm$, and the structure subdomain is the thin-layered arterial wall with a thickness $0.105mm$, which covers the fluid subdomain uniformly. The meshes for both subdomains are as illustrated in Figure 4.8. In all tests we take the fluid density

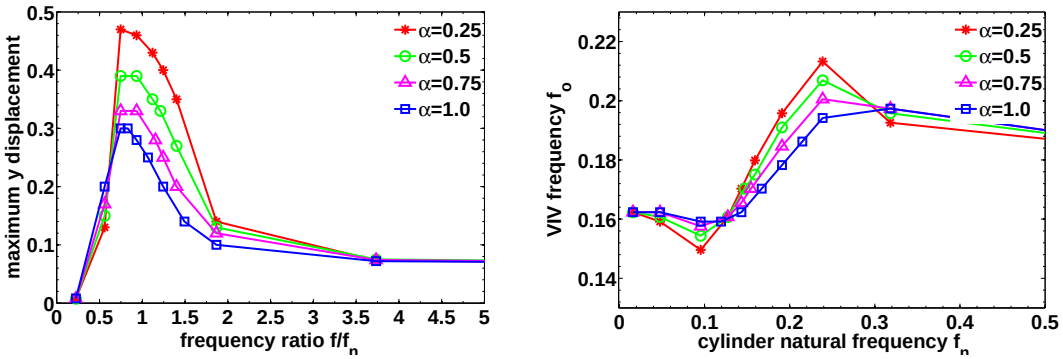

Figure 4.29: VIV results for cylinder y displacement. Taking $\xi = 0.25$. Left: amplitude. Right: frequency ratio.

Parameter	value
Young's Modulus	$0.3Mpa$
Poisson ratio	0.3
Blood density	$1.06g/cm^3$
Wall thickness	$0.0105cm$
Inlet radius	$0.1cm$
Kinematic viscosity	$3.8 \times 10^{-2} cm^2/s$
Average flow rate	$20ml/min$
Time step size	$9.4 \times 10^{-5}(sec)s$
Polynomial order	3

Table 4.13: Parameters used in the idealized artery model simulations.

as $\rho_f = 1060kg/m^3$, and the structure density $\rho_s = 1.2\rho_f$. On the fluid solver, a Womersley velocity profile with 8 Fourier coefficients is imposed at the inlet boundary, and on the outlet, a vanishing pressure boundary condition $p = 0MPa$ as well as a zero Neumann boundary condition for velocity are imposed. The arterial wall at the inlet are clamped, and we apply no traction load at the external surface and the outlet. All the other physical and numerical parameters are summarized in Table 4.13, noting that all the physical parameters are consistent with those in the second numerical example of chapter 4.1, except the Young's modulus which is adjusted to be 0.3MPa here. All the results shown here are generated on elements with polynomial order 3. For more details, we refer the interested readers to section 4.1.4.

Comparison between different models

While considering a pure elastic model for the arterial wall, in Figure 4.30 we show the distribution of structural displacements at four time instants: $2T$, $t = 2\frac{2T}{9}$, $t = 2\frac{T}{2}$ and $t = 2\frac{13T}{18}$. Similar as in [3], four viscoelastic models will be studied for the arterial wall. In Table 4.14 we summarize the viscoelastic parameters employed in these models, and we will compare their performances

	α	τ_E (sec)	τ_S (sec)
SLS1	N/A	0.05	0.025
SLS2	N/A	29.3	16.9
FOV-SLS1	0.29	1.84	0.076
FOV-SLS2	0.20	11.74	7.61

Table 4.14: Parameters employed in fractional-order SLS models: solid tube case.

with that from the pure elastic model. To compare with the results from viscoelastic models, in Figure 4.30 we first show the distribution of structural displacements from pure elastic arterial wall model, at four time instants: $2T$, $t = 2\frac{2T}{9}$, $t = 2\frac{T}{2}$ and $t = \frac{13T}{18}$. In figure 4.31, the displacement distribution from elastic models are displayed, at the systolic peak $t = 2\frac{2T}{9}$. It could be observed that all viscoelastic models the viscous dissipation decreases the deformation in different extents: the FOV-SLS2 case gives results which are the closest to that from the pure elastic model, and in cases SLS2 and FOV-SLS1 the new models greatly decrease the predicted deformation. To see the temporal changes of arterial wall deformation more clearly, in Figure 4.32, the time traces for displacement at a sample point $(1, 0, 2)$ are displayed, with the pressure-radial displacement hysteresis loop shown in Figure 4.33. Note that in the left plot of Figure 4.32, the black lines mark four time instants in the cardiac cycle, which correspond to the time instants for the displacement magnitudes shown in Figure 4.30. We can see that although the elastic response dominates in all models, the varying viscoelastic parameters result a significant change in displacements. Among all models, the SLS2 and FOV-SLS1 models produce relatively stiffer responses, and therefore predict much smaller arterial wall displacements. Moreover, it is shown in Figure 4.33 that the viscous dissipation can be clearly observed from SLS1 model, but not that much from the SLS2 model. This finding highlights that the integer order SLS model is sensitive to the relaxation parameters. However, the fractional order model appears to be much more sensitive to the parameters, while arising from 1D to 3D: Comparing the two fractional order model cases FOV-SLS1 and FOV-SLS2, the maximum radial displacement varies by 50%, which is opposite to the observations in [3] where these two models predicted very close results.

Effect of varying viscoelastic coefficients

To further evaluate the sensitivity of the 3D viscoelastic arterial wall models, we will study the behavior of fractional order arterial wall models by varying the viscoelastic parameters α, τ_E and τ_S. We first vary the fractional order α between $0 \leq \alpha \leq 1$ while keeping the same relaxation times of SLS1 model: $\tau_E = 0.050Sec$, $\tau_S = 0.025Sec$. The displacement time traces at the middle of tube are compared in Figure 4.34, for $\alpha = 0.0$, 0.2, 0.4 and 1.0. Note that while $\alpha = 0$ the

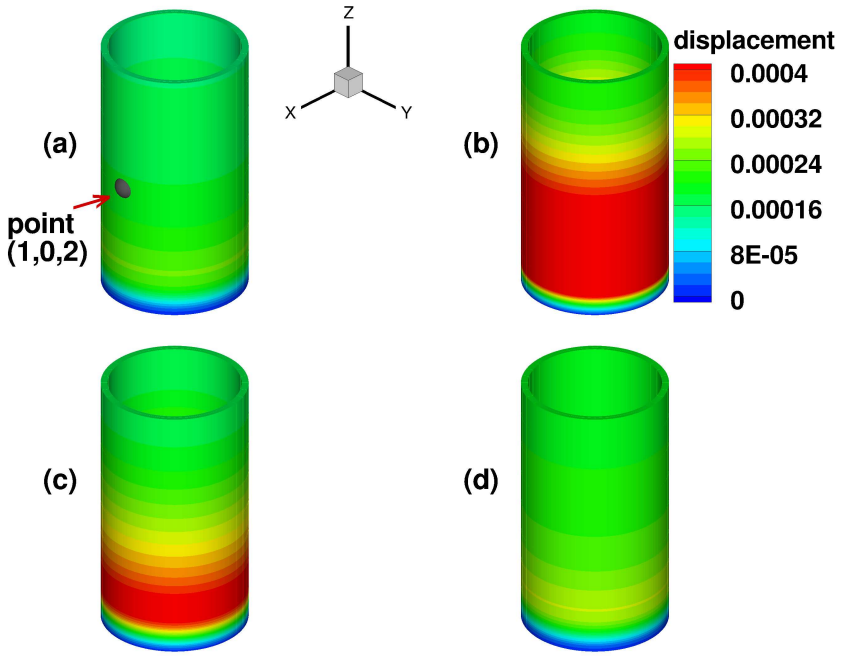

Figure 4.30: Displacements (in millimeters) for the elastic tube test at $t = 2T$ (upper left), $t = 2\frac{2T}{9}$ (upper right), $t = 2\frac{T}{2}$ (lower left), $t = 2\frac{13T}{18}$ (lower right).

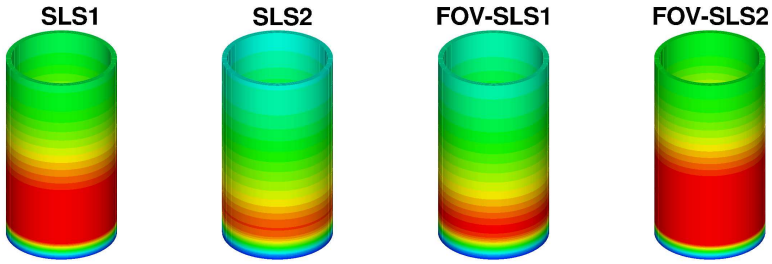

Figure 4.31: Displacements (in millimeters) for the viscoelastic tube test at systolic peak $t = 2\frac{2T}{9}$. From left to right are obtained with: model SLS1; model SLS2; model FOV-SLS1 and model FOV-SLS2.

pure elastic model is recovered, and while $\alpha = 1.0$ we obtain the solution of the SLS1 model. Although the displacement time trace results in Figure 4.34 do not vary much, from the pressure-radial displacement hysteresis loop in Figure 4.35 we can see that when α increases the viscous dissipation becomes more important. This is consistent with the discussions in [3]. Moreoever, now we will investigate how sensitive the solution is to the choice of relaxation parameters τ_E and τ_S. In Figures 4.36-4.37, we include results for fixed $\alpha = 0.2$ with various relaxation time

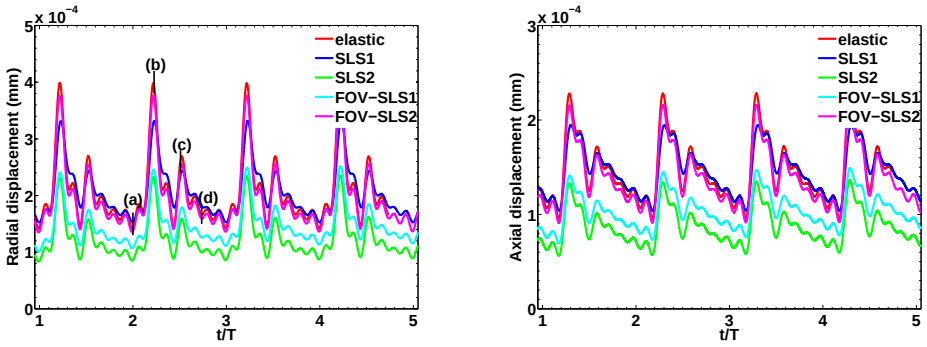

Figure 4.32: Time traces at point $(1, 0, 2)$ in the tube test, from varying viscoelastic models. Left: radial displacement; right: axial displacement.

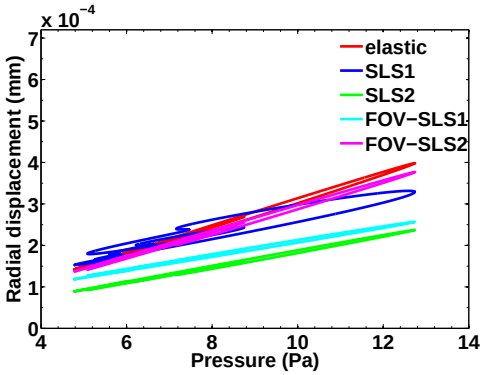

Figure 4.33: Pressure-radial displacement hysteresis loop at point $(1, 0, 2)$ in the tube test, from varying viscoelastic models.

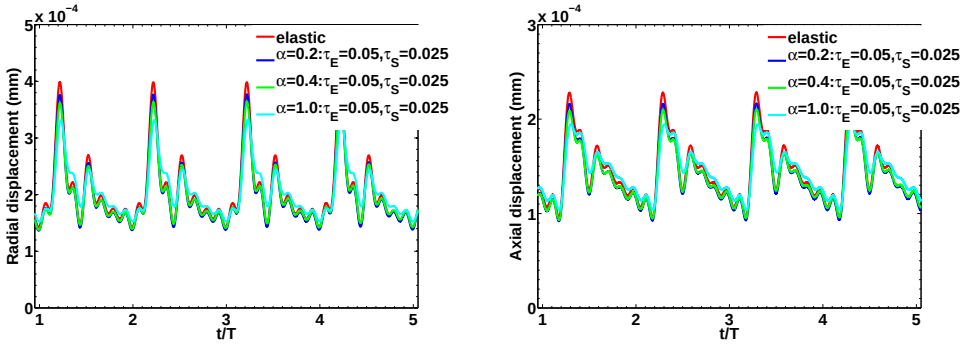

Figure 4.34: Time traces at point $(1, 0, 2)$ in the tube test, from fixed $\tau_E = 0.05$, $\tau_S = 0.025$ and varying α. Left: radial displacement; right: axial displacement.

parameters, and the solutions for $\alpha = 1.0$ are displayed in Figures 4.38-4.39. When $\alpha = 1.0$, more noticeable visous response can be observed, and the arterial wall deformation is more sensitive to the relaxation spectrum used. That means, when the fractional order α is relatively small, the

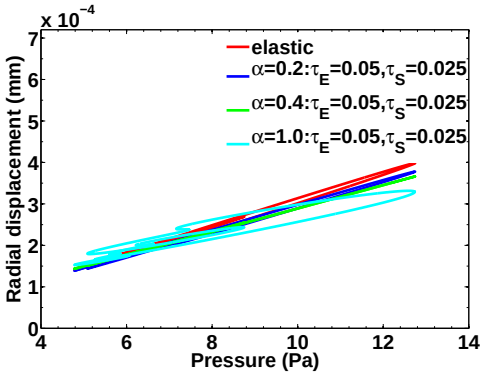

Figure 4.35: Pressure-radial displacement hysteresis loop at point $(1, 0, 2)$ in the tube test, from fixed $\tau_E = 0.05$, $\tau_S = 0.025$ and varying α.

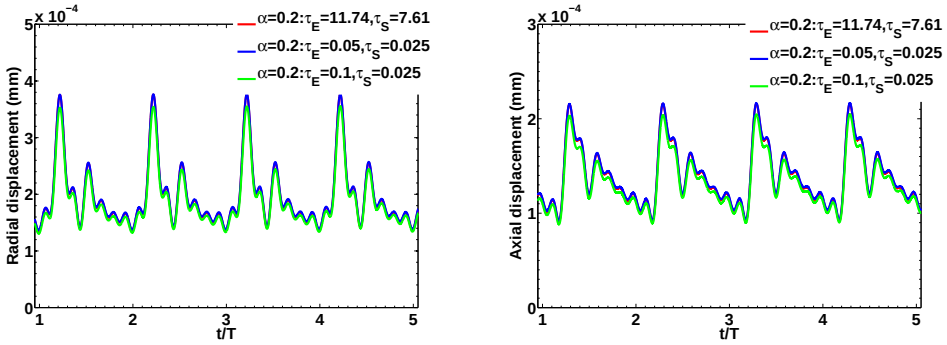

Figure 4.36: Time traces at point $(1, 0, 2)$ in the tube test, from fixed $\alpha = 0.2$ and varying relaxation parameters. Left: radial displacement; right: axial displacement.

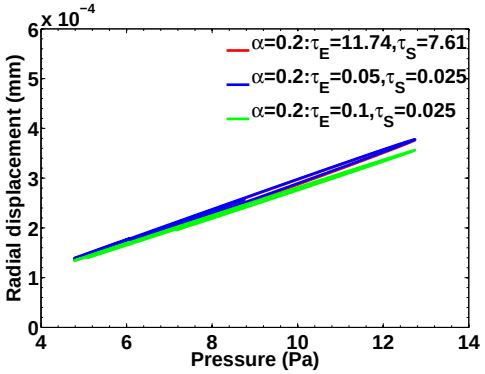

Figure 4.37: Pressure-radial displacement hysteresis loop at point $(1, 0, 2)$ in the tube test, from fixed $\alpha = 0.2$ and varying relaxation parameters.

effect of the fractional order SLS model (2.3.2) has low sensitivity on the relaxation parameters. Therefore it overcomes the caveat for using the integer order SLS model in simulating arterial networks, because we can only hope to get estimates of τ_E and τ_S at limited anatomic locations.

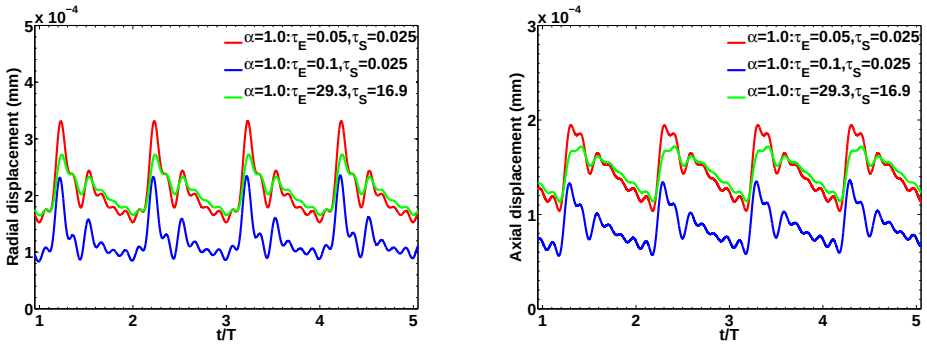

Figure 4.38: Time traces at point $(1, 0, 2)$ in the tube test, from fixed $\alpha = 1.0$ and varying relaxation parameters. Left: radial displacement; right: axial displacement.

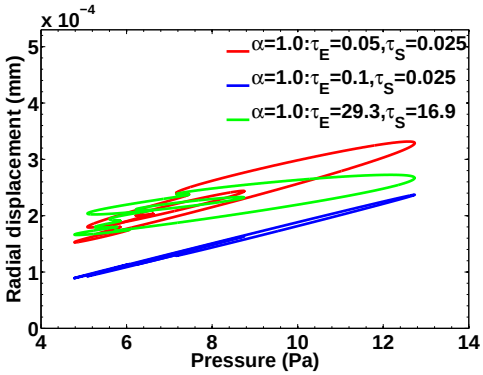

Figure 4.39: Pressure-radial displacement hysteresis loop at point $(1, 0, 2)$ in the tube test, from fixed $\alpha = 1.0$ and varying relaxation parameters.

Comparison between 1D and 3D simulations

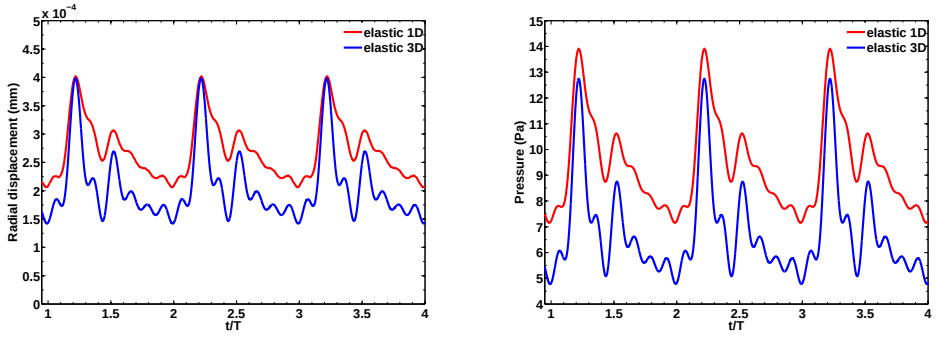

Figure 4.40: 1D-3D comparison of time traces at point $(1, 0, 2)$ in the tube test, from pure elastic model. Left: radial displacement; right: pressure.

The above findings reveal differences between 1D and 3D simulations, i.e., the 3D solutions

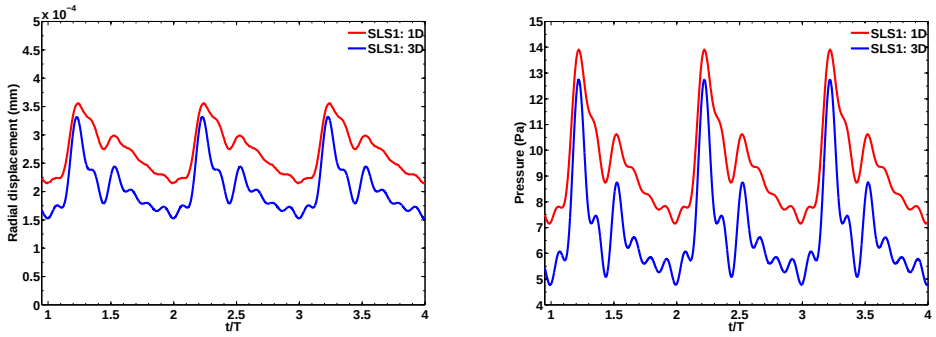

Figure 4.41: 1D-3D comparison of time traces at point $(1, 0, 2)$ in the tube test, from SLS1 model. Left: radial displacement; right: pressure.

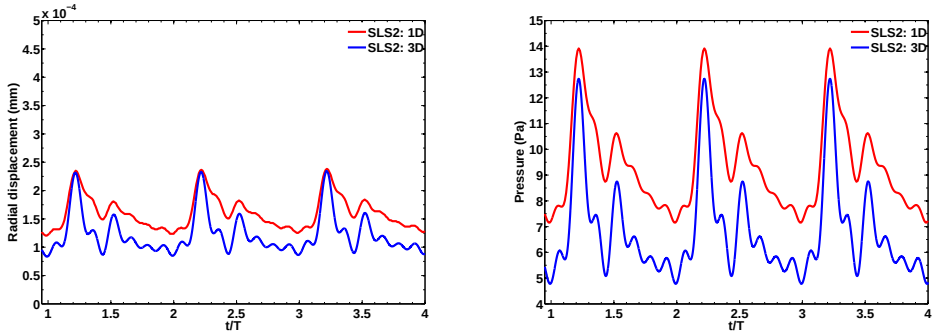

Figure 4.42: 1D-3D comparison of time traces at point $(1, 0, 2)$ in the tube test, from SLS2 model. Left: radial displacement; right: pressure.

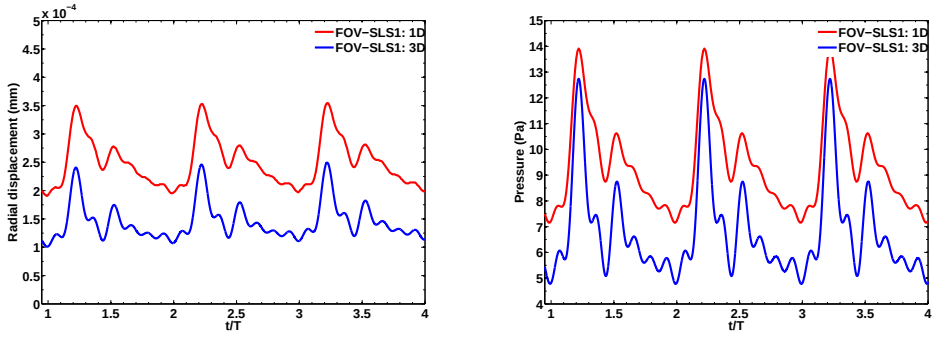

Figure 4.43: 1D-3D comparison of time traces at point $(1, 0, 2)$ in the tube test, from FOV-SLS1 model. Left: radial displacement; right: pressure.

seem more sensitive to the viscoelastic parameters. Now we will compare the 1D and 3D computed solutions in the terms of radial displacement and the pressure waveform at the middle point. In Figures 4.40-4.44 we present the results from the pure elastic model and the viscoelastic models with parameters listed in Table 4.14. Generally the 1D simulations overestimate the blood pressures

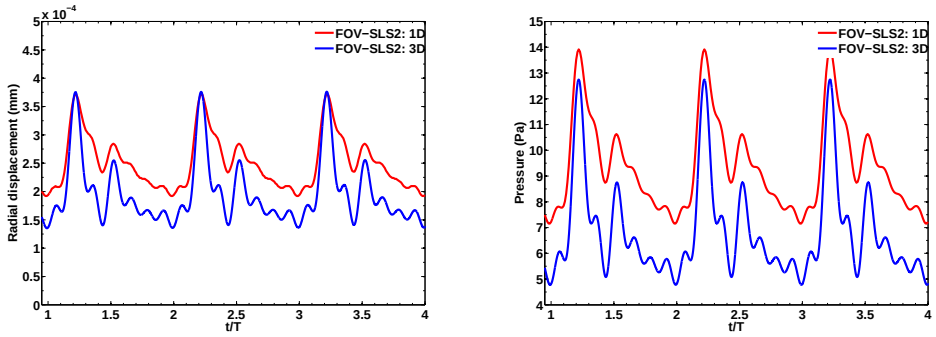

Figure 4.44: 1D-3D comparison of time traces at point $(1, 0, 2)$ in the tube test, from FOV-SLS2 model. Left: radial displacement; right: pressure.

and therefore also the arterial wall deformations. In most of cases (except the FOV-SLS1 model), the 1D models provide good prediction on the maximum radial displacement. However, to get more reliable predictions and to enable the possibility of simulating on complicated geometries, the 3D models are recommended.

4.3.3 Blood flow in a patient-specific aneurysm

In this section we will investigate the fractional order models on a patient-specific aneurysm geometry, which was extracted from Magnetic Resonance Imaging data [4], and also employed in the FSI simulations with pure elastic arterial wall model in chapter 4.1. This aneurysm locates at the eye level, in the cavernous segment of the right internal carotid artery. We will perform our simulations on the meshes as shown in Figures 2.27, where the fluid subdomain has finer elements near the vessel wall to resolve the boundary layers, and the solid subdomain is composed of two layers of prismatic elements on the vessel wall. A Womersley velocity profile with 8 harmonics is imposed at the inlet boundary of the fluid solver, and a zero Neumann boundary condition for velocity is employed at the outlet. The outlet pressure $\bar{p}$ is determined from the flow rate $Q(t)$, the resistant R, and the capacitance C following [4]

$$\bar{p}(t) + RC\frac{d\bar{p}(t)}{dt} = Q(t)R. \tag{4.3.9}$$

The arterial outlet is assumed to be undeformed when the outlet pressure $\bar{p}(t)$ reaches its lowest point at $t = 0.0571sec$. We start the FSI simulations from the resultant flow field of rigid wall simulations on the fluid subdomain (where we set $t = 0$ as the starting time of FSI). The structure is considered undeformed at $t = 0$. To integrate in time, we employed the second-order splitting scheme for the fluid solver, as illustrated in section 4.1.2. On the structure side, the first-order

Parameter	value
Young's Modulus	$3Mpa$
Poisson ratio	0.3
Blood density	$1.06g/cm^3$
Arterial wall density	$1.06g/cm^3$
Wall thickness	$0.01cm$
Inlet radius	$0.224cm$
Kinematic viscosity	$3.8 \times 10^{-2} cm^2/s$
Womersley Number	4.2
Average flow rate	$70ml/min$
Time step size	$6.3 \times 10^{-4} s$
Mass damping parameter	$0s^{-1}$
Stiffness damping parameter	$0s$
Resistant parameter	$7.844 \times 10^2 dyn \cdot s/cm^5$
Capacitance parameter	$7.285 \times 10^{-5} cm^5/dyn$
Polynomial order	3
Fictitious mass coefficient	2.08

Table 4.15: Parameters used in the patient-specific aneurysm simulations with fractional order models.

Grüwald-Letnikov formula introduced in chapter 2.3 is used, with fictitious mass method applied to stabilize the FSI partitioned procedure. All the simulations are done with the physical and numerical parameters summarized in Table 4.15.

To compare the computed evolution of the aneurysm deformation from different models, we first display the displacement time traces of three points on the interface. The locations of these points are shown in Figure 4.13. The computed inlet pressure and the time traces for displacements at these three points are shown in Figure 4.45, for the pure elastic model, the FOV-SLS1 and the FOV-SLS2 models. Similar to what we have observed in section 4.3.2, the FOV-SLS1 model predicts a much smaller deformation comparing with that from the other two models, which results a larger blood pressure drop in each cardiac cycle. To investigate the displacement distribution on the whole aneurysm, we take four time instants in a cardiac cycle: $\frac{T}{7}$, $\frac{2T}{7}$, $\frac{3T}{7}$, $\frac{5T}{7}$ (as marked by black lines in the inlet pressure plot of Figure 4.45), and display their corresponding displacement amplitudes from the pure elastic, FOV-SLS1 and FOV-SLS2 arterial wall models in Figures 4.46, 4.47 and 4.48, respectively. It can be observed that although the displacement magnitudes vary while simulating with different arterial wall models, they all reach the maximum deformation near the systolic peak, and the distribution pattern does not change much.

4.3.4 Summary

In this chapter, we investigate the performances of viscoelatic models in fluid-structure interaction simulations. To be more specific, we first analyze and simulate the vortex-induced vibration problem with fractional order damping terms, with special emphasis on the resultant lock-in region. It is observed that when α increases, stronger damping can be observed, but the resonant

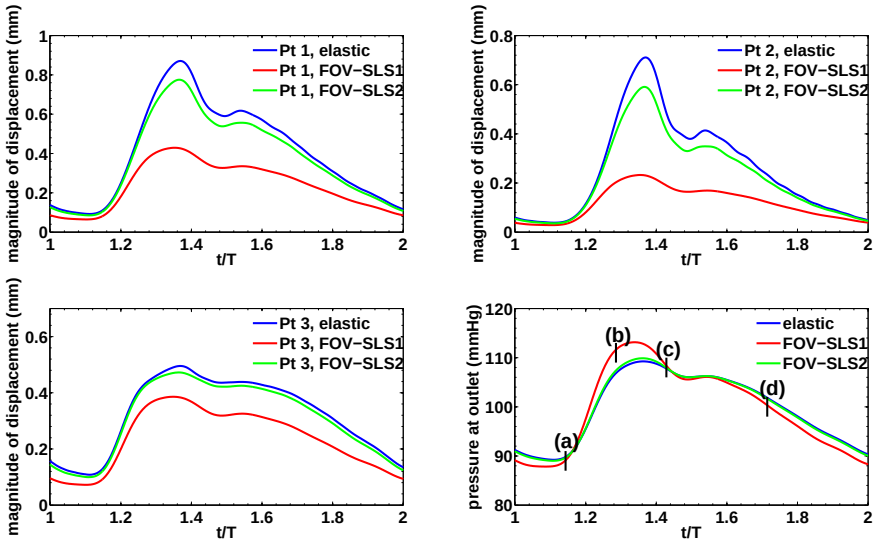

Figure 4.45: Time traces in patient-specific aneurysm with viscoelastic arterial wall models. Upper left, upper right, bottom left: displacement profiles for corresponding points; bottom right: pressure imposed at the inlet.

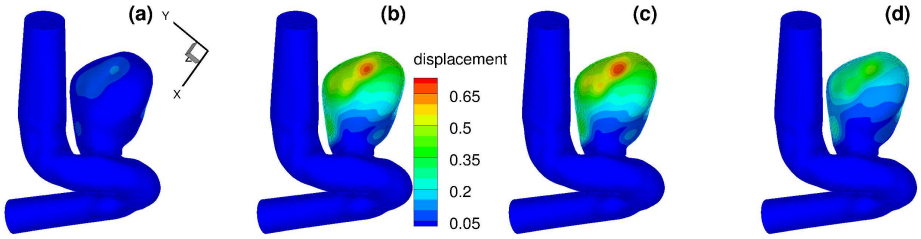

Figure 4.46: Displacements (in mm) for patient-specific aneurysm with pure elastic arterial wall model, at $\frac{T}{7}$ (upper left), $\frac{2T}{7}$ (upper right), $\frac{3T}{7}$ (bottom left) and $\frac{5T}{7}$ (bottom right).

behavior does not vary much. In the second part, the coupled problem of blood flow and arterial wall movements is studied. We compare several models with the same elasticity parameters and different viscoelastic parameters which are calibrated from data in the literature. This comparison study indicates that for the integer order SLS models, the viscous behavior strongly depends on the relaxation parameters τ_E and τ_S, while the fractional order models are less sensitive. Especially when the fractional order $\alpha \to 0$, the viscous response gets less noticeable, and the fractional model is tuned by the fractional order α. This finding is consistent with what observed in the 1D models [3]. The only difference is, in the 3D cases varying the viscoelstic parameters from model FOV-SLS1

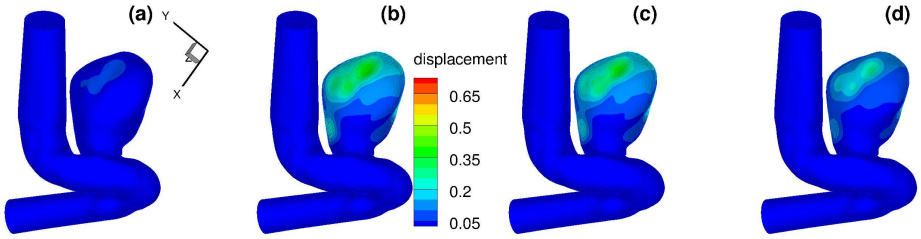

Figure 4.47: Displacements (in mm) for patient-specific aneurysm with FOV-SLS1 model, at $\frac{T}{7}$ (upper left), $\frac{2T}{7}$ (upper right), $\frac{3T}{7}$ (bottom left) and $\frac{5T}{7}$ (bottom right).

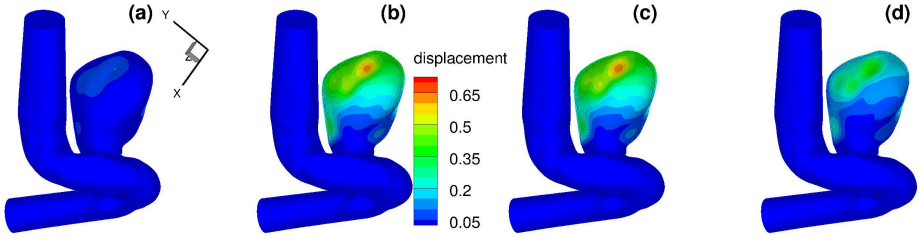

Figure 4.48: Displacements (in mm) for patient-specific aneurysm with FOV-SLS2 model, at $\frac{T}{7}$ (upper left), $\frac{2T}{7}$ (upper right), $\frac{3T}{7}$ (bottom left) and $\frac{5T}{7}$ (bottom right).

to model FOV-SLS2 results to a significant change in the arterial wall deformation, which is not observed in the 1D simulations. This finding shows that when the fractional order is small, the 3D fractional-order models are more sensitive to the fractional order α comparing with the 1D models.

4.4 Application: fairing performance evaluation

4.4.1 Background

In deepwater offshore oil operations, riser interference and vortex-induced vibrations (VIV) are severe problems for risers, umbilicals and tendons in areas of strong currents. Such industry demands have greatly motivated the investigations of various methods for suppressing vortex-induced vibrations either experimentally [146, 147, 148, 149, 150, 151] or numerically [152, 95], over the past decades. In theory, an effective VIV suppression device should not only eliminate the vortex shedding, but also help reducing the drag force thereby resolving the concern of the loads caused by strong currents. To get a comprehensive review of solutions for VIV suppression, we refer the readers to [153, 154] and the references therein. Among all these VIV suppression solutions, free-

to-rotate suppressors such as splitter plates and fairings with different sharps are widely studied and employed to mitigate VIV and avoid interference as they reduce both drag forces and VIV [146, 148, 149]. Assi et al [148] found that with a pair of parallel plates installed on the sides of the cylinder, the maximum VIV suppression and drag reduction occurred, and the level of rotational friction between the fairing and the cylinder played an important role. Specificly, the rotational damping and friction needs to be high enough to stablize the device and achieve a better suppression performance. This requirement draws attention to the importance of parametric studies in fairing design and analysis. Hence, the critical parameters for fairing stability and performance need to be identified, and the effects of varying Reynolds number needs to be investigated. However, experimentally the hydrodynamic performance evaluation for fairings is done by tank testing, which is expensive and very difficult to find model basis availability. Therefore, computational fluid dynamics seems a favored option for fairing design and analysis, because it avoids schedule issues with testing, reduces the cost of testing, and improves quality. In the present work we will contribute to the understanding of a type of fairing (see Figure 4.49) employed in industry, by running fluid-structure interaction (FSI) simulations with our general purpose spectral element solver NEKTAR. To the authors' best knowledge, this is the first thorough numerical study of the VIV suppressing performances for varying rotational damping and friction coefficients, and also for a fairing with a pair of parallel plates attached.

In the numerical simulations, we are going to adopt the partitioned method where the fluid-structure interaction system is split into separate fluid and structure solvers, because of its better computational scalability and software modularity. However, the partitioned procedure in the fairing simulations is problematic, because of the so-called added-mass effect [83]. Especially when the structure is light, or when the fairing has low rotational inertia, the added-mass effect becomes stronger and severely affects the stability of the fluid-structure interaction (FSI) procedure. To resolve these instabilities, a strong coupling is required to impose continuity at the interface at each time step. A number of approaches have been developed more recently to accelerate the convergence of the partitioned algorithm, including the Robin-Robin scheme [112, 113, 120], the interface artificial compressibility [110, 132], the stabilized explicit method [133, 122], and our fictitious methods [4, 81]. In this work, we will adopt and generalize the fictitious methods, by developing a similar modified governing equation for the fairing rotational equation. In this new *fictitious inertia method*, additional acceleration terms are introduced in the structure solver to balance the added-mass effect caused by low rotational inertia and to provide further stabilization for problems with large fairing rotations.

The chapter is organized as follows. In section 4.4.2 we describe the FSI governing equations

and discretization methods: firstly the governing equations of cylinder and fairing models are derived from conservation laws; then the numerical methods for the fluid and solid models are described; lastly, we introduce the fictitious inertia method in the solid model, and summarize the FSI coupling procedure at each time step for the full partitioned algorithm. Various numerical tests are performed in section 4.4.3, for two values of Reynolds numbers. To demonstrate the effect of our method and investigate the optimal fictitious coefficient, firstly we apply the fictitious method with varying coefficients, and compare the averaged subiteration numbers required for each time step. With the optimal fictitious coefficients, we then provide a thorough parametric study on the fairings, with emphasis on their performances in VIV suppression and drag force reduction. When $Re = 100$ and $Re = 500$, the critical parameters for fairing stability and performance are identified, more specifically the rotational damping and friction. We end in section 4.4.4 with a brief summary. Additional details on the expression for friction between the cylinder and fairing are derived in the appendix.

4.4.2 Models and formulation

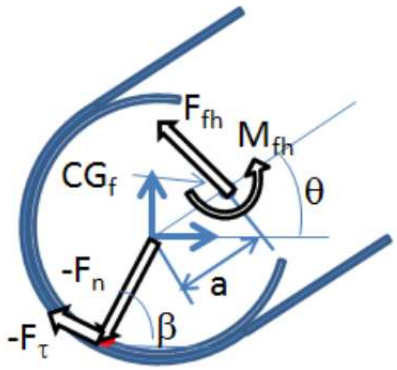

Figure 4.49: Coordinate system and symbol definition for fairing and cylinder motions.

In this section we will describe the formulation for VIV of a rigid, spring mounted cylinder, which is covered with fairings as shown in Figure 4.49. The cylinder is free to respond in both cross-flow and stream-wise directions. The fairing moves following the cylinder, with an additional degree of freedom because it can rotate around the cylinder axis subjected to the hydrodynamic torque. The equations for fairing and cylinder motions will be derived, and our fluid-structure interaction procedure with fictitious methods will be employed to solve these equations. The geometry and mesh used in the following derivations and simulations are shown in Figure 4.50. To be more specific, the flow is simulated in a 2D domain $[-5, 20] \times [-5, 5]$, with a solid cylinder of radius

0.5 at the origin and a fairing surrouding the cylinder. At the inlet, a uniform steady flow with $U_\infty = 1$ is imposed, and at the outlet a zero Neumann boundary condition is employed. Along the crossflow direction, a periodic boundary condition is applied. Therefore, we are simulating the motions of an array of cylinders which are arranged in the crossflow direction. The domain in Figure 4.50 is of length 10 in y direction, which yields a gap size between each two neighboring cylinders as 10. The fairing is composed by two parts: firstly the circular body part, which covers $\frac{3}{4}$ of the cylinder and centered at the cylinder center with radius 0.6; the other part is a pair of parallel plates attached to the top and bottom points of the fairing circular part (see Figure 4.49). As shown in the right plot of Figure 4.50, in the initial configuration the plates are parallel to the stream-wise direction, with a length of 1.0, i.e., one cylinder diameter D. The mass on fairing is assumed to be evenly distributed, and therefore in the initial configuration the fairing's center of gravity locates at $(0.085, 0)$.

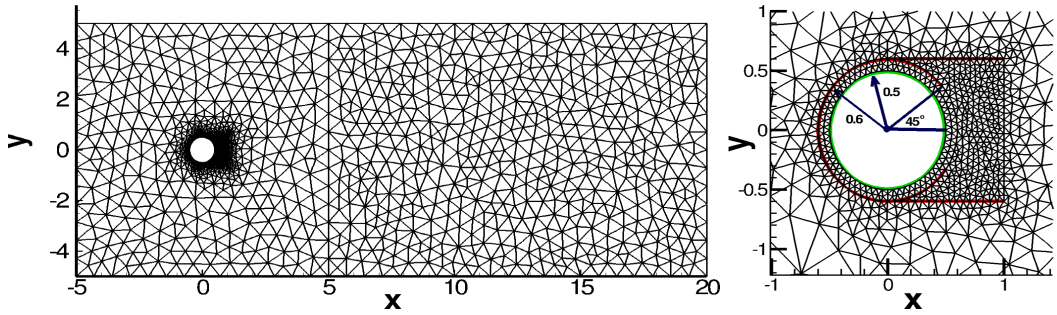

Figure 4.50: Left: mesh and geometry for fluid solver. Right: detailed mesh near the fairing and cylinder and structure geometries; here we use green to represent the cylinder and red to represent the fairing.

Cylinder and fairing models

The cylinder is assumed to be subjected to vortex-induced vibration with two degrees of freedom (DOF) in the (x, y) plane. The fairing is in contact with the cylinder and is free to rotate. There is a small gap between the fairing and cylinder with a single point of contact, where the fairing is pressed against the cylinder. As shown in Figure 4.49, the system allows body motions with five degrees of freedom, including the cylinder's horizontal and vertical motions (c_x and c_y), and the fairing's horizontal, vertical motions (f_x and f_y) and rotational angle (θ). Here we define the following symbols to be used in the equations of motions:

- CG_c, CG_f: gravity center of cylinder and fairing, respectively.
- a: distance from CG_c to CG_f.

- f_c: coefficient of friction between the cylinder and fairing.
- F_{chx}, F_{chy}: hydrodynamic force applied on the cylinder in the x and y directions, respectively.
- k_x, k_y: cylinder spring constant in the x and y directions, respectively.
- F_{fhx}, F_{fhy}: hydrodynamic force applied on the fairing in the x and y directions, respectively.
- I_f: fairing rotational inertia about CG_f.
- m_c, m_f: mass of cylinder and fairing, respectively.
- M_{fh}: hydrodynamic angular momentum applied on the fairing about CG_f.
- R: cylinder radius.
- β: contact angle.
- F_n: cylinder-fairing normal contact force.
- F_t: cylinder-fairing tangentail contact force.

To derive the equations of motions for the cylinder and fairing, we make the following assumptions:

1. There is no damping from the structure in translational and rotational directions;
2. The cylinder and the fairing are always in touch and have only one contact point;
3. The tangential contact Force F_t between the cylinder and the fairing is related to the normal contact force F_n following $F_t = f_c F_n$, where f_c is proportional to the sign function of $\dfrac{\partial \theta}{\partial t}$ with a constant sliding friction coefficient C_f, i.e.,

$$f_c = C_f \mathrm{sgn}\left(\frac{d\theta}{dt}\right). \tag{4.4.1}$$

   Here C_f can be seen as an index for the rotational damping and friction. More details about this formula are provided in Appendix A.9.

Based on these assumptions, the equations of motions for the *cylinder* are written about CG_c:

$$\begin{aligned} m_c\frac{\partial^2 c_x}{\partial t^2} + k_x c_x - F_n(\cos\beta + f_c \sin\beta) &= F_{chx}, \\ m_c\frac{\partial^2 c_y}{\partial t^2} + k_y c_y - F_n(\sin\beta - f_c \cos\beta) &= F_{chy}, \end{aligned} \tag{4.4.2}$$

and the equations of motions for the *fairing* are written about CG_f:

$$\begin{aligned} m_f \frac{\partial^2 f_x}{\partial t^2} + F_n(\cos\beta + f_c \sin\beta) &= F_{fhx}, \\ m_f \frac{\partial^2 f_y}{\partial t^2} + F_n(\sin\beta - f_c \cos\beta) &= F_{fhy}. \end{aligned} \tag{4.4.3}$$

From the right plot of Figure 4.49 we can see that the gravity centers of the cylinder and fairing are geometrically related as

$$\begin{aligned} c_x &= f_x - a\cos\theta, \\ c_y &= f_y - a\sin\theta. \end{aligned} \tag{4.4.4}$$

Substituting these expressions into (4.4.2), the equations of motion for cylinder become:

$$\begin{aligned} m_c \left[\frac{\partial^2 f_x}{\partial t^2} + a\left(\left(\frac{\partial \theta}{\partial t} \right)^2 \cos\theta + \frac{\partial^2 \theta}{\partial t^2} \sin\theta \right) \right] + k_x \left[f_x - a\cos\theta \right] - F_n \left(\cos\beta + f_c \sin\beta \right) &= F_{chx}, \\ m_c \left[\frac{\partial^2 f_y}{\partial t^2} + a\left(\left(\frac{\partial \theta}{\partial t} \right)^2 \sin\theta - \frac{\partial^2 \theta}{\partial t^2} \cos\theta \right) \right] + k_y \left[f_y - a\sin\theta \right] - F_n \left(\sin\beta - f_c \cos\beta \right) &= F_{chy}. \end{aligned} \tag{4.4.5}$$

In addition, we can derive another equation from the conservation of angular momentum. The total angular momentum $I_f \ddot{\theta}$ about CG_f should be equivalent to the resultant angular momentum exerted by cylinder-fairing contact force and the hydrodynamic angular momentum M_{fh} from the fluid. To be more specific, the torque of the cylinder-fairing normal contact force F_n about CG_f is $a\sin(\beta-\theta)$, and the torque of the cylinder-fairing tangential contact force F_t is $-(a\cos(\beta-\theta)+R)$. Therefore, we have the resultant angular momentum as

$$M_{fh} + F_n a \sin(\beta - \theta) - F_t(a\cos(\beta - \theta) + R).$$

By substituting the relation $F_t = f_c F_n$, the conservation of angular momentum can be expressed as

$$I_f \frac{\partial^2 \theta}{\partial t^2} - F_n[a\sin(\beta - \theta) - a f_c \cos(\beta - \theta) - R f_c] = M_{fh}. \tag{4.4.6}$$

Combining the equations of motion for the fairing (4.4.3) and the equations for cylinder (4.4.5), we obtain a system with 5 equations consisting of 5 unknowns $(f_x, f_y, \theta, \beta, F_n)$:

$$m_c\left[\frac{\partial^2 f_x}{\partial t^2}+a\left(\left(\frac{\partial\theta}{\partial t}\right)^2\cos\theta+\frac{\partial^2\theta}{\partial t^2}\sin\theta\right)\right]+k_x\left[f_x-a\cos\theta\right]-F_n\left(\cos\beta+f_c\sin\beta\right)=F_{chx}, \tag{4.4.7a}$$

$$m_c\left[\frac{\partial^2 f_y}{\partial t^2}+a\left(\left(\frac{\partial\theta}{\partial t}\right)^2\sin\theta-\frac{\partial^2\theta}{\partial t^2}\cos\theta\right)\right]+k_y\left[f_y-a\sin\theta\right]-F_n\left(\sin\beta-f_c\cos\beta\right)=F_{chy}, \tag{4.4.7b}$$

$$m_f\frac{\partial^2 f_x}{\partial t^2}+F_n(\cos\beta+f_c\sin\beta)=F_{fhx}, \tag{4.4.7c}$$

$$m_f\frac{\partial^2 f_y}{\partial t^2}+F_n(\sin\beta-f_c\cos\beta)=F_{fhy}, \tag{4.4.7d}$$

$$I_f\frac{\partial^2\theta}{\partial t^2}-F_n[a\sin(\beta-\theta)-af_c\cos(\beta-\theta)-Rf_c]=M_{fh}. \tag{4.4.7e}$$

Fluid-structure interaction

The right hand sides in the governing equations (4.4.7) for cylinder and fairing indicate that the motions of cylinder and fairing are subjected to the hydrodynamic forces and hydrodynamic angular momentum. On the other hand, the motions of cylinder and fairing in turn change the fluid domain and the boundary conditions. Therefore, this is a coupled fluid-structure interaction problem whose domain $\Omega \subset \mathbb{R}^2$ is composed of two parts: the fluid subdomain $\Omega_f(t)$ occupied by the fluid, and the structure subdomain Ω_s occupied by the cylinder and fairing. There is a common boundary between the two subdomains, which is the fluid-structure interface $\Sigma(t) = \Omega_f(t) \cap \Omega_s$. For the structure kinematics we solve the system (4.4.7) with the Newton-Raphson procedure. On the other hand, the fluid problem is solved with the spectral element solver NEKTAR [6]. The Navier-Stokes equation is stated in an arbitrary Lagrangian-Eulerian framework [136] since the fluid domain is changing with the movement of the cylinder and fairing. Roughly speaking, we aim to solve for three sets of variables in this FSI system: the fluid velocity $\mathbf{u}(\mathbf{x}, t)$, the fluid mesh velocity $\mathbf{w}(\mathbf{x}, t)$, and the 5 structure unknowns $(f_x, f_y, \theta, \beta, F_n)$. Here $\mathbf{x} = \mathbf{x}(t)$ and $\mathbf{X}$ are the position vectors in the deformed configuration and initial configuration, respectively. In the current work, we will employ the partitioned procedure as illustrated in [4, 81] to solve the fluid-structure interaction problem. To ensure the continuity on the interface, subiterations are employed at each time step. In the following sections, we will denote the subiteration number by the subscript k, and the time step number by the superscript n.

Fluid solver

In the fluid model we employ the incompressible Navier-Stokes equation:

$$\frac{\partial \mathbf{u}}{\partial t} + (\mathbf{u} - \mathbf{w}) \cdot \nabla \mathbf{u} = -\frac{\nabla p}{\rho_f} + \nu \nabla^2 \mathbf{u}, \quad \text{in } \Omega_f(t), \tag{4.4.8a}$$

$$\nabla \cdot \mathbf{u} = 0, \quad \text{in } \Omega_f(t), \tag{4.4.8b}$$

combined with the initial condition

$$\mathbf{u}(\mathbf{x}, t = 0) = \mathbf{u}_0(\mathbf{x}), \quad \text{in } \Omega_f(0), \tag{4.4.9}$$

and the Dirichlet boundary conditions on the interface, i.e.,

$$\mathbf{u} = \frac{\partial \boldsymbol{\eta}}{\partial t}, \quad \text{on } \Sigma(t), \tag{4.4.10}$$

which enforces the continuity of velocities. Here, $\mathbf{w}$, p, ρ_f, and ν stand for the mesh velocity, pressure, fluid density, and the kinematic viscosity, respectively; $\boldsymbol{\eta}$ is the displacement of the specific point at the cylinder or fairing surface, which can be calculated from the structure simulation results as:

$$\boldsymbol{\eta}(\mathbf{x}, t) = \begin{cases} \begin{pmatrix} c_x(t) \\ c_y(t) \end{pmatrix} + \mathbf{X}, & \text{on cylinder;} \\ \begin{pmatrix} c_x(t) \\ c_y(t) \end{pmatrix} + \begin{pmatrix} \cos\theta(t) & -\sin\theta(t) \\ \sin\theta(t) & \cos\theta(t) \end{pmatrix} \mathbf{X}, & \text{on fairing.} \end{cases} \tag{4.4.11}$$

At each time step, the mesh position $\mathbf{x}$ will be obtained from the integration of the mesh velocity. To generate the mesh velocity $\mathbf{w}$, we define a "lifting" from the structure displacement on the interface: given the displacement on the interface $\boldsymbol{\eta}|_\Sigma$, we employ a harmonic extension mapping from the initial fluid configuration $\Omega_f(0)$ to the current configuration $\Omega_f(t)$. The mesh velocity $\mathbf{w}$ satisfies (4.1.4).

To solve equations (4.4.8) and (4.1.4) numerically, we employ the Navier-Stokes solver NEKTAR [6] in which the spectral element method with Jacobi polynomial basis is used to represent the fluid velocity, fluid pressure and mesh velocity. To integrate in time, we use a high-order splitting scheme with three parts: first the nonlinear terms are treated explicitly, then the pressure is obtained by a Poisson equation solver, and finally the viscous terms are treated implicitly [73]. In the strongly coupled FSI system, we solve for $\mathbf{u}_k^n$ and p_k^n following the numerical scheme described in (4.1.6) of chapter 4.1. Similar to the Navier-Stokes equation, at each time step the mesh velocity is obtained

by solving the Laplace equation (4.1.4), and the current configuration $\mathbf{x}(t)$ is updated from (4.1.9). For more details, we refer the interested readers to chapter 4.1.

Structure (cylinder and fairing) solver

We discretize the structure system (4.4.7) in time with the Newmark scheme: for the object function $a(t)$, based on the current value a^n, previous time step values a^{n-1}, velocity approximation $\dot{a}^{n-1}$ and acceleration approximation $\ddot{a}^{n-1}$, we can approximate the acceleration and velocity at the n-th step as:

$$\dot{a}^n = \dot{a}^{n-1} + \Delta t\left((1-D_1)\ddot{a}^{n-1} + D_1\ddot{a}^n\right), \tag{4.4.12a}$$

$$\ddot{a}^n = \frac{1}{\Delta t^2 D_2}\left(a^n - a^{n-1} - \Delta t\dot{a}^{n-1} - \frac{\Delta t^2}{2}(1-2D_2)\ddot{a}^{n-1}\right), \tag{4.4.12b}$$

where we have used " $\cdot$ " to denote the approximated temporal derivative. Depending on the requirements of accuracy and stability, different values can be set for the parameters (D_1, D_2). In the following, we will use the parameters $(D_1, D_2) = (0.5, 0.25)$ which lead to a second-order scheme. Substituting into (4.4.7), we obtain the discretized formulation for cylinder and fairing equations in the strongly coupled FSI system at time step n and subiteration step k:

$$\begin{aligned}
&m_c[(\ddot{f}_x)_k^n + a((\dot{\theta}_k^n)^2\cos\theta_k^n + \ddot{\theta}_k^n\sin\theta_k^n)] + k_x[(f_x)_k^n - a\cos\theta_k^n] \\
&- (F_n)_k^n(\cos\beta_k^n + (f_c)_{k-1}^n\sin\beta_k^n) = (F_{chx})_{k-1}^n, &\text{(4.4.13a)}\\
&m_c[(\ddot{f}_y)_k^n + a((\dot{\theta}_k^n)^2\sin\theta_k^n - \ddot{\theta}_k^n\cos\theta_k^n)] + k_y[(f_y)_k^n - a\sin\theta_k^n] \\
&- (F_n)_k^n(\sin\beta_k^n - (f_c)_{k-1}^n\cos\beta_k^n) = (F_{chy})_{k-1}^n, &\text{(4.4.13b)}\\
&m_f(\ddot{f}_x)_k^n + (F_n)_k^n(\cos\beta_k^n + (f_c)_{k-1}^n\sin\beta_k^n) = (F_{fhx})_{k-1}^n, &\text{(4.4.13c)}\\
&m_f(\ddot{f}_y)_k^n + (F_n)_k^n(\sin\beta_k^n - (f_c)_{k-1}^n\cos\beta_k^n) = (F_{fhy})_{k-1}^n, &\text{(4.4.13d)}\\
&I_f\ddot{\theta}_k^n - (F_n)_k^n[a\sin(\beta_k^n - \theta_k^n) - a(f_c)_{k-1}^n\cos(\beta_k^n - \theta_k^n) - R(f_c)_{k-1}^n] = (M_{fh})_{k-1}^n, &\text{(4.4.13e)}
\end{aligned}$$

where the hydrodynamic forces and angular momentum are updated from the following expressions:

$$\begin{pmatrix} (F_{chx})_{k-1}^n \\ (F_{chy})_{k-1}^n \end{pmatrix} = \oint_{\Sigma(t)_c} \mathbf{n}_f \cdot [-p_{k-1}^n\mathbf{I} + 2\rho_f\nu(\nabla\mathbf{u}_{k-1}^n + (\nabla\mathbf{u}_{k-1}^n)^T)]ds, \tag{4.4.14}$$

$$\begin{pmatrix} (F_{fhx})_{k-1}^n \\ (F_{fhy})_{k-1}^n \end{pmatrix} = \oint_{\Sigma(t)_f} \mathbf{n}_f \cdot [-p_{k-1}^n\mathbf{I} + 2\rho_f\nu(\nabla\mathbf{u}_{k-1}^n + (\nabla\mathbf{u}_{k-1}^n)^T)]ds, \tag{4.4.15}$$

$$(M_{fh})^n_{k-1} = \oint_{\Sigma(t)_f} \mathbf{r}(\mathbf{x}) \times [-p^n_{k-1}\mathbf{I} + 2\rho_f \nu(\nabla \mathbf{u}^n_{k-1} + (\nabla \mathbf{u}^n_{k-1})^T)] ds, \tag{4.4.16}$$

where $\Sigma(t)_c$ is the interface between fluid and cylinder, $\Sigma(t)_f$ is the interface between fluid and fairing, and $\mathbf{r}(\mathbf{x})$ is a vector pointing from $\mathbf{x}$ to the fairing gravity center at the current configuration.

Fictitious FSI stabilization method

In industrial applications, the values of fairing rotational inertia I_f are generally very low. In this case, the convergence of partitioned procedure is problematic because of the so-called added-mass effect [83]. In this work, additional acceleration schemes are employed to enhance the convergence rate. To be more specific, the Aitken acceleration [130, 124, 131] and the fictitious methods [4, 81] are used. The combination of these two approaches was shown to be successful in the previous study [81].

The main idea of the Aitken relaxation in the fluid solver [130, 155] is to perform under-relaxation at each sub-iteration step. At time step n and subiteration step k, we obtain the results $\tilde{\mathbf{c}}^n_k$ from the unrelaxed ones $\mathbf{c}^n_k$ and a relaxation parameter τ_k, based on the rule described in Appendix A.4.

On the other hand, in the fictitious inertia method additional terms are introduced in (4.4.6) to balance the added-mass operators. At time step n and subiteration step k, the discretized moment equation for fairing (4.4.13e) is replaced by:

$$I_f(1+f_I)\ddot{\theta}^n_k - (F_n)^n_k[a\sin(\beta^n_k - \theta^n_k) - a(f_c)^n_{k-1}\cos(\beta^n_k - \theta^n_k) - R(f_c)^n_{k-1}] = (M_{fh})^n_{k-1} + I_f f_I \ddot{\theta}^n_{k-1}, \tag{4.4.17}$$

where f_I is the fictitious inertia coefficient. Here we note that when the subiteration converges, we have $\ddot{\theta}^n_k \approx \ddot{\theta}^n_{k-1}$. Therefore, the scheme (4.4.17) with fictitious inertia method should converge to the same results as the original scheme of equation (4.4.13) at the end of each time step. Moreover, as discussed in [81], the fictitious method works the best if it approximates an exact coupled algorithm, which happens when $I_f f_I$ is close to the actual added-mass operator. In the applications with complicated geometries such as the fairings here, we cannot obtain any reasonable analytical value for the optimal fictitious coefficient I_f. Therefore, we will investigate this optimal coefficient from numerical tests.

In summary, at the n-th time step, we solve the FSI system following the fixed point algorithm:

1. Set

$$\text{(Solid) } (f_x)^n_0 = (f_x)^{n-1},\ (f_y)^n_0 = (f_y)^{n-1},\ \theta^n_0 = \theta^{n-1},\ \beta^n_0 = \beta^{n-1},\ (F_n)^n_0 = (F_n)^{n-1}, \tag{4.4.18a}$$

(Fluid) $\mathbf{u}_0^n = \mathbf{u}^{n-1},\ p_0^n = p^{n-1}.$ (4.4.18b)

2. **for** $k = 1 : k_{max}$, **do**

   (a) (Solid) Solve the cylinder/fairing equations (4.4.17) with hydrodynamic forces generated as in (4.4.14)-(4.4.15) and hydrodynamic angular momentum as in (4.4.16), then update the cylinder/fairing results

   $$((f_x)_k^n, (f_y)_k^n, \theta_k^n, \beta_k^n, (F_n)_k^n).$$

   (b) (Solid) From $((f_x)_k^n, (f_y)_k^n, \theta_k^n, \beta_k^n, (F_n)_k^n)$, calculate the velocity and acceleration approximations based on the Newmark scheme (4.4.12).

   (c) (Solid) Generate $\boldsymbol{\eta}_k^n$ at the fluid-strucuture interface following (4.4.11) and approximate velocity approximation $\dot{\boldsymbol{\eta}}_k^n$ and acceleration approximation $\ddot{\boldsymbol{\eta}}_k^n$. Pass these approximations to the fluid solver.

   (d) (Fluid) Update the velocity boundary condition $\mathbf{u}_k^n = \dot{\boldsymbol{\eta}}_k^n$ and the pressure boundary condition $\dfrac{\partial p_k^n}{\partial \mathbf{n}_f} = -\rho_f \left(\ddot{\boldsymbol{\eta}}_k^n + \nu \nabla \times \nabla \times \mathbf{u}_{k-1}^n + \mathbf{N}_{k-1}^n\right) \cdot \mathbf{n}_f$ at the interface.

   (e) (Fluid) Solve the Navier-Stokes equation (4.1.6), and obtain updated velocity and pressure $(\mathbf{u}_k^n, p_k^n)$.

   (f) (Fluid) Apply the Aitken relaxation on $\mathbf{u}_k^n$ to obtain the relaxed velocity $\tilde{\mathbf{u}}_k^n$.

   (g) (Fluid) Calculate the normal stress $-[-p_k^n \mathbf{I} + \rho_f \nu (\nabla \tilde{\mathbf{u}}_k^n + (\nabla \tilde{\mathbf{u}}_k^n)^T)]\mathbf{n}_f$at the interface.

   (h) (Fluid) Pass the normal stress at the interface to the structure solver.

   (i) (Fluid) Check convergence: if

   $$||\tilde{\mathbf{u}}_k^n - \tilde{\mathbf{u}}_{k-1}^n||,\ ||p_k^n - p_{k-1}^n|| < \epsilon, \tag{4.4.19}$$

   set $k = k_{max}$ and update the results as

   (Solid) $(f_x)^n = (f_x)_k^n,\ (f_y)^n = (f_y)_k^n,\ \theta^n = \theta_k^n,\ \beta^n = \beta_k^n,\ (F_n)^n = (F_n)_k^n,$ (4.4.20a)

   (Fluid) $\mathbf{u}^n = \tilde{\mathbf{u}}_k^n,\ p^n = p_k^n.$ (4.4.20b)

   Else, continue to the $(k+1)$-th subiteration.

3. (Mesh) Update the mesh velocity boundary condition at the interface with $\mathbf{w}^n = \dot{\boldsymbol{\eta}}^n$.

Parameter	value
m_c	6.0
m_f	1.0
k_x, k_y	10.949
I_f	0.6
a	0.0851
R	0.5
ρ_f	1.0
Polynomial order	3

Table 4.16: Non-dimensional parameters used in the numerical simulations.

4. (Mesh) Obtain the mesh velocity $\mathbf{w}^n$ by solving (4.1.4).

5. (Mesh) Update the mesh positions for the fluid subdomain using the numerical integration as in (4.1.9).

6. Go to time step $n+1$.

4.4.3 Numerical results

In this section, we present series of numerical tests on the fairings' suppression of vortex-induced vibrations. With these tests, we aim to demonstrate the capability of our fictitious inertia method in stabilizing the fluid-structure interaction simulations, and investigate parametrically the effect of fairings on VIV suppression and drag force reduction. To be more specific, the effect of varying the rotational damping and friction is investigated with different Reynolds numbers. In particular, we consider cases with two Reynolds numbers based on the cylinder diameter $D = 1$: $Re = 100$ and $Re = 500$. To perform simulations for $Re = 500$ in a relatively short domain, a robust and accurate outflow boundary condition as shown in [156] is employed at the outlet in the fluid solver. All the simulations are performed with the physical and numerical parameters summarized in Table 4.16 unless stated otherwise. All the parameters are in non-dimensional units. Note that the mass ratio between cylinder and fairing is $m_c/m_f = 6$, which is consistent with the settings in industrial use.

Effect of fictitious method

Before performing the simulations, we first investigate the numerical performance of our fictitious inertia method and look for the optimal fictitious coefficient. With $C_f = 0$, various values of f_I from 0.0 to 15.0 are tested and the averaged subiteration numbers needed for each f_I are compared in Table 4.17. The optimal fictitious coefficient f_I will be employed in all the simulations in the later simulations.

$Re = 100$												
f_I	0.0	0.5	1.0	1.5	2.0(o)	2.5	3.0	4.0	5.0	7.0	10.0	15.0
Avg subiter	No conv	13.8	10.1	8.6	7.7	7.9	8.0	8.0	8.1	8.2	8.3	8.6
$Re = 500$												
f_I	0.0	0.5	1.0	1.5	2.0	2.5(o)	3.0	4.0	5.0	7.0	10.0	15.0
Avg subiter	No conv	12.8	9.3	7.9	7.5	7.3	7.7	8.2	8.3	8.7	9.3	9.7

Table 4.17: Averaged subiteration number for VIV test for $C_f = 0$. When $Re = 100$, $\Delta t = 0.0025$; when $Re = 500$, $\Delta t = 0.0005$.

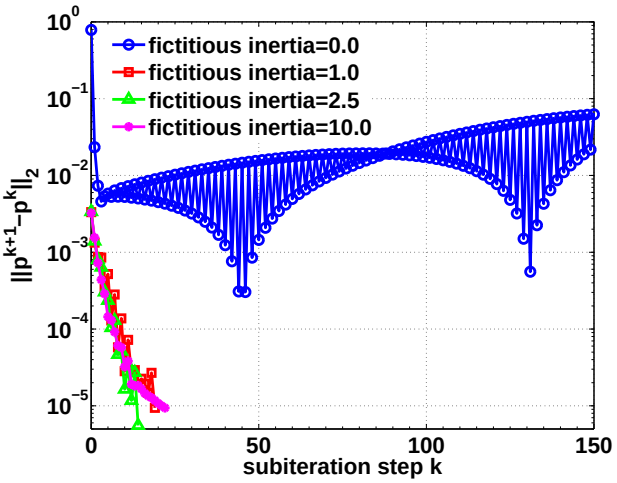

Figure 4.51: Pressure change of each subiteration in the first time step, when $Re = 100$ and $C_f = 0.0$.

$Re = 100$

For the case $C_f = 0$ and time step size $\Delta t = 0.0025$, we study systematically various values of f_I. To demonstrate the effect on accelerating the convergence, we take the average of subiteration numbers over one vortex shedding cycle (Strouhal period) as a comparison index. In the first part of table 4.17 we list these averaged subiteration numbers with different fictitious coefficients, where the value nearest to the optimal is marked by "(o)". To illustrate the effect of various fictitious coefficients more clearly, in Figure 4.51 we plot the pressure changes of each subiteration in the first time step, for four cases with different I_f. From the results we can see that when no fictitious method is applied ($f_I = 0.0$), the subiteration diverges in the first time step. Therefore, the fictitious inertia method helps stablizing the simulations and accelerating the subiteration convergence. Among all cases, the best performance is achieved when $f_I = 2.0$, which would be the coefficient we employ for all the $Re = 100$ simulation cases.

$Re = 500$

For $Re = 500$ cases, a smaller time step size $\Delta t = 0.0005$ is employed to enhance the stability and accuracy. We also investigate the optimal fictitious coefficient through performing numerical tests for the $C_f = 0$. The averaged subiteration numbers over one vortex shedding cycle (Strouhal period) are computed for f_I from 0.0 to 15.0, and listed in the second part of table 4.17. Here the value nearest to the optimal is also marked with "(o)". Since the subiteration is not converged when $f_I = 0.0$, in this higher Reynolds number case the fictitious inertia method is also required to stabilize the fluid-structure interaction simulations. On the other hand, the smallest subiteration number is obtained by $f_I = 2.5$, which is close to the optimal fictitious coefficient for the $Re = 100$ case. This implies that the added-mass operator does not change much with the increase of Reynolds number. In the remaining simulations of $Re = 500$ cases, the fictitious inertia method with fictitious coefficient $f_I = 2.5$ will be applied.

Simulation results

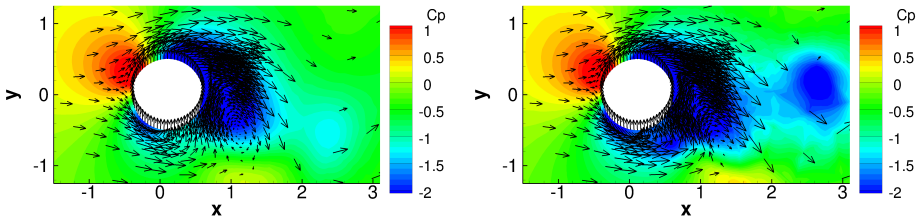

Figure 4.52: Instantaneous pressure coefficient contours and velocity vectors for plain cylinder cases. Left: $Re = 100$; right: $Re = 500$ (small domain).

Next we present the simulation results from various friction coefficient C_f from 0.0 to 0.5, to study its effect in suppressing VIV. Figure 4.53 presents the instantaneous pressure coefficient contours and velocity vectors when the cylinder is crossing the centerline from bottom to top, i.e., when the transverse velocity of cylinder reaches the maximum. Here the pressure coefficient is defined with respect to the pressure at the inlet center $(-5, 0)$ as:

$$C_p(x, y) = \frac{2(p(x, y) - p(-5, 0))}{\rho_f U_\infty^2}.$$

To provide a comparison and demonstrate the effects of fairing more clearly, Figure 4.52 shows the instantaneous pressure coefficient contours and velocity vectors obtained from plain moving cylinder, i.e., without any fairing. In Figure 4.54 and Figure 4.55 we show trajectories of motions and forces along various values of friction coefficient, for $Re = 100$ and $Re = 500$, respectively,

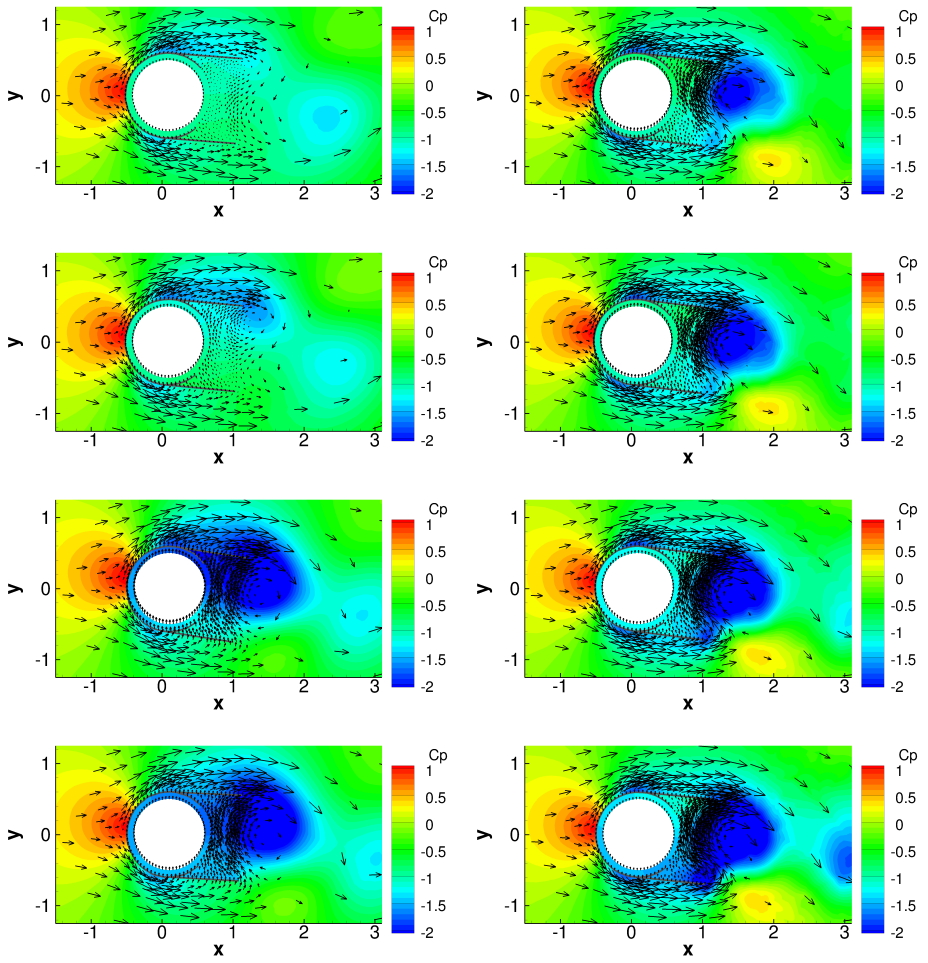

Figure 4.53: Instantaneous pressure coefficient contours and velocity vectors for fairing cases. Left column: $Re = 100$; right column: $Re = 500$ (small domain). First row: $C_f = 0.0$; second row: $C_f = 0.1$; third row: $C_f = 0.2$; fourth row: $C_f = 0.3$

compared with the response of a plain cylinder (in red). The amplitudes of vibration, the averages and frequencies in each cycle are provided in Figure 4.56 as functions of friction coefficient C_f for both $Re = 100$ (in the left column) and $Re = 500$ (in the right column), with different colors and symbols representing the results of different variables of $(c_x, c_y, \theta, \beta, F_n)$. Similarly, in Figure 4.57 we show the results of hydrodynamic forces and angular momentum. Note that the hydrodynamic forces are calculated as the total forces on the whole structure system including the fairing and cylinder, and the hydrodynamic angular momentum is calculated on the fairing only.

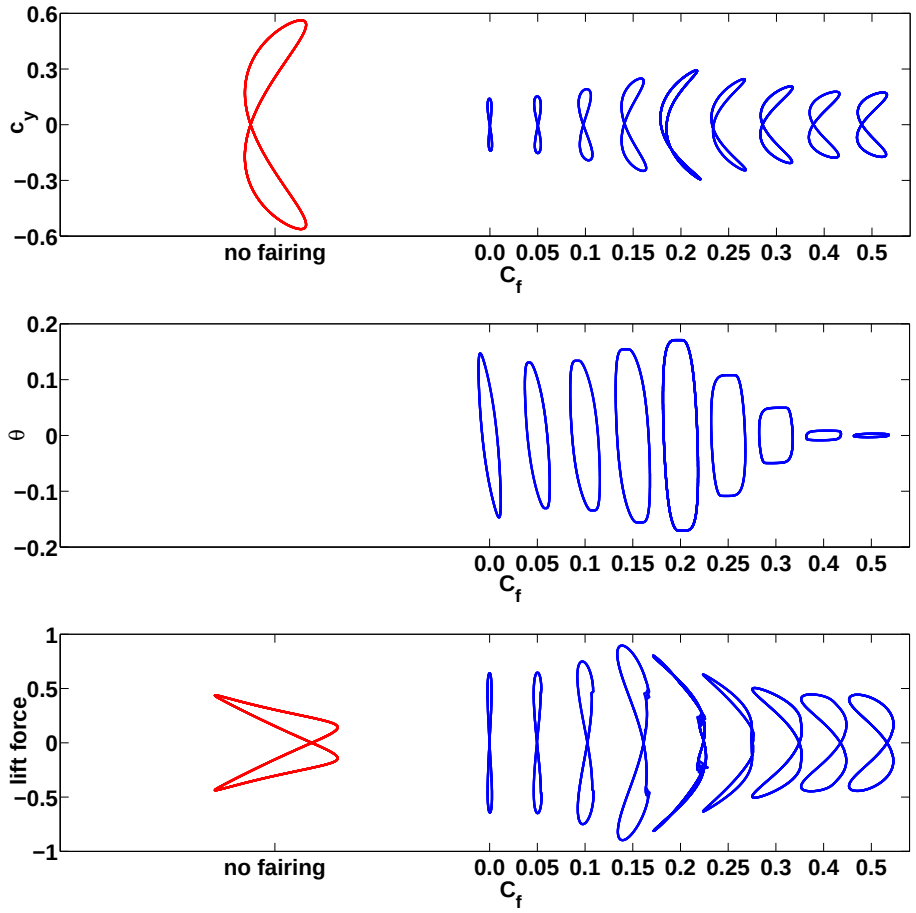

Figure 4.54: Trajectories of motion and force when $Re = 100$. The horizontal axis represents selected values of C_f and the trajectory centered at a specific value of C_f shows the computational results of that friction coefficient. Upper: $c_x - c_y$ trajectories. Middle: $\theta - \beta$ trajectories. Bottom: total hydrodynamic drag forces-lift forces trajectories.

$Re = 100$

Comparing the velocity vectors in the left column of Figure 4.53 with the results from the plain cylinder in Figure 4.52, it can be observed that in all the cases with fairing the instantaneous transverse velocities of cylinder are smaller than that from the plain cylinder simulation. Regarding the pressure coefficient contours, when $C_f = 0.2$ the pressure contours show a region of lower pressure developed along the upper side of the upper fairing plate especially, which indicates a stronger transverse force in the same direction as the cylinder motion comparing with that in the lower C_f cases. As we further increase C_f to 0.3, there also exists a lower pressure region near the cylinder and fairing. However, this region is attached at the tip of the upper fairing plate instead of covering the whole upper side of the fairing plate as in the $C_f = 0.2$ case. This suggests that

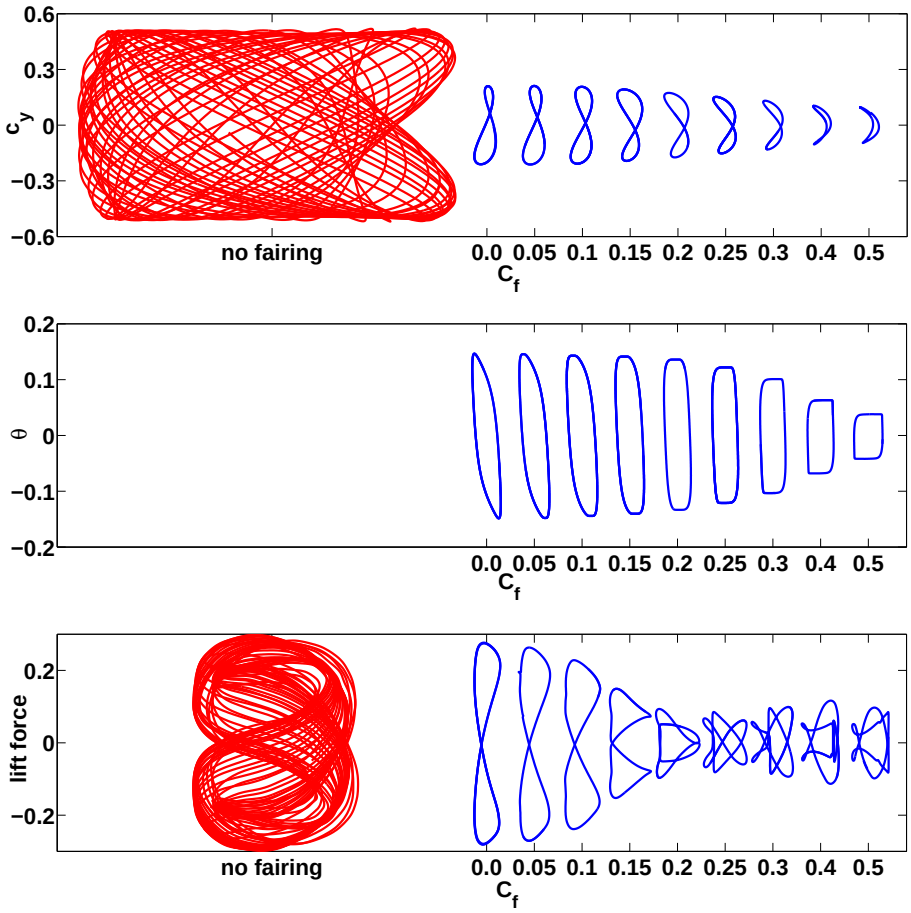

Figure 4.55: Trajectories of motion and force when $Re = 500$ (small domain). The horizontal axis represents selected values of C_f and the trajectory centered at a specific value of C_f showes the computational results of that friction coefficient. Upper: $c_x - c_y$ trajectories. Middle: $\theta - \beta$ trajectories. Bottom: total hydrodynamic drag forces-lift forces trajectories.

the shear layers that stem from the cylinder are now attached to the tip of fairing plate, and this pattern has the effect of stabilizing the near wake flow. Therefore, the transverse force developed in the $C_f = 0.3$ case should be smaller than that in the $C_f = 0.2$ case. The above observations are further reinforced in Figure 4.54 and Figure 4.56. In the upper plot of Figure 4.54 we can see that the cylinder motion trajectories with fairing show lower amplitudes of vibration for both the streamwise and transverse responses than those for a plain cylinder. However, this is not evident from computing the hydrodynamic forces. Although in all cases the fairing helps reducing the amplitude of drag forces, when $C_f < 0.3$ the hydrodynamic lift forces with fairing are even higher than that computed for the plain cylinder. While comparing the effects of different C_f values, among all cases $C_f = 0.0$ performs the best in suppressing VIV and reducing the drag force. On

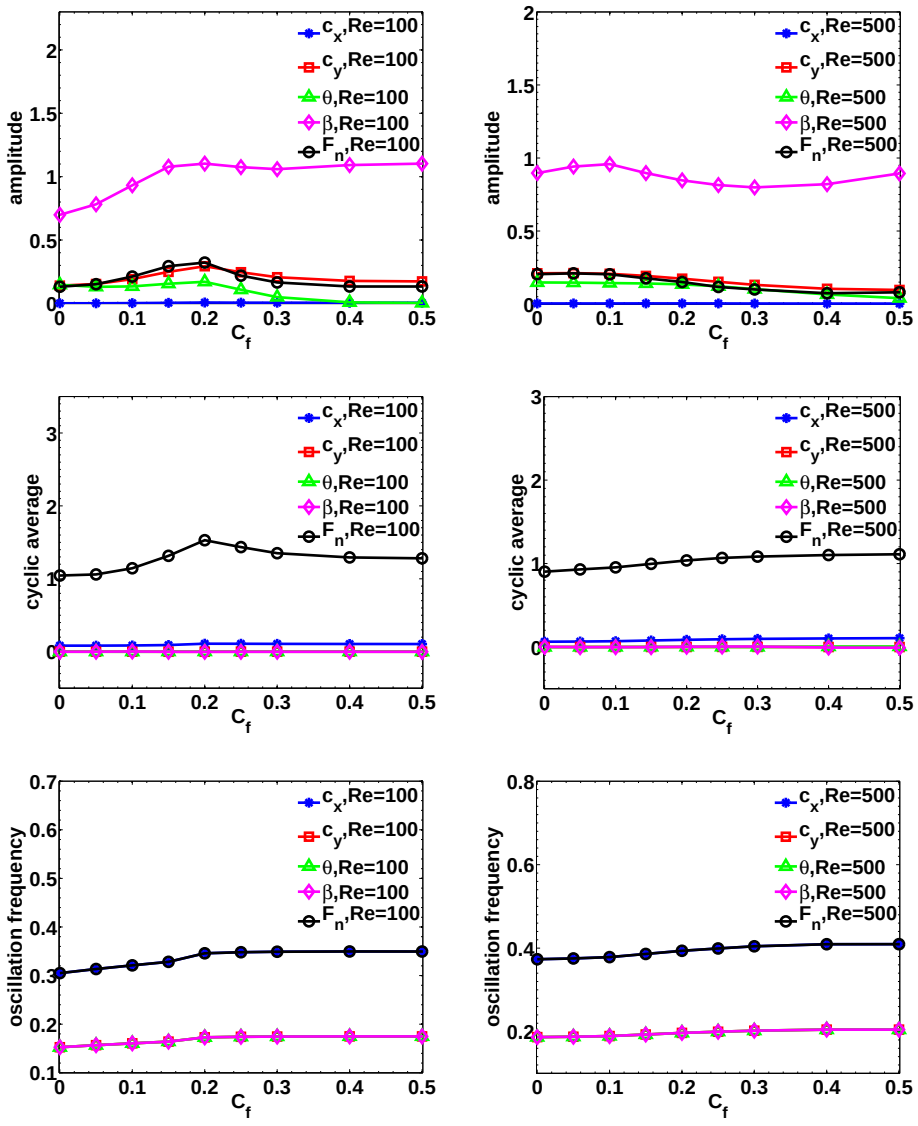

Figure 4.56: Computational results of $(c_x, c_y, \theta, \beta, F_n)$ from increasing C_f. Left column: $Re = 100$; right column: $Re = 500$ (small domain). Upper row: amplitudes of vibration in each cycle. Middle row: averages of cyclic response. Bottom row: frequencies of cyclic response.

the other hand, in the left column of Figure 4.56 it is especially worth noticing that when C_f is around $0.15 - 0.2$, the amplitudes of vibration and the averages of all variables reach the maximum. Moreover, in the upper plot of Figure 4.54 we can observe that only the $C_f = 0.2$ case generates a non-symmetrical $c_x - c_y$ trajectory. Therefore, in this low Reynolds number case $C_f = 0.2$ seems to be a critical value for the dynamic responses.

In summary, when $Re = 100$ the fairing in all cases helps in reducing the displacement responses

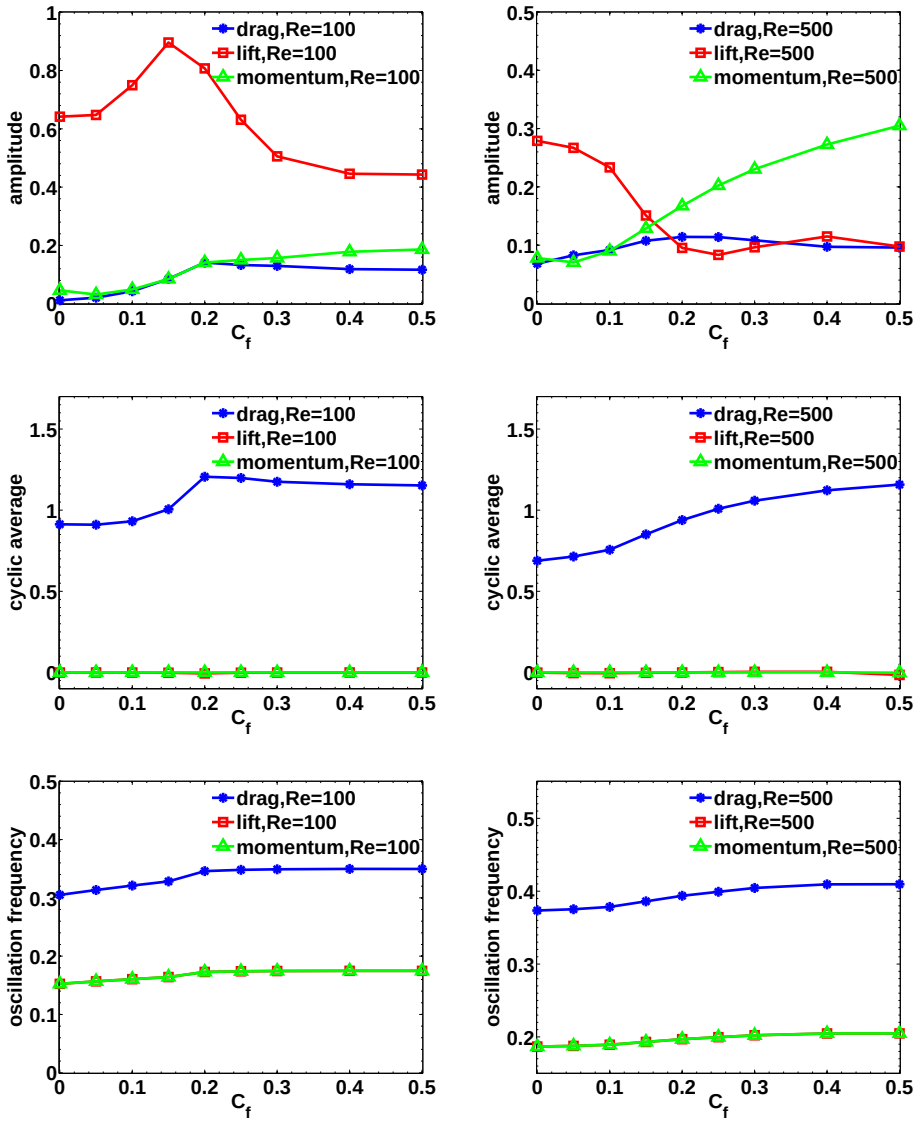

Figure 4.57: Computational results of total hydrodynamic drag/lift forces and fairing angular momentum from increasing C_f. Left column: $Re = 100$; right column: $Re = 500$ (small domain). Upper row: amplitudes of vibration in each cycle. Middle row: averages of cyclic response. Bottom row: frequencies of cyclic response.

and the hydrodynamic drag forces, but not the hydrodynamic lift forces applied on the cylinder and fairing. To achieve the best performance in VIV suppression and drag reduction, $C_f = 0.0$ is the most effective choice. Moreover, there exists a critical value of the friction coefficient C_f around $0.15 - 0.2$: when C_f is lower than this value, larger values of C_f are less effective in VIV suppression. On the other hand, when C_f exceeds this critical value, further increasing C_f will help more in supressing the VIV.

$Re = 500$ **(small domain)**

Similar to the simulations for $Re = 100$, when $Re = 500$ the comparison of the velocity vectors in Figure 4.52 and those in Figure 4.53 also implies that the fairing helps reducing the magnitudes of cylinder transverse velocities. Comparing the pressure coefficient contours at $Re = 100$ to that at $Re = 500$, we can see that when $Re = 500$ the lower pressure regions are attached at the tip of the upper fairing plate, which is close to the pattern we observed in the $Re = 100$, $C_f = 0.3$ case. Therefore, we can expect that the transverse forces are reduced in the fairing cases. Moreover, in the $Re = 500$ cases, when C_f increases the low pressure region expends more to the tip of the lower fairing plate, which indicates a smaller transverse force. These findings can be seen more clearly in Figure 4.55, where the trajectories of motion and force for various values of friction coefficient are presented. Compared with the trajectory of the plain cylinder (in red), the fairing is found to suppress not only the cylinder displacments but also the hydrodynamic forces. While considering the effect of different values of C_f, in the right column of Figure 4.56 the computations of responses suggest that a higher C_f is generally more effective in suppressing VIV for the cylinder displacements and fairing rotational angle. In contrast to the findings in the $Re = 100$ cases, there exists no obvious critical value of C_f in the $Re = 500$ cases. The trajectory patterns are more complicated for all fairing cases when $Re = 500$, as all the cylinder motion trajectories are non-symmetric. On the other hand, the motion trajectory in the plain cylinder case shows a more complicated behavior: a quasi-periodic flow occurs because of the secondary frequency in the x displacement time trace, as displayed in the left plot of Figure 4.58. To investigate the cause, we increase the cylinder gap size from 10 to 20 and show the results in the right plot of Figure 4.58: the secondary frequency disappears and the cylinder motion becomes periodic. Therefore, this secondary frequency is generated from the effect of the periodic boundary condition in the vertical direction i.e., the influences from neighboring cylinders. In the next section, we will further investigate the results from this larger domain as shown in Figure 4.59.

In summary, when $Re = 500$ the fairing helps to reduce both the displacement responses and the hydrodynamic forces, and the device with higher C_f works more effectively. This finding is also consistent with the experiments in [148, 149] where fairings with different designs were employed and tested.

$Re = 500$ **(large domain)**

In this section, a larger domain as shown in Figure 4.59 is employed, to diminish the influences of neighboring cylinder interactions and outflow boundary conditions. Because of the increased

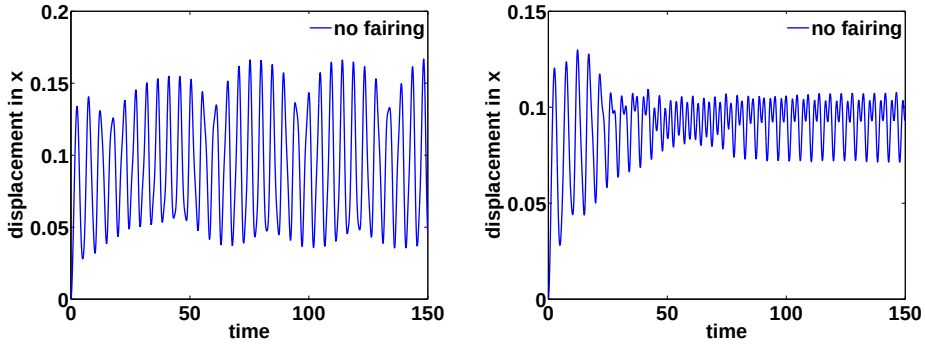

Figure 4.58: Computational results of plain cylinder displacement in x direction when $Re = 500$. Left: with smaller domain ($[-5, 20] \times [-5, 5]$) we get a quasi-periodic flow; right column: with larger domain ($[-10, 40] \times [-10, 10]$) a single frequency limit cycle emerges in the simulations.

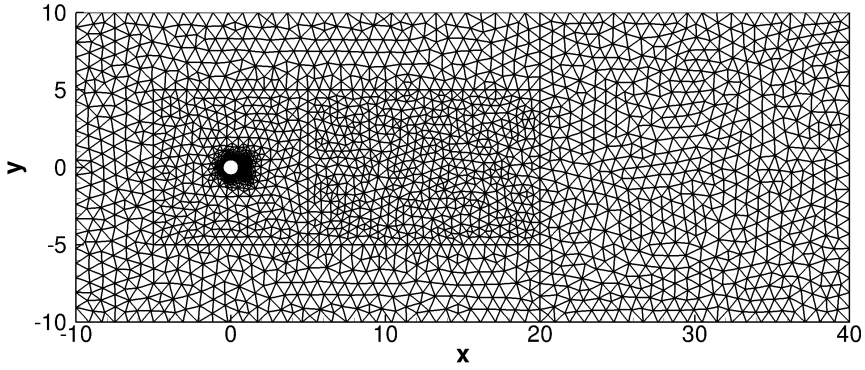

Figure 4.59: Fluid mesh in the larger domain simulations.

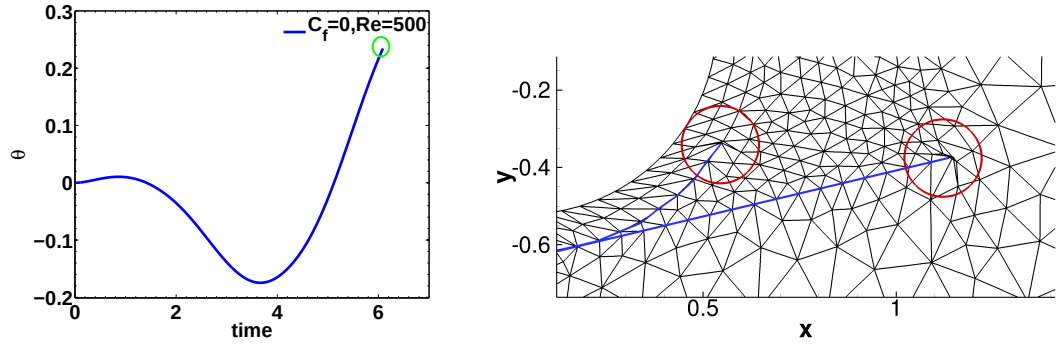

Figure 4.60: Computational difficulty of the arbitrary Lagrangian Eulerian (ALE) framework (4.1.4) when using a larger domain. Left: time trace of rotational angle θ when $C_f = 0$, at the starting stage; right column: distorted mesh generated from ALE, with low aspect ratio elements near the fairing tips circled by red.

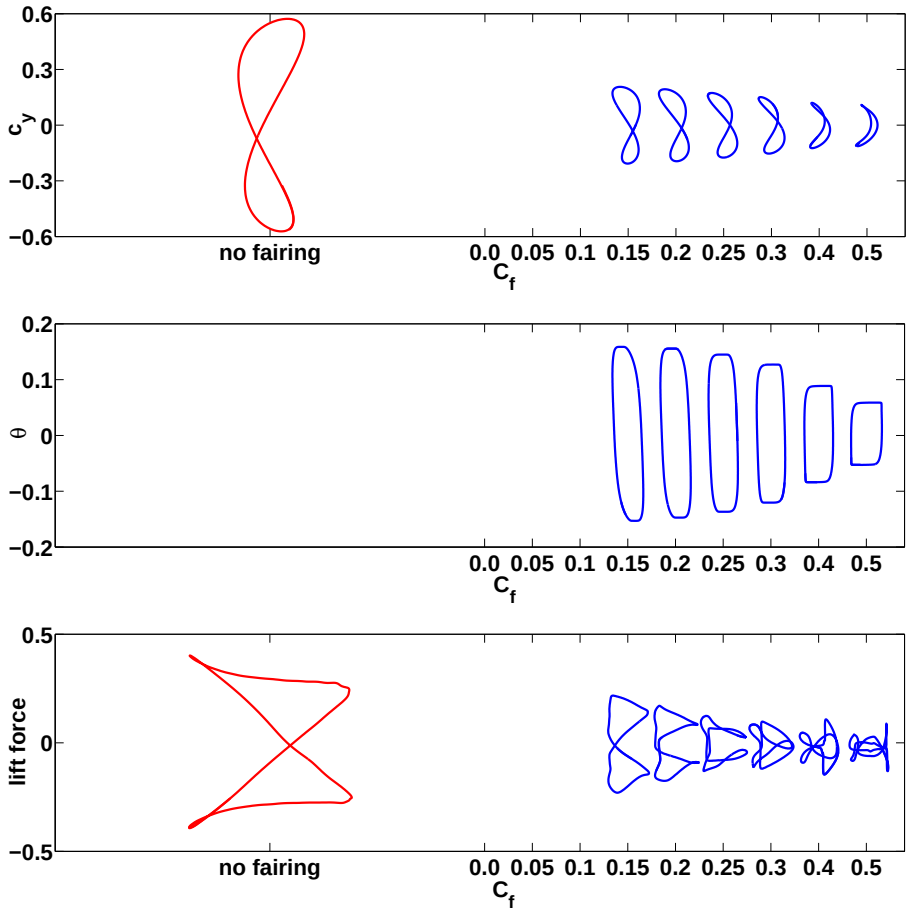

Figure 4.61: Trajectories of motion and force with cylinder gap size 20 and $Re = 500$. The horizontal axis represents selected values of C_f and the trajectory centered at a specific value of C_f showes the computational results of that friction coefficient. Upper: $c_x - c_y$ trajectories. Middle: $\theta - \beta$ trajectories. Bottom: total hydrodynamic drag forces-lift forces trajectories.

element number and thereby the computational cost, all the following simulations are based on lower (2nd) order polynomial elements.

For the plain cylinder case, the amplitude of cylinder transverse displacement is slightly increased compared to the results from the smaller domain, namely from 0.516 to 0.575. Regarding the fairing cases, this larger domain also generates approximately 10% larger vibration amplitudes for $(c_x, c_y, \theta, \beta, F_n)$ and hydrodynamic forces. The increased rotational angle θ is problematic while updating the mesh in the arbitrary Lagrangian Eulerian (ALE) framework (4.1.4) for the cases with $C_f \leq 0.15$. As illustrated in the left plot of Figure 4.60 where the simulation starts from developed flow around the static cylinder and fairing at time 0, it can be observed that the amplitude of rotational angle grows rapidly and reaches 0.24 at the time instant marked by a green circle. At that time instant, the right plot of Figure 4.60 demonstrates the updated mesh generated from

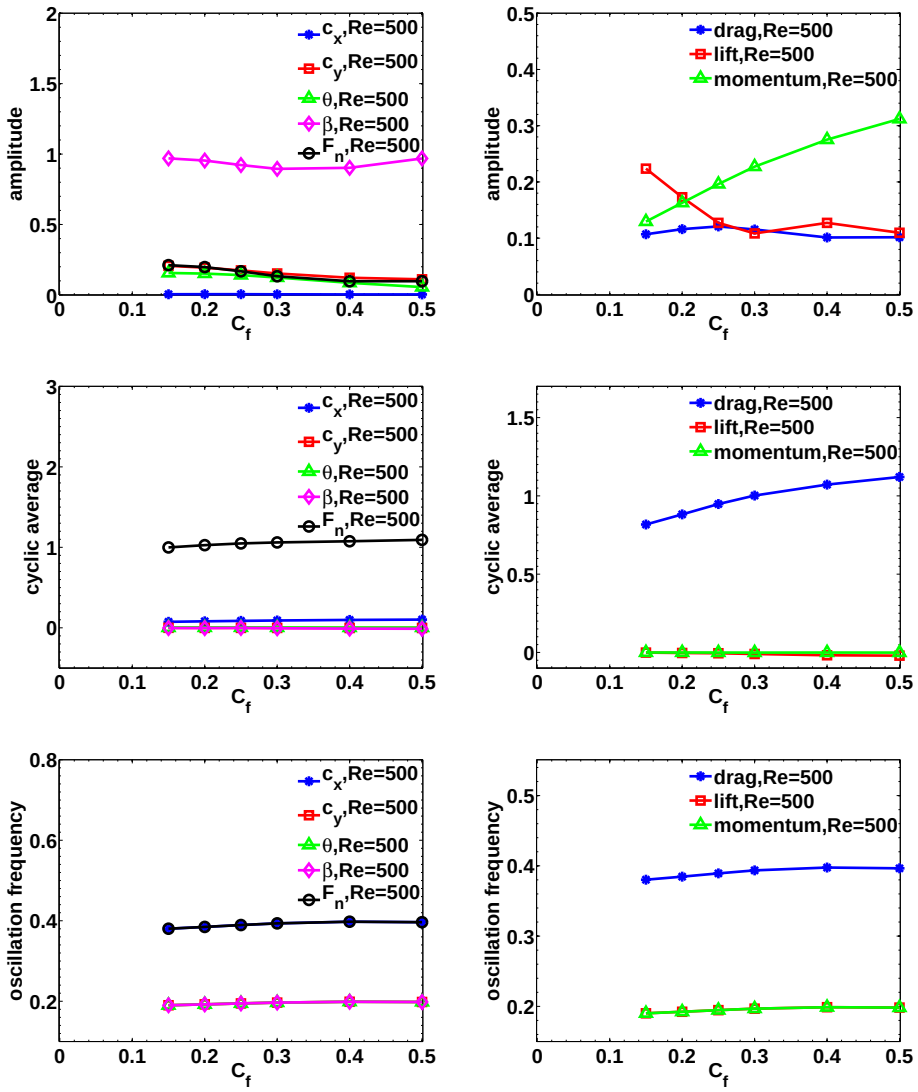

Figure 4.62: Computational results from increasing C_f with cylinder gap size 20 and $Re = 500$. Left column: motion variables $(c_x, c_y, \theta, \beta, F_n)$; right column: total hydrodynamic drag/lift forces and fairing angular momentum. Upper row: amplitudes of vibration in each cycle. Middle row: averages of cyclic response. Bottom row: frequencies of cyclic response.

ALE, in which the mesh is greatly distorted near the fairing tips. The aspect ratios of the nearby elements become very small, which renders the simulation unstable. To resolve this problem, we note that our fictitious inertia method (4.4.17) can not only balance the added-mass effect, but also play as a relaxation for the rotational angle. When $C_f = 0.15$, we take a large fictitious coefficient $I_f = 200$ at the starting stage, then graduatly decrease it to the optimal coefficient $I_f = 2.5$ after a periodic fluctuation is reached. On the other hand, if we further investigate a smaller friction coefficient $C_f = 0.1$, the amplitude of θ reaches $\theta = 0.35$ at the starting stage. To stablize this

case, a further larger fictitious coefficient I_f is required, which however greatly slows down the subiteration convergence as can be seen in Table 4.17. Fortunately, we are less interested in the small friction coefficient cases since they are less effective in suppressing VIV, as studied in the previous section. Therefore, in this section we concentrate on the simulation results for $C_f > 0.1$ cases.

To be consistent with the results in Figure 4.52, we also define the pressure coefficient with respect to the pressure at $(-5, 0)$, and observe the same patterns as that in the corresponding cases on small domain. Similar as the plots for small domain results, in Figures 4.61 we display the trajectories of motions and forces, and in Figure 4.62 the amplitudes of vibration, the averages and frequencies are ploted as functions of C_f. Comparing these plots with the results in Figures 4.53-4.57 in the last section, we can see that although the vibration amplitudes and trajectory patterns vary, the main observation still holds: fairings with larger C_f are generally more effective in supppressing both the cylinder motions and hydrodynamic forces.

4.4.4 Summary

Physical findings:

- At $Re = 100$ there exists a critical value of friction coefficient f_c, around which large oscillations and non-symmetric trajectories are observed.
- At $Re = 500$ a different behavior emerges, i.e. VIV are suppressed continuously as f_c increases.

Numerical findings:

- Fictitious inertia method is effective in stabilizing the FSI procedure in two ways: firstly in balancing the added-mass effect, and secondly when fairing rotational angle is as large as 0.25, large fictitious inertia I_f is needed for stabilization at the starting stage.
- In larger domain simulations, the observation on fairing performances still holds.

Chapter 5

Summary and Future Work

This thesis centered around numerical analysis and large-scale scientific computing for physical and biomedical real-life problems with specific focus on fluid-structure interaction problems. Specifically, this thesis can be summarized into three parts:

- *Structure*: A *pressure/displacement mixed formulation* in high-order spectral/*hp* elements is developed, and it is documented that the most robust choice of interpolation order in the mixed formulation is $O_p = O_u - 1$ leading to stable and accurate results. Compared to the displacement-only formulation presented in [18], the mixed formulation has superior accuracy and is overall more efficient, especially for problems with high bulk modulus [121]. Moreover, an efficient *semi-local method* is designed for speeding up the solution of the linear systems of the high-order element discretization of the 3D linear elasticity equations. By approximating the element-wise residual distribution with a localization operator and subsequently solving smaller linear systems on each element, good parallel scalability and substantial speed-up are achieved, especially for FSI simulations. Furthermore, a 3D viscoelastic arterial wall model is investigated numerically, whose constitutive law is derived using fractional-order differential equations. Comparing with the classical integer-order model, it is shown that the fractional-order model offers a more powerful alternative for describing patient-specific arterial wall mechanics, because the later is less sensitive to the parameter estimation.

- *Fluid*: A parallel advection-diffusion solver is implemented with high-order spectral/*hp* element method, and the injection procedure of contrast agent into a precomputed patient-specific model is numerically simulated. By comparing the virtual angiographic images with the real X-ray CT images, we examine via visualization the structure of flow in internal carotid arteries laden with different types of aneurysms. To further validate the fluid solver directly,

our prediction of pressure and flow are compared with that from 24 different research groups, on a given giant aneurysm geometry. Remarkable consistency in the pressure patterns and pressure drops are obtained [1].

- *Fluid-structure interaction*: A family of fictitious methods is developed and analyzed for FSI problems, where additional terms are introduced in the fluid/structure equations to balance the added-mass effect and make the partitioned FSI solver perform more like an exact coupled solver [4, 81]. The fictitious methods can be implemented by changing the coefficients of the pressure or acceleration terms in the fluid or structure equations, respectively, and therefore can be easily extended and adopted in any existing FSI solver. As a validation for the methods on complex geometries, we also conducted simulations and provided theoretical analysis to obtain optimal values for the fictitious parameters in 3D patient-specific brain arterial geometries with aneurysms. Furthermore, the fictitious method is extended to applications of deepwater offshore oil operations, and various salient features of free-to-rotate devices for VIV suppression are quantified numerically for the first time [157]. Moreover, to further accelerate the FSI procedure, a new stabilized explicit coupling partitioned scheme is proposed for FSI [158], whose stability does not depend on the added-mass effect, and no subiteration is needed. On vortex-induced vibration problems, it is numerically validated that with sufficiently large penalty coefficients, stability is achieved irrespective of the fluid-solid density ratio.

In the future, we will further develop coupling schemes for FSI with better efficiency and accuracy, and apply the related domain decomposition approaches in other multiscale and multiphysics problems, for example, multi-phase flows, atomistic-to-continuum coupling problems, etc.

Appendix A

Appendix

A.1 Shape functions

We employ the hierarchical shape functions based on Jacobi polynomials (see [6] for details). Firstly, we introduce three principal functions $\phi_i^a(x)$, $\phi_{ij}^b(x)$ and $\phi_{ijk}^c(x)$ (where the integers i, j, k are in the ranges $0 \le i \le I$, $0 \le i \le I$, $0 \le i \le I$, respectively), which are defined on the domain $-1 \le x \le 1$:

$$\psi_i^a(x) = \begin{cases} \frac{1-x}{2}, & i = 0, \\ \frac{1-x}{2}\frac{1+x}{2}P_{i-1}^{1,1}(x), & 1 \le i < I, \\ \frac{1+x}{2}, & i = I, \end{cases} \tag{A.1.1}$$

$$\psi_{ij}^b(x) = \begin{cases} \psi_j^a(x), & i = 0,\ 0 \le j \le J, \\ (\frac{1-x}{2})^{i+1}, & 1 \le i < I,\ j = 0, \\ (\frac{1-x}{2})^{i+1}\frac{1+x}{2}P_{j-1}^{2i+1,1}(x), & 1 \le i < I,\ 1 \le j < J, \\ \psi_j^a(x), & i = I,\ 0 \le j \le J, \end{cases} \tag{A.1.2}$$

$$\psi_{ijk}^c(x) = \begin{cases} \psi_{jk}^b(x), & i = 0,\ 0 \le j \le J,\ 0 \le k \le K, \\ \psi_{ik}^b(x), & 0 \le i \le I,\ j = 0,\ 0 \le k \le K, \\ (\frac{1-x}{2})^{i+j+1}, & 1 \le i < I,\ 1 \le j < J,\ k = 0, \\ (\frac{1-x}{2})^{i+j+1}\frac{1+x}{2}P_{k-1}^{2i+2j+1,1}(x), & 1 \le i < I,\ 1 \le j < J,\ 1 \le k < K, \\ \psi_{ik}^b(x), & 0 \le i \le I,\ j = J,\ 0 \le k \le K, \\ \psi_{jk}^b(x), & i = I,\ 0 \le j \le J,\ 0 \le k \le K, \end{cases} \tag{A.1.3}$$

here $P_n^{\alpha,\beta}(x)(\alpha, \beta > -1)$ are the Jacobi polynomials.

Next we define the shape functions in three-dimensional space based on these three principal

functions. Denote the coordinates of the standard domain as ξ_1, ξ_2, ξ_3, respectively. Then the hierarchical shape functions are

- For a hexahedral element $\{(\xi_1, \xi_2, \xi_3) | -1 \leq \xi_1, \xi_2, \xi_3 \leq 1\}$, the shape function is defined by

$$\phi_{pqr}(\xi_1, \xi_2, \xi_3) = \psi_p^a(\xi_1)\psi_q^a(\xi_2)\psi_r^a(\xi_3). \tag{A.1.4}$$

- For a prismatic element $\{(\xi_1, \xi_2, \xi_3) | -1 \leq \xi_1, \xi_3; \xi_1 + \xi_3 \leq 1; -1 \leq \xi_2 \leq 1\}$, the shape function is defined by

$$\phi_{pqr}(\xi_1, \xi_2, \xi_3) = \psi_p^a(\bar{\eta}_1)\psi_q^a(\xi_2)\psi_{pr}^b(\xi_3), \tag{A.1.5}$$

  where $\bar{\eta}_1 = \frac{2(1+\xi_1)}{1-\xi_3} - 1$.

- For a tetrahedral element $\{(\xi_1, \xi_2, \xi_3) | -1 \leq \xi_1, \xi_2, \xi_3; \xi_1 + \xi_2 + \xi_3 \leq 1\}$, the shape function is defined by

$$\phi_{pqr}(\xi_1, \xi_2, \xi_3) = \psi_p^a(\eta_1)\psi_{pq}^b(\eta_2)\psi_{pqr}^c(\xi_3), \tag{A.1.6}$$

  where $\eta_1 = \frac{2(1+\xi_1)}{-\xi_2-\xi_3} - 1$, $\eta_2 = \frac{2(1+\xi_2)}{1-\xi_3} - 1$.

- For a pyramid element $\{(\xi_1, \xi_2, \xi_3) | -1 \leq \xi_1, \xi_2, \xi_3; \xi_1 + \xi_3 \leq 1; \xi_2 + \xi_3 \leq 1\}$, the shape function is defined by

$$\phi_{pqr}(\xi_1, \xi_2, \xi_3) = \psi_p^a(\bar{\eta}_1)\psi_q^a(\eta_2)\psi_{pqr}^c(\xi_3), \tag{A.1.7}$$

  where $\bar{\eta}_1 = \frac{2(1+\xi_1)}{1-\xi_3} - 1$, $\eta_2 = \frac{2(1+\xi_2)}{1-\xi_3} - 1$.

A.2 Increment method

The increment method is a widely used method in solving nonlinear elastic problem such as (2.1.28). By dividing the external load

$$r^{ext} = \int_{\partial\Omega_N} \mathbf{T} \cdot \mathbf{v} d\Gamma + \int_\Omega \rho \mathbf{f} \cdot \mathbf{v} d\Omega \tag{A.2.1}$$

into N parts, one can enhance the stability in the Newton-Raphson iterative procedure while applying a large load directly. Take the displacement formulation, for example, (the increment method for mixed formulation can be derived similarly), this method can be rewritten as follows:

- With the initial condition of problem (2.1.28), solve

$$\begin{aligned}\mathcal{P}(\mathbf{w}_1) = &\int_\Omega \mathbf{S}(\mathbf{w}_1) : \frac{1}{2}\left(\left(\frac{\partial \mathbf{v}}{\partial \mathbf{X}}\right)^T \mathbf{F}(\mathbf{w}_1) + \mathbf{F}(\mathbf{w}_1)^T \left(\frac{\partial \mathbf{v}}{\partial \mathbf{X}}\right)\right) d\Omega \\ &- \frac{1}{N}\left(\int_{\partial\Omega_N} \mathbf{T}\cdot\mathbf{v} d\Gamma + \int_\Omega \rho\mathbf{f}\cdot\mathbf{v} d\Omega\right) \\ =&0,\ \forall \mathbf{v} \in \mathbf{U}_0,\end{aligned} \tag{A.2.2}$$

  by Newton-Raphson iterative procedure, and get $\mathbf{w}_1$.

- For the i-th step, take $\mathbf{w}_{i-1}$ and its derivative as the initial condition, solve

$$\begin{aligned}\mathcal{P}(\mathbf{w}_i) = &\int_\Omega \mathbf{S}(\mathbf{w}_i) : \frac{1}{2}\left(\left(\frac{\partial \mathbf{v}}{\partial \mathbf{X}}\right)^T \mathbf{F}(\mathbf{w}_i) + \mathbf{F}(\mathbf{w}_i)^T \left(\frac{\partial \mathbf{v}}{\partial \mathbf{X}}\right)\right) d\Omega \\ &- \frac{i}{N}\left(\int_{\partial\Omega_N} \mathbf{T}\cdot\mathbf{v} d\Gamma + \int_\Omega \rho\mathbf{f}\cdot\mathbf{v} d\Omega\right) \\ =&0,\ \forall \mathbf{v} \in \mathbf{U}_0,\end{aligned} \tag{A.2.3}$$

  by Newton-Raphson iterative procedure, and get $\mathbf{w}_i$, until $i = N$.

- Take $\mathbf{w}_N$ as the final solution for problem (2.1.28).

A.3 Fictitious mass method for semi-local method

In the fictitious mass method [4, 81], the structure problem (2.1.10) is solved with additional acceleration terms. Considering the fictitious mass coefficient f_m, at the n-th time step and k-th subiteration the Newmark formulation (2.2.9) can be modified as:

$$\left(\frac{(1+f_m)\mathbf{M}}{\Delta t^2\theta_2} + \mathbf{K}\right)\mathbf{U}^{n,k} = \mathbf{F} + \frac{\mathbf{M}}{\Delta t^2\theta_2}\left(\mathbf{U}^{n-1} + \Delta t\dot{\mathbf{U}}^{n-1} + \frac{\Delta t^2}{2}(1-2\theta_2)\ddot{\mathbf{U}}^{n-1} + f_m\mathbf{U}^{n,k-1}\right); \tag{A.3.1}$$

and the BDF formulation (2.2.11) can be modified as:

$$\begin{aligned}(A_1A_2(1+f_m)\mathbf{M} + \mathbf{K})\,\mathbf{U}^{n,k} =&\mathbf{F} - \mathbf{M}(A_2(B_1\mathbf{U}^{n-1} + C_1\mathbf{U}^{n-2} + D_1\mathbf{U}^{n-3}) \\ &+ (B_2\dot{\mathbf{U}}^{n-1} + C_2\dot{\mathbf{U}}^{n-2} + D_2\dot{\mathbf{U}}^{n-3}) + A_1A_2f_m\mathbf{U}^{n,k-1}).\end{aligned} \tag{A.3.2}$$

Here the modified terms aim to balance the added-mass operator. On the other hand, in the

semi-local method, the formulations (2.2.15) can be modified as

$$\begin{aligned}
\text{Newmark: } \left(\frac{(1+f_m)\mathbf{M}_e}{\Delta t^2\theta_2}+\mathbf{K}_e\right)\mathbf{U}_e^{n,k} &= \mathcal{L}_e\left(\hat{\mathbf{F}}^{n,k-1}-\left(\frac{\mathbf{M}}{\Delta t^2\theta_2}+\mathbf{K}\right)\mathbf{U}^{n,k-1}\right)\\
&\quad+\left(\frac{(1+f_m)\mathbf{M}_e}{\Delta t^2\theta_2}+\mathbf{K}_e\right)\mathbf{U}_e^{n,k-1},\\
\text{BDF: } \left(A_1A_2(1+f_m)\mathbf{M}_e+\mathbf{K}_e\right)\mathbf{U}_e^{n,k} &= \mathcal{L}_e\left(\hat{\mathbf{F}}^{n,k-1}-\left(A_1A_2\mathbf{M}+\mathbf{K}\right)\mathbf{U}^{n,k-1}\right)\\
&\quad+\left(A_1A_2(1+f_m)\mathbf{M}_e+\mathbf{K}_e\right)\mathbf{U}_e^{n,k-1}.
\end{aligned} \tag{A.3.3}$$

Here we note that when the subiteration is completed, we have $\mathbf{U}_e^{n,k} \approx \mathbf{U}_e^{n,k-1}$. Therefore, the scheme with fictitious mass should converge to the same results as the original semi-local scheme of equation (2.2.15) at the end of each time step. Moreover, as analyzed in section 2.2.1, when increasing the f_m, the mass matrix part $\frac{(1+f_m)\mathbf{M}_e}{\Delta t^2\theta_2}$ or $A_1A_2(1+f_m)\mathbf{M}_e$ dominates more in the system (A.3.3). Therefore, the fictitious mass method would help accelerating the convergence of the subiterations in the semi-local method.

A.4 Aitken relaxation

In both the structure and fluid solvers we employ the Aitken relaxation to accelerate the convergence of the FSI system [130, 155]. The main idea is to perform under-relaxation at each sub-iteration step. At time step n and subiteration step k, we obtain the results $\tilde{\mathbf{c}}_k^n$ from the unrelaxed ones $\mathbf{c}_k^n$ and a relaxation parameter τ_k, based on the following rule:

$$\tilde{\mathbf{c}}_k^n = \tau_k\tilde{\mathbf{c}}_{k-1}^n + (1-\tau_k)\mathbf{c}_k^n. \tag{A.4.1}$$

Here τ_k is updated according to the Aitken rule [130]:

$$\tau_k = \tau_{k-1} + (\tau_{k-1}-1)\frac{(\mathbf{Q}_{k-1}-\mathbf{Q}_k)\cdot\mathbf{Q}_k}{||\mathbf{Q}_{k-1}-\mathbf{Q}_k||^2}, \text{ where } \mathbf{Q}_k = \tilde{\mathbf{c}}_{k-1}^n - \mathbf{c}_k^n. \tag{A.4.2a}$$

To get a better control on the convergence rate, we can set the relaxation parameter τ_k within a range $[\tau_{min}, \tau_{max}]$, depending on the specific applications [4].

A.5 Analysis of the fictitious mass and damping methods

In this section we give the proof for property 4.1.1. Since the problem involved here is linear, in the following we analyze the convergence to the zero solution when $F_1 = F_2 = F_3 = 0$, without loss of generality.

By applying the divergence operator on (4.1.41a) and combining the resulted equation with the

divergence-free condition on $\mathbf{u}$, we obtain an equation for the unknown pressure in Ω_f:

$$\Delta p_k = 0. \tag{A.5.1}$$

Applying the Fourier decomposition $p_k = \hat{p}_k(x,\gamma)e^{i\gamma y}$ in the y direction, the above Laplacian equation can be rewritten as an ordinary differential equation

$$-\frac{\partial^2 \hat{p}_k}{\partial x^2} + \gamma^2 \hat{p}_k = 0, \tag{A.5.2}$$

in the range of $x \in (-\infty, 0)$. This equation has solutions with the general form $\hat{p}_k(x,\gamma) = P_k(\gamma)e^{\gamma x} + Q_k(\gamma)e^{-\gamma x}$. Since p_k is assumed to be bounded at $-\infty$, $Q_k(\gamma)$ must vanish. Therefore

$$\hat{p}_k(x,\gamma) = P_k(\gamma)e^{\gamma x}. \tag{A.5.3}$$

For notational simplicity, all the (x,γ) is omitted in the Fourier coefficients $\hat{p}_k(x,\gamma)$ and $\hat{\eta}_k(x,\gamma)$ in this section.

At the x direction, (4.1.41a) gives the relation between pressure p_k and velocity in the x direction, u_k:

$$\frac{\partial p_k}{\partial x} = -\rho_f \frac{\beta u_k}{\Delta t} \quad \text{in } \Omega_f. \tag{A.5.4}$$

Substituting it into the Dirichlet interface condition (4.1.41c), we can write the interface conditions on Σ as

$$-\frac{\Delta t}{\beta \rho_f}\frac{\partial p_k}{\partial x} = A_1 \eta_k, \tag{A.5.5}$$

which is combined with the expression for the structure model (4.1.44) and obtain

$$\begin{aligned} &(1+f_m)A_1A_2\rho_s H_s\eta_k + f_d A_1\rho_s H_s\eta_k + G_1 H_s\eta_k - G_2 H_s\frac{\partial^2\eta_k}{\partial y^2} \\ =&p_{k-1} + f_m A_1A_2\rho_s H_s\eta_{k-1} + f_d A_1\rho_s H_s\eta_{k-1}. \end{aligned} \tag{A.5.6}$$

Taking the Fourier transform in the y direction for the above equations, the Fourier coefficients corresponding to y should obey a similar relation, i.e.,

$$-\frac{\Delta t}{\beta \rho_f}\frac{\partial \hat{p}_k}{\partial x} = A_1 \hat{\eta}_k, \tag{A.5.7}$$

and

$$\begin{aligned} &(1+f_m)A_1A_2\rho_s H_s\hat{\eta}_k + f_d A_1\rho_s H_s\hat{\eta}_k + G_1 H_s\hat{\eta}_k + \gamma^2 G_2 H_s\hat{\eta}_k \\ =&\hat{p}_{k-1} + f_m A_1A_2\rho_s H_s\hat{\eta}_{k-1} + f_d A_1\rho_s H_s\hat{\eta}_{k-1}. \end{aligned} \tag{A.5.8}$$

Given the general solution (A.5.3) for $\hat{p}_k$, we get

$$-\frac{\Delta t}{\beta\rho_f}\gamma P_k(\gamma)e^{\gamma x} = A_1\hat{\eta}_k, \tag{A.5.9}$$

and

$$\begin{aligned}&\left[(1+f_m)A_1A_2\rho_sH_s + f_dA_1\rho_sH_s + G_1H_s + \gamma^2G_2H_s\right]\hat{\eta}_k\\ =&P_{k-1}(\gamma)e^{\gamma x} + A_1\rho_sH_s(f_mA_2+f_d)\hat{\eta}_{k-1},\end{aligned} \tag{A.5.10}$$

which yield

$$\begin{aligned}P_k(\gamma) &= -\frac{A_1\beta\rho_f e^{-\gamma x}}{\gamma\Delta t}\hat{\eta}_k\\ &= -\frac{A_1\beta\rho_f e^{-\gamma x}}{\gamma\Delta t}\cdot\frac{P_{k-1}(\gamma)e^{\gamma x} + A_1\rho_sH_s(f_mA_2+f_d)\hat{\eta}_{k-1}}{(1+f_m)A_1A_2\rho_sH_s + f_dA_1\rho_sH_s + G_1H_s + \gamma^2G_2H_s}\\ &= -\frac{A_1\beta\rho_f e^{-\gamma x}}{\gamma\Delta t}\cdot\frac{P_{k-1}(\gamma)e^{\gamma x} - \gamma(f_mA_2+f_d)\rho_sH_s\Delta t P_{k-1}(\gamma)e^{\gamma x}/(\beta\rho_f)}{(1+f_m)A_1A_2\rho_sH_s + f_dA_1\rho_sH_s + G_1H_s + \gamma^2G_2H_s}\\ &= \frac{-A_1(\beta\rho_f - \gamma(f_mA_2+f_d)\rho_sH_s\Delta t)}{\gamma\Delta t[(1+f_m)A_1A_2\rho_sH_s + f_dA_1\rho_sH_s + G_1H_s + \gamma^2G_2H_s]}P_{k-1}(\gamma).\end{aligned} \tag{A.5.11}$$

On the third step of the above derivations, the relation between P and $\hat{\eta}$ in the $(k-1)$-th subiteration $-\frac{\Delta t}{\beta\rho_f}\gamma P_{k-1}(\gamma)e^{\gamma x} = A_1\hat{\eta}_{k-1}$ was applied. From the definition (4.1.43), we obtain the reduction factor for fictitious mass and damping methods as

$$\rho_k^{FM}(\gamma) = \left|\frac{P_k(\gamma)-0}{P_{k-1}(\gamma)-0}\right| = \left|\frac{A_1[\beta\rho_f - \gamma(f_mA_2+f_d)\rho_sH_s\Delta t]}{\gamma\Delta t[(A_2+f_mA_2+f_d)A_1\rho_sH_s + G_1H_s + \gamma^2G_2H_s]}\right|, \tag{A.5.12}$$

which is actually independent of the subiteration step k.

A.6 Analysis of the fictitious pressure method

In this section, we provide the proof from Fourier transform for property 4.1.2. Similar to the former section, with forcing terms F_1, F_2, F_3 vanished, the divergence free condition (4.1.41b) on the fluid velocity allows us to rewrite (4.1.48) into

$$(1+f_p)\Delta p_k = f_p\Delta p_{k-1}. \tag{A.6.1}$$

From the fact that the fictitious pressure method converges to the same result $\mathbf{u}^{n-1}$ as the original Navier-Stokes splitting algorithm (4.1.41a), the pressure p^{n-1} satisfies $\Delta p^{n-1} = 0$. Combining this with our initialization at the beginning of subiterations (4.1.22b), in the first subiteration step the pressure satisfies $\Delta p_0 = 0$. Recursively, $\Delta p_k = 0$ can be obtained, which means (A.5.1) is recovered, and hence the general solution for $\hat{p}_k(x,\gamma)$ in equation (A.5.3) is recovered as well.

For the pressure and the velocity along the x direction, (4.1.48) gives the relation:

$$\rho_f \frac{\beta u_k}{\Delta t} = -(1+f_p)\frac{\partial p_k}{\partial x} + f_p \frac{\partial p_{k-1}}{\partial x}, \tag{A.6.2}$$

and correspondingly the interface conditions (4.1.41c) and (4.1.40) can be written as

$$\begin{aligned} -\frac{\Delta t}{\beta \rho_f}\left((1+f_p)\frac{\partial p_k}{\partial x} - f_p \frac{\partial p_{k-1}}{\partial x}\right) &= A_1 \eta_k, \\ A_1 A_2 \rho_s H_s \eta_k + G_1 H_s \eta_k - G_2 H_s \frac{\partial^2 \eta_k}{\partial y^2} &= p_{k-1}. \end{aligned} \tag{A.6.3}$$

Therefore, the Fourier coefficients of p_k and η_k satisfy

$$\begin{aligned} -\frac{\Delta t}{\beta \rho_f}\left((1+f_p)\frac{\partial \hat{p}_k}{\partial x} - f_p \frac{\partial \hat{p}_{k-1}}{\partial x}\right) &= A_1 \hat{\eta}_k, \\ A_1 A_2 \rho_s H_s \hat{\eta}_k + G_1 H_s \hat{\eta}_k + \gamma^2 G_2 H_s \hat{\eta}_k &= \hat{p}_{k-1}. \end{aligned} \tag{A.6.4}$$

Having $\hat{p}_k(x,\gamma) = P_k(\gamma)e^{\gamma x}$ as given in (A.5.3), the above equations read

$$\begin{aligned} -\frac{\Delta t \gamma e^{\gamma x}}{\beta \rho_f}\left((1+f_p)P_k(\gamma) - f_p P_{k-1}(\gamma)\right) &= A_1 \hat{\eta}_k, \\ A_1 A_2 \rho_s H_s \hat{\eta}_k + G_1 H_s \hat{\eta}_k + \gamma^2 G_2 H_s \hat{\eta}_k &= P_{k-1}(\gamma) e^{\gamma x}, \end{aligned} \tag{A.6.5}$$

and correspondingly:

$$\begin{aligned} P_k(\gamma) &= \frac{\Delta t \gamma e^{\gamma x} f_p P_{k-1}(\gamma)/(\beta\rho_f) - A_1 \hat{\eta}_k}{\Delta t \gamma e^{\gamma x}(1+f_p)/(\beta\rho_f)} \\ &= \frac{\Delta t \gamma e^{\gamma x} f_p/(\beta\rho_f) - A_1 e^{\gamma x}/(A_1 A_2 \rho_s H_s + G_1 H_s + \gamma^2 G_2 H_s)}{\Delta t \gamma e^{\gamma x}(1+f_p)/(\beta\rho_f)} P_{k-1}(\gamma) \\ &= \frac{f_p \Delta t \gamma (A_1 A_2 \rho_s H_s + G_1 H_s + \gamma^2 G_2 H_s) - A_1 \beta \rho_f}{(1+f_p)\Delta t \gamma (A_1 A_2 \rho_s H_s + G_1 H_s + \gamma^2 G_2 H_s)} P_{k-1}(\gamma) \end{aligned} \tag{A.6.6}$$

Therefore, the reduction factor for the fictitious pressure coefficient f_p is obtained

$$\rho_k^{FP}(\gamma) = \left|\frac{P_k(\gamma) - 0}{P_{k-1}(\gamma) - 0}\right| = \left|\frac{A_1 \beta \rho_f - f_p \Delta t \gamma (A_1 A_2 \rho_s H_s + G_1 H_s + \gamma^2 G_2 H_s)}{(1+f_p)\Delta t \gamma (A_1 A_2 \rho_s H_s + G_1 H_s + \gamma^2 G_2 H_s)}\right|. \tag{A.6.7}$$

Note that this expression is independent of the subiteration number k.

A.7 Analysis of the combined fictitious methods

Now we investigate the effect of combining the fictitious mass (and damping) method with the fictitious pressure method. Similarly to the previous sections, we perform the Fourier transform for

conditions on the fluid-structure interface and obtain

$$-\frac{\Delta t}{\beta\rho_f}\left((1+f_p)\frac{\partial p_k}{\partial x}-f_p\frac{\partial p_{k-1}}{\partial x}\right)=A_1\eta_k, \tag{A.7.1}$$

$$\begin{aligned}&(1+f_m)A_1A_2\rho_sH_s\eta_k+f_dA_1\rho_sH_s\eta_k+G_1H_s\eta_k-G_2H_s\frac{\partial^2\eta_k}{\partial y^2}\\ =&p_{k-1}+f_mA_1A_2\rho_sH_s\eta_{k-1}+f_dA_1\rho_sH_s\eta_{k-1},\end{aligned} \tag{A.7.2}$$

which lead to the relationship for the Fourier coefficients $\hat{p}_k$ and $\hat{\eta}_k$ as

$$-\frac{\Delta t}{\beta\rho_f}\left((1+f_p)\frac{\partial \hat{p}_k}{\partial x}-f_p\frac{\partial \hat{p}_{k-1}}{\partial x}\right)=A_1\hat{\eta}_k, \tag{A.7.3}$$

and

$$\begin{aligned}&(1+f_m)A_1A_2\rho_sH_s\hat{\eta}_k+f_dA_1\rho_sH_s\hat{\eta}_k+G_1H_s\hat{\eta}_k+G_2H_s\gamma^2\hat{\eta}_k\\ =&\hat{p}_{k-1}+f_mA_1A_2\rho_sH_s\hat{\eta}_{k-1}+f_dA_1\rho_sH_s\hat{\eta}_{k-1}.\end{aligned} \tag{A.7.4}$$

From the divergence-free condition (4.1.41b) on the fluid velocity, the pressure p_k satisfies the Laplacian equation (A.5.1), as derived in A.6. Therefore, we can substitute the general solution $\hat{p}_k(x,\gamma)=P_k(\gamma)e^{\gamma x}$ into (A.7.3)-(A.7.4) and obtain:

$$-\frac{\Delta t\gamma e^{\gamma x}}{\beta\rho_f}((1+f_p)P_k(\gamma)-f_pP_{k-1}(\gamma))=A_1\hat{\eta}_k, \tag{A.7.5}$$

$$\begin{aligned}&(1+f_m)A_1A_2\rho_sH_s\hat{\eta}_k+f_dA_1\rho_sH_s\hat{\eta}_k+G_1H_s\hat{\eta}_k+G_2H_s\gamma^2\hat{\eta}_k\\ =&P_{k-1}(\gamma)e^{\gamma x}+f_mA_1A_2\rho_sH_s\hat{\eta}_{k-1}+f_dA_1\rho_sH_s\hat{\eta}_{k-1}.\end{aligned} \tag{A.7.6}$$

At the k-th and $(k-1)$-th subiteration steps, (A.7.5) gives the expressions for $\hat{\eta}$ as

$$\begin{aligned}\hat{\eta}_k&=-\frac{\Delta t\gamma e^{\gamma x}}{A_1\beta\rho_f}((1+f_p)P_k(\gamma)-f_pP_{k-1}(\gamma)),\\ \hat{\eta}_{k-1}&=-\frac{\Delta t\gamma e^{\gamma x}}{A_1\beta\rho_f}((1+f_p)P_{k-1}(\gamma)-f_pP_{k-2}(\gamma)),\end{aligned} \tag{A.7.7}$$

which can be combined with (A.7.6):

$$(J_1+J_2)(1+f_p)P_k(\gamma)-\left((J_1+J_2)f_p+J_1(1+f_p)-\frac{\beta\rho_fA_1}{\Delta t\gamma}\right)P_{k-1}(\gamma)+J_1f_pP_{k-2}(\gamma)=0, \tag{A.7.8}$$

where

$$J_1=A_1\rho_sH_s(f_mA_2+f_d),\ J_2=A_1A_2\rho_sH_s+G_1H_s+\gamma^2G_2H_s. \tag{A.7.9}$$

When $f_m A_2 + f_d \neq 0$ and $f_p \neq 0$, we can get the roots for the quadratic function

$$(J_1 + J_2)(1 + f_p)q^2 - \left((J_1 + J_2)f_p + J_1(1 + f_p) - \frac{\beta\rho_f A_1}{\Delta t\gamma}\right) q + J_1 f_p P_{k-2}(\gamma) = 0 \tag{A.7.10}$$

as

$$\begin{aligned} q_1 &= \frac{-\left((J_1 + J_2)f_p + J_1(1 + f_p) - \frac{\beta\rho_f A_1}{\Delta t\gamma}\right) + J_3}{2(J_1 + J_2)(1 + f_p)}, \\ q_2 &= \frac{-\left((J_1 + J_2)f_p + J_1(1 + f_p) - \frac{\beta\rho_f A_1}{\Delta t\gamma}\right) - J_3}{2(J_1 + J_2)(1 + f_p)}. \end{aligned} \tag{A.7.11}$$

where

$$J_3 = \sqrt{\left((J_1 + J_2)f_p + J_1(1 + f_p) - \frac{\beta\rho_f A_1}{\Delta t\gamma}\right)^2 - 4(J_1 + J_2)(1 + f_p)J_1 f_p}.$$

A general expression for $P_k(\gamma)$ can be obtained as

$$\begin{aligned} P_k(\gamma) &= Q_1 q_1^k + Q_2 q_2^k, \quad \text{when } q_1 \neq q_2, \\ P_k(\gamma) &= (Q_1 + Q_2 k)q_1^k, \quad \text{when } q_1 = q_2; \end{aligned} \tag{A.7.12}$$

where the constants Q_1 and Q_2 are given by the initial values $P_0(\gamma)$ and $P_1(\gamma)$. When $k \gg 1$, we have the following trends for the reduction factor:

$$\begin{aligned} \rho_k^{FM+FP}(\gamma) &= \left|\frac{P_k(\gamma)}{P_{k-1}(\gamma)}\right| \approx \max(|q_1|, |q_2|), \quad \text{when } q_1 \neq q_2, \\ \rho_k^{FM+FP}(\gamma) &= \left|\frac{P_k(\gamma)}{P_{k-1}(\gamma)}\right| \approx |q_1|, \quad \text{when } q_1 = q_2. \end{aligned} \tag{A.7.13}$$

Therefore, the combined fictitious method converges when $|q_1| < 1$ and $|q_2| < 1$.

A.8 Robin based coupling method

The Robin based coupling scheme in this paper is a modified version of that in [112]. It follows the steps we demonstrated in section 4.1.1, but with the interface boundary conditions changed to the Robin type. To be more specific, for any given Robin coefficient θ, on the structure side, instead of the Neumann boundary condition (4.1.11) we impose

$$\mathbf{S}_k^n \mathbf{n}_s = -[-p_{k-1}^n \mathbf{I} + \rho_f \nu(\nabla \mathbf{u}_{k-1}^n + (\nabla \mathbf{u}_{k-1}^n)^T)]\mathbf{n}_f + \theta\nu(\mathbf{u}_{k-1}^n - \frac{\partial \boldsymbol{\eta}_k^n}{\partial t}), \tag{A.8.1}$$

at the n-th time step and k-th subiteration. Correspondingly, on the fluid side, the pressure

boundary condition (4.1.8) is kept the same, but the velocity condition (4.1.3) is modified:

$$2\epsilon(\mathbf{u}_k^n)\cdot\mathbf{n}_f+\theta\mathbf{u}_k^n=2\epsilon(\frac{\partial\boldsymbol{\eta}_k^n}{\partial t})\cdot\mathbf{n}_f+\theta\mathbf{u}_{k-1}^n, \tag{A.8.2}$$

where $\epsilon(\mathbf{c})=\frac{1}{2}(\nabla\mathbf{c}+\nabla\mathbf{c}^T)$. Comparing with what proposed in [112], our Robin based coupling reinforced the implicitness by including their explicit viscous-structure coupling into subiterations. This not only helps the convergence, but also generates a more fair comparison with our fixed-point methods.

In our comparisons, only the results from the optimal Robin coefficients were presented. To obtain the optimal Robin coefficient in each case, various Robin coefficients are tested with numerical simulations, and we took the one that generated the smallest number of averaged subiterations without affecting the accuracy at the interface.

A.9 Expression for coefficient of friction between the cylinder and fairing

To evaluate the relative velocity of fairing with respect to the cylinder, we consider the expressions of cylinder/fairing velocities at the contact point C. Since the cylinder does not rotate, every point on it has the same velocity as CG_c. Therefore, the tangential velocity of point C on the cylinder can be expressed as

$$\frac{\partial c_x}{\partial t}\sin\beta-\frac{\partial c_y}{\partial t}\cos\beta. \tag{A.9.1}$$

On the other hand, now we consider the fairing side. Along the x direction, we have the velocity of fairing gravity center CG_f as $\frac{\partial f_x}{\partial t}$, the relative velocity of CG_c to CG_f as $a\frac{\partial\theta}{\partial t}\sin\theta$, and the relative velocity of contact point to CG_c as $R\frac{\partial\theta}{\partial t}\sin\beta$. Therefore, the velocity of point C along x direction is

$$\frac{\partial f_x}{\partial t}+a\frac{\partial\theta}{\partial t}\sin\theta+R\frac{\partial\theta}{\partial t}\sin\beta, \tag{A.9.2}$$

and the velocity along the y direction can be similarly written as

$$\frac{\partial f_y}{\partial t}-a\frac{\partial\theta}{\partial t}\cos\theta-R\frac{\partial\theta}{\partial t}\cos\beta. \tag{A.9.3}$$

Based on (A.9.2) and (A.9.3), we have the tangential velocity of point C on the fairing as

$$\left(\frac{\partial f_x}{\partial t}+a\frac{\partial\theta}{\partial t}\sin\theta+R\frac{\partial\theta}{\partial t}\sin\beta\right)\sin\beta-\left(\frac{\partial f_y}{\partial t}-a\frac{\partial\theta}{\partial t}\cos\theta-R\frac{\partial\theta}{\partial t}\cos\beta\right)\cos\beta. \tag{A.9.4}$$

Combining (A.9.1) with the geometry relation (4.4.4), we can rewrite the tangential velocity expression on the cylinder side as

$$\left(\frac{\partial f_x}{\partial t} + a\frac{\partial \theta}{\partial t}\sin\theta\right)\sin\beta - \left(\frac{\partial f_y}{\partial t} - a\frac{\partial \theta}{\partial t}\cos\theta\right)\cos\beta. \tag{A.9.5}$$

Substracting (A.9.5) from the tangential velocity on the fairing side (A.9.4), we have the relative tangential velocity of fairing to cylinder at point C as $R\frac{\partial \theta}{\partial t}$. Therefore, the coefficient of friction between the cylinder and fairing should be proportional to the sign function of $\frac{\partial \theta}{\partial t}$. Note that $\text{sgn}\left(\frac{\partial \theta}{\partial t}\right)$ is not a C^1 function since it has a jump when $\frac{\partial \theta}{\partial t} = 0$. In the numerical simulations, this formulation might cause problems known as the Gibbs phenomena. Therefore, we employ a smoothed expression for f_c as

$$f_c = -C_f \text{sgn}\left(\frac{\partial \theta}{\partial t}\right)\exp\left(\frac{-0.001}{\left|\frac{\partial \theta}{\partial t}\right|}\right)$$

in all the numerical simulations.

A.10 Manual for structure solver–StressNEKTAR

This document is meant as an introduction to the parallel spectral/hp element solver "StressNEKTAR", in the user and developer level.

A.10.1 For users

Installation

Before we start, first check if the software package contains the following seven folders:

`include, Flags, Veclib, gs, Metis, HlibFS, Nektar3dS,`

then make sure that the mpi compiler and the linear algebra packages

`scalapack, lapack, blas, blacs`

are all properly installed. To use the StressNEKTAR to solve linear elastic problems, first compile and install following the steps:

1. Edit the manifest file *Linux.inc* in the directory *Flags*, by providing the pathes of all required compilers and libararies.

2. In the folder *Veclib*, enter the commands in a shell window as

```
gmake ARCH=Linux
```

and copy the resultant library *libvec.a* into the directory $HlibFS/Linux$.

3. In the folder *gs*, compile with the commands

```
gmake ARCH=Linux mopt
```

and also copy the resultant library *libgs.a* into the directory $HlibFS/Linux$.

4. Now enter the folder Metis/metis-4.0/Lib and type

```
gmake ARCH=Linux
```

then find the resultant library *libmetis.a* in $Metis/metis-4.0$ and copy it into $HlibFS/Linux$.

5. In the directory $HlibFS/Linux$, compile the library for structure solver by entering

```
gmake ARCH=Linux PARALLEL=1 SOLID=1 mopt
```

6. Lastly, we can generate the structure solver *nektarSLinm* in the directory $Nektar3dS/Linux$ with the commands

```
gmake ARCH=Linux PARALLEL=1 mopt
```

To compile the structure solver for nonlinear elastodynamics, finish the first five steps of the above procedure, and in the last step we compile in the directory $Nektar3dSN/Linux$ with the commands

```
gmake ARCH=Linux PARALLEL=1 mopt
```

Then the numerical solver *nektarSNonLm* for hyperelastic materials is generated.

Learning by example

Now we introduce the input file format for StressNEKTAR with an example file, which is in flat text and can be downloaded at

```
https://www.dropbox.com/s/d31u05t2egrs1md/skewcubic.rea
```

This input file describes the test problem employed in section 2.3.3 for testing the $p-$convergence of the semi-local method. The input file is composed by eight main sections: PARAMETERS, MESH DATA, CURVED SIDE DATA, BOUNDARY CONDITIONS, INITIAL CONDITIONS, HISTORY AND INTEGRAL DATA, DRIVE FUNCT DATA and Exact, among which the sections MESHDATA, CURVED SIDE DATA, HISTORY AND INTEGRAL DATA, DRIVE FUNCT DATA and Exact are completely inherited from the fluid solver NEKTAR, and we therefore refer the interested readers to the fluid NEKTAR manual [159] to avoid redundancy. Next we explain the other three sections one by one, with special emphasis on the parts which differ from the fluid NEKTAR.

PARAMETERS

The purpose of each parameter line can be described as

```
 ****** PARAMETERS *****
24 PARAMETERS FOLLOW
0.01    DT                --time step size
10      NSTEPS            --number of time steps to run for
1        IOSTEP           --the frequency that the output will be dumped to file
1.9      YUA              --constant used in this input file
0.1      YUB              --constant used in this input file
1.4      YUC              --constant used in this input file
1.0      YUa              --constant used in this input file
10.2      YUb             --constant used in this input file
100      DMODULUS         --Youngs modulus
1000      STRUCTDENSITY   --the structure density
0.3      DPOISSONRATIO    --the Poisson ratio
(1.0-DPOISSONRATIO)*DMODULUS/((1.0+DPOISSONRATIO)*(1.0-2.0*DPOISSONRATIO))  DE1
                          --constant used in this input file
DPOISSONRATIO*DMODULUS/((1.0+DPOISSONRATIO)*(1.0-2.0*DPOISSONRATIO))        DE2
                          --constant used in this input file
0.25     DNM_BETA         --the second parameter for the Newmark scheme
0.5      DNM_GAMMA        --the first parameter for the Newmark scheme
0.5      DTHETA1          --the first parameter for the BDF scheme
0.5      DTHETA2          --the second parameter for the BDF scheme
500     IMAXIT            --maximum number of subiterations in each time step
```

```
0.000000000001  DITTOL    --convergence tolerance for subiterations
0.0      DLOWER_LIMIT     --lower bound of \tau_k in the Aitken relaxation
0.98      DUPPER_LIMIT    --upper bound of \tau_k in the Aitken relaxation
0.3      DINITRELAX       --initial value of \tau_k in the Aitken relaxation
0       PRECON            --choice of preconditioner: 0=diagonal; 3=low energy
0.0000000000001 TOLCG     --convergence tolerance for the conjugate gradient method
0  Lines of passive scalar data follows   --dummy line
0  LOGICAL SWITCHES FOLLOW                --dummy line
```

BOUNDARY CONDITIONS

This section provides the information about which elements share a common face, and specifies the boundary conditions on the boundary faces. We now discuss the format for element 2:

```
s 2 1 0. 0. 0.  --non-follower traction load applied on the 1st face of element2
tx = 0                                          --x-component of surface load
ty = 0                                          --y-component of surface load
tz = DE2*(YUA+YUB*sin(YUa*t)+YUb*YUC*cos(YUb*x))   --z-component of surface load
s 2 2 0. 0. 0.   --non-follower traction load applied on the 2nd face of element2
tx = 0
ty = -DE2*(YUA+YUB*sin(YUa*t)+YUb*YUC*cos(YUb*x))
tz = 0
v 2 3 0. 0. 0.  --Dirichlet type boundary for displacement on the 3rd face of element 2
u = YUC*sin(YUb*x)                              --x-component of displacement
v = 0                                           --y-component of displacement
w = 0                                           --z-component of displacement
E 2 4 4 2       --the 4th face of element 2 is connected with the 2nd face of element 4
E 2 5 1 3       --the 5th face of element 2 is connected with the 3rd face of element 1
E 2 6 6 1       --the 6th face of element 2 is connected with the 1st face of element 6
```

and there is another possible type of boundary condition not employed in this example, namely

```
W 1 1 0. 0. 0.  --zero Dirichlet boundary for displacement on the 1st face of element 1
```

INITIAL CONDITIONS

As the initial condition, both the displacement field and the velocity field should be provided, with the format explained as below

```
7         INITIAL CONDITIONS *****   --number of lines to read in
Given                                --specify initial condition as functions
u = YUA*x+YUC*sin(YUb*x)             --x-component of initial displacement
v = 0.0                              --y-component of initial displacement
w = 0.0                              --z-component of initial displacement
dudt = YUB*YUa*x                     --x-component of initial velocity
dvdt = 0.0                           --y-component of initial velocity
dwdt = 0.0                           --z-component of initial velocity
```

Alternatively, the user could start from the checkpoint files as

```
2         INITIAL CONDITIONS *****   --number of lines to read in
Restart                              --read checkpoint file for the initial fields
skewcubic_0.chk.rst                  --name of the check file
```

at the same time, the user should copy the other two checkpoint files following the commands

```
cp skewcubicold_0.chk.rst skewcubic_old
cp skewcubicoldt_0.chk.rst skewcubic_oldt
```

Here the file *skewcubic_old*, *skewcubic_oldt* stores the displacement and velocity fields of the previous two time steps. By doing so, we diminish the fluctuations caused by restarting.

Running and post-processing

Copy the executable file *nektarSLinm* and the input file *skewcubic.rea* into the current directory, then the command line to start up a simulation should be

```
./nektarSLinm -n6 -i -v -V -S -chk skewcubic.rea
```

The parameters used in the command line have the following functions:

```
-n6: use 6th expansion order in each element, which is equivalent to 5th order polynomials.
-i: solve the linear system with the iterative solver.
-v: print out details of solving process to help debuggers.
-V: the boundary conditions and the body forces may be time-dependent.
-S: do not overwrite the checkpoint files.
-chk: dump the solution fields into checkpoint file every IOSTEP.
```

For post processing, we introduce the .chk files which are slightly different with that from the fluid solver. As mentioned above, in every IOSTEP three classes of checkpoint files are produced to record:

```
skewcubic_3.chk      --the displacement, velocity, acceleration fields at step 4*IOSTEP
skewcubicold_3.chk   --the displacement, velocity, acceleration fields at step 4*IOSTEP-1
skewcubicoldt_3.chk  --the displacement, velocity, acceleration fields at step 4*IOSTEP-2
```

A.10.2 For developers

In this section, we describe the principal functions in drive.C, as a reference for future developers. Firstly, for the linear elastic solver:

- **StartUp_Newmark_Schur:** computes the initial acceleration following

$$\ddot{\mathbf{U}}^0 = \mathbf{M}^{-1}(-\mathbf{K}\mathbf{U}^0 + \mathbf{F}^0).$$

- **StiffMat_Schur_new:** forms and saves the mass matrix $\mathbf{M}$ in $Usys- > Mmat$ and the stiffness matrix $\mathbf{K}$ in $Usys- > Gmat$.

- **BuildLoad_Schur_new:** calculates and saves the external load

$$\int_{\partial\Omega_N} (T)_i \phi_p d\Gamma + \int_{\Omega} (f)_i \phi_p d\Omega, \ i = 1, 2, 3 \tag{A.10.1}$$

  into $uf[0]$, $vf[0]$ and $wf[0]$.

- **AddInertiaForceToLoad_Schur:** when step$<$ 2 generates the internal load following the Newmark scheme as

$$\frac{1}{\Delta t^2 \theta_2}\left(\mathbf{U}^{n-1} + \Delta t \dot{\mathbf{U}}^{n-1} + \frac{\Delta t^2}{2}(1-2\theta_2)\ddot{\mathbf{U}}^{n-1}\right)\mathbf{M}, \tag{A.10.2}$$

  or calculates the internal load following the BDF scheme when step$\geq$ 2

$$(A_2(B_1\mathbf{U}^{n-1} + C_1\mathbf{U}^{n-2} + D_1\mathbf{U}^{n-3}) + (B_2\dot{\mathbf{U}}^{n-1} + C_2\dot{\mathbf{U}}^{n-2} + D_2\dot{\mathbf{U}}^{n-3}))\mathbf{M}, \tag{A.10.3}$$

  and adds the results into $uf[0]$, $vf[0]$ and $wf[0]$.

- **D_solve_Schur:** inverts the linear system with Conjugate Gradient method, to solve for $\mathbf{U}^n$.

- **DAnalyser_Schur:** dumps the history data into .his files and saves the displacement, velocity and acceleration fields into the checkpoint files.

Similarly, for the nonlinear elastodynamics solver there are eight principal functions:

- **NONLStartUp_Newmark_Schur:** computes the initial acceleration with the algorithm described in [27]:

$$\ddot{\mathbf{U}}^0 = \mathbf{M}^{-1}\left(-\int_\Omega \mathbf{S} : \frac{1}{2}\left(\left(\frac{\partial \mathbf{v}}{\partial \mathbf{X}}\right)^T \mathbf{F}(\boldsymbol{\eta}) + \mathbf{F}(\boldsymbol{\eta})^T\left(\frac{\partial \mathbf{v}}{\partial \mathbf{X}}\right)\right) d\Omega + \mathbf{F}^0\right).$$

- **BuildLoad_Schur_new:** calculates and saves the external load (A.10.1) into $uf[1]$, $vf[1]$ and $wf[1]$.

- **AddInertiaForceToLoad_Schur:** generates and adds the internal load (A.10.2) or (A.10.3) into $uf[1]$, $vf[1]$ and $wf[1]$.

- **NONL_PreCalc_Schur_new:** computes the Green-Lagrange strain tensor, the second Green-Kirchoff stress tensor and the elasticity tensor and stores them into $StrainE$, $Stress2nd$ and $ElasTensor$, respectively.

- **NONL_StiffMat_Schur:** forms and saves the stiffness matrix $\mathbf{K}$ into $Usys->Gmat$, and stores the contribution from the internal stress

$$-\sum_{k,l=1}^{3}\int_\Omega \mathbf{S}_{kl}\frac{1}{2}\left(\frac{\partial \phi_j}{\partial X_k}\mathbf{F}_{il} + \mathbf{F}_{ik}\frac{\partial \phi_j}{\partial X_l}\right) d\Omega, \tag{A.10.4}$$

into Uf, Vf and Wf.

- **NONL_IterDepInertiaLoad_Schur:** calculates the sum of (A.10.4) and

$$-\frac{1}{\Delta t^2 \theta_2}\mathbf{M}\mathbf{U}^{n,k} \text{ for Newmark scheme}$$

or

$$A_1 A_2 \mathbf{M}\mathbf{U}^{n,k} \text{ for BDF scheme,}$$

then saves the resultant vectors into Uf, Vf and Wf.

- **NONL_D_solve_Schur:** inverts the linear system and solves for the displacement increment $\triangle\mathbf{U}$ of the Newton-Raphson iterative procedure.

- **DAnalyser_Schur:** dumps the history data and saves the displacement, velocity and acceleration fields into the checkpoint files. Additionally, the second Green-Kirchoff stress tensor is stored in the stress checkpoint files.

A.11 Manual for FSI solver

In the part, we introduce the coupling of the parallel spectral/*hp* element fluid solver "NEKTAR" and the structure solver "StressNEKTAR".

A.11.1 For users

Installation

To compile for the needed executable files, the package should include all the folders listed in Appendix A.10.1, as well as a folder for the fluid part

`Nektar3dF.`

The mpi compiler and the linear algebra packages are also required. Additionally, the mpi commands should support the "multiple program multiple data" (MPMD) style launches, either from the command line or from a file. First, compile for the basic libraries

$$libvec.a,\ libgs.a,\ libmetis.a$$

following the steps 1-4 in the installation part of Appendix A.10.1. Then:

1. In the directory $HlibFS/Linux$, compile the library for structure solver by entering

   ```
   gmake ARCH=Linux PARALLEL=1 SOLID=1 mopt
   ```

   and compile the library for fluid solver with the command

   ```
   gmake ARCH=Linux PARALLEL=1 FLUID=1 mopt
   ```

2. In the directory $Nektar3dS/Linux$, generate the structure numerical solver $nektarSLin.fsim$ with the command

   ```
   gmake ARCH=Linux PARALLEL=1 FSI=1 mopt
   ```

   and similarly obtain the fluid numserical solver $nektarF.woom.fsi.alem$ by typing

   ```
   gmake ARCH=Linux PARALLEL=1 FSI=1 ALE=1 WOMERR=1 mopt
   ```

To compile the nonlinear elastodynamics solver for FSI, simular as in Appendix A.10.1 in the last step we compile in the directory $Nektar3dSN/Linux$ by typing as follows

```
gmake ARCH=Linux PARALLEL=1 FSI=1 mopt
```

Then the numerical solver $nektarSNonL.fsim$ for hyperelastic materials could be employed in FSI.

Learning by example

We now study the input files for the straight tube with pulsatile inflow case in section 4.1.4. The input files involved can be downloaded at

```
https://www.dropbox.com/s/cp1i1f8sbbe8qbt/tube_fluid_L4_6.rea
https://www.dropbox.com/s/dnib05zkz7co3oa/tube04_yyu_solid_6.rea
https://www.dropbox.com/s/r6dqdh7w4oka8g3/tube_fluid_L4_6.RC
```

The last file gives the needed constants for fluid outflow boundary condition (4.1.68):

```
0.0 0.0
```

where the first 0.0 indicates the parameter R and the second 0.0 is the parameter C, which together determine the flow-dependent outlet pressure $\bar{p}$. The first and second files provide the input for fluid solver and for structure solver, respectively. Here we only describe the parameters and boundary conditions related with fluid-structure interaction, to avoid redundacy. Note that other details regarding the fluid input file are described in the manual [159] and for more about the structure input file we refer the interested readers to Appendix A.10.

PARAMETERS

In the fluid input file, the following 8 parameters are required for the coupling:

```
0.0   DSEND_ZERO_FORCES_TIME  --before this time, set the hydrodynamic stress to zero.
1000       IMAXIT             --maximum subiteration number in each time step.
1e-6     DITTOL               --tolerance for subiteration convergence.
0.3      DINITRELAX           --initial relaxation parameter \tau_0 for Aitken.
0       ITSTART               --the time step number where subiteration starts.
0.      DLOWER_LIMIT          --lower bound for the Aitken relaxation parameter.
0.98      DUPPER_LIMIT        --upper bound for the Aitken relaxation parameter.
0.0     DADDEDMASS            --fictitious pressure coefficient.
```

On the structure side, there are 10 parameters related with fluid-structure interaction coupling:

```
2.0     DADDEDMASS          --fictitious mass coefficient.
0.0     DAMPING_C1          --the first Rayleigh damping parameter.
0.0     DAMPING_C2          --the second Rayleigh damping parameter.
0.0     FICDAMPING          --fictitious damping coefficient.
1000       IMAXIT           --maximum subiteration number in each time step.
0.3      DINITRELAX         --initial relaxation parameter \tau_0 for Aitken.
0        ITSTART            --the time step number where subiteration starts.
0.0      DLOWER_LIMIT       --lower bound for the Aitken relaxation parameter.
0.98      DUPPER_LIMIT      --upper bound for the Aitken relaxation parameter.
1e-5     DITTOL             --tolerance for subiteration convergence.
```

BOUNDARY CONDITIONS

On the fluid-structure interface, the "L" type of boundary condition should be specified for the related element faces on both the fluid and structure sides

```
L 1 1 0. 0. 0.  --FSI interface boundary for displacement on the 1st face of element 1
```

A.11.2 For developers

In this section, we describe the FSI related functions employed in drive.C for future developers. In the fluid solver we have

- **data_zero:** zeros out the normal hydrodynamic stress.
- **data_send:** sends the normal hydrodynamic stresses to the structure side.
- **data_receive:** receives the structure velocity and acceleration information from the structure side.
- **macc_save:** saves the structure acceleration information.
- **mvel_save:** saves the structure velocity information.
- **forces:** calculates the normal hydrodynamic stresses on the fluid-structure interface, and copies them into *send_datax*, *send_datay* and *send_dataz*.
- **BndryMeshAcc:** copies the structure acceleration information into Ubc, Vbc and Wbc.
- **BndryMeshVelocity:** copies the structure velocity information into Ubc, Vbc and Wbc.

- **Update_Mesh_Velocity:** generates the mesh velocity and saves the corresponding components in $MeshV[0]$, $MeshV[1]$ and $MeshV[2]$.
- **Update_Mesh_Outside:** numerically integrates the mesh velocity and obtains the updated fluid mesh.

In the structure side, we have the following functions for coupling:

- **data_send:** sends the velocity and acceleration information to the fluid side.
- **data_receive:** receives the normal hydrodynamic stresses from the fluid side.
- **macc_save:** stores the normal hydrodynamic stresses into $macc\_datax$, $macc\_datay$ and $macc\_dataz$.
- **data_prepare:** copies the structure velocity/acceleration information into $send\_datax$, $send\_datay$ and $send\_dataz$.

Bibliography

[1] D. A. Steinman, Y. Hoi, others (authors are ordered alphabetically by first author within the group), Variability of CFD solutions for pressure and flow in a giant aneurysm: The SBC2012 CFD challenge, Journal of biomechanical engineering 1 (2013) 542.

[2] J. Van Gijn, G. J. E. Rinkel, Subarachnoid haemorrhage: diagnosis, causes and management, Brain 124 (2) (2001) 249–278.

[3] P. Perdikaris, G. E. Karniadakis, Fractional-order viscoelasticity in one-dimensional blood flow models, Submitted to Annals of Biomedical Engineering.

[4] H. Baek, G. E. Karniadakis, A convergence study of a new partitioned fluid-structure interaction algorithm based on fictitious mass and damping, Journal of Computational Physics 231 (2) (2012) 629 – 652.

[5] L. G. Giorda, F. Nobile, C. Vergara, Analysis and optimization of Robin-Robin partitioned procedures in fluid-structure interaction problems, SIAM Journal on Numerical Analysis 48 (6) (2010) 2091–2116.

[6] G. E. Karniadakis, S. J. Sherwin, Spectral/hp Element Methods for Computational Fluid Dynamics (Numerical Mathematics and Scientific Computation), 2nd Edition, Oxford University Press, Oxford, 2005.

[7] C. Schwab, M. Suri, Mixed *hp* finite element methods for Stokes and non-Newtonian flow, Computer Methods in Applied Mechanics and Engineering 175 (3-4) (1999) 217–241.

[8] I. Babuska, M. Suri, The p and $h-p$ versions of the finite element method, basic principles and properties, SIAM Review 36 (4) (1994) 578 – 632.

[9] D. Schotzau, $hp-$ DGFEM for parabolic evolution problems, Doctoral Dissertation, ETH Zurich.

[10] R. Stenberg, M. Suri, Mixed *hp* finite element methods for problems in elasticity and Stokes flow, Numerische Mathematik 72 (3) (1996) 367–389.

[11] L. Chilton, M. Suri, Locking-free mixed *hp* finite element methods for curvilinear domains, Computer Methods in Applied Mechanics and Engineering 190 (26-27) (2001) 3427–3442.

[12] M. Suri, Analytical and computational assessment of locking in the *hp* finite element method, Computer Methods in Applied Mechanics and Engineering 133 (3-4) (1996) 347–371.

[13] M. Suri, A reduced constraint *hp* finite element method for shell problems, Mathematics of Computation 66 (217) (1997) 15–29.

[14] M. Vogelius, An analysis of the $p-$version of the finite-element method for nearly incompressible materials - uniformly valid, optimal error-estimates, Numerische Mathematik 41 (1) (1983) 39–53.

[15] C. Schwab, $p-$ and $hp-$ Finite Element Methods: Theory and Applications in Solid and Fluid Mechanics, Oxford University Press, Oxford, 1998.

[16] A. Duster, S. Hartmann, E. Rank, $p-$FEM applied to finite isotropic hyperelastic bodies, Computer Methods in Applied Mechanics and Engineering 192 (2003) 5147–5166.

[17] Z. Yosibash, S. Hartmann, U. Heisserer, A. Duster, E. Rank, M. Szanto, Axisymmetric pressure boundary loading for finite deformation analysis using $p-$FEM, Computer Methods in Applied Mechanics and Engineering 196 (7) (2007) 1261 – 1277.

[18] U. Heisserer, S. Hartmann, A. Duster, Z. Yosibash, On volumetric locking-free behaviour of $p-$version finite elements under finite deformations, Communications in Numerical Methods in Engineering 24 (2008) 1019 – 1032.

[19] S. M. Holzer, Z. Yosibash, The $p-$version of the finite element method in incremental elasto-plastic analysis, International Journal for Numerical Methods in Engineering 39 (11) (1996) 1859–1878.

[20] O. C. Zienkiewicz, R. L. Taylor, The Finite Element Method, 5th ed, Butterworth-Heinemann, 2000.

[21] B. A. Szabo, I. Babuska, Finite Element Analysis, John Wiley & Sons, New York, USA, 1991.

[22] A. Duster, A. Niggl, E. Rank, Applying the $hp-d$ version of the FEM to locally enhance dimensionally reduced models, Computer Methods in Applied Mechanics and Engineering 196 (37-40) (2007) 3524–3533.

[23] J. T. Oden, J. R. Cho, Adaptive $hpq-$finite element methods of hierarchical models for plate- and shell-like structures, Computer Methods in Applied Mechanics and Engineering 136 (3-4) (1996) 317–345.

[24] C. Schwab, A-posteriori modeling error estimation for hierarchic plate models, Numerische Mathematik 74 (2) (1996) 221–259.

[25] Y. Basar, U. Hanskotter, C. Schwab, A general high-order finite element formulation for shells at large strains and finite rotations, International Journal for Numerical Methods in Engineering 57 (15) (2003) 2147–2175.

[26] R. Tews, W. Rachowicz, Application of an automatic *hp* adaptive finite element method for thin-walled structures, Computer Methods in Applied Mechanics and Engineering 198 (21-26) (2009) 1967–1984.

[27] S. Dong, Z. Yosibash, A parallel spectral element method for dynamic three-dimensional nonlinear elasticity problems, Computers & Structures 87 (1-2) (2009) 59 – 72.

[28] J. C. Simo, F. Armero, Geometrically nonlinear enhanced strain mixed methods and the method of incompatible modes, International Journal for Numerical Methods in Engineering 33 (7) (1992) 1413–1449.

[29] J. C. Simo, F. Armero, R. L. Taylor, Improved versions of assumed enhanced strain tri-linear elements for 3D-finite deformation problems, Computer Methods in Applied Mechanics and Engineering 110 (3-4) (1993) 359–386.

[30] J. C. Simo, M. S. Rifai, A class of mixed assumed strain methods and the method of incompatible modes, International Journal for Numerical Methods in Engineering 29 (8) (1990) 1595–1638.

[31] R. L. Taylor, A mixed-enhanced formulation for tetrahedral finite elements, International Journal for Numerical Methods in Engineering 47 (1-3) (2000) 205–227.

[32] M. A. Puso, A highly efficient enhanced assumed strain physically stabilized hexahedral element, International Journal for Numerical Methods in Engineering 49 (8) (2000) 1029–1064.

[33] R. S. Falk, Nonconforming finite element methods for the equations of linear elasticity, Mathematics of Computation 57 (196) (1991) 529–550.

[34] T. Sussman, K. J. Bathe, A finite-element formulation for nonlinear incompressible elastic and inelastic analysis, Computers & Structures 26 (1-2) (1987) 357–409.

[35] M. E. Canga, E. B. Becker, An iterative technique for the finite element analysis of near-incompressible materials, Computer Methods in Applied Mechanics and Engineering 170 (1-2) (1999) 79–101.

[36] A. M. Maniatty, Y. Liu, O. Klaas, M. S. Shephard, Higher order stabilized finite element method for hyperelastic finite deformation, Computer Methods in Applied Mechanics and Engineering 191 (13-14) (2002) 1491 – 1503.

[37] O. Klaas, A. Maniatty, M. S. Shephard, A stabilized mixed finite element method for finite elasticity. formulation for linear displacement and pressure interpolation, Computer Methods in Applied Mechanics and Engineering 180 (1-2) (1999) 65–79.

[38] J. S. Chen, C. Pan, A pressure projection method for nearly incompressible rubber hyperelasticity, part i: Theory, Journal of Applied Mechanics 63 (4) (1996) 862–868.

[39] J. S. Chen, C. T. Wu, C. Pan, A pressure projection method for nearly incompressible rubber hyperelasticity, part ii: Applications, Journal of Applied Mechanics 63 (4) (1996) 869–876.

[40] K. J. Bathe, Finite Element Procedures, Prentice Hall, 2007.

[41] D. Pantuso, K. J. Bathe, On the stability of mixed finite elements in large strain analysis of incompressible solids, Finite Elements in Analysis and Design 28 (2) (1997) 83 – 104.

[42] D. Chapelle, K. J. Bathe, On the ellipticity condition for model-parameter dependent mixed formulations, Computers & Structures 88 (9-10) (2010) 581 – 587.

[43] F. Auricchio, L. B. da Veiga, C. Lovadina, A. Reali, A stability study of some mixed finite elements for large deformation elasticity problems, Computer Methods in Applied Mechanics and Engineering 194 (9-11) (2005) 1075 – 1092.

[44] A. F. Bower, Applied Mechanics of Solids, CRC Press, 2009.

[45] J. Bonet, R. D. Wood, Nonlinear Continuum Mechanics for Finite Element Analysis, Cambridge University Press, 1997.

[46] R. S. Rivlin, D. W. Saunders, Large Elastic Deformations of Isotropic Materials. VII. Experiments on the Deformation of Rubber, Philosophical Transactions of the Royal Society of London. Series A, Mathematical and Physical Sciences 243 (865) (1951) 251–288.

[47] R. W. Penn, Volume changes accompanying the extension of rubber, Journal of Rheology 14 (4) (1970) 509–517.

[48] D. Pantuso, K. J. Bathe, A finite element formulation for nonlinear incompressible elastic and inelastic analysis, Computers & Structures 26 (1-2) (1987) 357 – 409.

[49] L. R. Scott, M. Vogelius, Norm estimates for a maximal right inverse of the divergence operator in spaces of piecewise polynomials., Mathematical Modelling and Numerical Analysis 19 (1985) 111 – 143.

[50] M. Ainsworth, P. Coggins, The stability of mixed $hp-$finite element methods for Stokes flow on high aspect ratio elements, SIAM J. Numer. Anal. 38 (2000) 1721–1761.

[51] D. Chapelle, K. J. Bathe, The $inf - sup$ test, Computers & Structures 47 (4-5) (1993) 537 – 545.

[52] K. J. Bathe, The $inf - sup$ condition and its evaluation for mixed finite element methods, Computers & Structures 79 (2) (2001) 243 – 252.

[53] M. Ainsworth, P. Coggins, A uniformly stable family of mixed hpfinite elements with continuous pressures for incompressible flow, IMA Journal of Numerical Analysis 22 (2) (2002) 307–327.

[54] K. D. Papoulis, Fully nonlinear hyperelastic analysis of nearly incompressible solids: elements and material models in MSC/NASTRAN.

[55] H. Karlsson, S. Inc., ABAQUS manual, version 6.82ef.

[56] A. T. Patera, A spectral element method for fluid dynamics: Laminar flow in a channel expansion, Journal of Computational Physics 54 (3) (1984) 468 – 488.

[57] M. L. Bittencourt, Fully tensorial nodal and modal shape functions for triangles and tetrahedra, International Journal for Numerical Methods in Engineering 63 (11) (2005) 1530–1558.

[58] M. Ainsworth, J. Coyle, Hierarchic finite element bases on unstructured tetrahedral meshes, International Journal for Numerical Methods in Engineering 58 (14) (2003) 2103–2130.

[59] L. Demkowicz, J. T. Oden, W. Rachowicz, O. Hardy, Toward a universal h-p adaptive finite element strategy, part 1. constrained approximation and data structure, Computer Methods in Applied Mechanics and Engineering 77 (12) (1989) 79 – 112.

[60] J. T. Oden, L. Demkowicz, W. Rachowicz, T. A. Westermann, Toward a universal h-p adaptive finite element strategy, part 2. a posteriori error estimation, Computer Methods in Applied Mechanics and Engineering 77 (12) (1989) 113 – 180.

[61] J. Hesthaven, From electrostatics to almost optimal nodal sets for polynomial interpolation in a simplex, SIAM Journal on Numerical Analysis 35 (2) (1998) 655–676.

[62] M. Taylor, B. Wingate, R. Vincent, An algorithm for computing fekete points in the triangle, SIAM Journal on Numerical Analysis 38 (5) (2000) 1707–1720.

[63] P. Carnevali, R. B. Morris, Y. Tsuji, G. Taylor, New basis functions and computational procedures for p-version finite element analysis, International Journal for Numerical Methods in Engineering 36 (22) (1993) 3759–3779.

[64] X. Zheng, S. Dong, An eigen-based high-order expansion basis for structured spectral elements, Journal of Computational Physics 230 (23) (2011) 8573 – 8602.

[65] S. J. Sherwin, G. E. Karniadakis, A triangular spectral element method; applications to the incompressible Navier-Stokes equations, Computer Methods in Applied Mechanics and Engineering 123 (14) (1995) 189 – 229.

[66] T. C. Warburton, S. J. Sherwin, G. E. Karniadakis, Basis functions for triangular and quadrilateral high-order elements, SIAM Journal on Scientific Computing 20 (5) (1999) 1671–1695.

[67] J. P. Web, R. Abouchacra, Hierarchical triangular elements using orthogonal polynomials, International Journal for Numerical Methods in Engineering 38 (1995) 245–257.

[68] R. Abdul-Rahman, M. Kasper, Higher order triangular basis functions and solution performance of the CG method, Computer Methods in Applied Mechanics and Engineering 197 (14) (2007) 115 – 127.

[69] M. L. Bittencourt, M. G. Vazquez, T. G. Vazquez, Construction of shape functions for the h- and p-versions of the fem using tensorial product, International Journal for Numerical Methods in Engineering 71 (5) (2007) 529–563.

[70] A. Dster, E. Rank, A p-version finite element approach for two- and three-dimensional problems of the j2 flow theory with non-linear isotropic hardening, International Journal for Numerical Methods in Engineering 53 (1) (2002) 49 – 63.

[71] P. Ribeiro, A p-version, first order shear deformation, finite element for geometrically non-linear vibration of curved beams, International Journal for Numerical Methods in Engineering 61 (15) (2004) 2696–2715.

[72] M. L. Bittencourt, T. G. Vazquez, F. F. Bargos, F. A. Furlan, Elementwise least square interpolation and explicit procedures using an eigenvalue based mass matrix, manuscript.

[73] G. E. Karniadakis, M. Israeli, S. Orszag, High-order splitting methods for the incompressible Navier-Stokes equations, Journal of Computational Physics 97 (2) (1991) 414–443.

[74] J. L. Guermond, P. Minev, J. Shen, An overview of projection methods for incompressible flows, Computer Methods in Applied Mechanics and Engineering 195 (4447) (2006) 6011 – 6045.

[75] S. J. Sherwin, M. Casarin, Low-energy basis preconditioning for elliptic substructured solvers based on unstructured spectral/hp element discretization, Journal of Computational Physics 171 (1) (2001) 394–417.

[76] L. Grinberg, D. Pekurovsky, S. J. Sherwin, G. E. Karniadakis, Parallel performance of the coarse space linear vertex solver and low energy basis preconditioner for spectral/hp elements, Parallel Computing 35 (5) (2009) 284–304.

[77] S. Dong, BDF-like methods for nonlinear dynamic analysis, Journal of Computational Physics 229 (8) (2010) 3019 – 3045.

[78] J. Alastruey, K. H. Parker, J. Peiro, S. M. Byrd, S. J. Sherwin, Modelling the circle of Willis to assess the effects of anatomical variations and occlusions on cerebral flows, Journal of Biomechanics 40 (8) (2007) 1794 – 1805.

[79] K. Sunagawa, H. Kanai, M. Tanaka, Simultaneous measurement of blood flow and arterial wall vibrations in radial and axial directions, in: Ultrasonics Symposium, 2000 IEEE, Vol. 2, 2000, pp. 1541 –1544 vol.2.

[80] R. K. Warriner, K. W. Johnston, R. S. C. Cobbold, A viscoelastic model of arterial wall motion in pulsatile flow: implications for Doppler ultrasound clutter assessment, Physiological Measurement 29 (2) (2008) 157–179.

[81] Y. Yu, H. Baek, G. E. Karniadakis, Generalized fictitious methods for fluidstructure interactions: Analysis and simulations, Journal of Computational Physics 245 (0) (2013) 317 – 346.

[82] S. R. Idelsohn, F. Del Pin, R. Rossi, E. Oñate, Fluid-structure interaction problems with strong added-mass effect, International Journal for Numerical Methods in Engineering 80 (10) (2009) 1261–1294.

[83] P. Causin, J. F. Gerbeau, F. Nobile, Added-mass effect in the design of partitioned algorithms for fluid-structure problems, Computer Methods in Applied Mechanics and Engineering 194 (42-44) (2005) 4506 – 4527.

[84] H. J. Steiger, R. Aaslid, S. Keller, H.-J. Reulen, Strength, elasticity and viscoelastic properties of cerebral aneurysms, Heart and Vessels 5 (1989) 41–46.

[85] F. B. Meyer, J. Huston, S. S. Riederer, Pulsatile increases in aneurysm size determined by cine phase-contrast MR angiography, Journal of Neurosurgery 78 (6) (1993) 879–883.

[86] Y. Fung, Biomechanics: Mechanical Properties of Living Tissues, Springer-Verlag, 1993.

[87] E. O. C. Todd C. Doehring, Alan D. Freed, I. Vesely, Fractional order viscoelasticity of the aortic valve cusp: An alternative to quasilinear viscoelasticity, ASME Journal of Biomechanical Engineering 127 (4) (2005) 700–708.

[88] D. Craiem, R. L. Armentano, A fractional derivative model to describe arterial viscoelasticity, Biorheology 44 (4) (2007) 251–263.

[89] M. Lopez-Fernandez, C. Lubich, A. Schadle, Adaptive, fast, and oblivious convolution in evolution equations with memory, SIAM Journal on Scientific Computing 30 (2) (2008) 1015–1037.

[90] S. Larsson, F. Saedpanah, The continuous galerkin method for an integro-differential equation modeling dynamic fractional order viscoelasticity, IMA Journal of Numerical Analysis 30 (4) (2010) 964–986.

[91] I. Podlubny, Fractional differential equations: an introduction to fractional derivatives, fractional differential equations, to methods of their solution and some of their applications, Vol. 198, Academic press, 1998.

[92] D. Valdez-Jasso, D. Bia, Y. Zocalo, R. Armentano, M. Haider, M. Olufsen, Linear and nonlinear viscoelastic modeling of aorta and carotid pressurearea dynamics under in vivo and ex vivo conditions, Annals of Biomedical Engineering 39 (5) (2011) 1438–1456.

[93] A. Lundkvist, E. Lilleodden, W. Siekhaus, J. Kinney, L. Pruitt, M. Balooch, Viscoelastic properties of healthy human artery measured in saline solution by afm-based indentation technique, MRS Proceedings 436.

[94] D. O. Craiem, F. J. Rojo, J. M. Atienza, G. V. Guinea, R. L. Armentano, Fractional calculus applied to model arterial viscoelasticity, Latin American applied research 38 (2) (2008) 141–145.

[95] H. Baek, M. V. Jayaraman, G. E. Karniadakis, Wall shear stress and pressure distribution on aneurysms and infundibulae in the posterior communicating artery bifurcation, Annals of Biomedical Engineering 37 (12) (2009) 2469–2487.

[96] M. Zamir, The physics of pulsatile flow, Springer, 2000.

[97] H. Baek, G. E. Karniadakis, Sub-iteration leads to accuracy and stability enhancements of semi-implicit schemes for the Navier-Stokes equations, Journal of Computational Physics 230 (12) (2011) 4384 – 4402.

[98] H. Baek, M. Jayaraman, P. Richardson, G. Karniadakis, Flow instability and wall shear stress variation in intracranial aneurysms, Journal of The Royal Society Interface 7 (47) (2010) 967–988.

[99] M. D. Ford, G. R. Stuhne, H. N. Nikolov, D. F. Habets, S. P. Lownie, D. W. Holdsworth, D. A. Steinman, Virtual angiography for visualization and validation of computational models of aneurysm hemodynamics, Medical Imaging, IEEE Transactions on 24 (12) (2005) 1586–1592.

[100] R. Torii, M. Oshima, T. Kobayashi, K. Takagi, T. E. Tezduyar, Computer modeling of cardiovascular fluid-structure interactions with the deforming-spatial-domain/stabilized space-time formulation, Computer Methods in Applied Mechanics and Engineering 195 (13-16) (2006) 1885 – 1895.

[101] T. E. Tezduyar, K. Takizawa, T. Brummer, P. R. Chen, Space-time fluid-structure interaction modeling of patient-specific cerebral aneurysms, International Journal for Numerical Methods in Biomedical Engineering 27 (11) (2011) 1665–1710.

[102] R. Torii, M. Oshima, T. Kobayashi, K. Takagi, T. E. Tezduyar, Influencing factors in image-based fluid-structure interaction computation of cerebral aneurysms, International Journal for Numerical Methods in Fluids 65 (1-3) (2011) 324–340.

[103] E. Jarvinen, P. Raback, M. Lyly, J.-P. Salenius, A method for partitioned fluid-structure interaction computation of flow in arteries, Medical Engineering & Physics 30 (7) (2008) 917 – 923.

[104] P. Crosetto, P. Reymond, S. Deparis, D. Kontaxakis, N. Stergiopulos, A. Quarteroni, Fluid-structure interaction simulation of aortic blood flow, Computers & Fluids 43 (1) (2011) 46 – 57.

[105] P. Crosetto, S. Deparis, G. Fourestey, A. Quarteroni, Parallel algorithms for fluid-structure interaction problems in haemodynamics, SIAM Journal on Scientific Computing 33 (4) (2011) 1598–1622.

[106] F. Nobile, C. Vergara, An effective fluid-structure interaction formulation for vascular dynamics by generalized Robin conditions, SIAM Journal on Scientific Computing 30 (2) (2008) 731–763.

[107] Y. Bazilevs, M. C. Hsu, Y. Zhang, W. Wang, X. Liang, T. Kvamsdal, R. Brekken, J. G. Isaksen, A fully-coupled fluid-structure interaction simulation of cerebral aneurysms, Computational Mechanics 46 (1) (2010) 3–16.

[108] M. C. Hsu, Y. Bazilevs, Blood vessel tissue prestress modeling for vascular fluid-structure interaction simulation, Finite Elements in Analysis and Design 47 (6) (2011) 593–599.

[109] J. F. Gerbeau, M. Vidrascu, A quasi-Newton algorithm based on a reduced model for fluid-structure interaction problems in blood flows, Esaim-Mathematical Modelling and Numerical Analysis-Modelisation Mathematique Et Analyse Numerique 37 (4) (2003) 631–647.

[110] J. Degroote, A. Swillens, P. Bruggeman, R. Haelterman, P. Segers, J. Vierendeels, Simulation of fluid-structure interaction with the interface artificial compressibility method, International Journal for Numerical Methods in Biomedical Engineering 26 (3-4) (2010) 276–289.

[111] F. Nobile, Coupling strategies for the numerical simulation of blood flow in deformable arteries by 3d and 1d models, Mathematical and Computer Modelling 49 (11-12) (2009) 2152–2160.

[112] M. Astorino, F. Chouly, M. A. Fernández, Robin based semi-implicit coupling in fluid-structure interaction: Stability analysis and numerics, SIAM Journal on Scientific Computing 31 (6) (2009) 4041–4065.

[113] S. Badia, F. Nobile, C. Vergara, Fluid-structure partitioned procedures based on Robin transmission conditions, Journal of Computational Physics 227 (14) (2008) 7027–7051.

[114] S. Badia, F. Nobile, C. Vergara, Robin-Robin preconditioned Krylov methods for fluid-structure interaction problems, Computer Methods in Applied Mechanics and Engineering 198 (33-36) (2009) 2768–2784.

[115] M. W. Gee, U. Kuttler, W. A. Wall, Truly monolithic algebraic multigrid for fluid-structure interaction, International Journal for Numerical Methods in Engineering 85 (8) (2011) 987–1016.

[116] J. Degroote, J. Vierendeels, Multi-solver algorithms for the partitioned simulation of fluid-structure interaction, Computer Methods in Applied Mechanics and Engineering 200 (25-28) (2011) 2195–2210.

[117] M. M. Joosten, W. G. Dettmer, D. Peric, Analysis of the block Gauss-Seidel solution procedure for a strongly coupled model problem with reference to fluid-structure interaction, International Journal for Numerical Methods in Engineering 78 (7) (2009) 757–778.

[118] G. Guidoboni, R. Glowinski, N. Cavallini, S. Canic, Stable loosely-coupled-type algorithm for fluid-structure interaction in blood flow, Journal of Computational Physics 228 (18) (2009) 6916–6937.

[119] C. Michler, H. van Brummelen, R. de Borst, An investigation of interface-GMRES(R) for fluid-structure interaction problems with flutter and divergence, Computational Mechanics 47 (1) (2011) 17–29.

[120] F. X. Roux, J. D. Garaud, Domain decomposition methodology with Robin interface matching conditions for solving strongly coupled fluid-structure problems, International Journal for Multiscale Computational Engineering 7 (1) (2009) 29–38.

[121] Y. Yu, H. Baek, M. L. Bittencourt, G. E. Karniadakis, Mixed spectral/hp element formulation for nonlinear elasticity, Computer Methods in Applied Mechanics and Engineering 213 - 216 (0) (2012) 42 – 57.

[122] E. Burman, M. A. Fernández, Stabilization of explicit coupling in fluid-structure interaction involving fluid incompressibility, Computer Methods in Applied Mechanics and Engineering 198 (5-8) (2009) 766–784.

[123] C. Förster, W. A. Wall, E. Ramm, Artificial added mass instabilities in sequential staggered coupling of nonlinear structures and incompressible viscous flows, Computer Methods in Applied Mechanics and Engineering 196 (7) (2007) 1278 – 1293.

[124] U. Kuttler, W. A. Wall, Fixed-point fluid-structure interaction solvers with dynamic relaxation, Computational Mechanics 43 (1) (2008) 61–72.

[125] S. Deparis, M. A. Fernández, L. Formaggia, Acceleration of a fixed point algorithm for fluid-structure interaction using transpiration conditions, ESAIM: Mathematical Modelling and Numerical Analysis 37 (04) (2003) 601–616.

[126] J. Degroote, K.-J. Bathe, J. Vierendeels, Performance of a new partitioned procedure versus a monolithic procedure in fluid-structure interaction, Computers & Structures 87 (11-12) (2009) 793 – 801.

[127] A. T. Barker, X.-C. Cai, NKS for fully coupled fluid-structure interaction with application, in: Domain Decomposition Methods in Science and Engineering XVIII, Vol. 70 of Lecture Notes in Computational Science and Engineering, Springer Berlin Heidelberg, 2009, pp. 275–282.

[128] H. G. Matthies, J. Steindorf, Partitioned strong coupling algorithms for fluid-structure interaction, Computers & Structures 81 (8-11) (2003) 805 – 812.

[129] J. Vierendeels, L. Lanoye, J. Degroote, P. Verdonck, Implicit coupling of partitioned fluid-structure interaction problems with reduced order models, Computers & Structures 85 (11-14) (2007) 970 – 976.

[130] D. Mok, W. Wall, E. Ramm, Accelerated iterative substructuring schemes for instationary fluid-structure interaction, in: First MIT conference on computational fluid and solid mechanics, Elsevier, Cambridge, MA, USA, 2001.

[131] S. Deparis, M. Discacciati, A. Quarteroni, A domain decomposition framework for fluid-structure interaction problems, in: C. Groth, D. W. Zingg (Eds.), Computational Fluid Dynamics 2004, Springer Berlin Heidelberg, 2006, pp. 41–58.

[132] J. Degroote, On the similarity between Dirichlet-Neumann with interface artificial compressibility and Robin-Neumann schemes for the solution of fluid-structure interaction problems, Journal of Computational Physics 230 (17) (2011) 6399–6403.

[133] E. Burman, M. A. Fernández, Stabilized explicit coupling for fluid-structure interaction using Nitsche's method, Comptes Rendus Mathematique 345 (8) (2007) 467 – 472.

[134] R. Govardhan, C. H. K. Williamson, Resonance forever: existence of a critical mass and an infinite regime of resonance in vortex-induced vibration, Journal of Fluid Mechanics 473 (2002) 147–166.

[135] C. H. K. Williamson, R. Govardhan, Vortex-induced vibrations, Annual Review of Fluid Mechanics 36 (2004) 413–455.

[136] T. J. R. Hughes, W. K. Liu, T. K. Zimmermann, Lagrangian-Eulerian finite element formulation for incompressible viscous flows, Computer Methods in Applied Mechanics and Engineering 29 (3) (1981) 329 – 349.

[137] A. Quarteroni, L. Formaggia, Mathematical modelling and numerical simulation of the cardiovascular system, in: N. Ayache (Ed.), Computational Models for the Human Body, Vol. 12 of Handbook of Numerical Analysis, Elsevier, 2004, pp. 3 – 127.

[138] S. S. Chen, H. Chung, Design guide for calculating hydrodynamics mass, part i: circular cylindrical structures, Argonne National Laboratory, Report No. ANL-CT-76-45.

[139] D. J. Newman, G. E. Karniadakis, A direct numerical simulation study of flow past a freely vibrating cable, Journal of Fluid Mechanics 344 (1997) 95–136.

[140] D. Shiels, A. Leonard, A. Roshko, Flow-induced vibration of a circular cylinder at limiting structural parameters, Journal of Fluids and Structures 15 (1) (2001) 3 – 21.

[141] J. P. Den Hartog, Mechanical VIbrations, Dover, 1934.

[142] J. R. Hutchinson, Shear coefficients for Timoshenko beam theory, Journal of Applied Mechanics 68 (1) (2001) 87–92.

[143] H. Tomiyama, A. Yamashina, T. Arai, K. Hirose, Y. Koji, T. Chikamori, S. Hori, Y. Yamamoto, N. Doba, S. Hinohara, Influences of age and gender on results of noninvasive brachial-ankle pulse wave velocity measurementa survey of 12517 subjects, Atherosclerosis 166 (2) (2003) 303 – 309.

[144] E. Burman, M. A. Fernández, Explicit strategies for incompressible fluid-structure interaction problems: Nitsche type mortaring versus robin–robin coupling, International Journal for Numerical Methods in Engineering 97 (10) (2014) 739–758.

[145] F. Hecht, New development in freefem++, Journal of Numerical Mathematics 20 (3-4) (2012) 251–265.

[146] J. M. Cimbala, S. Garg, Flow in the wake of a freely rotatable cylinder with splitter plate, AIAA journal 29 (6) (1991) 1001–1003.

[147] J. C. Owen, P. W. Bearman, A. A. Szewczyk, Passive control of VIV with drag reduction, Journal of Fluids and Structures 15 (34) (2001) 597 – 605.

[148] G. R. S. Assi, P. W. Bearman, N. Kitney, Low drag solutions for suppressing vortex-induced vibration of circular cylinders, Journal of Fluids and Structures 25 (4) (2009) 666 – 675.

[149] G. R. S. Assi, P. W. Bearman, M. A. Tognarelli, J. R. H. Rodrigues, The effect of rotational friction on the stability of short-tailed fairings suppressing vortex-induced vibrations, in: Proceedings of OMAE2011, 30th International Conference on Ocean, Offshore and Arctic Engineering, Rotterdam, The Netherlands, 2011.

[150] I. Korkischko, J. R. Meneghini, Experimental investigation of flow-induced vibration on isolated and tandem circular cylinders fitted with strakes, Journal of Fluids and Structures 26 (4) (2010) 611–625.

[151] G. Assi, P. Bearman, N. Kitney, M. Tognarelli, Suppression of wake-induced vibration of tandem cylinders with free-to-rotate control plates, Journal of Fluids and Structures 26 (7) (2010) 1045–1057.

[152] S. Dong, G. S. Triantafyllou, G. E. Karniadakis, Elimination of vortex streets in bluff-body flows, Physical Review Letters 100 (20) (2008) 204501.

[153] M. M. Zdravkovich, Review and classification of various aerodynamic and hydrodynamic means for suppressing vortex shedding, Journal of Wind Engineering and Industrial Aerodynamics 7 (2) (1981) 145–189.

[154] M. J. Every, R. King, D. S. Weaver, Vortex-excited vibrations of cylinders and cables and their suppression, Ocean Engineering 9 (2) (1982) 135–157.

[155] I. Borazjani, L. Ge, F. Sotiropoulos, Curvilinear immersed boundary method for simulating fluid-structure interaction with complex 3d rigid bodies, Journal of Computational Physics 227 (16) (2008) 7587–7620.

[156] S. Dong, G. E. Karniadakis, C. Chryssostomidis, A robust and accurate outflow boundary condition for incompressible flow simulations on highly-truncated unbounded domains, submitted to Journal of Computational Physics.

[157] Y. Yu, H. Yan, Y. Constantinides, O. Oakley, G. E. Karniadakis, Suppression of vortex-induced vibrations by fairings: a numerical study, Submitted to Journal of Fluids and Structures.

[158] Y. Yu, J. Guzman, G. E. Karniadakis, A penalty method for coupling fluid-structure interactions, In preparation.

[159] T. C. Warburton, S. J. Sherwin, G. E. Karniadakis, Nektar v4.0.1 an hp finite element code for CFD.